

INFORMATION TO USERS

This was produced from a copy of a document sent to us for microfilming. While the most advanced technological means to photograph and reproduce this document have been used, the quality is heavily dependent upon the quality of the material submitted.

The following explanation of techniques is provided to help you understand markings or notations which may appear on this reproduction.

1. The sign or "target" for pages apparently lacking from the document photographed is "Missing Page(s)". If it was possible to obtain the missing page(s) or section, they are spliced into the film along with adjacent pages. This may have necessitated cutting through an image and duplicating adjacent pages to assure you of complete continuity.
2. When an image on the film is obliterated with a round black mark it is an indication that the film inspector noticed either blurred copy because of movement during exposure, or duplicate copy. Unless we meant to delete copyrighted materials that should not have been filmed, you will find a good image of the page in the adjacent frame. If copyrighted materials were deleted you will find a target note listing the pages in the adjacent frame.
3. When a map, drawing or chart, etc., is part of the material being photographed the photographer has followed a definite method in "sectioning" the material. It is customary to begin filming at the upper left hand corner of a large sheet and to continue from left to right in equal sections with small overlaps. If necessary, sectioning is continued again—beginning below the first row and continuing on until complete.
4. For any illustrations that cannot be reproduced satisfactorily by xerography, photographic prints can be purchased at additional cost and tipped into your xerographic copy. Requests can be made to our Dissertations Customer Services Department.
5. Some pages in any document may have indistinct print. In all cases we have filmed the best available copy.

University
Microfilms
International

300 N. ZEEB RD., ANN ARBOR, MI 48106

8200324

ANTOS, RONALD LEON

THE INFLUENCE OF ADJACENCY EFFECTS ON THE RESTORATION OF
NOISY PHOTOGRAPHIC IMAGES

The University of Arizona

PH.D. 1981

University
Microfilms
International 300 N. Zeeb Road, Ann Arbor, MI 48106

THE INFLUENCE OF ADJACENCY EFFECTS ON THE
RESTORATION OF NOISY PHOTOGRAPHIC IMAGES

by

Ronald Leon Antos

A Dissertation submitted to the Faculty of the
COMMITTEE ON OPTICAL SCIENCES (GRADUATE)

In Partial Fulfillment of the Requirements
For the Degree of

DOCTOR OF PHILOSOPHY

In the Graduate College

THE UNIVERSITY OF ARIZONA

1981

THE UNIVERSITY OF ARIZONA
GRADUATE COLLEGE

As members of the Final Examination Committee, we certify that we have read
the dissertation prepared by Ronald Leon Antos

entitled The Influence of Adjacency Effects on the Restoration of
Noisy Photographic Images

and recommend that it be accepted as fulfilling the dissertation requirement
for the Degree of Doctor of Philosophy.

Jack D. Graskill

12/15/80
Date

P. N. Slater

12/15/80
Date

James J. Burke

12/15/80
Date

Date

Date

Final approval and acceptance of this dissertation is contingent upon the
candidate's submission of the final copy of the dissertation to the Graduate
College.

I hereby certify that I have read this dissertation prepared under my
direction and recommend that it be accepted as fulfilling the dissertation
requirement.

J.J. Burke by Jack D. Graskill
Dissertation Director

8/10/81
Date

STATEMENT BY THE AUTHOR

This dissertation has been submitted in partial fulfillment of requirements for an advanced degree at The University of Arizona and is deposited in the University Library to be made available to borrowers under rules of the Library.

Brief quotations from this dissertation are allowable without special permission, provided that accurate acknowledgment of source is made. Requests for permission for extended quotation from or reproduction of this manuscript in whole or in part may be granted by the head of the major department or the Dean of the Graduate College when in his judgment the proposed use of the material is in the interests of scholarship. In all other instances, however, permission must be obtained from the author.

SIGNED: Ronald Leon Curtis

ACKNOWLEDGEMENTS

The completion of a dissertation "in absentia" is as much a test of dedication and planning ability as it is of technical ability. This is particularly true when one is raising a family. My wife, Pat, has been a constant source of faith in my ability and encouragement throughout my effort to complete this program of study. Her patience is truly admirable and I am forever indebted to her for this support. To my sons, Christopher and Brian, I give thanks for their understanding and sacrifice of some of the time that we could have shared together. I hope that these years of effort have a positive effect on their understanding of the importance of continued education. I am also most appreciative of my parents for providing the initial opportunity for my education.

The subject of this study was proposed by Jim Burke, my dissertation advisor. His inherent interest in the subject of image processing, technical advice and continued encouragement are greatly appreciated. He has always found the time to share his insight into the details of the this topic. This appreciation is also extended to Phil Slater, Jack Gaskill and Roland Shack. Their instruction and overall counseling regarding my graduate curriculum and the arrangement of financial assistantship support during my internship at the Optical Sciences Center enabled the completion of this degree and further broadened my interest in optics. Also, I am very grateful for the opportunity that I had to work with Bob Schowenderdt, on the Landsat Program referenced in Chapter 2. The approach I used in the development of the software supporting this dissertation was based on concepts I learned under Bob's guidance.

I would also like to thank all those that provided instrumentation support, computer resources and technical consultation. Eastman Kodak Company for the laboratory support which helped me to obtain all of the calibrated photographic images. C. N. "Kelly" Nelson, who was kind enough to review my results and provide additional insight into his previous investigation of

adjacency effects. Mead Technology Laboratories (formerly Data Corporation and an Industrial Associate of the Optical Sciences Center) for microdensitometer support. Particularly, Lsyle Cahill and Jim Madden for their encouragement and support of a "leave of absence" policy which allowed my enrollment in the Optical Sciences program. Also, Arnie Fife and Jim Berteri for providing the microdensitometer data and the associated instrument calibration data. Xerox Corporation, for overall support during the data analysis and composition phases of this study. Particularly, J. Terrance Flynn, Pierre Lavallee, Rodney Shaw and Vsevolod Mihajlov for their interest, encouragement and arrangement of the computer resources. Don Lehmbeck and Jim Jakubowski for their initial suggestions regarding the use of the Zeiss microdensitometer and the Sigma computer facilities. Also, Bruce Levine for consultation regarding his previous application of cubic spline functions and Sidney Marshall for advise concerning the computer composition of this manuscript.

In addition, I sincerely appreciate the efforts of Norma Emptage of the Optical Sciences Center for providing outstanding coordination with regards to my continued enrollment as a student "in absentia" and for her suggestions regarding my preparation of this manuscript.

TABLE OF CONTENTS

| | Page |
|--|------|
| LIST OF ILLUSTRATIONS | vii |
| LIST OF TABLES | xi |
| ABSTRACT | xii |
| 1. INTRODUCTION | 1 |
| Problem Definition | 1 |
| Historical Background | 2 |
| Outline of Remaining Chapters | 4 |
| 2. DERIVATION OF STATISTICAL RESTORATION MODEL | 6 |
| Edge and Line Effects | 6 |
| Definition of Terms | 8 |
| Optical Scattering Stage | 13 |
| Chemical Diffusion Stage | 15 |
| Photographic System Model | 22 |
| System Model Comparisons | 24 |
| 3. EXPERIMENTAL APPROACH | 31 |
| Experimental Design | 31 |
| Radiometric Sources | 32 |
| Object Target Description | 33 |
| Film and Process Selection | 36 |
| Experimental Procedure | 39 |
| 4. DATA SAMPLING AND PREPROCESSING | 41 |
| Description of Microdensitometer System | 41 |
| Data Sampling Requirements | 42 |
| Sampling Theorem Requirements | 42 |
| Digital Preprocessing Considerations | 43 |
| Selection of Film Scanning Parameters | 44 |
| Microdensitometer Calibration Results | 46 |
| Mann-Data Micro-Analyzer | 46 |
| Modified Zeiss SPM05 | 53 |

TABLE OF CONTENTS -- Continued

| | Page |
|--|------|
| Sensitometric Calibration | 57 |
| Characteristic Curves | 57 |
| Callier's Q Factor | 60 |
| Mass of Silver Conversion | 67 |
| 5. IMAGE RESTORATION ANALYSIS | 69 |
| Determination of the Chemical Spread Function (CSF) | 69 |
| Edge Data Preprocessing | 69 |
| Nelson's CSF Algorithm | 70 |
| Similiarity to Edge Gradient Analysis (EGA) | 72 |
| Edge Noise Smoothing Algorithms | 74 |
| Calculation of Smooth CSF's | 78 |
| Evaluation of the Eberhard Effect (EE) | 96 |
| EE for Exposure Levels | 96 |
| Magnitude Estimate of EE | 98 |
| Eberhard Ratio Calculations | 101 |
| Application of Image Restoration "Recipe" | 109 |
| Selection of One Dimensional Images | 109 |
| Data Resampling Considerations | 110 |
| Review of Gross Grain Mass of Silver Algorithm (GGMSA) | 111 |
| Analysis Approach | 112 |
| Restoration of Line Images | 114 |
| 6. CONCLUSIONS | 148 |
| Summary of Results | 148 |
| Experimental Error Sources | 151 |
| Recommendations | 152 |
| APPENDIX A: U.M.L.E. OF THE IDEAL IMAGE | 154 |
| APPENDIX B: RMS ERROR OF THE IDEAL IMAGE | 156 |
| APPENDIX C: U.M.L.E. OF THE LATENT IMAGE | 157 |
| APPENDIX D: DERIVATION OF THE DIFFERENTIAL MEAN | |
| GRAIN DENSITY | 159 |
| APPENDIX E: THEORETICAL COMPARISON TO NELSON'S MODEL | 162 |
| REFERENCES | 164 |

LIST OF ILLUSTRATIONS

| Figure | Page |
|---|------|
| 2.1. Edge boundary | 7 |
| 2.2. Eberhard Effect | 9 |
| 2.3. Statistical model | 10 |
| 2.4. Model representation in terms of cell elements | 11 |
| 2.5. Edge effect | 19 |
| 2.6. Burke's photographic system restoration model | 23 |
| 2.7. Nelson's photographic system forward model | 25 |
| 2.8. Eikonex photographic system forward model | 28 |
| 2.9. Eikonex photographic system inverse model | 29 |
| 3.1. Illumination contour plot | 34 |
| 3.2. Vertical profile of x-ray slit targets | 35 |
| 3.3. "Tri-slit" x-ray target | 35 |
| 3.4. Apparent modulation transfer function for Panatomic-X for two development conditions | 38 |
| 4.1. Calibration edge spectrum. Mann-Data Micro-Analyzer (0.001 mm. x 0.080 mm. slit) | 47 |
| 4.2. Calibration edge spectrum: focusing - alignment effects. Mann-Data Micro-Analyzer (0.001 mm. x 0.080 mm. slit) | 49 |
| 4.3. Calibration edge spectrum: hysteresis effects. Mann-Data Micro-Analyzer (0.001 mm. x 0.080 mm. slit) | 50 |
| 4.4. Calibration edge spectrum. Mann-Data Micro-Analyzer (0.005 mm. circular aperture) | 51 |

LIST OF ILLUSTRATIONS -- Continued

| Figure | Page |
|---|------|
| 4.5. Calibration edge spectrum. Mann-Data Micro-Analyzer (0.005 mm. circular aperture) | 52 |
| 4.6. Calibration edge spectrum. Zeiss microdensitometer (0.005 mm. x 0.080 mm. slit aperture) | 54 |
| 4.7. Calibration edge spectrum: focusing - alignment effects. Zeiss microdensitometer (0.005 mm. x 0.080 mm. slit aperture) | 55 |
| 4.8. Calibration edge spectrum: hysteresis effects. Zeiss microdensitometer (0.005 mm. x 0.080 mm. slit aperture) | 56 |
| 4.9. Sensitometric curve: x-ray exposure quanta | 59 |
| 4.10. Sensitometric curve: light exposure quanta | 61 |
| 4.11. Callier Q factor for Micro-Analyzer | 64 |
| 4.12. Callier Q factor for Zeiss microdensitometer | 65 |
| 4.13. Mass of silver conversion curve | 68 |
| 5.1. Edge data from images created by X-ray exposures. Selected edges from 1.0 mm. line width set | 71 |
| 5.2. Nelson's CSF calculated from edge number 5. Analysis used discrete edge derivative | 73 |
| 5.3. Exponential fit to data from edge number 5 | 76 |
| 5.4. Cubic spline fit to data from edge number 1 | 84 |
| 5.5. Cubic spline fit to data from edge number 2 | 85 |
| 5.6. Cubic spline fit to data from edge number 3 | 86 |
| 5.7. Cubic spline fit to data from edge number 4 | 87 |
| 5.8. Cubic spline fit to data from edge number 5 | 88 |
| 5.9. Nelson's CSF from analytic fit of edge number 1 | 89 |
| 5.10. Nelson's CSF from analytic fit of edge number 2 | 90 |
| 5.11. Nelson's CSF from analytic fit of edge number 3 | 91 |

LIST OF ILLUSTRATIONS -- Continued

| Figure | Page |
|--|------|
| 5.12. Nelson's CSF from analytic fit of edge number 4 | 92 |
| 5.13. Nelson's CSF from analytic fit of edge number 5 | 93 |
| 5.14. Integrated area under analytic CSF | 95 |
| 5.15. Eberhard effect from X-ray exposures | 97 |
| 5.16. Eberhard effect as a function of mass of silver | 99 |
| 5.17. Eberhard effect as a function of density | 100 |
| 5.18. Eberhard ratio as a function of mass of silver for Nelson's data | 103 |
| 5.19. Eberhard ratio as a function of density for Nelson's data. | 104 |
| 5.20. Eberhard ratio as a function of mass of silver for experimental data | 105 |
| 5.21. Eberhard ratio as a function of density for experimental data | 106 |
| 5.22. Restoration analysis procedure | 113 |
| 5.23. CSF obtained from edge number 5 | 116 |
| 5.24. Modulus of CTF for edge number 5. | 117 |
| 5.25. Density profiles for 0.5 mm. line widths (lines number 7, 8 and 9) | 118 |
| 5.26. Density profile for 0.5 mm. line width (line number 8) | 119 |
| 5.27. Mass of silver profiles for 0.5 mm. line widths (lines number 7, 8 and 9) | 120 |
| 5.28. Mass of silver profile for 0.5 mm. line width (line number 8) | 121 |
| 5.29. Modulus of input spectrum (line number 8). | 122 |
| 5.30. Product of CTF modulus and input modulus (line number 8). | 123 |
| 5.31. Reduction product term for 0.5 mm. line widths (lines number 7, 8 and 9) | 124 |
| 5.32. Reduction product term for 0.5 mm. line width (line number 8) | 125 |
| 5.33. Gross grain mass of silver for 0.5 mm. line width (line number 8) | 126 |
| 5.34. Correction ratio for 0.5 mm. line width (line number 8) | 127 |

LIST OF ILLUSTRATIONS -- Continued

| Figure | Page |
|--|------|
| 5.35. Gross grain density for 0.5 mm. line width (line number 8) | 129 |
| 5.36. Gross grain density (line number 8) compared to target image density profiles (lines number 7, 8 and 9) | 130 |
| 5.37. Modulus of CTF for edges number 1 and 5 | 131 |
| 5.38. Product of edge modulus values and input modulus (line number 8) | 132 |
| 5.39. Correction ratio for 0.5 mm. line width (line number 8) using two CSF values . . | 133 |
| 5.40. Gross grain density for 0.5 mm. line width (line number 8) using two CSF values. | 134 |
| 5.41. Gross grain mass of silver for 0.5 mm. line width (line number 8) using several beta values | 136 |
| 5.42. Correction ratio for 0.5 mm. line width (line number 8) using several beta values . | 137 |
| 5.43. Gross grain density for 0.5 mm. line width (line number 8) using several beta values | 138 |
| 5.44. Density profiles for 10 cycle/ mm. line images | 139 |
| 5.45. Product of CTF modulus and input modulus (10 cycle/ mm. line images) | 140 |
| 5.46. Reduction product term for 10 cycle/ mm. line images | 141 |
| 5.47. Gross grain mass of silver for 10 cycle/ mm. line images | 142 |
| 5.48. Correction ratio for 10 cycle/ mm. line images | 143 |
| 5.49. Gross grain density for 10 cycle/ mm. line images | 144 |
| 5.50. Gross grain density for 19.56 and 25.12 cycle/ mm. line images | 146 |
| 5.51. Gross grain density for 15.85 and 39.82 cycle/ mm. line images | 147 |

LIST OF TABLES

| Table | Page |
|--|------|
| 3.1 Resolution target spatial frequency values | 36 |
| 3.2. Experimental exposure and processing parameters. | 39 |
| 4.1. Microdensitometer scanning parameters for film images. | 44 |
| 4.2. Large area diffuse density data | 58 |
| 4.3. Large area specular density data | 63 |
| 5.1. Cubic spline parameters: Edge number 1 | 79 |
| 5.2. Cubic spline parameters: Edge number 2 | 80 |
| 5.3. Cubic spline parameters: Edge number 3 | 81 |
| 5.4. Cubic spline parameters: Edge number 4 | 82 |
| 5.5. Cubic spline parameters: Edge number 5 | 83 |
| 5.6. Chemical spread function area values | 94 |
| 5.7. Calculation of Eberhard ratios from experimental data | 107 |
| 5.8. Calculation of Eberhard ratios from Nelson's published data | 108 |
| 5.9. Selected line images for use in restoration "recipe" | 110 |
| 6.1. Restoration summary for magnitude of correction | 149 |

ABSTRACT

The objective of this study was to enable the removal of developer depletion and diffusion effects (ie., adjacency effects) from noisy photographic images, thus, providing a potential for improvement in the reliability of restored object and aerial image estimates. The investigation was based on the use of a previously formulated image restoration model which characterized the exposure, latent image and development interactions of the photographic process in terms of statistical estimation theory. This study addressed the application and appropriate modification of the formulated model in the removal of adjacency effects from noisy images of selected line targets.

Literature pertaining to the initial observations of adjacency effects, their recognition as a nonlinear chemical development effect and the pertinent models (forward) used to predict their effects was reviewed. This was followed with a review of the statistical restoration (inverse) model and its comparison to previously derived forward models.

X-ray quanta exposures were then used to obtain noisy photographic images, free of optical scattering effects, for the purpose of empirically determining a chemical spread function to characterize chemical adjacency effects. Photographic images were obtained that contained lines of 0.010, 0.100 and 1.000 mm widths to enable comparison between the magnitude of the chemical spread function and the Eberhard effect. A segmented polynomial (cubic spline function) approach was used to calculate the chemical spread function. Separate light quanta exposures were used to obtain gross grain density sensitometric curves and noisy line images. The covering power relationship between mass of developed silver and diffuse density was empirically derived for Panatomic-X film processed without agitation in D-76 developer (diluted 1:1).

Empirical verification of the statistical restoration model was achieved. Chemical adjacency effects were successfully removed from noisy line images using an appropriately scaled version of the statistical restoration model. The spatial frequency content of the noisy line images was approximately 1, 10, 15, 20, 25 and 40 cycles/mm. The proportionality factor, used to scale the chemical spread function required in the restoration model, was found to be equivalent to the ratio of the empirically derived chemical spread function and a magnitude estimate of the Eberhard effect. The maximum diffuse density correction for edge effects was found to be 0.14, or approximately 11.1% of the gross grain density level, 1.20. Similar diffuse density corrections for fine line images were found to range between 0.14 and 0.36, or approximately 11.1% to 28.3% of the gross grain density level associated with a specific line element.

CHAPTER 1

INTRODUCTION

Scientific applications of photographic film to obtain information about various object scenes have been well documented. In some of these applications, particularly in aerial reconnaissance and astronomical photography, the information gathering capability of the photographic material is stretched to its limits. Cases of very low contrast images nearing the sensitivity threshold of the film, resolution requirements limited by granularity and mensuration requirements of the order of a few micrometers are typical examples. Due to the importance of these applications analytic methods have been developed in an attempt to make maximum use of the recorded information. The evolution of these methods has required that they accurately model the complicated physical process that takes place during exposure and development of the material. In addition, that the resources required to use the model be reasonable for the application intended.

The subject of this thesis concerns the development and application such a model. The inherent nonlinearities of the photographic process are investigated in the context of a model capable of enabling the restoration of noisy photographic images.

Problem Definition

The problem was to develop an analytical characterization of the photographic process sufficient to the task of obtaining a reliable estimate of the object that produced a noisy photographic image. Because the photographic image consists of a random distribution of silver grains, it is reasonable to expect that the restoration of a noisy image can be accomplished by the application of statistical estimation theory. An initial formulation of this kind has been developed,

predicated on a statistical model relating the developed image, the latent image, the exposure image and the estimated object (Burke, 1974). This study addresses the theoretical development and initial experimental investigation of a portion of this statistical model. Primary emphasis is placed on compensation for developer depletion and diffusion effects (ie. adjacency effects). Edge and line target x-ray exposures were used to quantify nonlinear diffusion effects.

Restoration procedures were initiated by removal of these nonlinear effects from photographic line images without the requirement of noise smoothing procedures. Several assumptions made during the development of the model are reviewed in terms of experimental results. Several recommendations for future work are given to add further clarification to the limits to which this model can be applied. Extensive software was developed toward the application and understanding of the model.

Historical Background

Early scientific applications made use of only the large-area sensitometric characteristics of a photographic material (Hurter and Driffield, 1890). As time passed, however, changes in density level were observed that could not be explained by the theory of the characteristic curve. These effects were mainly attributed to local changes in the rate of development and inhibiting action of reaction products (Colson, 1898).

The chemical nature of these effects was recognized but the details were disputed. One of the initial systematic studies of these effects provided the first densitometric evidence of their existence (Eberhard, 1912, and 1926). In these studies Eberhard referred to the "Nachbareffekt" which was translated as "adjacency effect". Further insight was then provided by many investigators and several descriptors were adopted such as Eberhard effect, Kostinsky effect, Ross effect and edge effects which include border and fringe effects (Barrows and Wolfe, 1971).

The true significance of adjacency effects was not appreciated until after the application of Fourier techniques in the analysis of optical systems (Duffieux, 1970; and Hopkins, 1950 and 1956) and television systems (Schade, 1951 and 1955). This approach was widely used in the characterization of optical and photographic systems (Fellgett and Linfoot, 1955; O'Neill, 1955; Marechal 1956; and Ingelstram, 1956). A thorough review of the overall significance of these and other investigators is well documented (Ingelstam, 1960; Mees and James, 1966; and Dainty and Shaw, 1974).

Initial applications to the treatment of adjacency effects emphasized the caution that must be used in applying a linear systems theory to a nonlinear problem (Powell, 1959 and 1961; Hendeberg, 1960). In the presence of adjacency effects the output spatial frequency response would not be independent of the input target as demonstrated by edge, line and sine wave input targets. Early mathematical models were proposed to predict the spatial frequency response, but none really described the overall physical process (Eyer, 1958; and Sayanagi, 1960).

The first significant attempt at a physical description was Kelly's (1960) three- stage, nonlinear isotropic model. Kelly combined Fourier methods of system analysis with the large-area characteristic curve (zero frequency characterization) to obtain descriptions for three successive physical processes defined as optical scattering, large-area sensitometry and chemical diffusion. This was immediately followed by a description of experimental techniques that could be used for determining the optical scattering and chemical diffusion spread functions (Kelly, 1961). The model predicted output density values for given input exposure values and set the basic framework for future models.

The chemical diffusion transfer function was considered as a negative feedback component of shorter bandwidth than that of the positive image component (Schade, 1974). The use of such a linear filter to represent the nonlinear diffusion process was further investigated with additional models proposed (Simonds, 1964; Nelson, 1971).

Simonds attempted to account for linear and nonlinear interactions by using optical and chemical spread functions that were combined prior to large-area sensitometric correction. Nelson's model expanded upon Kelly's (1960) third stage through the use of an isotropic nonlinear formula. The model predicted film density values corrected for adjacency effects for a given input exposure profile. It was very significant in that it related terms that represented image density values free of development retardation to an inhibition or retardation term based on the use of a chemical spread function. Nelson experimentally verified that the model accurately predicted adjacency effects for edge exposures of moderate and low contrast. The model was also used to predict the apparent overall system modulation transfer function (Higgins, 1971; Kriss, Nelson and Eisen, 1974).

A diffusion model was then presented that predicted adjacency effects in viscous development processes (Ehn and Silevitch, 1974). This model was not limited by an experimentally determined chemical spread function as were the previous empirical models of Kelly, Simonds and Nelson. This model, known as the Eikonix forward diffusion model, was based on dynamic rate equations describing the fundamental diffusion process. The model is very detailed in its description of the process and apparently quite accurate. It represented the state of the art for modeling and predicting adjacency effects for given input exposures.

Outline of Remaining Chapters

In image restoration the objective is to predict (restore) the object from an image that may have been degraded by noise, nonlinearities or system bandwidth limitations. In terms of adjacency effects the purpose is to remove the inherent film processing nonlinearity from a given photographic image which may be substantially degraded by film grain noise and resolution limitations of the image forming system.

Burke (1974) had considered electro-optical image forming systems in terms of the restoration of blurred and noisy images. A statistical model based on a Unconditional Maximum Likelihood Estimator (U.M.L.E) was developed and experimentally verified for diffraction blurred images of stellar objects, line and bar images.

Chapter 2 addresses the theoretical development of Burkes electro-optical restoration model and its application to the restoration of noisy photographic images containing adjacency effects. Its relationship to some of the previously developed historical models is systematically defined. Chapter 3 presents the empirical approach used to provide photographic images. These images were used to determine a required input to the model, the chemical spread function, as well as object images degraded by adjacency effects and film grain noise. The microdensitometer data sampling of these images and initial data preprocessing are discussed in Chapter 4. The data analysis required to determine the chemical spread function and the restored photographic images is reviewed in Chapter 5. In addition, the experimental verification of the model is provided. Conclusions and recommendations for future investigation are given in the final chapter. Appendices are included which review all significant mathematical developments supporting the statistical model.

CHAPTER 2

DERIVATION OF STATISTICAL RESTORATION MODEL

Adjacency effects are reviewed in terms of their known modifications on edge and fine line images (Nelson,1971). The statistical restoration model, developed by Burke (1974), is then reviewed in terms of its proven application to the restoration of blurred and noisy images. The model is then extended to include photographic adjacency effects based on apriori knowledge of a chemical spread function. The functional steps of this model and some of the historical models reviewed in Chapter 1, are then compared.

Edge and Line Effects

Consider the one-dimensional case of a sharp exposure boundary (edge) of figure 2.1. Once development has been initiated, more developer solution will be depleted on the side of higher exposure than on the side of lower exposure. Simultaneously, development inhibiting reaction products will build up at a much higher rate on the side of higher exposure than on the side of lower exposure. The development inhibiting reaction products from the side of high exposure and the fresh developer from the side of low exposure will diffuse in all directions. As some of the inhibiting reaction products diffuse across the boundary to the side of low exposure, they strongly inhibit development and cause a low density band, called the "fringe effect". At the same time, some relatively fresh developer diffuses across the boundary to the side of high exposure; this enhances development and produces a high density band, called the "border effect". Both the "fringe effect" and the "border effect" are called "edge effects".

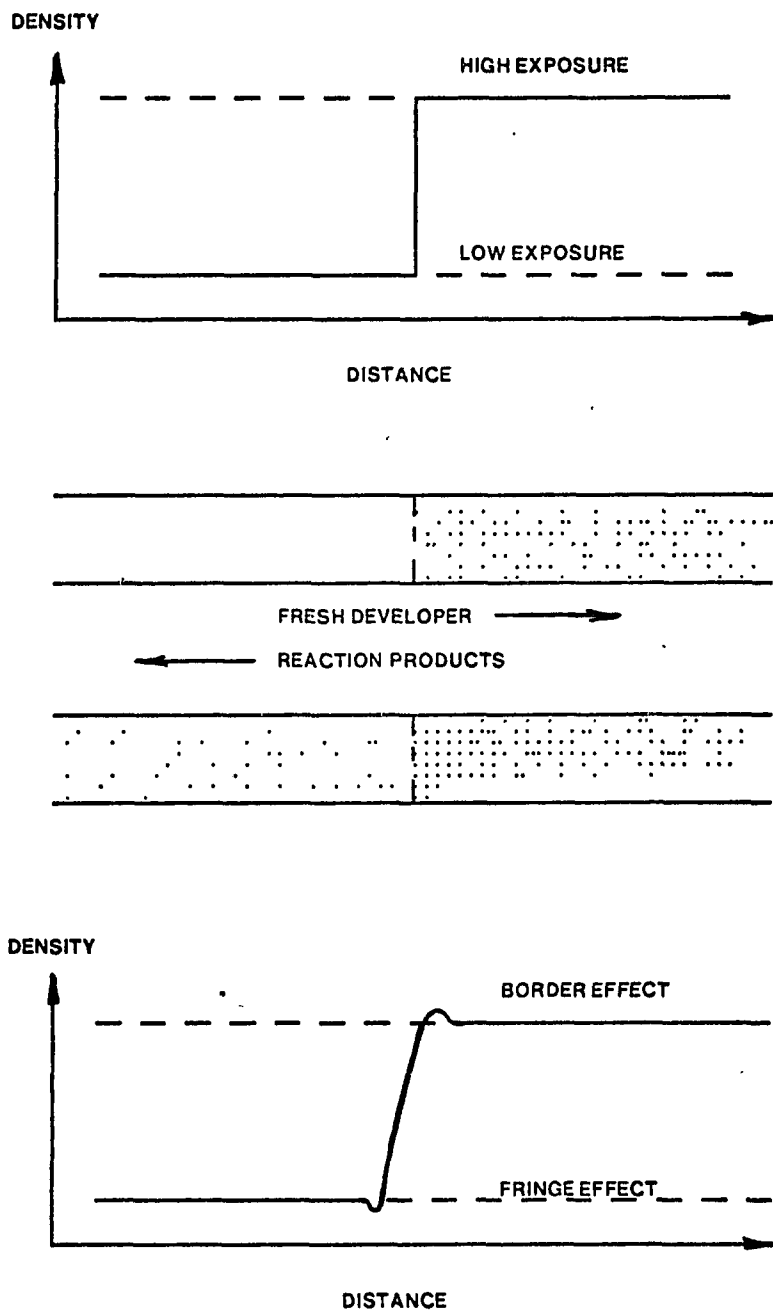


Fig. 2.1. Edge boundary.

Alternatively, the photographic lines of figure 2.2 serve to demonstrate the influence of adjacency effects on images of different sizes and at different exposure levels. For a given exposure level the density difference between edge and fine line images emphasizes the adjacency effect and creates the interesting sensitometric feature of small-area and large-area D-Log H curves. The adjacency effect on lines can be explained as a special case of edge effects since for wide lines the equivalent of two edges exist. Near the sides of the line the typical border and fringe effects occur while in the middle of the line a gross density trough exists due to the depletion of the developer, the creation of development inhibiting reaction products and the lack of fresh developer being able to diffuse over the long distance from the sides of the line. Alternatively, lines of narrow width (fine lines) do not have a large mass of silver being developed to cause depletion so that the constant supply of fresh developer enhances their development.

Definition of Terms

The problem is to characterize the photographic process for the purposes of obtaining an accurate estimate of an ideal aerial image from a noisy photographic image. In applying statistical estimation theory to this problem a set of definitions were developed based upon the general schematic realization of the photographic process presented by Kelly (1960), but restructured in terms of a restoration process as indicated in figure 2.3.

It is the relationship between the developed image and the ideal image that we desire. Consider that we take each of the schematic image spaces and conceptually divide them into an array of smaller cells as indicated in figure 2.4. Then we count the number of photons (photo electrons) that could be detected in each cell during some finite exposure time. Based upon such an arrangement we can define the following quantities:

σ_k = "ideal image" = number of photons that would be counted in the k^{th} cell of the ideal (Gaussian) image of an unknown scene by a perfect quantum detector (unit quantum efficiency).

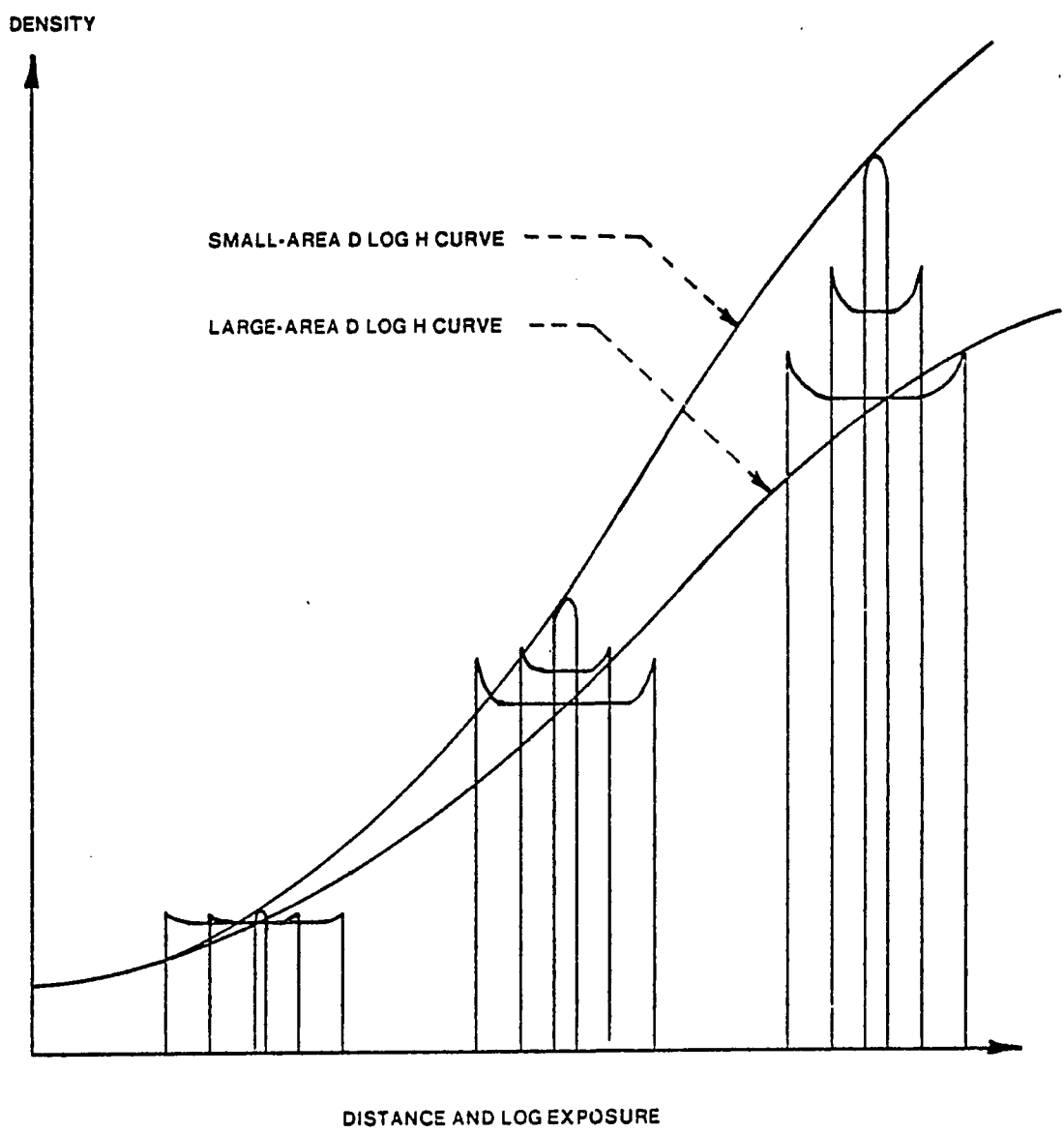


Fig. 2.2. Eberhard Effect.

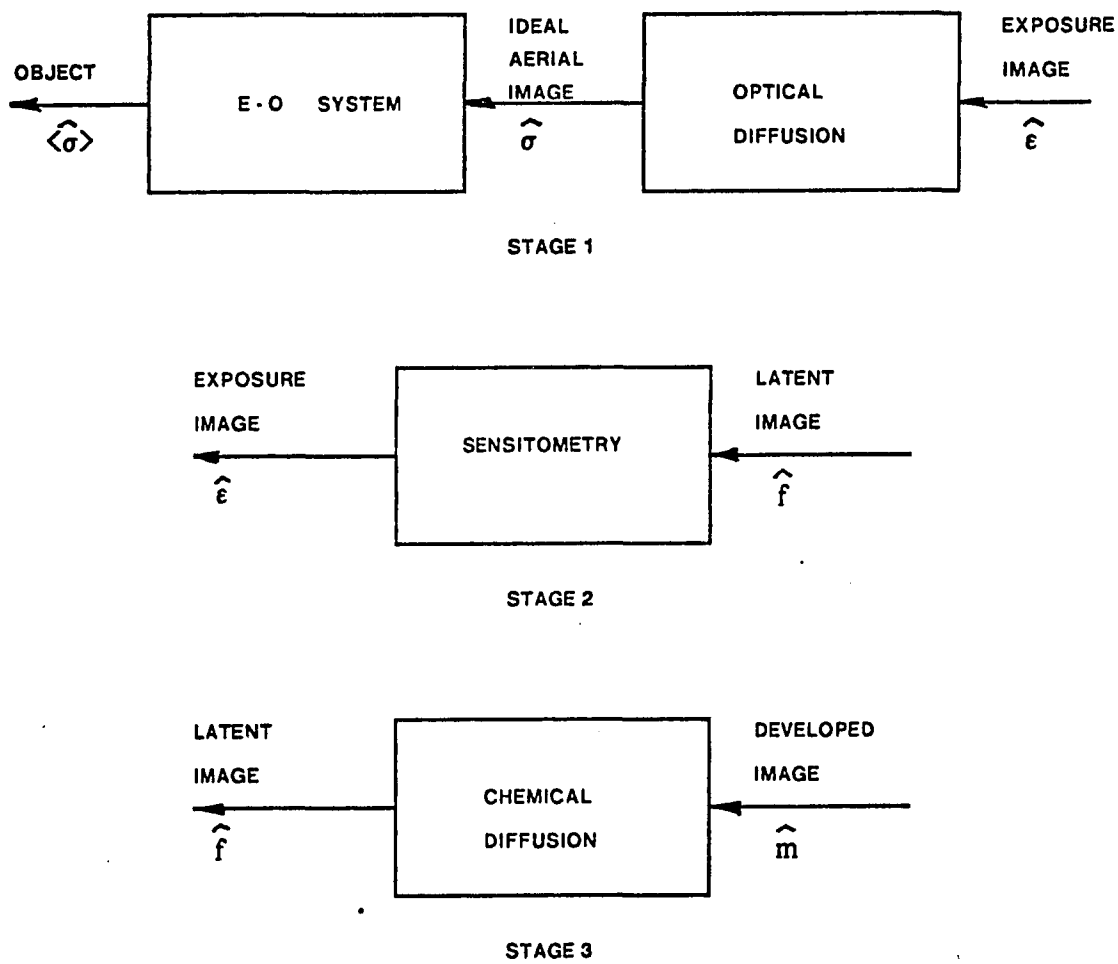


Fig. 2.3. Statistical model.

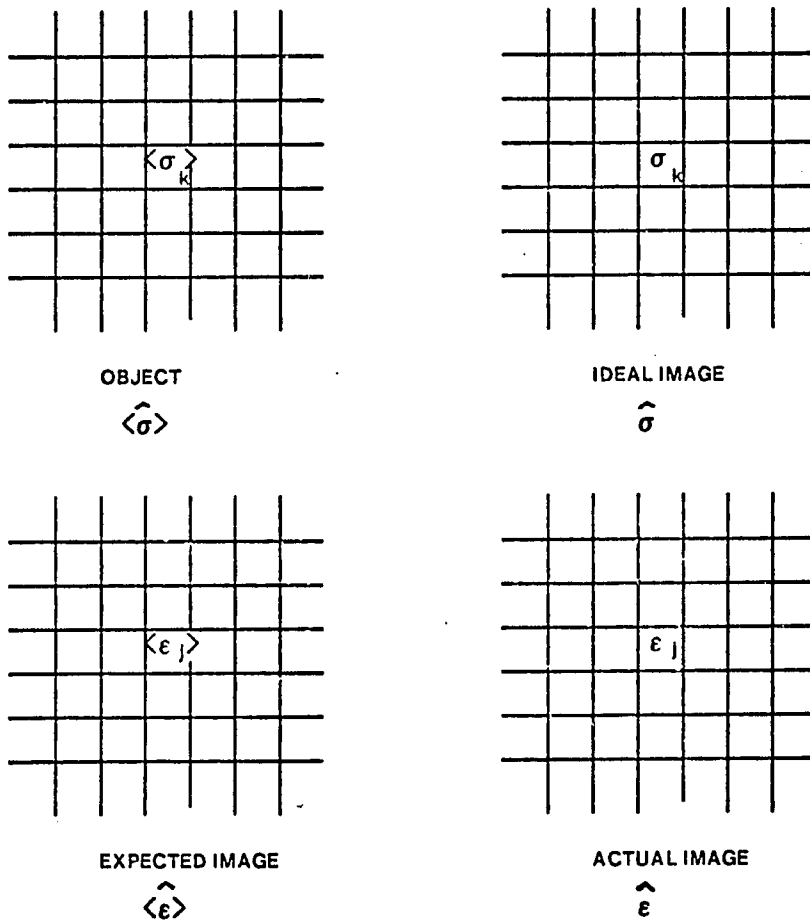


Fig. 2.4. Model representation in terms of cell elements.

ϵ_j = "exposure image" = number of photons (photoelectrons) counted in the j^{th} cell of the actual imperfect image by an imperfect quantum detector. For the photographic case, we will assume that ϵ_j includes the effects of light scattering in the emulsion. The cells of the exposure image are large enough to contain many grains and the "photoelectrons" are conduction electron-hole pairs produced photoelectrically in the grains.

f_j = "latent image" = number of emulsion grains in the j^{th} cell that have a probability greater than 1/2 of being developed, in the absence of adjacency effects. This also defines what is meant by a "developable grain".

m_i = "developed image" = number of developed grains in the i^{th} cell (measured).

g_i = "large area grain density" = number of developed grains in the i^{th} cell when the exposure is "uniform".

s_{jk} = "point spread function" ; The quantity $s_{jk} \sigma_k$ gives the expected number of photons (ensemble mean) from the k^{th} element of an ideal image scene that would be counted at the j^{th} element of the exposure image by a perfect detector.

A_{ij} = "chemical spread function" ; The quantity $f_i A_{ij} \langle m_j \rangle$ gives the most probable number of developable grains in the i^{th} element of the emulsion that are not developed because of reaction products produced in the development of the j^{th} element.

The ideal aerial image is what would be obtained for a perfect imaging system, ie., one of unit quantum efficiency and Kronecker delta spread function. Each quanta entering it from a given object element would be imaged at the geometrically conjugate image element. The ideal image, $\hat{\sigma}$, would then contain σ_k counts of quanta at the k^{th} element. If we can estimate the vector $\hat{\sigma}$ with the components σ_k then we have all the pertinent information available for describing the object during the given exposure time. In addition, the actual object distribution, defined by $\langle \hat{\sigma} \rangle$ with components

$\langle \sigma_k \rangle$, can be estimated by recording an infinite number of ideal images, $\hat{\sigma}$, and forming their cell-by-cell (ensemble) averages, $\langle \sigma_k \rangle$.

Optical Scattering Stage

Burke's (1974) previously verified restoration model for blurred and noisy images applies directly to the optical scattering stage of the photographic restoration model. The emulsion spreads the quanta it collects from a given cell in the ideal image over several cells in the exposure image with a quantum efficiency of β . This spreading is described by an optical point spread function s_{jk} which in effect is a probability density function. It is the probability that a quantum from the ideal image cell k will be counted at the j^{th} exposure cell.

Thus, given the ideal image, $\hat{\sigma}$, we characterize the most probable (the statistically expected) exposure image by the vector $\langle \hat{\epsilon} \rangle$, whose components $\langle \epsilon_j \rangle$ are given by

$$\langle \epsilon_j \rangle = \beta \sum_k s_{jk} \sigma_k \quad (2.1)$$

where

$$\sum_k s_{jk} = \sum_j s_{jk} = 1$$

The area under the point spread function follows from the conservation of energy.

Note that this does not relate the actual exposure image, $\hat{\epsilon}$, to the ideal image, $\hat{\sigma}$. Such a deterministic relation cannot be defined. We cannot specify the exact location of a single quanta emitted by the ideal image in the actual exposure array.

We can, however, look at the statistical relationships between the ideal image, $\hat{\sigma}$, and the exposure image, $\hat{\epsilon}$. Knowledge of the statistics, ie. mean, variance, etc. are based on knowledge of the probability density functions (p.d.f.'s) describing the process.

Consider the conditional p.d.f. of the ideal image

$$P(\hat{\sigma} / \langle \hat{\sigma} \rangle) = P(\hat{\sigma}, \langle \hat{\sigma} \rangle) / P(\langle \hat{\sigma} \rangle) \quad (2.2)$$

Neglecting the relatively minor consequences of photon correlations, we assume that the counts, σ_k , are statistically independent poisson variates with means, $\langle \sigma_k \rangle$, (Rice, 1954). Then the conditional p.d.f. becomes $P(\hat{\sigma})$ given by

$$P(\hat{\sigma}) = \prod_k ((\exp\{-\langle \sigma_k \rangle\} \langle \sigma_k \rangle^{\sigma_k}) / \sigma_k!) \quad (2.3)$$

Since the quantum efficiency of detection, β , is small for the photographic process, the exposure image can similiarly be described as

$$P(\hat{\epsilon} / \langle \hat{\epsilon} \rangle) = P(\hat{\epsilon}) = \prod_j ((\exp\{-\langle \epsilon_j \rangle\} \langle \epsilon_j \rangle^{\epsilon_j}) / \epsilon_j!) \quad (2.4)$$

where

$$\langle \epsilon_j \rangle = \beta \sum_k s_{jk} \sigma_k$$

We now have all the statistical relationships necessary to describe the diffusion model. An estimate of the ideal image, σ_k^* , can be obtained through application of an Unconditional Maximum Likelihood Estimator (U.M.L.E.) (Middleton, 1960; Van Trees, 1968). This maximizes the joint probability density function (j.p.d.f.) for a given estimate, σ_k^* , of the random variable, σ_k (Appendix A). For the poisson models of $\hat{\epsilon}$ and $\hat{\sigma}$, this leads to the estimates

$$\sigma_k^* = \langle \sigma_k \rangle \exp\{-\beta \sum_j ((\epsilon_j - \langle \epsilon_j \rangle) / \langle \epsilon_j \rangle) s_{jk}\} \quad (2.5)$$

where

$$\langle \epsilon_j \rangle = \beta \sum_k s_{jk} \sigma_k^*$$

This estimate yields a set of simultaneous nonlinear equations for of the unknown quantities σ_k^* and $\langle \sigma_k \rangle$ in terms of the number and distribution of known recorded counts, ϵ_j , in the exposure cells. The ϵ_j are known since they are physical measures. The cell-by-cell statistical means, $\langle \sigma_k \rangle$, of the ideal image, $\hat{\sigma}$, are unknown because we have based our theory on an experiment for which a single finite exposure time is used. Thus, there are twice as many unknowns as there are equations.

To overcome this problem we can make some assumption regarding the most likely estimate of the ideal image, σ_k . We employ the Poisson model which has equal mean and variance values. Assuming a most likely estimate of the ideal image, σ_k , as being $\langle \sigma_k \rangle$, use of the Poisson model yields an expected rms error of $\langle \sigma_k \rangle^{1/2}$ (Appendix B). It thus seems reasonable to seek a solution of Eq. (2.5) in which σ_k^* approaches $\langle \sigma_k \rangle$.

Applying iterative techniques to Eq. (2.5), we seek a new estimate of $\sigma_k^{(n+1)}$ based upon the previous estimate of $\sigma_k^{(n)}$ used on the right-hand side. Initially we assume that the best estimate of σ_k is the data ϵ_j . Thus, the first estimates can be stated as $\sigma_k^* = \langle \sigma_k^0 \rangle$ where

$$\begin{aligned} \langle \sigma_k^0 \rangle &= \sum_j s_{jk} \epsilon_j \\ \langle \epsilon_j \rangle &= \sum_j s_{jk} \langle \sigma_k^0 \rangle \end{aligned} \quad (2.6)$$

The total number of counts, $\sum_n \sigma_k^{(n)}$ are preserved from each iteration to the next. The recursive relation for the $(n+1)$ estimate is, thus,

$$\sigma_k^{(n+1)} = \sigma_k^{(n)} \exp\{-\beta \sum_j ((\epsilon_j / \beta \sum_l s_{jl} \sigma_l^{(n)}) - 1) s_{jk}\} \quad (2.7)$$

with

$$\sum_k \sigma_k^{(n)} = \sum_j \epsilon_j$$

Chemical Diffusion Stage

The statistical methods applied to the optical diffusion model can similarly be applied to the chemical diffusion stage. There is, however, greater difficulty due to the combination of the statistical nature of the latent image process and the nonlinear chemical diffusion effects.

The primary process, latent image formation, cannot be observed and absorbed quanta in an exposure cell do not necessarily lead to the formation of silver atoms in that cell. The theory of latent image formation initially proposed by Gurney and Mott (1938), and supported by considerable experimental evidence (Mees and James, 1966, pg. 90), defined the basic process.

A photoelectron, raised to the conduction band of the silver halide crystal by the absorption of light quanta, migrates to a preferred site on the grain. A silver ion is then attracted to the site and combines with the photoelectron to form a speck of silver. The process repeats, with the absorption of more light quanta, until a stable latent image is obtained. Thus, a minimum of several quanta must be absorbed to obtain a stable latent image. Actually, more are required, since all of the absorbed quanta and all of the photoelectrons subsequently produced do not necessarily contribute to latent image formation. The primary process is therefore one of low quantum efficiency.

A secondary process, chemical amplification (development), then transforms the silver halide crystal to a silver grain. During this secondary process developer depletion and the formation of development inhibiting reaction products produces a nonlinear change in the rate of development. Thus, development based on the statistics of the latent image formation step is altered in a nonlinear fashion.

The absorption process can be characterized in terms of the latent image, f_j which describes the number of developable grains in the j^{th} cell of the exposure image. By latent image we mean "any exposure-induced change which increases the development probability from < 0.5 to ≥ 0.5 ", when developed in the absence of adjacency effects (Mees and James, 1966). Note that since the silver halide crystals are randomly distributed in the emulsion, f_j is not a deterministic quantity. Also, the one dimensional realization of a developed latent image is a fine line image which includes photographic grain noise. This definition allows us to describe the latent image in terms of developed silver grains per unit area (mass of silver).

In general, the developed image can be defined in terms of m_i , the measured number of grains per unit area that are actually developed in the i^{th} cell. Also, a third function, g_i , will be used to describe the number of grains per unit area that would be obtained for large areas of uniform exposure, (ie. large area sensitometric characteristics).

The functions \hat{m} , \hat{f} and \hat{g} are interrelated stochastic processes. They are best remembered as follows: \hat{m} is the measured grain density; \hat{g} is the gross scale grain density; and \hat{f} is the fine scale grain density that would be obtained in the absence of adjacency effects.

In the primary process, \hat{f} , the grains are distributed at random over a very large area with independent and identical statistics. The grain locations in each cell can be described by Poisson statistics (Benton, 1971; O'Neill, 1963, pp. 115-120). Since the number of incident photons per unit area during exposure time is also Poisson (Rice, 1954), we can characterize the latent image, \hat{f} , as being a compound Poisson process (Feller, 1968, pp. 288-293).

The measured density, \hat{m} , is a much more complicated process. In the absence of adjacency effects it could also be described as a compound Poisson process because the measured number of grains in the i^{th} sample, m_i , would depend only on the number of developable grains, f_i , in that area. However, the developer depletion and reaction products alter the number of developed grains, m_i , in the final image. The most accurate method used to account for the process would be in terms of the time rate of change, during development, of the probability that a grain in the i^{th} sample would develop. However such a method would involve solution of stochastic partial differential equations. If we assume that the effects of chemical diffusion are small with respect to the initial strength of the developer, as is usually the case, then their major effect on the statistics of m_i is that of reducing the mean $\langle m_i \rangle$. This allows the characterization of adjacent samples, m_i and m_j , as being statistically independent. They are weakly correlated over the area of the chemical spread function (diffusion reaction products).

Based on this assumption the average adjacency effect (expectation value) can be described as

$$\langle m_i \rangle = f_i (\alpha - \sum_j A_{ij} \langle m_j \rangle) \quad (2.8)$$

The term αf_i represents the number of grains that would be developed in the absence of adjacency effects, where α is a constant determined for particular film/developer combinations and

development time. The term $f_i \sum_j A_{ij} \langle m_j \rangle$ gives the average number of developable grains that are inhibited because of adjacency effects, where the matrix A_{ij} describes the adjacency effect in terms of a chemical spread function (CSF). Such a description indicates the nonlinear relationship between the average number of developable grains $\langle m_i \rangle$ and the latent image as expected from previous experimental efforts (Nelson, 1971). It also indicates that the chemical development depends upon the random variable describing the number of developable grains in the latent image, \hat{f} , not on the ensemble average of the latent images, $\langle \hat{f} \rangle$.

Additional insight to this description can be gained by reconsidering the edge effect depicted in figure 2.1. Now, however, consider the edge in terms of the density levels that would be obtained after development in both the presence and absence of adjacency effects as shown in figure 2.5. In the absence of adjacency effects, ie. developer depletion and migration effects, a higher density level, \hat{f} , is obtained on both sides of the edge. When we include developer depletion, but no migration, a lower density level, \hat{g} , is obtained on both sides of the edge. This represents the gross grain solid area density. When development depletion and migration are included we obtain the developed image, \hat{m} , characterized by the expected fringe and border effects.

In the case where we have a uniform exposure (regions I and V of figure 2.5) the measured grain density, m_i , is equal to the gross grain density, g_i , characteristic of the large-area sensitometric curve. In terms of Eq. (2.8) this means that $\langle m_i \rangle = \langle m_j \rangle$ for all j within that area spanned by the chemical spread function. Since the term $\sum_j A_{ij} \langle m_j \rangle$ is a convolution process and $\langle m_j \rangle = g_i$, a constant, Eq. (2.8) reduces to

$$\langle g_i \rangle = f_i (\alpha - A_i \langle g_i \rangle) \quad (2.9)$$

$$\langle g_i \rangle = \alpha f_i / (1 + A_i f_i)$$

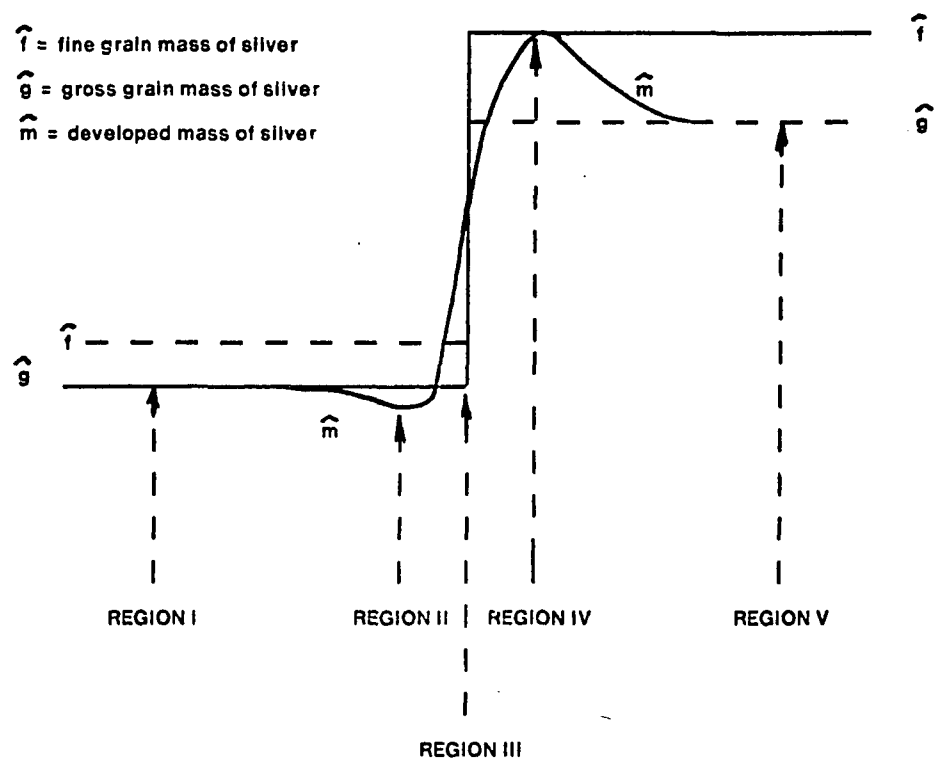


Fig. 2.5. Edge effect.

where

$$A = \sum_j A_{ij} = \iint A(x,y) dx dy$$

To express the measured grain density, $\langle m_i \rangle$, in terms of the gross grain density, $\langle g_i \rangle$, for the entire edge profile (regions I through V of figure 2.5), we solve Eqs. (2.8) and (2.9) for the fine grain density, f_i , and equate to obtain

$$\langle m_i \rangle = \langle g_i \rangle (\alpha \cdot \sum_j A_{ij} \langle m_j \rangle) / (\alpha - A \langle g_i \rangle) \quad (2.10)$$

The relationships between the important physical stages are now defined in terms of the statistically independent Poisson-distributed random variables, \hat{m} , \hat{f} and \hat{g} . The U.M.L.E. can again be applied, as in the case of the optical diffusion stage, to maximize the j.p.d.f. of the latent image, f_i , and the measured grain density, m_i . Thus we want

$$P(\hat{m}, \hat{f}) = P(\hat{f}) P(\hat{m}/\hat{f}) \quad (2.11)$$

The conditional p.d.f., $P(\hat{m}/\hat{f})$ is based on the previous assumptions that the measured number of developable grains, m_i , are uncorrelated Poisson-distributed random variables with means, $\langle m_i \rangle$, which depend upon all the components of \hat{f} . Thus,

$$P(\hat{m}/\hat{f}) = \prod_{i=1}^M P(m_i / \langle m_i(\hat{f}) \rangle) \quad (2.12)$$

$$P(\hat{m}/\hat{f}) = \prod_{i=1}^M (\exp\{-\langle m_i \rangle\} \langle m_i \rangle^{m_i}) / m_i!$$

The latent image follows from these same assumptions, so that

$$P(\hat{f}) = \prod_{i=1}^N (\exp\{-\langle f_k \rangle\} \langle f_k \rangle^{f_k}) / f_k! \quad (2.13)$$

Then the U.M.L.E., f_k^* , that maximizes the joint p.d.f., given by Eq.(2.11), can be shown to yield (Appendix C)

$$f_k^* = f_k \exp\{\sum_i ((m_i - \langle m_i \rangle) / \langle m_i \rangle) \partial \langle m_i \rangle / \partial f_k |_{f_k = f_k^*}\} \quad (2.14)$$

which is dependent upon the rate of change of the measured mean grain density with respect to the individual components of \hat{f} . An explicit expression for this derivative can be obtained from Eq. (2.8) using the assumption that the adjacency effect is small so that the quadratic and higher order terms can be neglected (Appendix D). This yields

$$\frac{\partial \langle m_i \rangle}{\partial f_k} = \frac{(\alpha \cdot \sum_j A_{ij} \langle m_j \rangle) \delta_{ik} - \langle m_i \rangle A_{ik} (\alpha \cdot \sum_j A_{kj} \langle m_j \rangle)}{(\alpha \cdot \sum_j A_{ij} \langle m_j \rangle)} \quad (2.15)$$

which, when inserted in Eq. (2.14) provides the U.M.L.E. of,

$$f_k^* = f_k \exp\left\{(\alpha \cdot \sum_j A_{kj} \langle m_j \rangle) \left(\frac{(m_k - \langle m_k \rangle)}{\langle m_k \rangle}\right) - \sum_i \left(\frac{(m_i - \langle m_i \rangle)}{A_{ik}}\right) / (\alpha \cdot \sum_j A_{ij} \langle m_j \rangle)\right\} \quad (2.16)$$

This set of nonlinear equations is similar to those of Eq. (2.5) which defined the ideal image estimate, $\hat{\sigma}$, in terms of the exposure image, $\hat{\epsilon}$. Proceeding as before and assuming that the most likely latent image estimate, f_k^* is its mean value, $\langle f_k \rangle$, we have

$$f_k^* = \langle f_k \rangle \quad (2.17)$$

and

$$m_k = \langle m_k \rangle$$

An iterative solution for $f_k^{(n+1)}$ could be obtained from $f_k^{(n)}$. Then Eq. (2.9) would be utilized to obtain an equivalent gross grain density, $\langle g_k \rangle$, in terms of f_k^* . The gross grain density would then be related to the exposure, ϵ_j , through the use of the characteristic curve.

The application of such a procedure would be quite time consuming and costly due to the complexity of the iteration procedures involved in estimating the latent image, f_k^* . It is quite possible that such a procedure would only be necessary when very large adjacency effects are present.

Looking again at Eq. (2.16) we see that the best estimate of f_k^* is f_k multiplied by an exponential describing the chemical spread function effects in terms of the noisy image ($m_j \cdot \langle m_j \rangle$). If we ignore the noise in this stage and project it all to the exposure image, the iterative relations there will treat it as if it were quantum noise in the exposure. In this case the best estimate of f_k^* is $f_k^* = \langle f_k \rangle$ for $m_k = \langle m_k \rangle$. Then from Eq. (2.8)

$$f_k^* = m_j / (\alpha \cdot \sum_j A_{kj} m_j) \quad (2.18)$$

and from Eq. (2.9)

$$\langle g_k \rangle = \alpha f_k^* / (1 + \alpha f_k^*) = \alpha m_k / (\alpha + \alpha m_k \cdot \sum_j A_{jk} m_j) \quad (2.19)$$

We now have an explicit measure of the gross density in the k^{th} sample in terms of the measured grain density in all samples.

Photographic System Model

The photographic system model can now be described in terms of Eq. (2.7), Eq. (2.19) and the characteristic curve. The covering power relationship

$$m_k = P d_k^n \quad (2.20)$$

where

m_k = mass of silver per unit area (grain density)

d_k = diffuse film density

P = photometric equivalent

n = nonlinear exponent determined from experimental measurement

The overall systems model then reduces to a "recipe" consisting of the following explicit relationships as schematically represented in figure 2.6.

1. Conversion of photographic image diffuse density values, d_m , to equivalent mass of silver/unit area, \hat{m} , using the covering power relationship, Eq. (2.20).

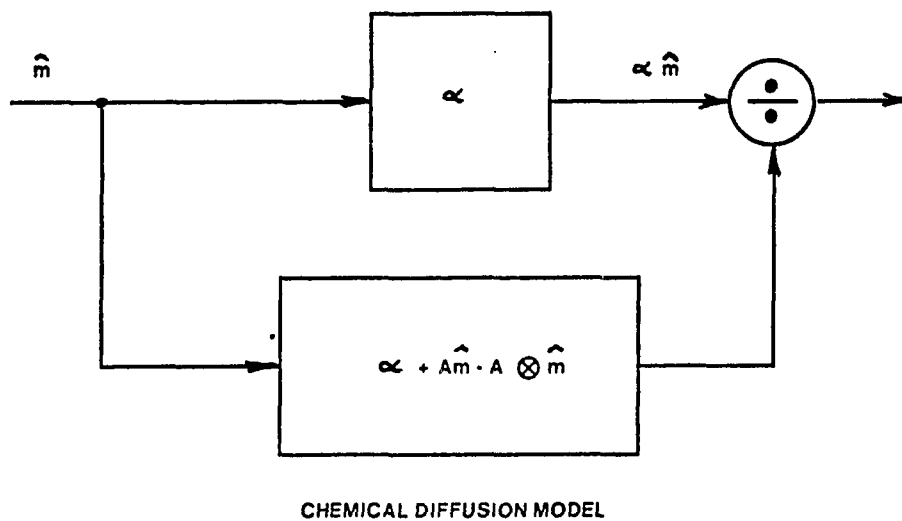
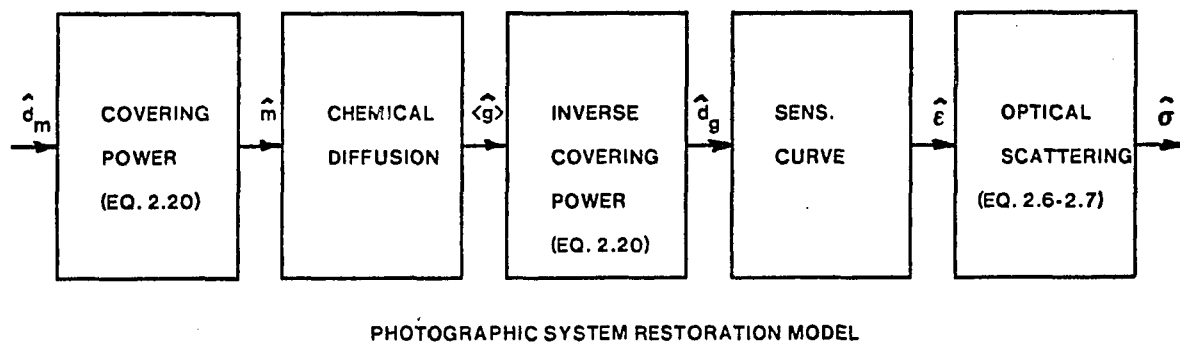


Fig. 2.6. Burke's photographic system restoration model.

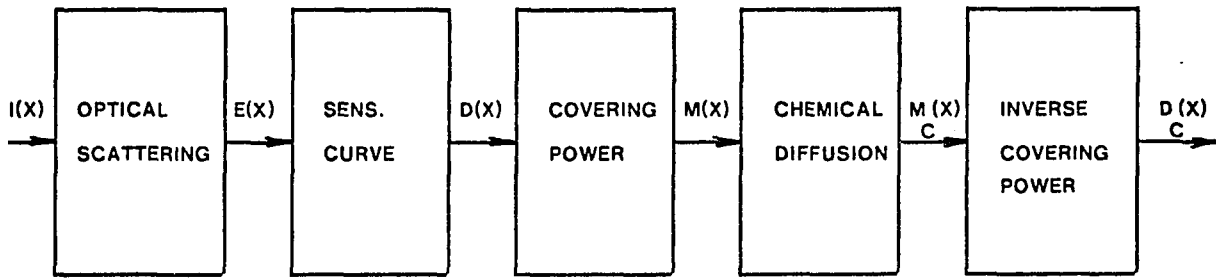
2. Determining the gross grain density, $\langle \hat{g} \rangle$, (equivalent to the estimated latent image, \hat{f}^*) using Eq. (2.19).
3. Converting the gross grain density, $\langle \hat{g} \rangle$, (mass of silver/unit area) to an equivalent gross diffuse density using the inverted covering power relationship based on Eq. (2.20).
4. Converting the diffuse density values, $\langle d_g \rangle$, to equivalent exposure values, \hat{e} , using the characteristic curve.
5. Estimating the ideal image, \hat{o} , from the equivalent exposure, \hat{e} , using the nonlinear iterative set of Eqs. (2.6) and (2.7).

The effects of the characteristic curve are well known (Mees and James, 1966 and Nelson, 1971) and the optical scattering stage has been previously verified (Burke, 1974). Thus, the main emphasis of this research involves the investigation of steps 1 through 3. This will provide a preliminary verification of the chemical diffusion portion of the model.

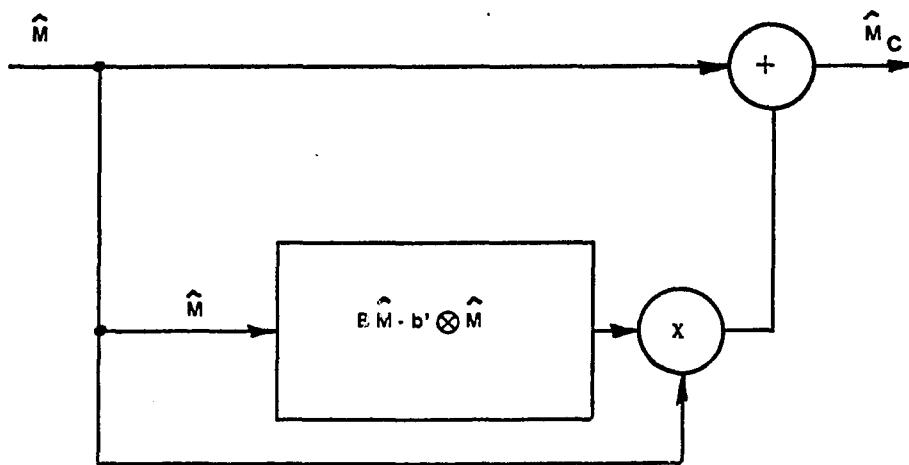
System Model Comparisons

The photographic system model based on statistical theory is unique in that it addresses the restoration of noisy images influenced by adjacency effects. The models that existed prior to the derivation of the statistical restoration model were mostly forward-working models in that they predicted an image given an input exposure profile uncorrupted by large amounts of photographic noise. The reverse-working restoration models did not account for photographic grain noise.

Nelson's model (1971) was the most accurate forward-working model due to the proper use of the large-area sensitometric stage to separate the optical scattering and chemical diffusion stages and the conversion of diffuse densities to mass of silver units. Nelson predicted the ensemble averaged gross grain density, $\langle m(x) \rangle$, given the input exposure profile and an empirically determined chemical spread function. Schematically, the model can be represented as shown in figure 2.7.



PHOTOGRAPHIC SYSTEM FORWARD MODEL



CHEMICAL DIFFUSION STAGE

Fig. 2.7. Nelson's photographic system forward model.

Assuming an input edge exposure profile and a typical large-area sensitometric curve the input to the chemical diffusion stage consists of a density edge profile. Converting the density edge profile to mass of silver units yields the basic form of Nelson's chemical diffusion stage:

$$\langle m(x) \rangle = \langle g(x) \rangle + B \langle g(x) \rangle^2 - \langle g(x) \rangle \int b(\xi) \langle g(x-\xi) \rangle d\xi \quad (2.21)$$

where

$\langle m(x) \rangle$ = ensemble averaged measured mass of silver/ unit area

$\langle g(x) \rangle$ = ensemble averaged gross grain mass of silver

$b(\xi)$ = chemical spread function (CSF)

B = area under chemical spread function

Nelson verified that this model accurately predicted adjacency effects for edges of moderate contrast.

Burke's model can be related to the forward prediction of Nelson's by comparing Eq.(2.21) to Eq.(2.10) and assuming relatively small adjacency effects, ie. $A \langle g_i \rangle < \alpha$, (Appendix E).

$$\langle m_i \rangle = \langle g_i \rangle + (A/\alpha) \langle g_i \rangle^2 - \langle g_i \rangle \sum_j (A_{ij}/\alpha) \langle g_j \rangle + \dots \quad (2.22)$$

The assumption $A \langle g_i \rangle < \alpha$ tends to reduce the effects of the last term of Eq.(2.22) making the two relationships nearly identical for the case of relatively small adjacency effects. Since Nelson indicated that his model predicted densities containing larger errors for higher contrasts, it is probable that the last term of Eq. (2.22) will provide a more accurate estimate. It should also be noted that the two chemical spread functions are related by the proportionality factor, α , and are equal only for the case $\alpha = 1$.

Just prior to Burke's publication, Ehn and Silevitch (1974) published a forward model based on an approximate solution of a formal chemical diffusion model (this model was derived independently of Burke's at about the same time). The formal diffusion model was very rigorous due to its characterization of the rate of development by the use of partial differential equations. It used the approximation that a small area mass of silver, $N(\xi)$, convolved with a chemical spread function,

$K_o(\xi)$, (consisting mainly of low spatial frequencies) could be replaced with a large-area mass of silver, $N_1(\xi)$, convolved with the same chemical spread function. Using this approximation the model reduced to

$$N(\xi) = N_1(\xi) (1 - \exp\{-A + kK_o(\xi) \otimes n_1(\xi)\}) / (1 - \exp\{-A + kN_1(\xi)\}) \quad (2.23)$$

where A and k are constants and $K_o(\xi)$ is a unit area chemical spread function. All are empirically determined for a given development process. Schematically the model can be represented as shown in figure 2.8. Under the restrictive conditions of low contrast edges the model has also been shown to reduce to a form equivalent to Nelson's model.

More recently, the inverse of this model has been derived in order to obtain the effective exposure distribution corresponding to a given optical density (Silevitch, Gonsalves and Ehn, 1977). The derivation requires solution of the nonlinear integral Eq. (2.23) when the denominator is taken as a point nonlinearity

$$f(x) = x / (1 - \exp\{-A + kx\}) \quad (2.24)$$

which yields

$$f(N_1(\xi)) = N(\xi) / (1 - \exp\{-A + kK_o(\xi) \otimes N_1(\xi)\}) \quad (2.25)$$

The procedure, as shown schematically in figure 2.9, would normally require an iterative solution. Such an approach has been shown to work with reasonable accuracy in approximately 15 iterations and is still a topic of current research. However, a "one-shot" inversion technique was also developed based on the assumption that the small area mass of silver, $N(\xi)$, could be used as the initial estimate of the large area mass of silver, $N_1(\xi)$, required by the right side of Eq. (2.25). This estimate is made assuming that the convolution with the chemical spread function will smooth the resulting error.

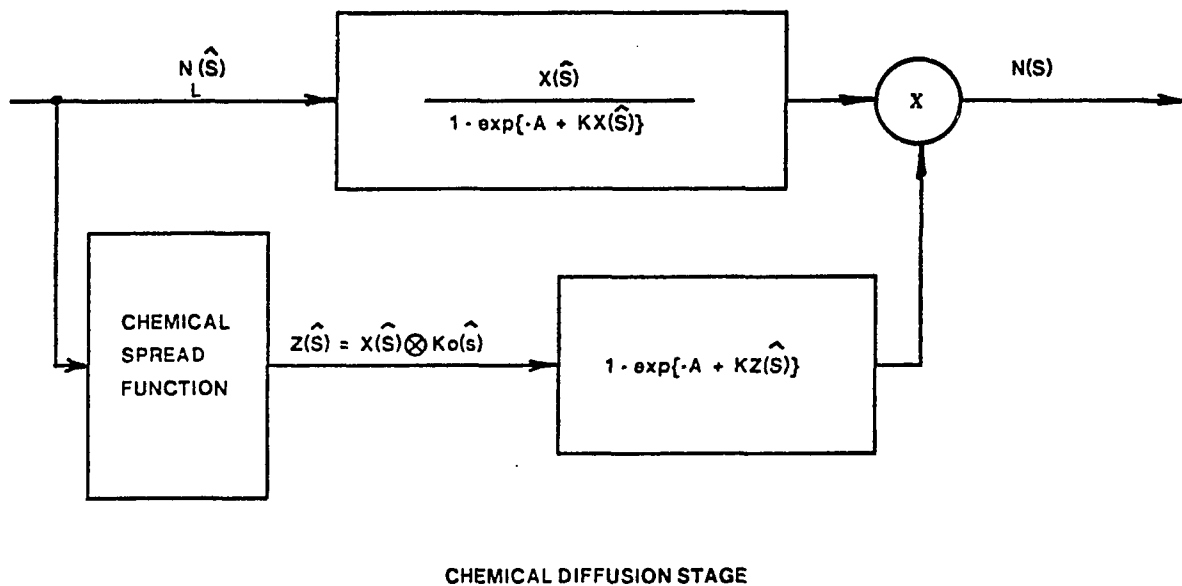
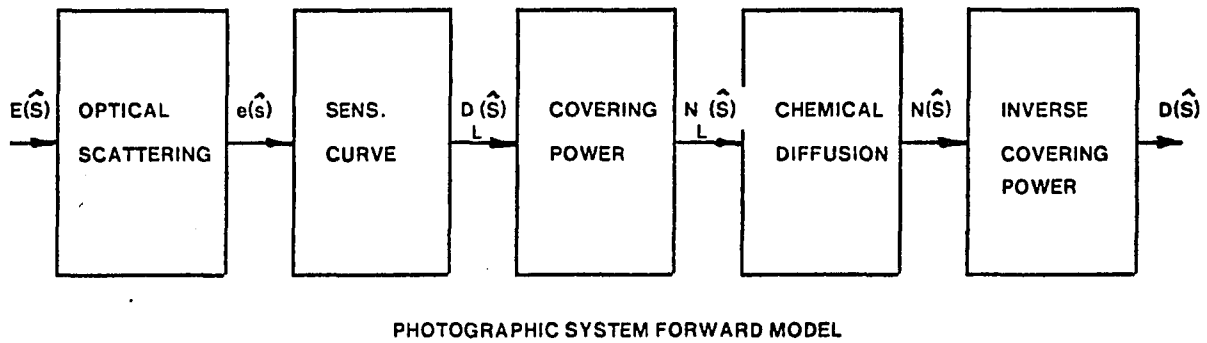


Fig. 2.8. Eikonex photographic system forward model.

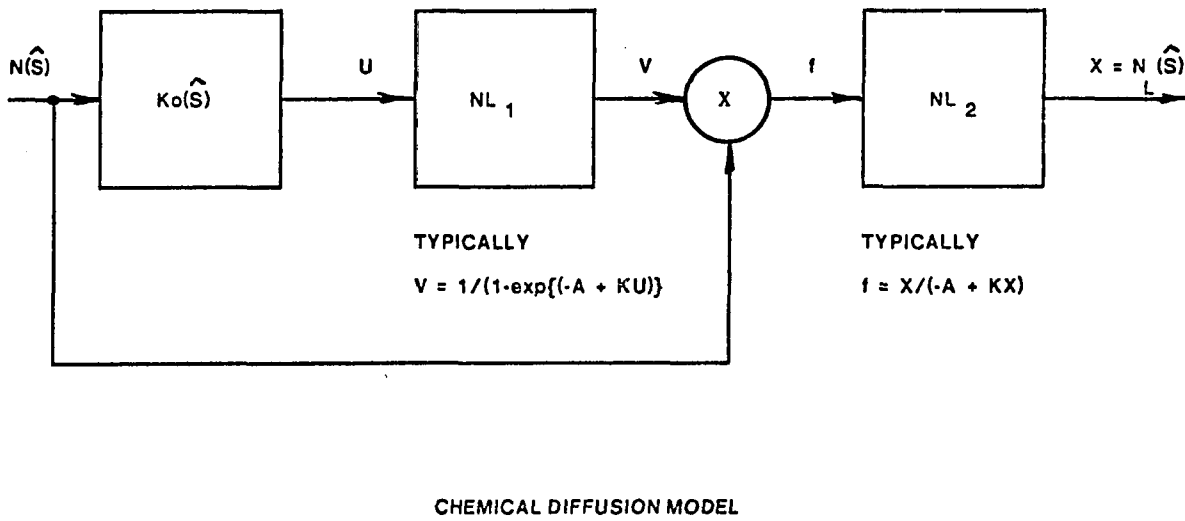
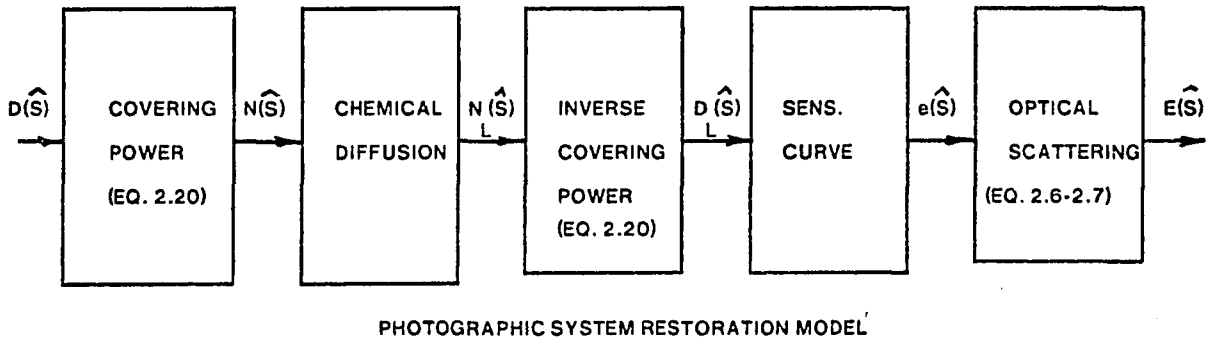


Fig. 2.9. Eikonix photographic system inverse model.

The model, using this assumption, has been demonstrated to provide quite accurate results for an edge, a sinusoid distribution and a more general scene consisting of a combined edge, triangular function and line exposure. The model has also demonstrated some noise suppression due to the use of the convolution process with the chemical spread function. It was not, however, intended to perform an optimization of restored images degraded by noise.

The use of rigorous development rate equations to model the physical process suggests that a high level of accuracy should be obtained. However, a realistic tradeoff must be made for this accuracy due to the complexity of the solution even with the use of a "one shot" inversion technique and the computer time required for data reduction and evaluation of the nonlinear coefficients. Comparison of figure 2.6 and 2.9 indicate the additional steps required by this iterative technique.

Although a thorough experimental comparison of all the models is desirable it is beyond the scope of this research. The state of the art is adequately identified by the preceding review of the theory of Burke's model and a relative comparison to all other known models. The experimental requirements to provide preliminary verification of the chemical diffusion stage, as suggested by this theory, must now be considered.

CHAPTER 3

EXPERIMENTAL APPROACH

The experimental approach is reviewed in terms of overall design considerations, descriptions of the important laboratory apparatus and the film exposure/processing procedures used to obtain developed film images that satisfy the requirements of the statistical restoration model. The chemical spread function is the most important variable in experimentally evaluating the removal of adjacency effects for this model. Thus, the emphasis of the experimental approach was on the accurate evaluation and use of this variable.

Experimental Design

The experimental design was based on the verification of the statistical restoration "recipe" given by Eq. (2.19). There are primarily two data sets that are required by this model and, thus, two experimental procedures to be considered in the overall design. The first involved the method used to determine the chemical spread function, which describes the primary chemical diffusion process. The second was concerned with the generation of film images such that a variety of images were available to allow comparisons to the types of images analyzed by some of the historical models.

Nelson's (1971) publication contained a very detailed account of the experimental procedures used to obtain chemical spread functions. Calibrated x-ray exposures of edge targets provided images with very sharp boundaries due to the efficient absorption of x-ray quanta by photographic films. Optical scattering phenomena, typical of light quanta exposures, did not occur with x-ray quanta. Even relatively small amounts of secondary radiation at higher exposure levels of x-ray quanta provided very little change in edge and line boundary widths. Based on these results

Nelson's procedure was selected for determination of the required chemical spread functions. In addition, it should be noted that Nelson's chemical spread function, for a given film/developer combination, is simply a scaled version of that required by Eq. (2.19) as previously indicated by comparison of Eq's. (2.21) and 2.22). Several exposure levels were considered to ensure that variations in shape and area of the chemical spread function could be investigated.

The method selected to generate film images consisted of light quanta exposures with an object target in direct contact with a black and white negative film material. The target was illuminated by incident plane waves to provide a uniform distribution of energy and unity magnification. Thus, the target was representative of the true aerial image profile. This eliminated the potential requirement of calculating aerial image degradation in terms of system transfer functions and magnification scale factors.

In addition to the gross grain density values provided by edge targets exposed to x-rays, it was important to obtain fine detail line density profiles from variable width line targets exposed to x-rays. This enabled the investigation of the Eberhard Effect so commonly associated with adjacency effects. It also allowed comparison with Nelson's observations on the relationship between the resultant magnitudes of the fine line and gross grain film density values.

Radiometric Sources

X-ray quanta exposures were produced using a Bracke-Seib X-Ray Unit and a target/film holder apparatus similar to the one described by Sherwood (1967). The unit contained a General Electric CA-7 x-ray diffraction tube, a beryllium window and a tungsten target with a 0.10 mm. x 10 mm. projected focal slit. The projected focal slit was located a distance of 76 cm from the film exposure plane. All exposures were made using a 20 kv peak voltage without filtration. The film platen was designed to hold 35 mm film strips in a vacuum cassette. Registration pins were provided to position the film accurately during exposure.

The light quanta exposures were produced using the contact printing technique with a point source. The selection of a point source, as opposed to a collimated projection system, simplified the experimental procedure. The point source consisted of a General Electric, 250 watt, frosted light bulb placed directly behind an opaque surface containing a 3 mm pinhole. The point source was placed 152 cm from the film plane which consisted of a vacuum cassette that held the target master in contact with a 35 mm film strip. The ratio of the source to film plane distance and the pinhole diameter was $1520/3 = 507$. Thus, the illuminated pinhole is an accurate representation of a point source over a region approximating 50 mm in diameter on the film plane (Smith, 1966, pg. 182; Wyatt, 1978, pg. 44).

The uniformity of the illumination was measured at 10 mm spacings across the film plane using an E.G. & G. Model 550-1 Radiometer/Photometer with a 1 mm detector aperture. An average of three measurements were taken at each individual location to provide the illumination contour plot given in Figure 3.1. A region 5 cm in diameter, centered on the optical axis, was found to provide a uniform illumination with a maximum error of 1.0 % .

Object Target Descriptions

The object test target used for x-ray exposures was similar to those described by Sherwood (1967) but of fixed width. It was made of two platinum alloy layers surrounding a precision ground steel block, as shown in Figure 3.2. The test target consisted of a "tri-slit" arrangement in that three fixed width slits were physically located on a single target and abutted along their lengthwise dimension, as shown in Figure 3.3. The slits were 10, 100 and 1000 micrometers in width and each was 10 mm in length. Thus, all x-ray line images were simultaneously exposed and all fit within the width of a 35 mm film strip. The 75 micrometer thickness of the platinum slits was based on the tradeoff of making the slits thick enough to eliminate the transmission of low concentrations of x-rays, yet thin enough to minimize reflection and scattering of x-rays off the vertical faces of the slits.

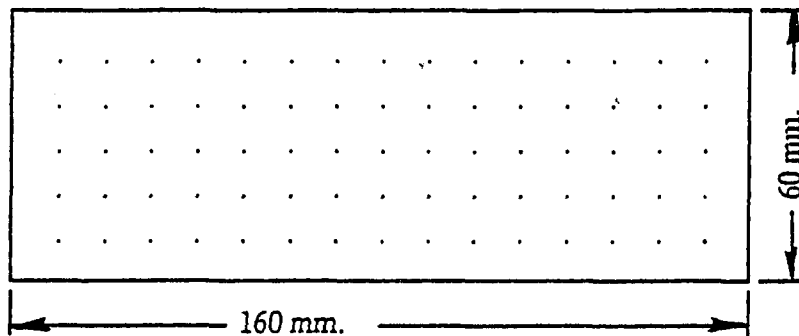


Fig. 3.1. Illumination contour plot.

The test target used for light quanta exposures had to be capable of providing a variety of high contrast images and yet be small enough to be contained in the 50 mm diameter region of the film plane that satisfied the point source approximations. It was preferable to use only one target to minimize the number of exposures and thus the amount of film to be processed. It was also desirable to process all x-ray and light quanta exposed film simultaneously to eliminate film density variations due to processing differences. In view of these requirements, an Ealing Corporation High Resolution Test Target was selected.

The Ealing target consists of three groups of high contrast bar targets covering an area 16 mm x 16 mm centered in a 50.8 mm square of 1.52 mm thick glass plate. Each of the three groups has eleven sets of fifteen bar targets providing a spatial frequency range for all groups of from 1 to 1000 line pairs per millimeter (lp/mm), as indicated in Table 3.1. The frequency ratio between successive sets is 10 and the density difference between opaque and transparent regions is greater than 2.0. The maximum variation in width between light and dark bars is less than 5% over the 1 to 300 lp/mm range. The bars contained in this spatial frequency range provided all the images necessary to compare fine line and gross grain film density values.

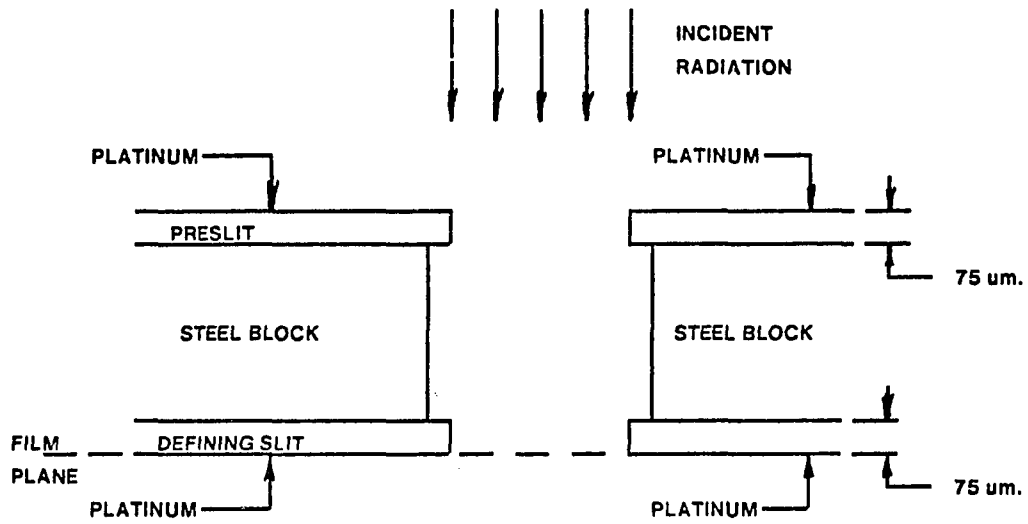


Fig. 3.2. Vertical profile of x-ray slit targets.

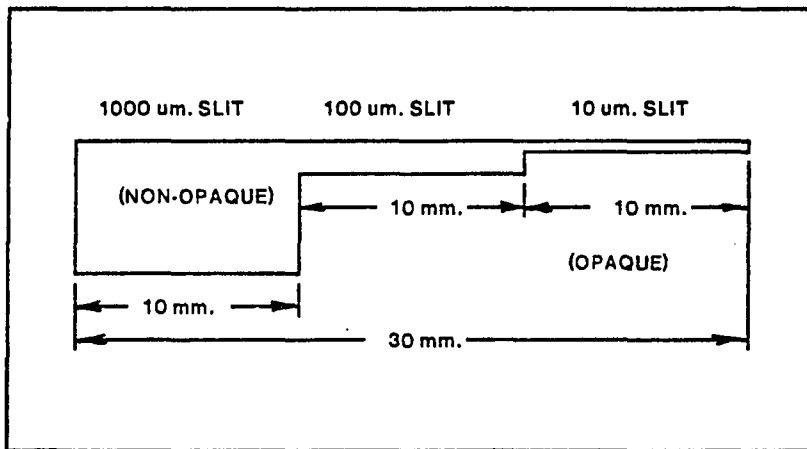


Fig. 3.3. "Tri-slit" x-ray target.

Table 3.1. Resolution target spatial frequency values.

| Group 1 | Group 2 | Group 3 |
|---------|---------|---------|
| 1.00 | 10.00 | 100.00 |
| 1.26 | 12.59 | 125.90 |
| 1.58 | 15.85 | 158.50 |
| 2.00 | 19.96 | 199.60 |
| 2.51 | 25.12 | 251.20 |
| 3.16 | 31.63 | 316.30 |
| 3.98 | 39.82 | 398.20 |
| 5.01 | 50.14 | 501.40 |
| 6.31 | 63.13 | 631.30 |
| 7.95 | 79.48 | 794.80 |
| 10.00 | 100.00 | 1000.00 |

Film and Process Selection

The selection of film type and processing conditions was based primarily on obtaining images that contained significant amounts of adjacency effects. In addition, a commercially available 35 mm film size was preferable to simplify film procurement and to fit available film vacuum cassettes. Films capable of providing very high resolving power were not required since the adjacency effect has been observed in films of lower resolution. However, it was desirable that the resolving power exceed the 100 lp/mm resolution required by the 10 micrometer line widths used for x-ray quanta exposures.

The film and developer selected were Eastman Kodak Panatomic-X processed in D-76 (diluted with an equal amount of water). Panatomic-X developed in D-76 (1:1), using brush or continuous agitation, was known to exhibit strong spatial interactions due to adjacency effects (Simonds, 1964 and 1965; Nelson, 1971). However, it was decided to develop the film without agitation since this would amplify the magnitude of the adjacency effects previously obtained by Simonds and Nelson (Wolfe and Barrows, 1947).

Published data was not available that accurately described the resolving power or the modulation transfer function of Panatomic-X exposed to an object target contrast of greater than 100:1 and processed without agitation of the developer. This was not unreasonable since films are typically processed with agitation. However, the apparent modulation transfer function (includes optical scattering and chemical diffusion) for Panatomic-X, processed in D-76 (1:4) for 7 minutes with continuous agitation, was known to have a cutoff frequency (modulation transfer factor 10 %) in the range of 170 -180 cycles per mm as shown in Figure 3.4 (Nelson, 1971). The elimination of development agitation would tend to localize the development and enhance adjacency effects (Wolfe and Barrows, 1947) while significantly reducing the gross grain sensitometric response (Mees and James, 1966, pg. 357). The reduced sensitometric response would reduce the absolute value of the zero-frequency components of the image. Thus, it was expected that the apparent transfer function would be bandlimited to a considerably lower cutoff frequency. An indication of this frequency response was provided by the film images of the high resolution test target exposures.

Experimental Procedure

Initial sensitometric exposures were made to define the desired exposure levels for both x-ray and light quanta exposures. These were followed by an additional sensitometric exposure series and then the final target exposure series.

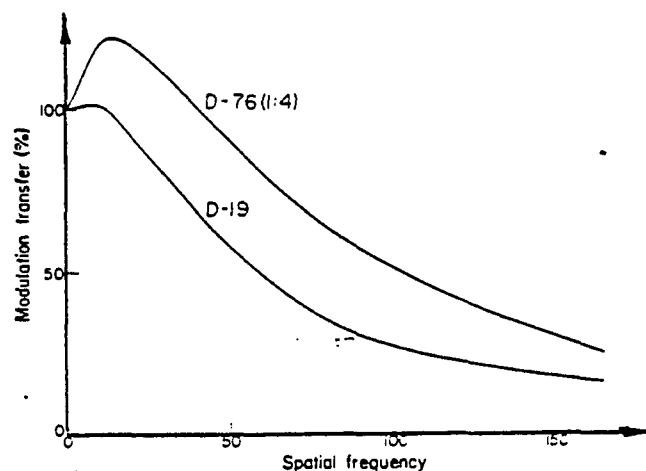


Fig. 3.4. Apparent modulation transfer function for E.K. Panatomic-X for two development conditions (Nelson, 1971).

The sensitometric x-ray quanta exposures were made using a 10 mm x 30 mm platinum slit target master with exposure times as indicated in Table 3.2. The construction of the target was similar to that shown in Figure 3.2. Several exposure levels were used to ensure that gross diffuse density values in the approximate range of 0.6 to 1.5 were obtained. This would allow subsequent comparison of chemical spread functions for several exposure levels without the high density peak of the edge effect or the maximum fine line density value from reaching the saturation level of the film/developer combination. The final x-ray exposures were then made using the target shown in Figure 3.3 over the exposure range identified by the sensitometric phase.

The sensitometric light quanta exposures were made using a calibrated Eastman Kodak Sensitometric Step Tablet No. 5. The step tablet contained 11 M-type carbon density steps laminated in acetate with nominal increments of 0.3 density units. An initial exposure of 16 seconds provided a characteristic curve with a sufficiently large exposure latitude to allow selection of the final high resolution test target exposures as given in Table 3.2.

Table 3.2. Experimental exposure and processing parameters.

| Exposure Parameters | | | |
|-----------------------|------------------------|------------------------|-------------|
| Target | Radiation Type | Time (Seconds) | |
| Sensitometric Slit | X-Ray (20 kv., 20 ma.) | 0.5, 1, 4, 16, 64, 128 | |
| Tri-Slit | X-Ray (20 kv., 20 ma.) | 0.5, 1, 4, 16, 32, 128 | |
| Carbon Step Tablet | Photometric | 16 | |
| High Resolution | Photometric | 1, 2, 4, 8, 16 | |
| Processing Parameters | | | |
| Step | Chemical | Time | Temperature |
| Development | D-76 (1:1) | 7 min. | 20 deg. C |
| Stop | SB-1A | 30 sec. | 20 deg. C |
| Fix | Rapid Fix | 5 min. | 20 deg. C |
| Wash | Water | 30 min. | 20 deg. C |
| Rinse | Photo-flo | 1 min. | 20 deg. C |

All of the final x-ray and light quanta exposures, including sensitometric replicates, were contained on 35 mm film strips and exposed for similar time intervals to eliminate possible density variations due to reciprocity law failure (Mees and James, 1966, pg. 132). The film strips were taped together, lengthwise, and processed simultaneously in an Ansco 35 mm processing tank. All of the exposed film was processed within one hour of the first exposure to minimize latent image decay. The processed sensitometric step tablet images were immediately measured on a MacBeth TD-203-A Quanta Log Densitometer to ensure that the desired gross diffuse density values were obtained.

CHAPTER 4

DATA SAMPLING AND PREPROCESSING

In preparation for use of the image restoration "recipe", Eq.'s (2.19) and (2.20), the experimental data was digitally sampled and some preprocessing functions were performed. This included selection and calibration of two microdensitometer scanning systems and conversion of diffuse density values to equivalent mass of silver units. The procedures used to perform these data sampling and preprocessing tasks are discussed in the following sections.

Description of Microdensitometer Systems

The conversion of the experimentally derived photographic images to digitally sampled data files was performed using two digital microdensitometer scanning systems. The x-ray exposed line images and the high resolution line image groups, representing spatial frequencies greater than 10 lp/mm (groups 2 and 3), were digitized using a Mann-Data Micro-Analyzer operated by Mead Technology Laboratories in Dayton, Ohio. The 1 lp/mm resolution target image element (group 1, element 1) was digitized using a modified Zeiss SPM05 microdensitometer system provided by Xerox Corporation and located in Webster, New York.

Exact specifications and some applications of both instruments have been well documented and will not be reiterated in this discussion (Data Corporation, 1970; Butler, 1973; Swing, 1976; Lehmbeck and Jakubowski, 1979). It is sufficient to state that both instruments have overall system transfer functions that exceed the necessary resolution limits required by this study. Also, each has a film stage capable of holding the photographic film very flat and translating it in increments of less than 0.001 mm with sufficient precision. Each instrument was independently calibrated, in terms of

overall system transfer function response, for the conditions under which it was used. The results of the tests are reported following a discussion of digital scanning parameteric requirements.

Data Sampling Requirements

The selection of the microdenstiometer parameters used for the scanning of the photographic images was governed by two factors. First, the necessity to satisfy the requirements of the Whittaker-Shannon sampling theorem (Bracewell, 1965, pg.189-215; Goodman, 1968, pg. 21-25) and second, a desire to eliminate a number of data preprocessing steps usually required for the correction of the optical transfer function associated with a digital scanning microdensitometer (Jones, 1967; Schowengerdt, Antos and Slater, 1974; Schowengerdt, 1975).

Sampling Theorem Requirements

The maximum spatial frequency contained in the photographic images must be less than the resolution limit of Panatomic-X processed under the development conditions described in Chapter 3. An estimate of this value was obtained by reading the resolution value of the high-resolution target images.

A monocular Bausch and Lomb microscope with a total magnification of 250X (12.5X eyepiece and a 20X objective with a 0.4 numerical aperture) was used to view the resolution target and a photographic film image. The original target was observed to provide 1000 lp/mm (Group 3, line number 1) as specified by the manufacturer. This ensured that the target and the microscope would not be the limiting factors of the observed resolution on the film. The maximum resolution observed on the photographic image of the high resolution target was 100 lp/mm (Group 2, line number 11).

Based upon this estimation of the maximum resolution of the film, the maximum dimension of the aperture used for microdensitometer measurements could be no greater than 0.010 mm. To

satisfy the sampling theorem a maximum sample spacing of 0.005 mm would be required, assuming a bandlimited frequency response.

Digital Preprocessing Considerations

Fulfillment of the minimum requirements of the sampling theorem typically requires the necessity of additional data preprocessing steps. Under this condition the overall transfer function of the microdensitometer system, determined by the product of the optical transfer function (OTF) of the microdensitometer optics and the spectrum of the scanning aperture, has a cutoff frequency just exceeding the desired cutoff frequency of the photographic film image. Thus, during the digital sampling process the higher frequency components contained within the photographic film images are significantly attenuated. This attenuation is removed by dividing the overall OTF of the microdensitometer system into the discrete Fourier transform of the transmission values of the digitally sampled image. This correction stage is absolutely necessary if the intent of the task is to accurately determine the MTF of an imaging system or some photographic film.

However, this study is primarily interested in the influence of adjacency effects on photographic film images which are known to enhance images containing reasonably low spatial frequency content (Nelson, 1971). Thus, it seems reasonable to select the scanning parameters such that the OTF of the microdensitometer system meets the minimum requirements of the sampling theorem for the cutoff frequency of the film and, in addition, provides a minimum attenuation (approximately less than 10 percent) in a specified lower frequency band. Under such conditions the influence of adjacency effects on photographic film images could be analyzed without the necessity of correcting for the microdensitometer OTF. Image degradation that might result in the higher spatial frequency range would be less dependent on adjacency effects and not important to the purpose of this investigation.

Selection of Film Scanning Parameters

The scan apertures and sample spacings that were selected for the microdensitometer scans were based on the image content of specific film areas and on the previously described data sampling and preprocessing considerations. The selected image scanning parameters are summarized in Table 4.1.

The photographic image areas of interest consisted of the variable width (0.010, 0.100, 1.000 mm) x-ray exposed line set and selected 1 lp/mm to 100 lp/mm line groups obtained from the high resolution test target images.

Table 4.1. Microdensitometer scanning parameters for film images.

| Imagery Type | Micro- densitometer Type | Objectives | | Scan Aperture | | Sample Spacing (mm.) |
|----------------------|--------------------------------|---------------------------|------------|---------------|---------------|----------------------------|
| | | Influx | Efflux | Geometry | Size | |
| | | (Mag./ N.A.) (Mag./ N.A.) | | (mm.) | | |
| Inconel-edge | Mann-Data | 10 X/ 0.25 | 10 X/ 0.25 | rectangular | 0.001 x 0.080 | 0.0005 |
| X-Ray slits | Mann-Data | 10 X/ 0.25 | 10 X/ 0.25 | rectangular | 0.001 x 0.080 | 0.0010 |
| Inconel-edge | Mann-Data | 10 X/ 0.25 | 10 X/ 0.25 | circular | 0.005 | 0.0025 |
| Resolution target | Mann-Data | 10 X/ 0.25 | 10 X/ 0.25 | circular | 0.005 | 0.0025 |
| Photographic edge | Zeiss | 8 X/ 0.20 | 4 X/ 0.10 | rectangular | 0.005 x 0.080 | 0.0025 |
| Resolution target | Zeiss | 8 X/ 0.20 | 4 X/ 0.10 | rectangular | 0.005 x 0.080 | 0.0025 |

The x-ray exposed line images contained large aspect ratios due to their 10 mm length, as shown in Figure 3.3. This length was much larger than the distance over which development diffusion and depletion effects could occur for panatomic-x film. Thus, the central region of these line images could contain only one dimensional (perpendicular to the length of the line) edge and Eberhard effects. Microdensitometer scans on these regions were performed with a one dimensional slit aperture.

A 0.001 mm slit width was selected for these image scans since exposures to x-ray quanta exhibit far less optical scattering than images exposed to light quanta. This aperture width is typical of that used by Nelson (1971) and should eliminate image degradation below approximately 100 cycles/mm caused by the microdensitometer OTF degradation. The 0.001 mm sample spacing was sufficiently small to accurately locate the high density cusp (a characteristic of the edge effect) of the 1.000 mm lines and the central peak of the 0.010 mm lines. The equivalence of the sample spacing and the scan aperture width did not create an aliasing problem since the effective cutoff frequency of the film (ignoring film grain noise) was approximately 100 cycles/mm. The slit length was set at 0.080 mm to reduce the film grain noise.

The 1 lp/mm resolution target images were also scanned with a one dimensional slit aperture. Again, the aspect ratio of these line images were sufficient to allow for investigation of one dimensional edge effects. However, since these images were created through exposure to light quanta, having greater optical scattering properties, the selected slit dimensions were 0.005 x 0.080 mm. The sample spacing was 0.0025 mm to satisfy the sampling theorem requirements.

For the higher spatial frequency line image groups, 10 lp/mm and greater, a 0.005 mm circular scanning aperture was selected with a sample spacing of 0.0025 mm. The entire central portion of the high resolution test target image, groups 2 and 3, was sampled two dimensionally to allow for subsequent analysis over a wide range of line image sizes.

Microdensitometer Calibration Test Results

The microdensitometers were calibrated based on the measurement of their respective OTF's. High quality edge targets were scanned and the data was analyzed following standard edge gradient analysis (EGA) procedures (Scott, Scott and Shack, 1963; Findley and Marshall, 1965; Schowengerdt, 1975). The edge derivative was determined using the method of finite differences.

Mann-Data Micro-Analyzer

The edge target selected for the calibration of the Mann-Data Micro-Analyzer consisted of a medium contrast (10:1) Inconel edge coated on a glass substrate. The edge was of very high quality and was successfully used in previous calibration tests for 0.001 mm slit apertures. Light scattering off the metallic edge surface had not previously caused significant transfer function degradation for properly focused objectives.

The setup configuration used matched numerical aperture (NA) objectives with the limiting aperture established by the influx objective (sample scanning mode). Assessment of the coherence properties of the optical beam and their effect on linearity of operation were not measured. However, a previous investigation using the Micro-Analyzer in the sample scanning mode with matched NA objectives had been reported (Swing, 1976) to closely approximate theoretical linear performance.

An edge scan using the 0.001 x 0.080 mm slit aperture was performed with a sample spacing of 0.0005 mm. The results of the EGA, as shown in Figure 4.1, represent the product of the actual OTF of the Micro-Analyzer and the spectrum of the scanned edge. The theoretical OTF of the Micro-Analyzer was derived from the product of the spectrum of the 0.001 mm slit aperture, $\text{sinc}(x/0.001)$, and the theoretical OTF of a diffraction-limited 0.25 NA objective. Comparison of the spectrum provided by the edge scans and the theoretical OTF of the Micro-Analyzer indicate that the Micro-Analyzer is performing very near its diffraction limit below 140 cycles/mm. This also implies that the spectrum of the input edge target is nearly unity below this same spatial frequency limit. The

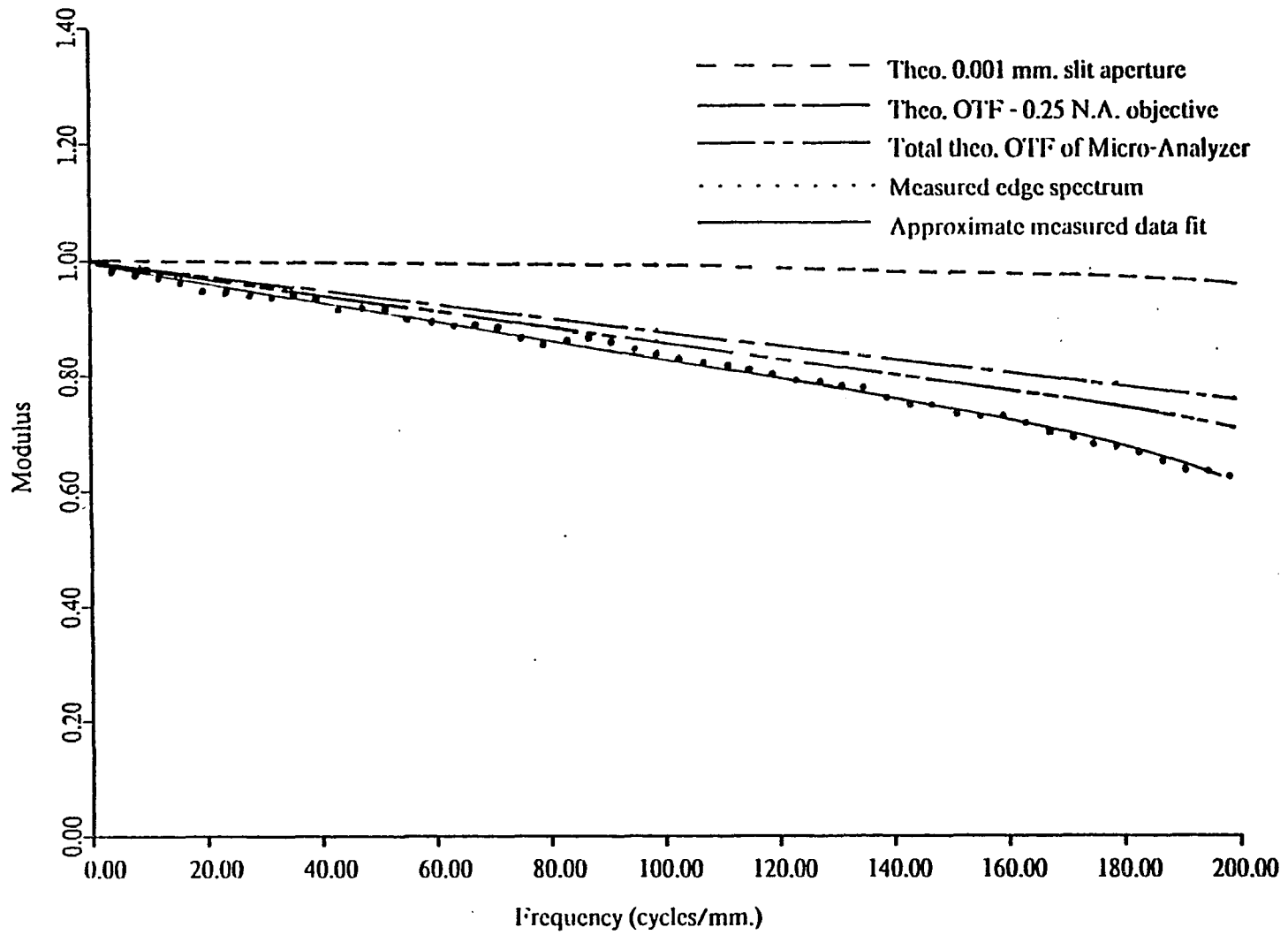


Fig. 4.1. Calibration edge spectrum.
Mann-Data Micro-Analyzer (0.001 mm. x 0.080 mm. slit).

differences between the two curves above 140 cycles/mm could be due to degradation of either the edge spectrum or the Micro-Analyzer performance. However, this spatial degradation occurs beyond the spatial frequency limits of concern in this investigation.

Three separate edge scans were performed using the 0.001 x 0.080 mm slit aperture to verify proper focusing of the microdensitometer objectives and to check slit alignment. The objectives were defocused and then refocused between scans. The location of best focus was based on maximizing the PMT signal, as read on a chart recorder, while the objectives were adjusted with the edge in the sample plane. A viewing microscope, an integral part of the Micro-Analyzer, allowed observation of the scanning aperture and the edge target, simultaneously. The slit aperture was initially aligned to the edge and then the edge was translated, on the image plane platen, parallel to the long dimension of the slit aperture. Visual verification of alignment was made over the entire length of the edge (which was much greater than the slit length) prior to each replicate scan. The results of the replicate scans, as represented by the edge scan spectra shown in Figure 4.2, indicate that the calibration was repeatable and operational errors were not significant.

Potential hysteresis effects were also investigated by performing two edge scans in opposite directions, one starting on the high contrast side of the edge and one starting on the low contrast side of the edge. The resulting edge scan spectra, shown in Figure 4.3, indicate that potential hysteresis effects were not significant.

Calibration of the 0.005 mm circular aperture was performed using a similar edge scan procedure with a sample spacing of 0.0025 mm. Five edge scans were performed in two orthogonal directions (corresponding to the x and y platen translation directions). The edge spectrum for each direction of each scan was calculated and averaged to provide the results shown in Figures 4.4 and 4.5. The theoretical OTF of a diffraction-limited 0.25 NA objective, the theoretical spectrum of a 0.005 mm circular aperture and their product, the total theoretical Micro-Analyzer OTF are shown

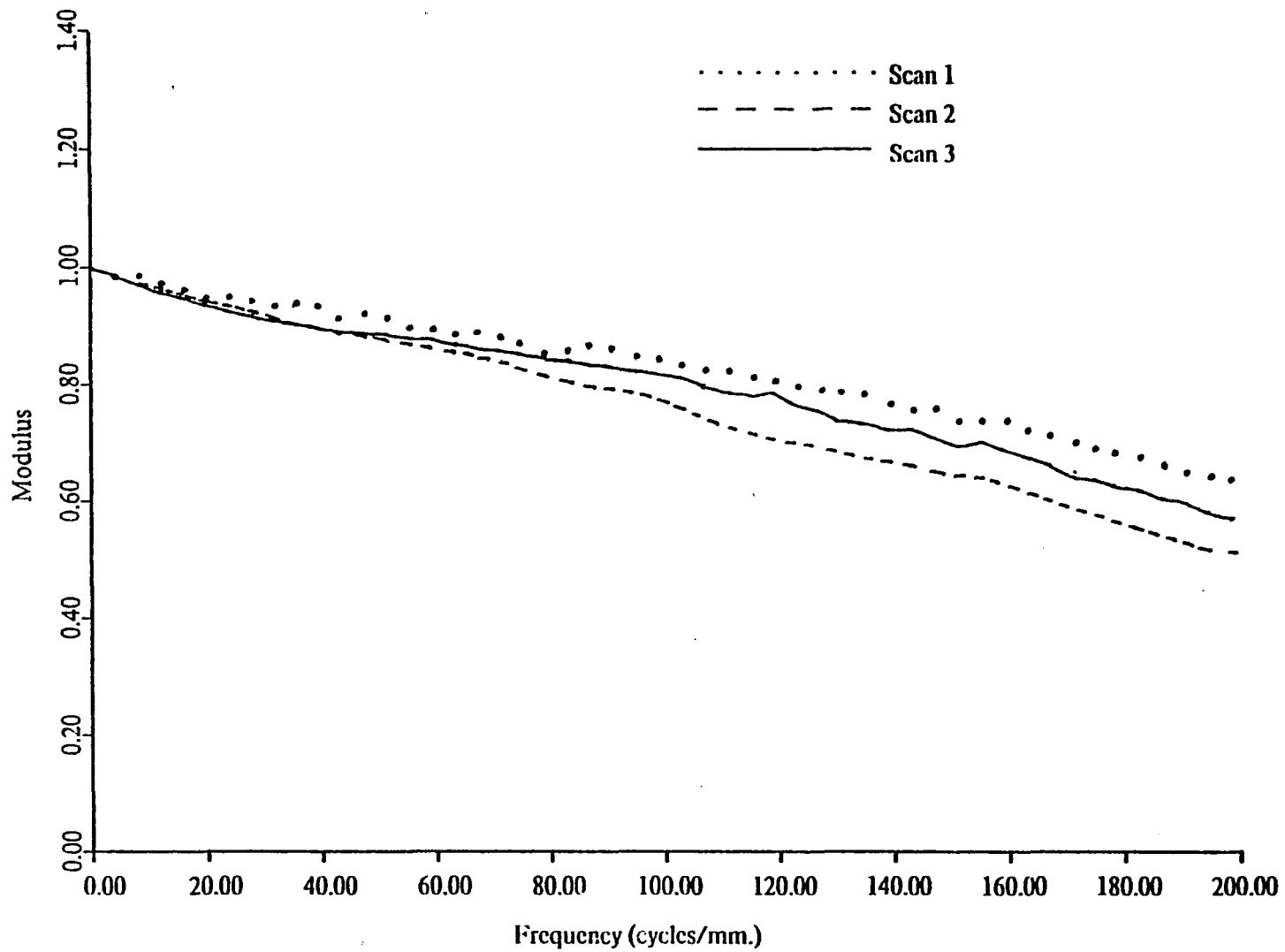


Fig. 4.2. Calibration edge spectrum: focusing - alignment effects.
Mann-Data Micro-Analyzer (0.001 mm. x 0.080 mm. slit).

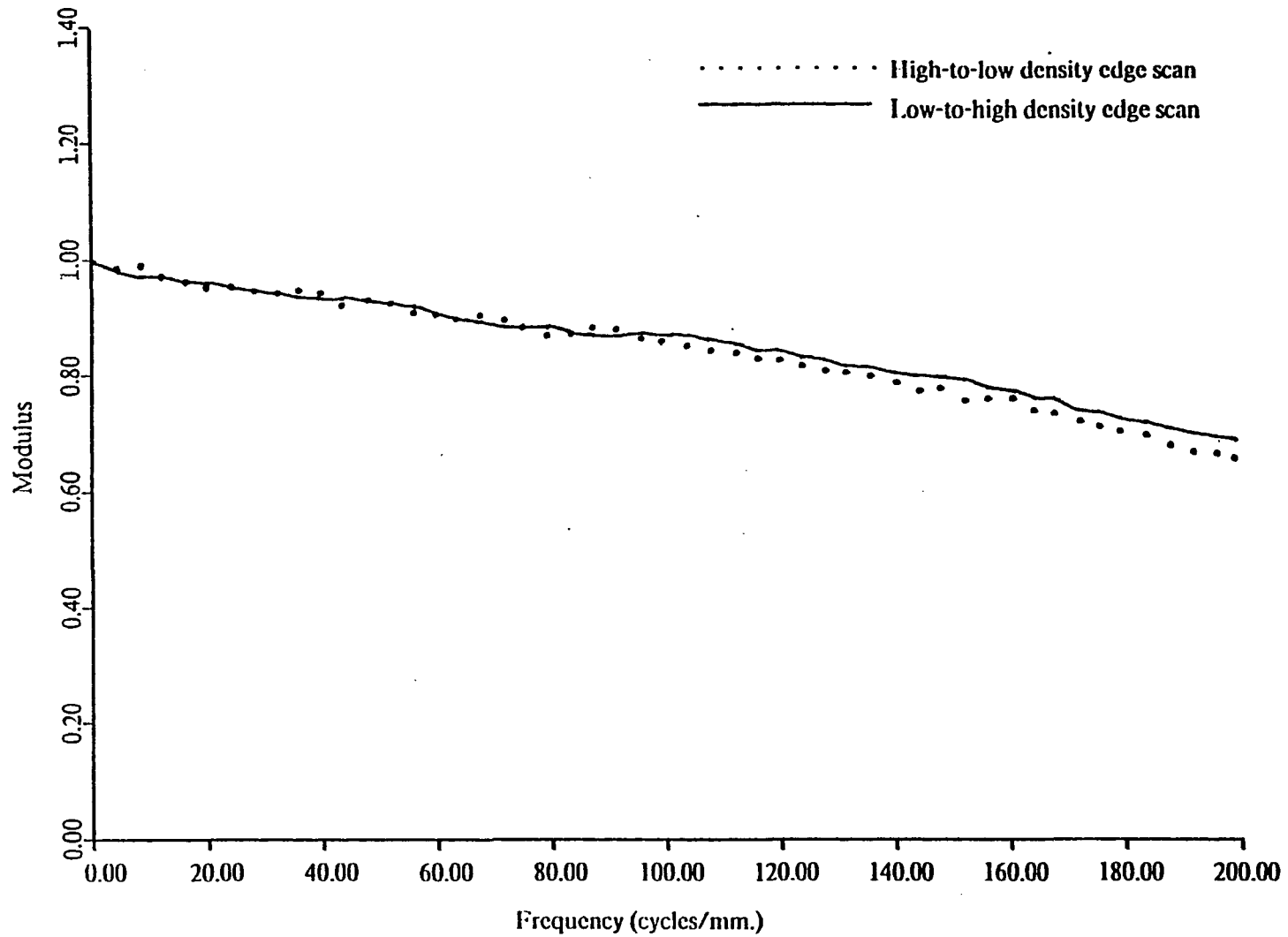


Fig. 4.3. Calibration edge spectrum: hysteresis effects.
 Mann-Data Micro-Analyzer (0.001 mm. x 0.080 mm. slit).

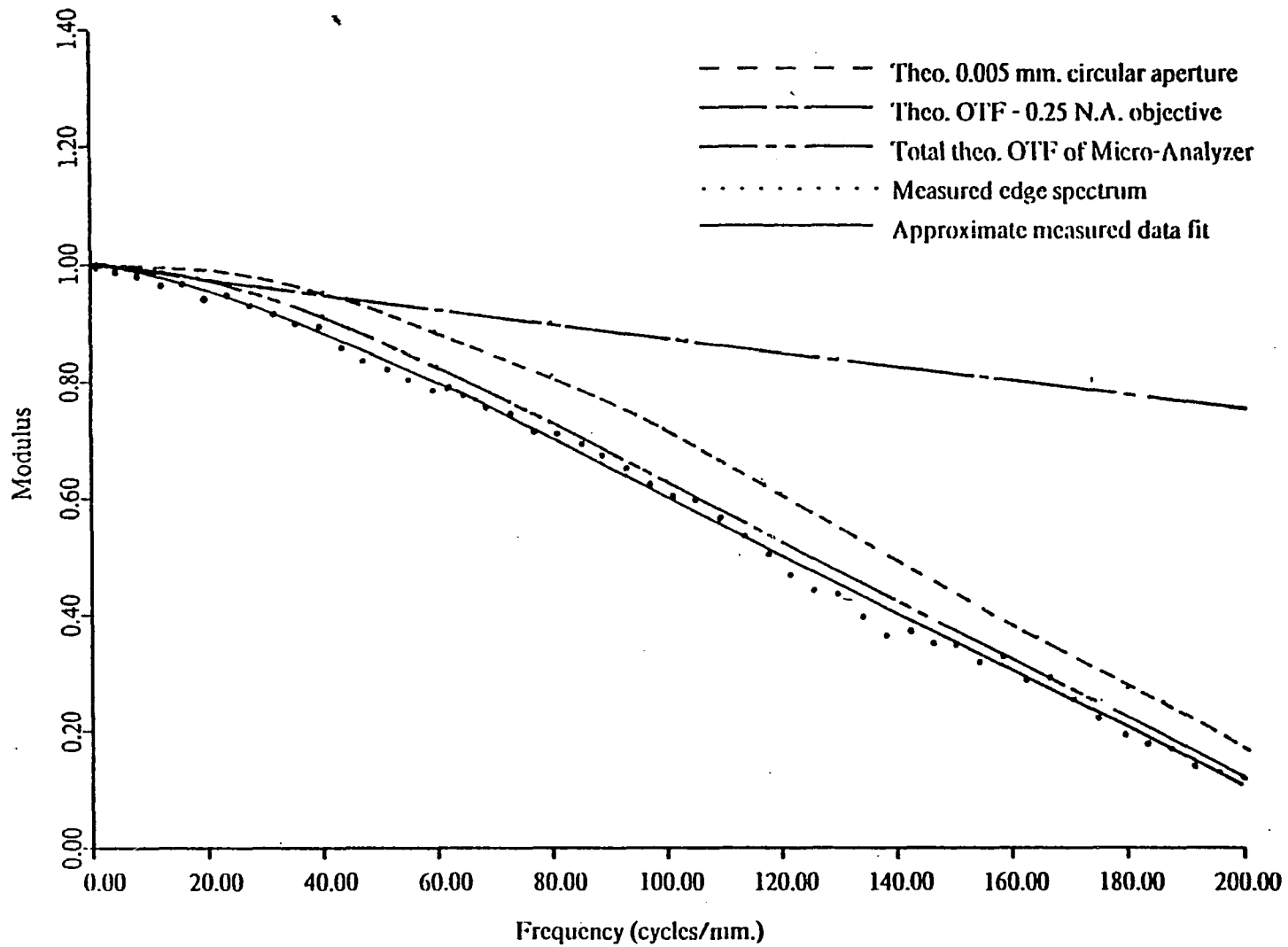


Fig. 4.4. Calibration edge spectrum.
Mann-Data Micro-Analyzer (0.005 mm. circular aperture).

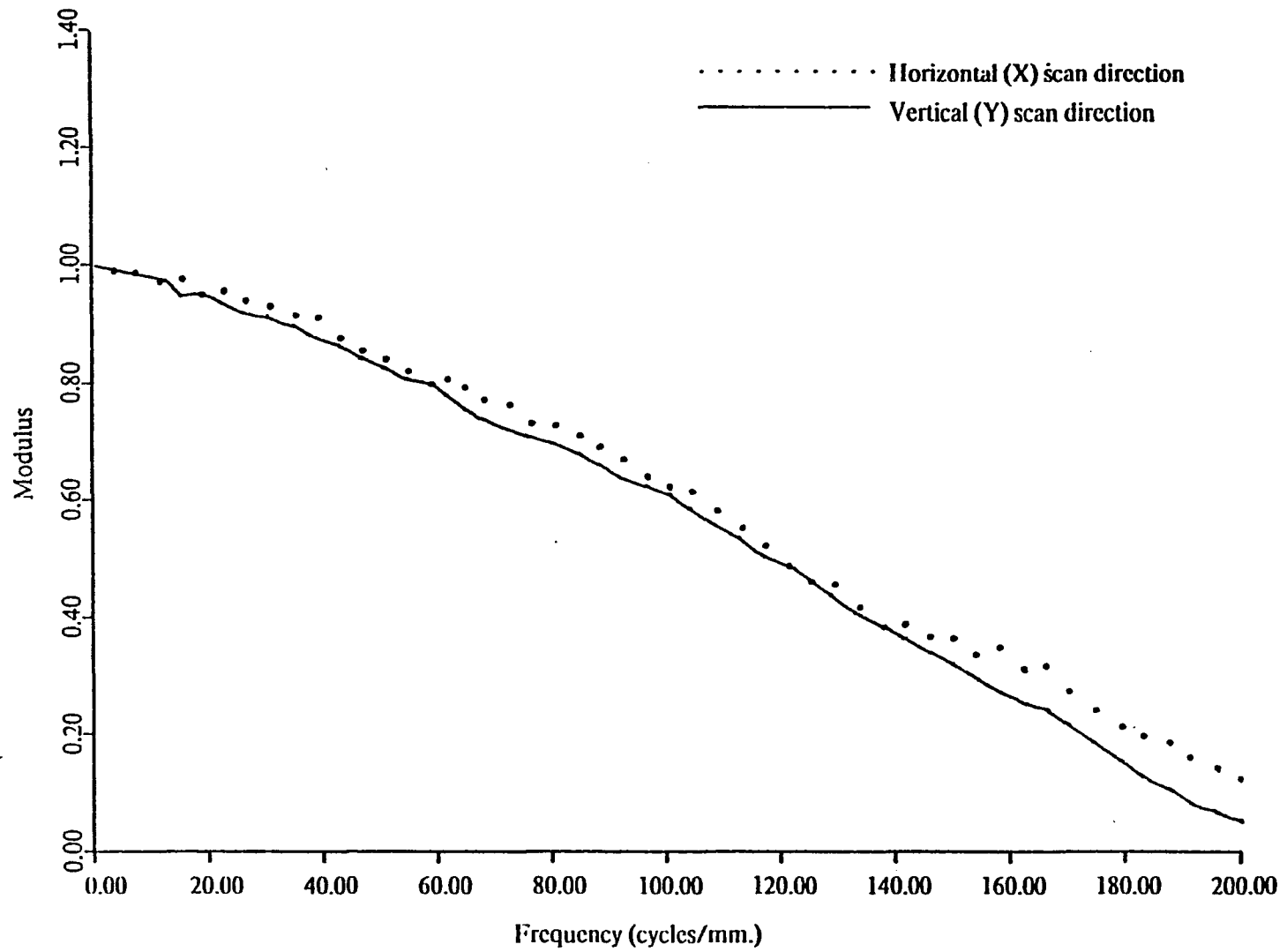


Fig. 4.5. Calibration edge spectrum.
Mann-Data Micro-Analyzer (0.005 mm. circular aperture).

in Figure 4.4. Comparison of the theoretical Micro-Analyzer OTF and the two calibration edge scan spectrums indicate that the MicroAnalyzer is operating near its diffraction limited capability over the entire 200 cycle/mm spatial frequency band for each scan direction.

Modified Zeiss SPM05

Subsequent to data collection using the Micro-Analyzer it was determined that additional microdensitometer scans were required for the low spatial frequency bars, 1 lp/mm, of the resolution target images. A modified Zeiss SPM05 microdensitometer with a 0.005 x 0.080 mm scan aperture was used at a sample spacing of 0.0025 mm. The Inconel edge target was no longer available so a photographic edge was used. The edge, exposed on a Eastman Kodak 649GH High Resolution Plate, was actually one side of a bar within the 1 lp/mm line group on the original high resolution target used during the exposure of the Panatomic-X film images. Since the resolution of this target had previously been observed to be at least 1000 lp/mm it was concluded that the edge sharpness would be adequate.

The Zeiss microdensitometer used an overfilled system configuration (influx NA = 0.20, efflux NA = 0.10), with the limiting aperture established by the efflux objective (image scanning mode). In general, this is not the optimum microdensitometer system configuration. However, it has been shown that such a configuration is capable of providing a very good spatial frequency response with only slight degradation over the lower spatial frequency band of interest in this study (Swing,1976).

The Zeiss microdensitometer edge scans were performed following the same general procedure described previously for the Micro-Analyzer edge scans. Comparison of the calibrated edge scan spectrum with the theoretical diffraction limited microdensitometer OTF's are given in Figures 4.6, 4.7 and 4.8. A greater deviation from the theoretical prediction for the Zeiss calibrated edge spectrum is shown to exist than was noted for the previous Micro-Analyzer results. This was

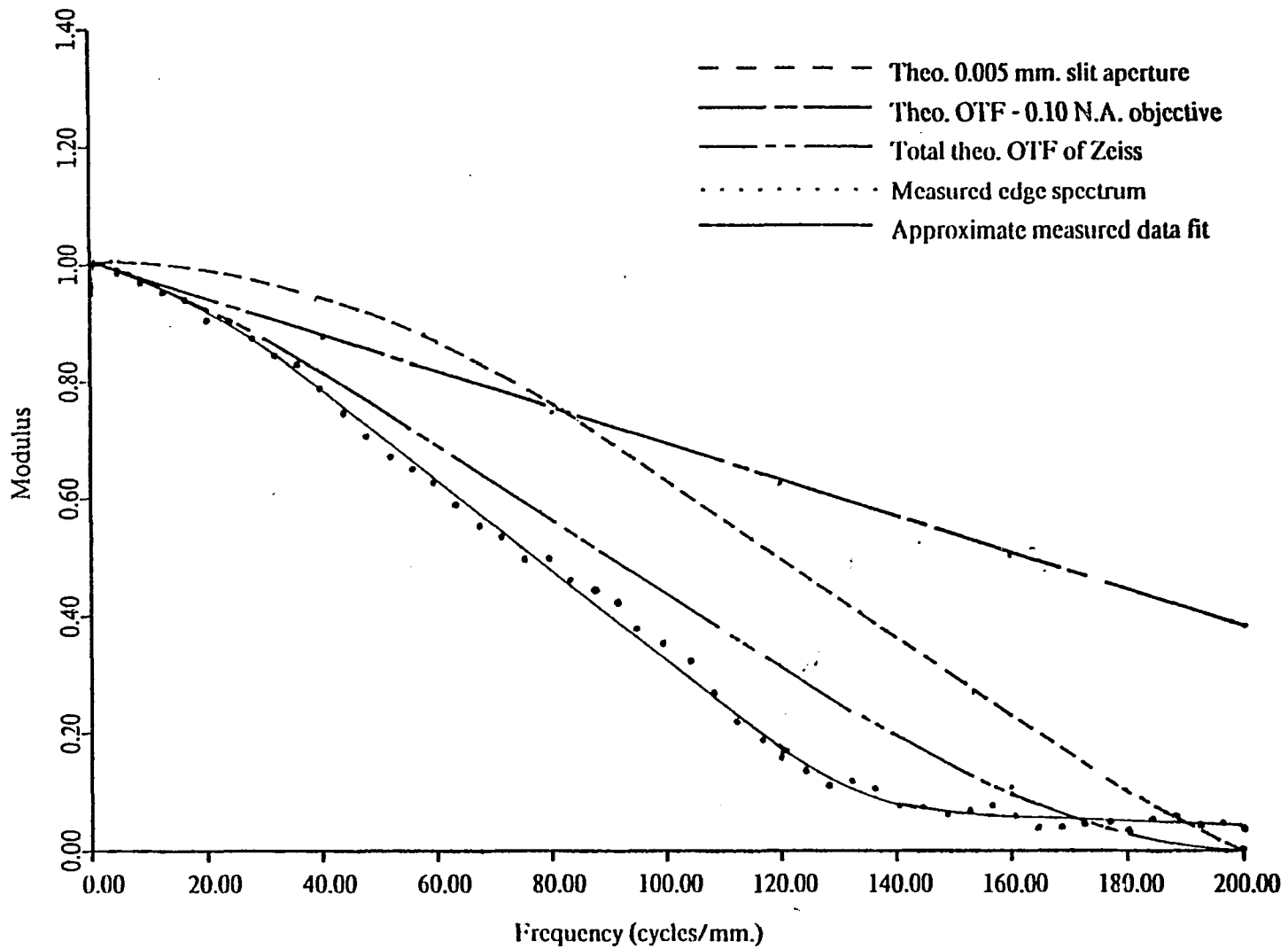


Fig. 4.6. Calibration edge spectrum.
Zeiss microdensitometer (0.005 mm. x 0.080 mm. slit aperture).

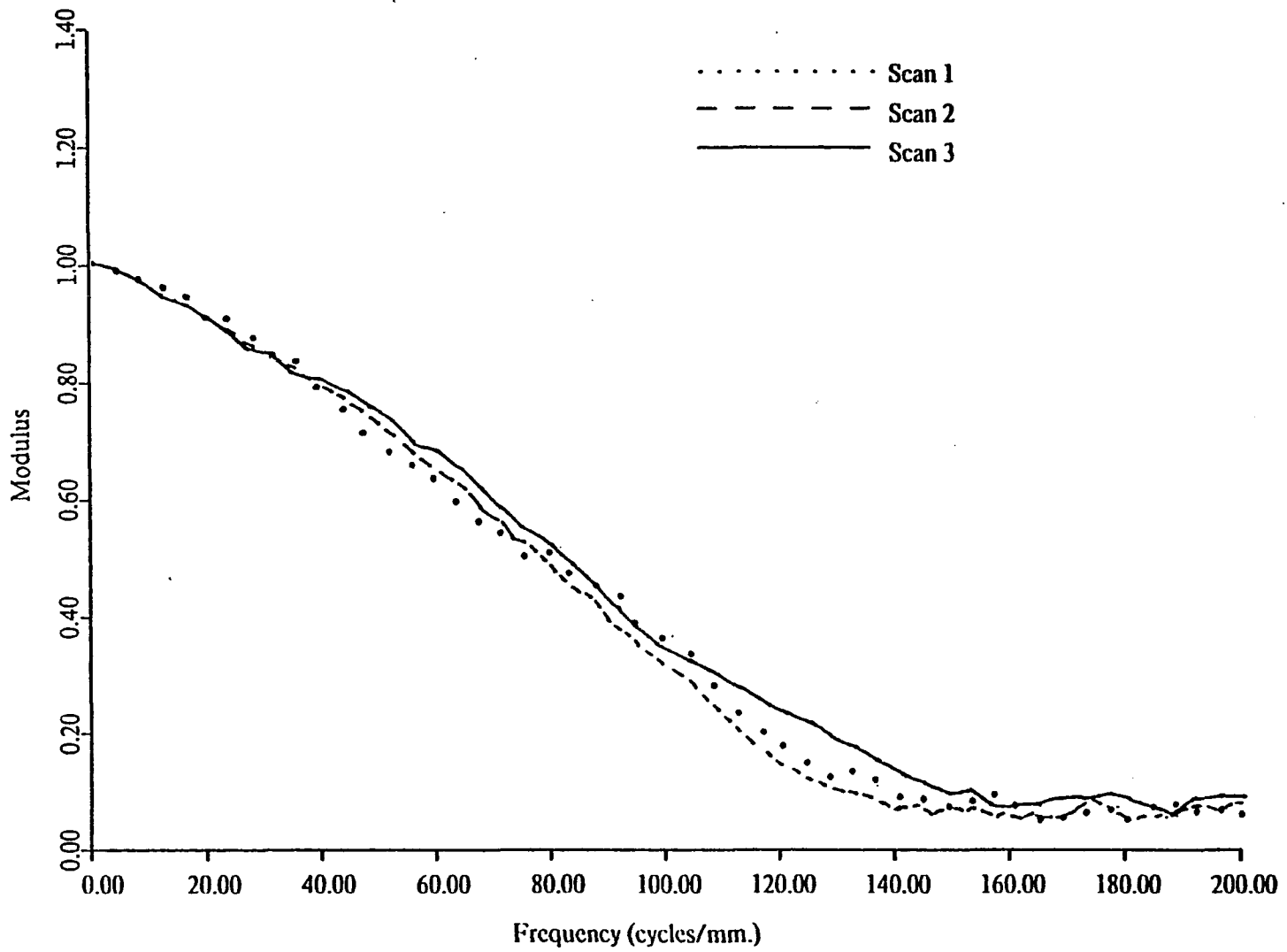


Fig. 4.7. Calibration edge spectrum: focusing - alignment effects.
Zeiss microdensitometer (0.005 mm. x 0.080 mm. slit aperture).

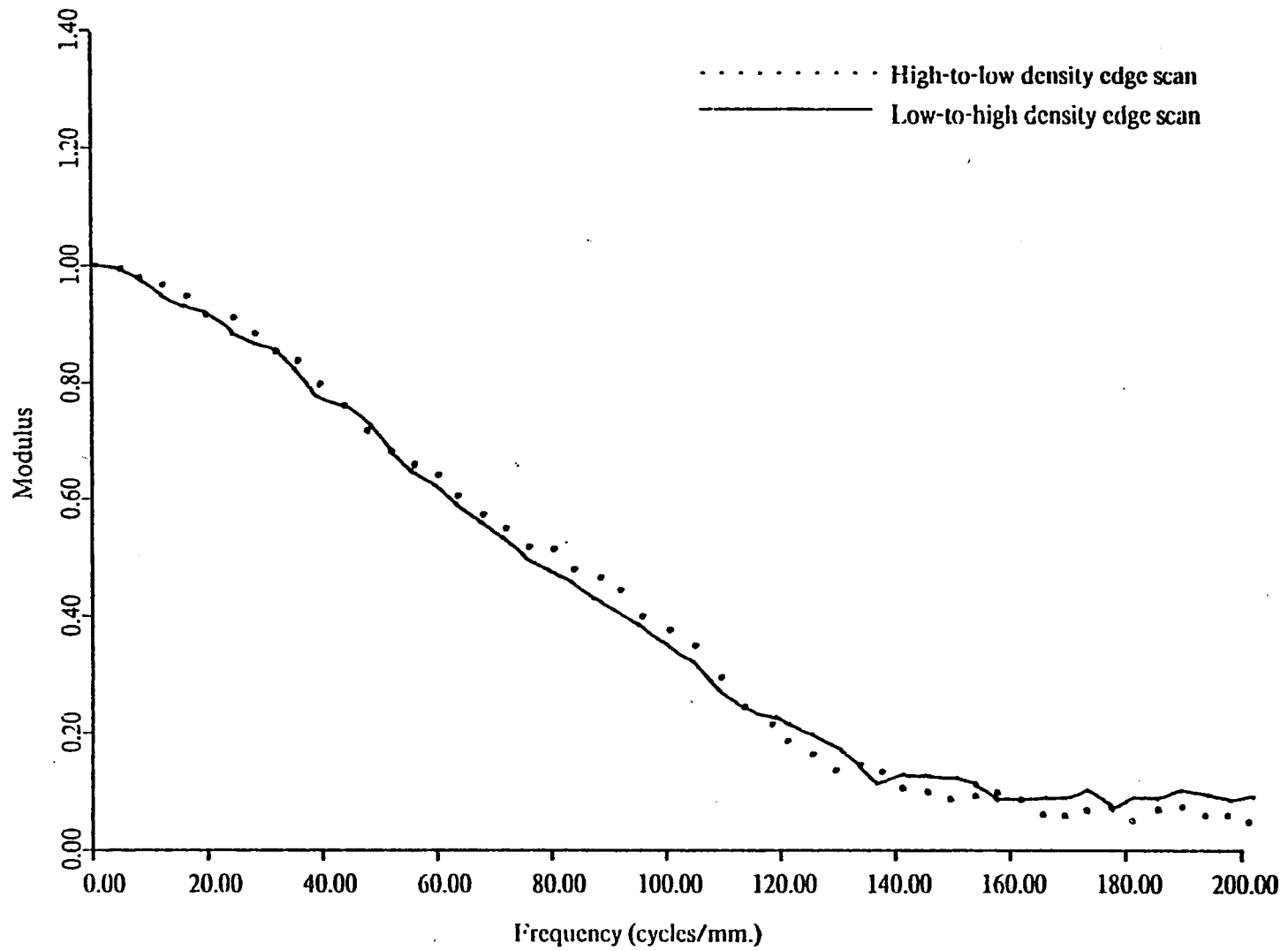


Fig. 4.8. Calibration edge spectrum: hysteresis effects.
 Zeiss microdensitometer (0.005 mm. x 0.080 mm. slit aperture).

anticipated, however, especially for the higher spatial frequency band due to the system configuration used by the Zeiss microdensitometer. Since the Zeiss microdensitometer was used for scanning only the very low frequency bar images, this performance was deemed acceptable. It should be noted that the edge profiles created from the digital data did not exhibit the presence of edge ringing effects, a known characteristic of microdensitometer nonlinear (coherent mode) operation.

Sensitometric Calibration

The diffuse density values of the large area sensitometric step tablets, created as described in Chapter 3, were measured using a calibrated Macbeth TD-203-A Quanta Log Densitometer equipped with a 4.0 mm aperture. The mean value and standard deviation of three replicate measurements of each step are given in Table 4.2. The measurement variability was not very significant. It should be noted, however, that these measurements represented selected film areas. Visual observation of the step tablet and high resolution target images indicated areas of gross nonuniformity. These areas of nonuniformity were attributed to the fact that lack of agitation during development of a photographic film can cause local development depletion. These areas were readily identified and separated from the uniform areas of development through visual observation and densitometer measurement verification. All film areas used to support digital data analysis and image restoration computations were selected from uniform areas of development..

Characteristic Curves

The sensitometric characteristics for the film exposures to x-ray quanta are given in Figure 4.9. As indicated, the selected exposure levels provided a 0.65 to 1.39 large-area diffuse density . This allowed subsequent evaluation of chemical spread functions and the Eberhard Effect for several exposure levels without truncation of edge or line peaks due to sensitometric saturation at the high density levels. The x-ray exposure levels selected to obtain the tri-slit images , as given in Table 3. 2 ,

Table 4.2. Large area diffuse density data.

| | Exposure Number | Step Number | Diffuse Density | |
|--------------|--------------------|----------------|-----------------|-----------|
| | | | Mean | Std. Dev. |
| Exposure to | 1 | | 0.65 | 0.010 |
| X-ray quanta | 2 | | 0.76 | 0.022 |
| | 3 | | 0.96 | 0.032 |
| | 4 | | 1.19 | 0.034 |
| | 5 | | 1.33 | 0.035 |
| | 6 | | 1.39 | 0.045 |
| Exposure to | | Base + Fog | 1.30 | 0.026 |
| Light quanta | | 1 | 1.14 | 0.031 |
| | | 2 | 1.07 | 0.020 |
| | | 3 | 0.93 | 0.018 |
| | | 4 | 0.77 | 0.021 |
| | | 5 | 0.65 | 0.017 |
| | | 6 | 0.52 | 0.015 |
| | | 7 | 0.38 | 0.022 |
| | | 8 | 0.33 | 0.018 |
| | | 9 | 0.30 | 0.020 |
| | | 10 | 0.30 | 0.017 |
| | 11 | 0.29 | 0.015 | |

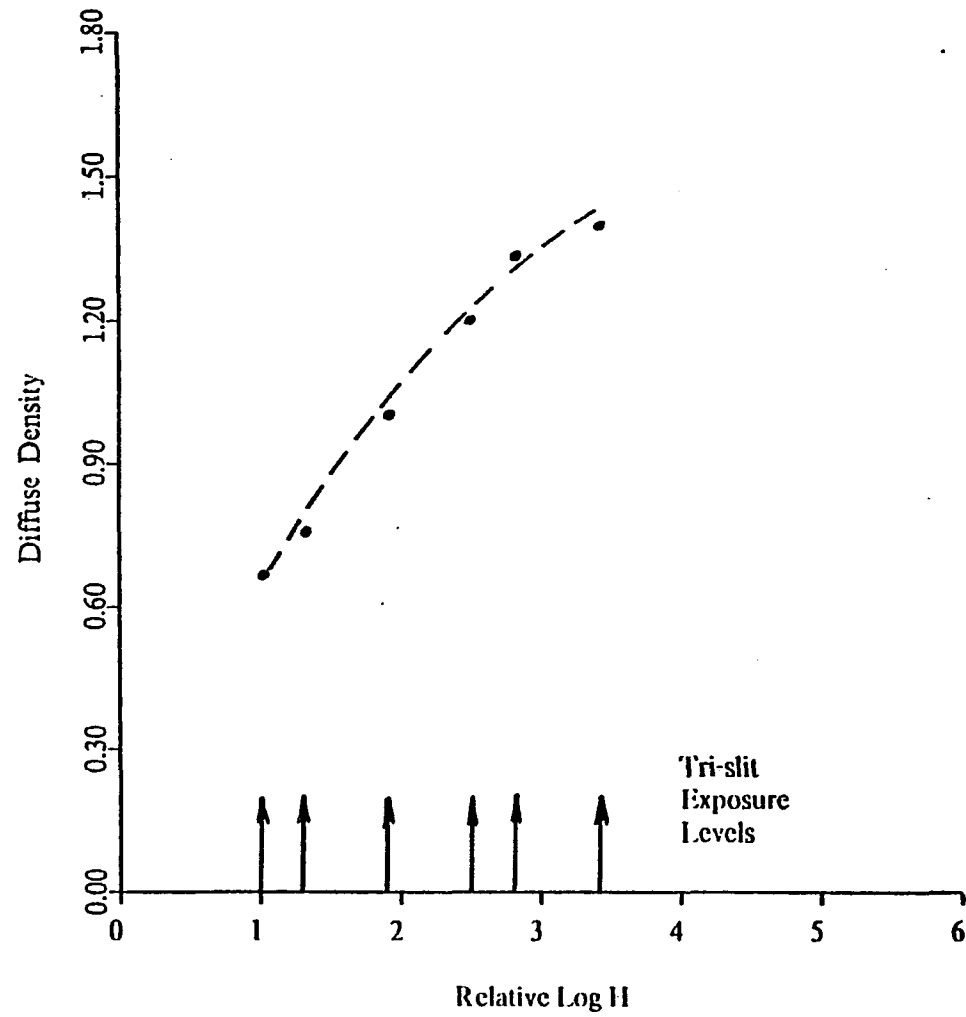


Fig. 4.9. Sensitometric curve: x-ray exposure quanta.

are marked on Figure 4.9. The average minimum diffuse density value found in the central portion of the 1 mm wide line images should clearly correlate to the gross diffuse density values given by this sensitometric curve. This comparison was made during subsequent digital data analysis as described in the next chapter.

The sensitometric characteristics for exposures to light quanta are given in Figure 4.10. The 16 second exposure used for the carbon step tablet provided almost the entire toe to shoulder region of the curve. Even though the density saturation level was not reached it was imminently close, based on the saturation density level of 1.39 obtained for the x-ray quanta exposures. The light quanta exposure levels used to obtain the high resolution target images, as given in Table 3. 2, are also marked on Figure 4.10.

A comparison of Figures 4.9 and 4.10 serves to emphasize the difference between the absorption rate of x-ray and light quanta. The maximum slope of the sensitometric curve for x-ray quanta occurs for zero exposure while that for light quanta occurs at some midrange exposure value. This is expected since a single x-ray quanta can initiate the development of one or more silver grains, whereas several light quanta are required for the same purpose (Dainty and Shaw, 1974, pg. 50).

Callier's Q Factor

The characteristic curves described the relationship between diffuse density of the step tablet images and the input exposure values. The measurement of photographic images containing fine detail requires the use of a microdensitometer, which measures specular density values. Unfortunately, diffuse density values are not equivalent to the specular density values. The specular density is always greater than the diffuse density. Their relationship is defined by the Callier Q factor, the ratio of specular to diffuse density. This ratio is a function of film/developer type, the microdensitometer optical system geometry and the density range of interest (Mees and James, 1966, pg. 420 - 421).

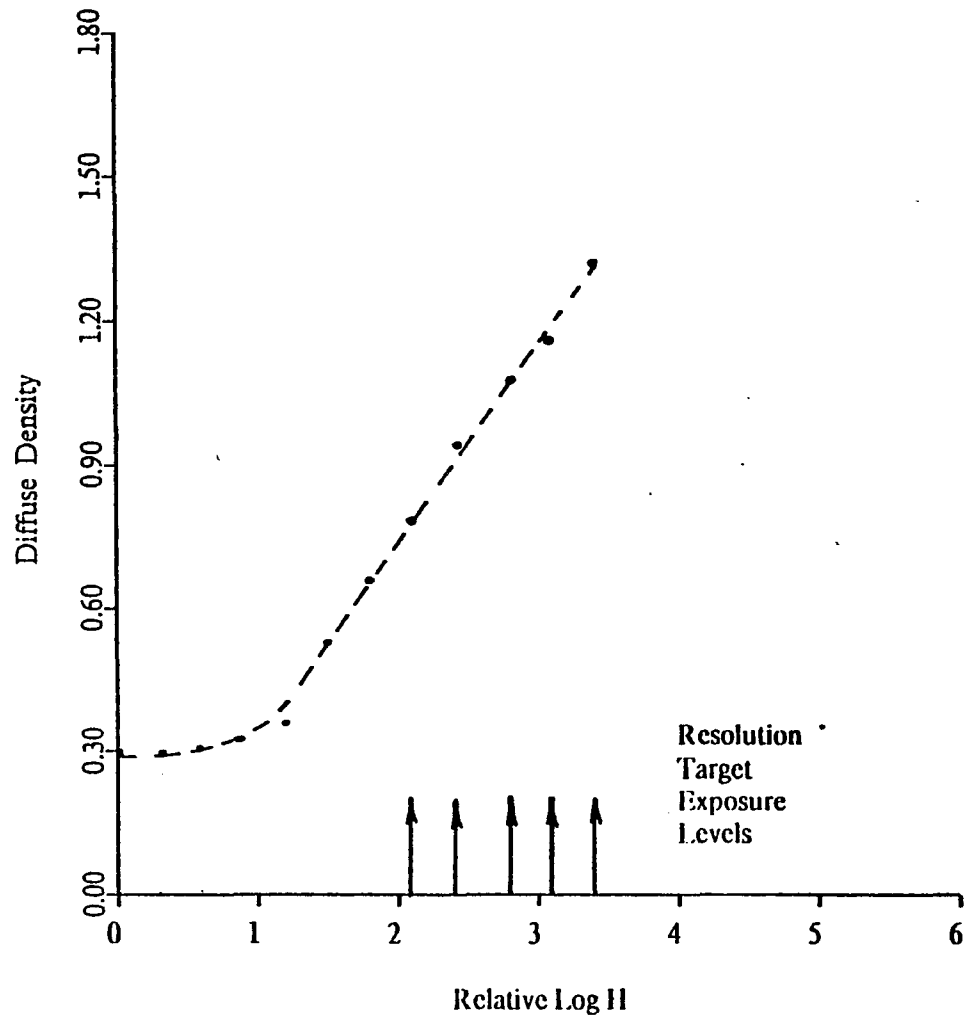


Fig. 4.10. Sensitometric curve: light exposure quanta.

The microdensitometers used in this study contained supporting electronic subsystems which could vary the slope (gain) and the intercept (zero adjust) of the measured output signal values. Thus, the recorded specular density values were adjustable over a relatively wide range of output values. Prior to the measurement of the tri-slit or resolution target images, the microdensitometers were calibrated using the step tablet which was exposed in the same manner as the specific target images to be scanned. The electronic subsystem was adjusted in an attempt to equate the microdensitometer output specular density values to the standard diffuse density values for each step of the calibration step tablet.

All calibration step tablets were scanned using the microdensitometer parameters given in Table 4.1. Three replicate scans, consisting of 600 samples, were made of each step. The mean and standard deviation of the measured specular density values resulting from these scans are given in Table 4.3. The relationship between the measured specular and diffuse density values are plotted in Figures 4.11 and 4.12 for the two microdensitometers. The specular and diffuse density values were found to be nearly identical over the density range provided by the step tablet. This indicates that a constant Callier Q factor existed over this density range and the microdensitometer calibration procedure simulated the multiplication of the actual specular density values by a constant to obtain equivalent diffuse density values.

All calibration step tablets were scanned using the microdensitometer parameters given in Table 4.1. Three replicate scans, consisting of 600 samples, were made of each step. The mean and standard deviation of the measured specular density values resulting from these scans are given in Table 4.3. The relationship between the measured specular and diffuse density values are plotted in Figures 4.11 and 4.12 for the two microdensitometers. The specular and diffuse density values were found to be nearly identical over the density range provided by the step tablet. This indicates that a constant Callier Q factor existed over this density range and the microdensitometer calibration

Table 4.3. Large area specular density data.

| Exposure | Step | Specular Density Mann-Data | | Specular Density Zeiss | | | |
|--------------|------|-------------------------------|--------|---------------------------|-----------|------|-----------|
| | | Number | Number | Mean | Std. Dev. | Mean | Std. Dev. |
| Exposure to | 1 | | | 0.64 | 0.029 | | |
| X-Ray quanta | 2 | | | 0.77 | 0.022 | | |
| | 3 | | | 0.98 | 0.027 | | |
| | 4 | | | 1.20 | 0.032 | | |
| | 5 | | | 1.34 | 0.036 | | |
| | 6 | | | 1.39 | 0.034 | | |
| Exposure to | | Base + Fog | | 1.29 | 0.043 | 1.28 | 0.037 |
| Light quanta | | 1 | | 1.19 | 0.024 | 1.15 | 0.027 |
| | | 2 | | 1.09 | 0.020 | 1.07 | 0.023 |
| | | 3 | | 0.95 | 0.019 | 0.92 | 0.031 |
| | | 4 | | 0.79 | 0.026 | 0.76 | 0.025 |
| | | 5 | | 0.66 | 0.020 | 0.65 | 0.018 |
| | | 6 | | 0.54 | 0.013 | 0.53 | 0.021 |
| | | 7 | | 0.39 | 0.029 | 0.37 | 0.027 |
| | | 8 | | 0.34 | 0.010 | 0.33 | 0.016 |
| | | 9 | | 0.30 | 0.018 | 0.29 | 0.015 |
| | | 10 | | 0.30 | 0.015 | 0.29 | 0.012 |
| | | 11 | | 0.30 | 0.012 | 0.28 | 0.010 |

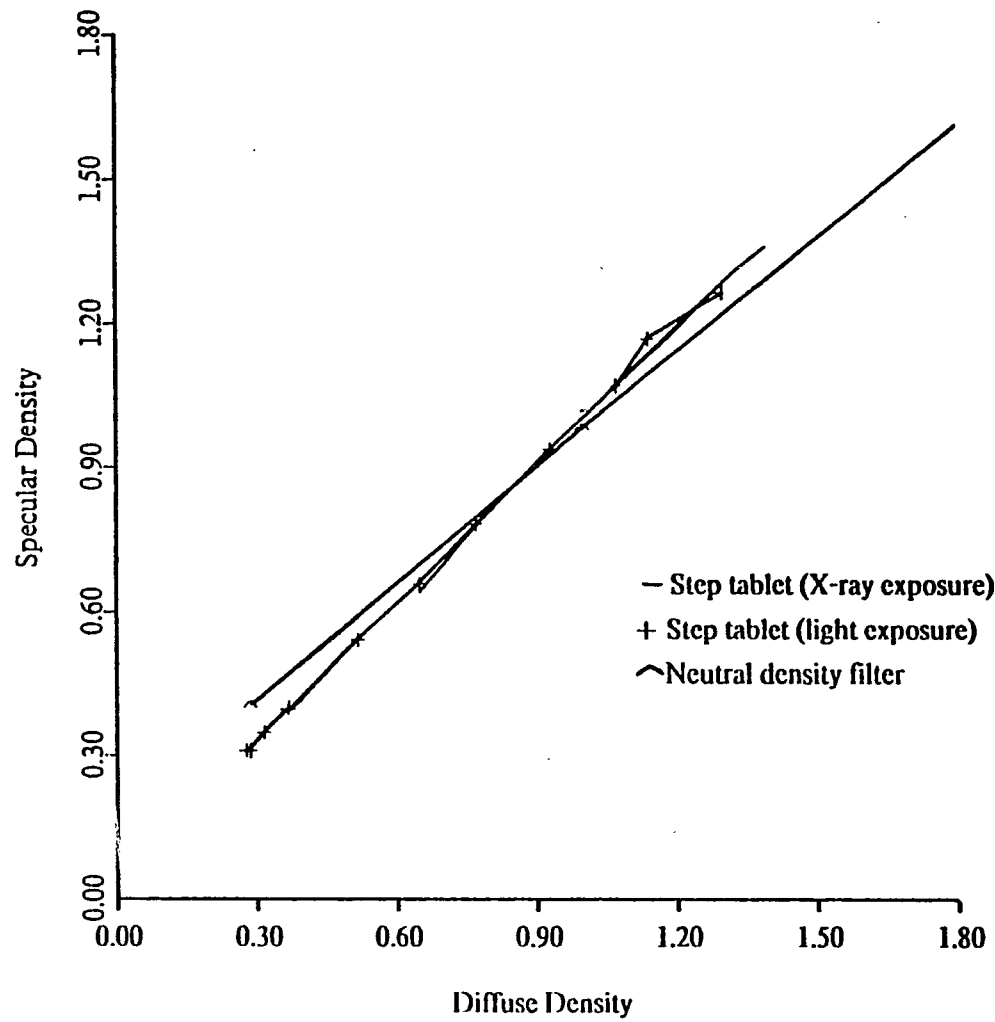


Fig. 4.11. Callier Q factor for Micro-Analyzer.

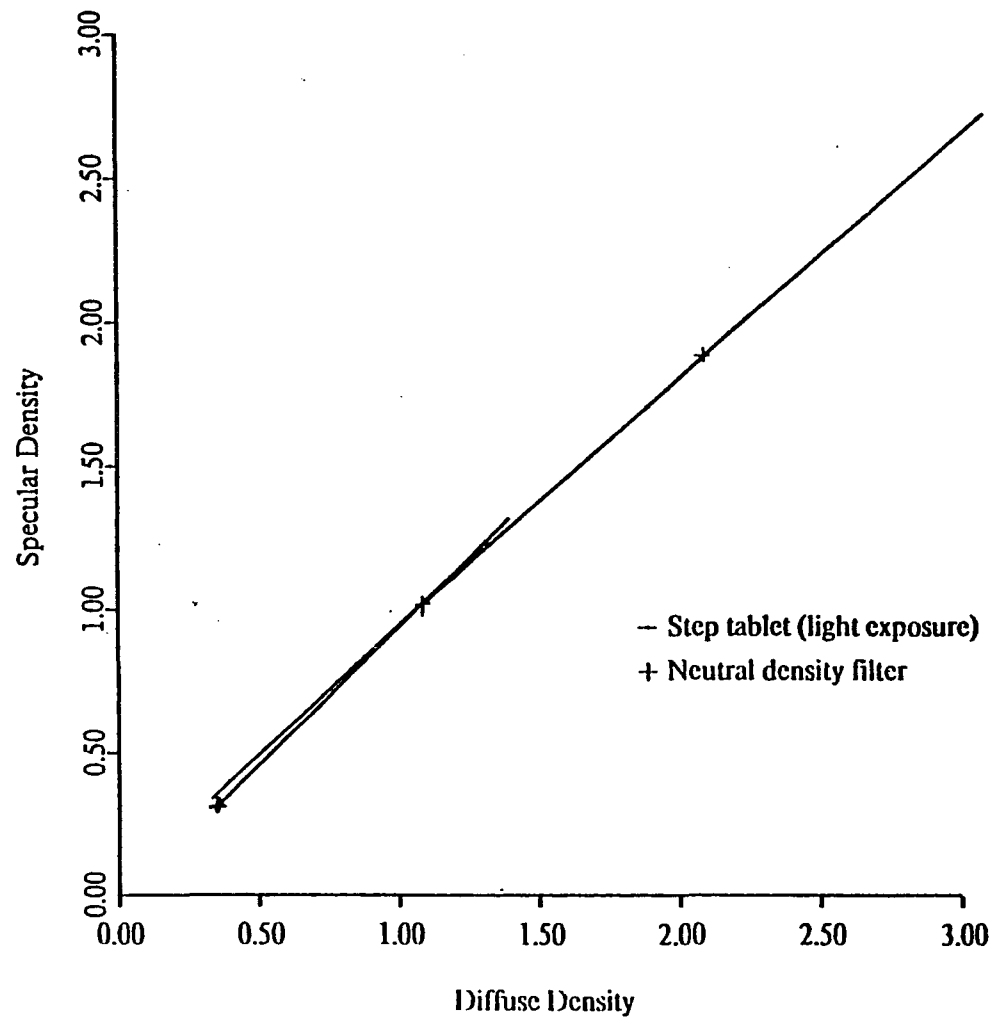


Fig. 4.12. Callier Q factor for Zeiss microdensitometer.

procedure simulated the multiplication of the actual specular density values by a constant to obtain equivalent diffuse density values.

The use of a step tablet, exposed and processed under the same conditions as the photographic imagery to be scanned, is a standard microdensitometer calibration procedure. A problem in the use of this procedure does arise, however, when the imagery contains density values which exceed those provided by the calibration step tablet. Such is the case when studying images containing adjacency effects. The peaks of edge and fine line images have diffuse density values which exceed the gross diffuse density values provided by the step tablet images. This is demonstrated by the Eberhard effect and is particularly true in this investigation since the maximum gross diffuse density values obtained were quite low due to the lack of agitation during development.

One solution to this problem is to ensure that the operation of the microdensitometer is linear over the maximum density range of interest. Then it is reasonable to assume that if a linear relationship exists between specular and diffuse density over a more limited range, it can be extrapolated to the higher density values. The microdensitometers used in this study were calibrated using the step tablet procedures previously described and then checked for linearity over a larger density range using Eastman Kodak No. 96 Neutral Density (ND) Filters, providing diffuse density values of 0.3, 1.0, 2.0, and 3.0. The relationship between specular and diffuse density using the ND filters is also shown in Figures 4.11 and 4.12. The microdensitometers had a linear response over the entire density range of interest. The reduced slope of the ND filter relationship represents the effects of the differences in the scattering properties between the material structure of the ND filters (colloidal carbon plus selected dyes in gelatin) and the photographic grain structure of the step tablet images (Eastman Kodak, 1969).

Mass of Silver Conversion

The conversion of optical diffuse density to equivalent mass of silver units was performed using an x-ray fluorescence analysis technique (Moore, Happ and Stewart, 1961; Mees and James, 1966, pg. 419). The technique used a digital recording x-ray spectrometer to measure fluorescent intensity, based on scintillation counts, which was linearly related to the mass of silver units within plus or minus 1.5% up to about 500 micrograms of silver/sq. cm. Correction values were then applied when the mass of silver exceeded 500 micrograms/sq. cm to maintain linearity. The samples that were used for this measurement were taken from a replicate set of step tablet exposure images made for this purpose.

The relationship between measured mass of silver and diffuse density can be expressed accurately by use of a power series, but is usually approximated by the covering power relationship given by Eq. (2.20). The results of the actual mass of silver measurement and their comparison with the covering power relationship, for $P=0.775$ and $n=0.5$, are given in Figure 4.13. Measured mass of silver values could not be obtained above the 1.39 maximum diffuse density value of the step tablet images. However, the covering power relationship is known to provide sufficient accuracy to much higher diffuse density values (Nelson, 1971). Since the covering power curve fit the measured data quite accurately over the measured set of diffuse density values, it was used for all mass of silver conversion requirements of this investigation. It is also interesting to note that the measured results shown in Figure 4.13 are also similar to those found by Nelson (1971) for Panatomic-X processed in D-76 (1:4) for 7 minutes.

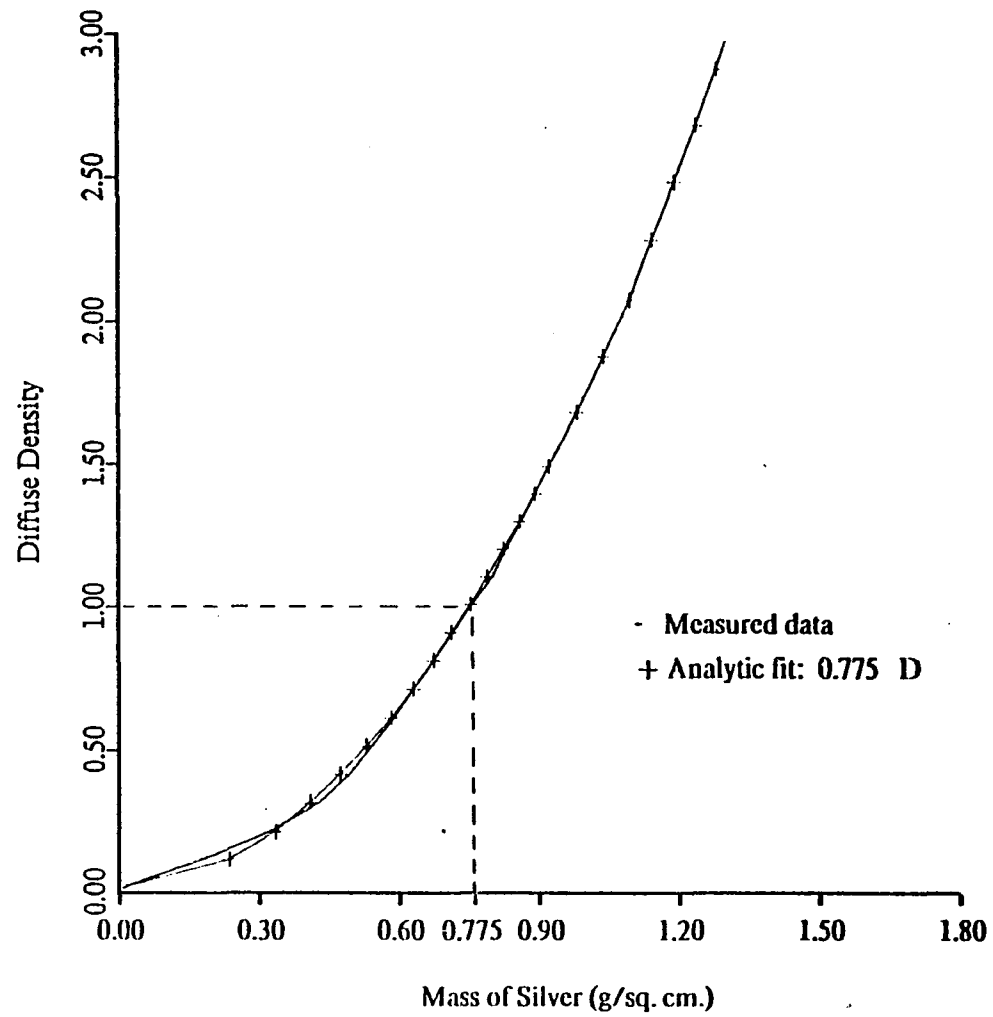


Fig. 4.13. Mass of silver conversion curve.

CHAPTER 5

IMAGE RESTORATION ANALYSIS

The application of the image restoration "recipe" to the photographic line images can now be considered. The determination of Nelson's (1971) CSF is reviewed in terms of edge data preprocessing procedures, the application of a CSF algorithm to the edge image pixels and the impact of several experimental x-ray exposure levels on the calculated CSF results. This is followed with a review of the data preprocessing procedures used to calculate the Eberhard Effect (EE) from x-ray exposure data. Comparisons are made between the magnitude of the EE and CSF area values.

The restoration "recipe" is then partially applied to various one-dimensional line image patterns. Intermediate results such as the chemical transfer function (CTF) and the reduction product term, the convolution term in Eq. (2.19), are provided.

Determination of the Chemical Spread Function

Nelson's (1971) CSF was calculated from the data provided by the microdensitometer scans of the line images 1.0 mm in width. As discussed in Chapter 4, five independent scans were made of each of the twelve line images using a 0.001 x 0.080 mm slit aperture and a sample spacing of 0.001 mm. The data was preprocessed and analytically fit with cubic spline functions to provide a reduction in the noise obtained in the edge derivative. The CSF was then calculated for several exposure levels and the results were compared in terms of CSF areas and profiles.

Edge Data Preprocessing

The data provided by the individual microdensitometer scans of the 1 mm line images exhibited a significant amount of noise. To reduce some of this noise several line images were

averaged (Blackman, 1968). The data contained in each replicate microdensitometer scan was shifted until the peak density point of one edge of each image was aligned. The data was then averaged point by point over the five scan records to provide an average line image for each of the twelve x-ray exposures.

Five representative edge images were then selected from the twelve averaged line images. The selected edges, shown in Figure 5.1, were created using the five highest x-ray exposure levels given in Table 3.2. The selection criterion was based on the desire to apply the initial part of the restoration "recipe" using CSF's of various magnitudes. As indicated in Figure 5.1, the selected edges contained a wide range of apparent adjacency effects and diffuse density levels. The edge density values illustrated include a film base density of 0.25.

During the selection process it was observed that the average line image profiles provided by the replicate exposure levels were nearly identical. Also, the average line images provided by the lowest x-ray exposure level exhibited a very small amount of apparent adjacency effect and contained some film processing nonuniformities which eliminated them from further analysis.

Nelson's CSF Algorithm

The CSF's used in this study were derived using an analytic version of Nelson's (1971) normalized edge derivative approach. Nelson (1971) assumed a symmetrical CSF and calculated one side of it using the derivative of the high density side of an edge exposed to x-ray quanta and the relationship

$$b = (n D^{n-1} dD/dx)/(D_2^n |D_2^n - D_1^n|) \quad (5.1)$$

where

b = magnitude of CSF

D = density value of upper portion of edge

n = nonlinear exponent given in Eq.(2.20)

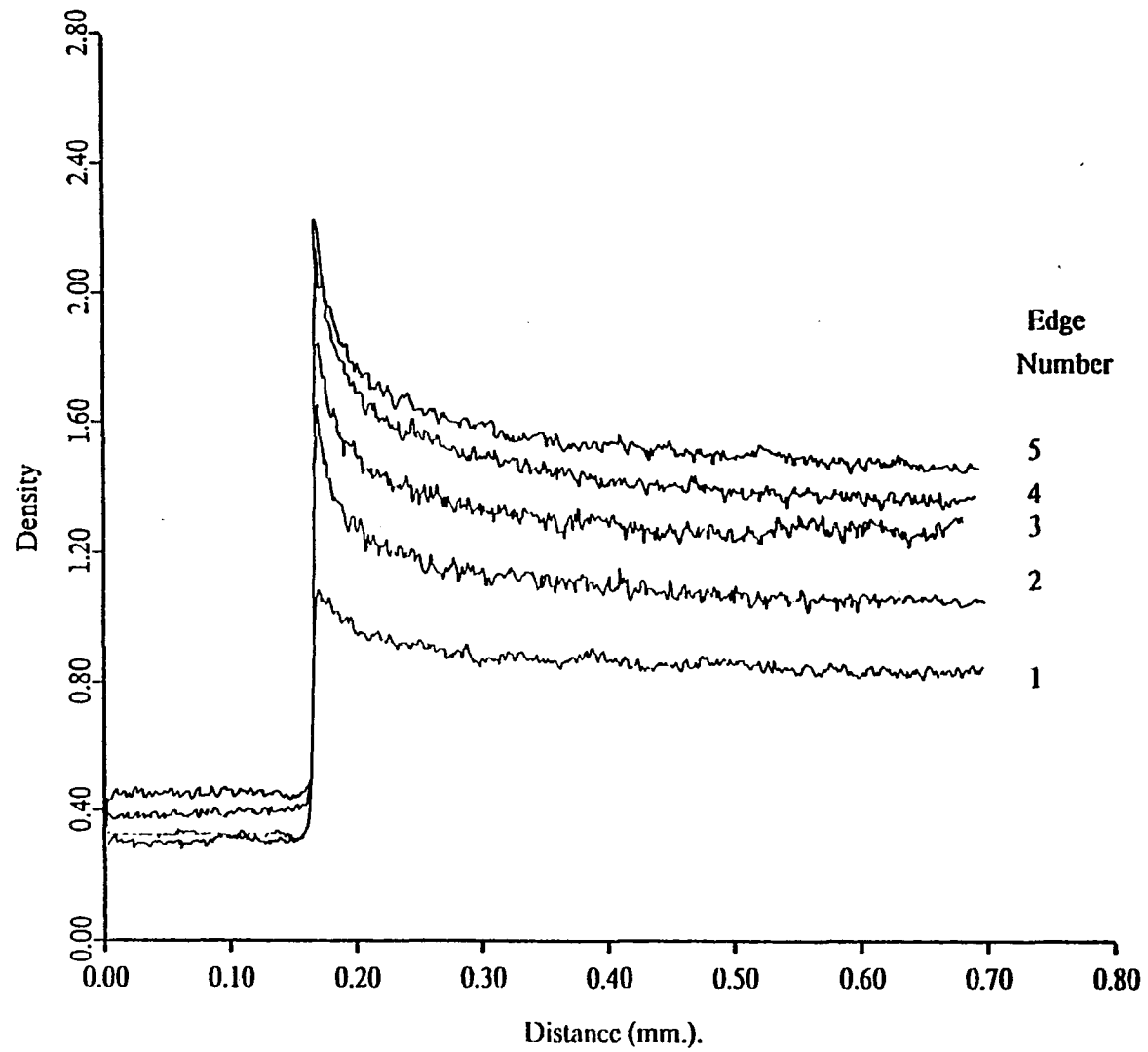


Fig. 5.1. Edge data from images created by x-ray exposures.
Selected edges from 1.0 mm. line width set.

dD/dx = first derivative of the upper portion of the edge at a
distance x (micrometers) from the edge boundary

D_1 = large-area density at low density side of edge

D_2 = large-area density at high density side of edge

In Nelson's (1971) investigation of adjacency effects, the film base density was subtracted from all image density values prior to calculation of the CSF or any other function. This procedure was followed in this study since nonlinear film processing effects can only inhibit development of latent image density values.

The direct application of this approach to the edge data shown in Figure 5.1 provided an unacceptably noisy CSF. The noise present in the edge was amplified by the edge derivative process. An illustration of this effect for edge number 5 is shown in Figure 5.2. The CSF has forced symmetry so that it is expected that the left and right halves should be identical. However, a CSF representative of the physical diffusion and depletion process should not contain the dual negative peak or the large noise amplitude that is evident in figure 5.2.

Similarity to Edge Gradient Analysis (EGA)

The effect of the noise contained in the derivative of the edge on the CSF and its Fourier transform, the CTF, have not been documented. However, the effect of the noise can be predicted reasonably well through its similarity to EGA techniques, which have been well documented (Scott, Scott, and Shack, 1963; Barakat, 1965; Tatian, 1965; Jones and Yeadon, 1969; Swing and McCamy, 1969). An excellent summary review on the application of these techniques to the analysis of noisy edge images has been written by Schowengerdt (1975).

The primary differences between standard EGA and Nelson's (1971) approach lie not in the method, but, in the functional form and the portions of the edge trace that are used in the analysis. If the entire edge trace was used, all of the errors associated with EGA would apply. An optimum edge

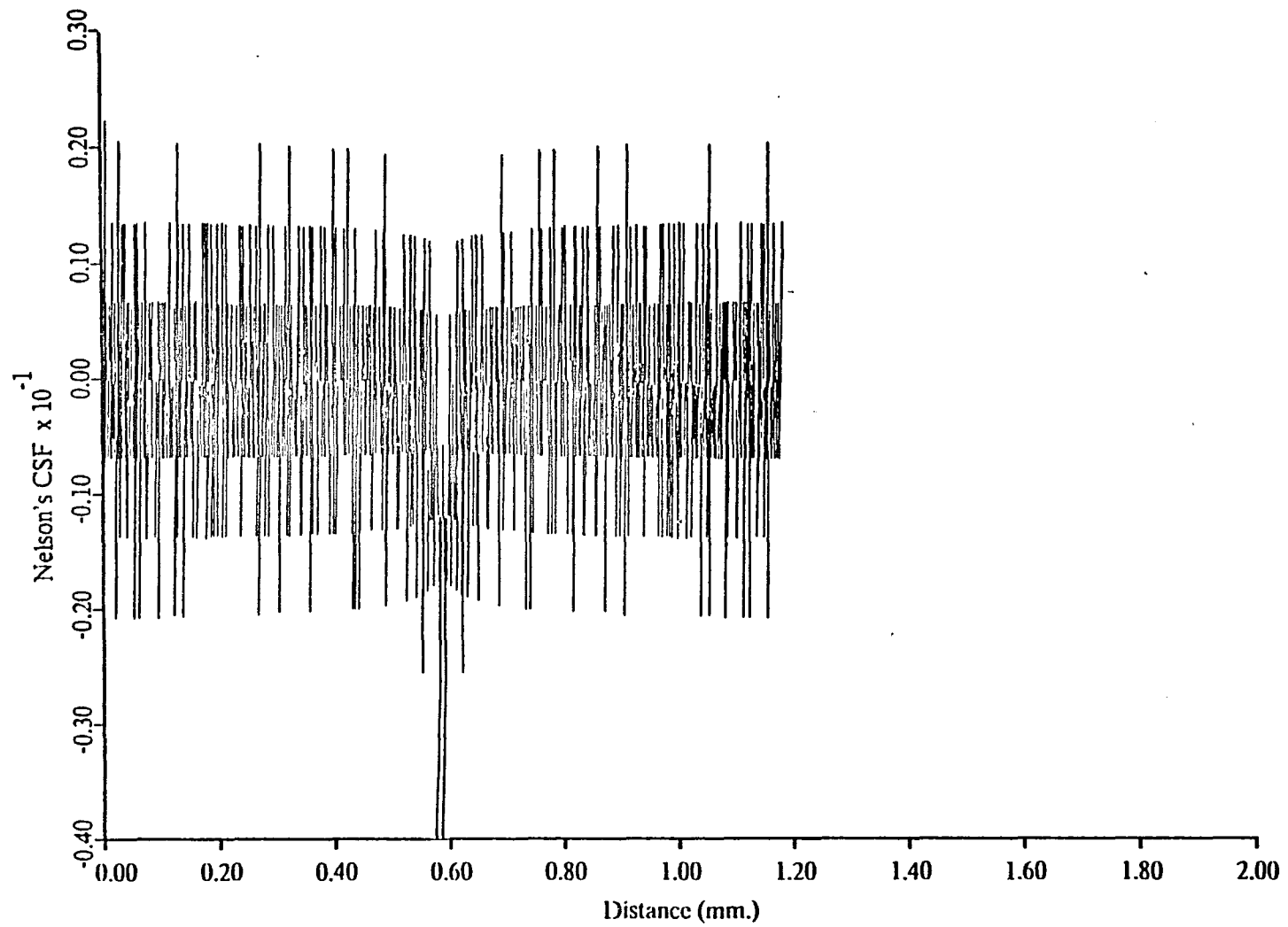


Fig. 5.2. Nelson's CSF calculated from edge number 5.
Analysis used discrete edge derivative.

scan length would have to be determined due to a tradeoff between OTF errors caused by edge truncation (Rabedeau, 1969; Tatian, 1971; Dutton, 1975) and the noise generated by longer scan lengths (Takeda and Ose, 1974). Point discontinuities and the nonmonotonic behavior associated with adjacency effects might cause further complications even in some of the EGA approaches which do not require explicit differentiation (Tatian, 1965).

Fortunately, it is not necessary to use the entire edge to obtain the CSF and the CTF, since the edge includes both optical scattering and chemical development effects. Nelson (1971) has shown that the CSF and CTF can be obtained from the analysis of only the high density side of the edge.

The chemical diffusion and development depletion effects occur over a large spatial distance from the edge boundary. Thus, a long data record is required in the analysis, most of which contains significant signal information. This eliminates, for all practical purposes, any truncation error that might have existed in the calculation of the CTF. In addition, the result of a very long and slowly varying signal is a CTF bandlimited to very low spatial frequencies. The variance due to edge noise, being quadratically related to spatial frequency (Schowengerdt, 1975), cannot be very large within this bandlimit.

Edge Noise Smoothing Algorithms

The usual edge noise effects for the evaluation of the CTF are not as important then, as in standard EGA applications. However they do play an important role in the determination of the precise location of the peak of the edge and the area under the CSF.

For these reasons several noise smoothing options were initially considered. These included a fixed width window recursive filter approach and analytic least squares fit methods using either exponential functions or segmented polynomials. The recursive filter approach was not pursued because an error due to data averaging within the window was anticipated near the edge boundary.

The exponential algorithms offered a very simple method of analytically fitting the entire high density side of the edge with a single algorithm. However, the accuracy was unknown. The segmented polynomial approach had been successfully applied in a number of applications. It also represented an approach which was extendable should one wish to evaluate the entire edge in order to calculate the apparent OTF.

The first analytic approach considered the application of two exponentially decaying algorithms of the form

$$C_1 + C_2 \exp \{-C_3 x\} \quad (5.2)$$

and

$$C_1 + C_2 \exp \{-(C_3 x + C_4 x^2)\} \quad (5.3)$$

where

C_1 = large-area density on high side of edge

C_2 = difference between peak edge density value and C_1

C_3, C_4 = constants defined by least squares fit

x = distance from edge boundary in mm

Analytic fits were made on the high density side of all the edges given in Figure 5.1 using a least squares error approach. Several general trends were noted.

1. The least squares error term was usually minimized for values of C_1 that were less than the peak density value. This was not acceptable since it would tend to reduce the magnitude of the CSF.
2. The analytic fits generated by Eq. (5.2) and Eq. (5.3) were not significantly different.
3. The exponential fit using a single curve could not follow the variable rate of change in the slope of the edge data.

An illustration of one of the best analytic fits, in terms of a small least squares error term and observations of the fit, is shown in Figure 5.3. Since both exponential functions provided nearly

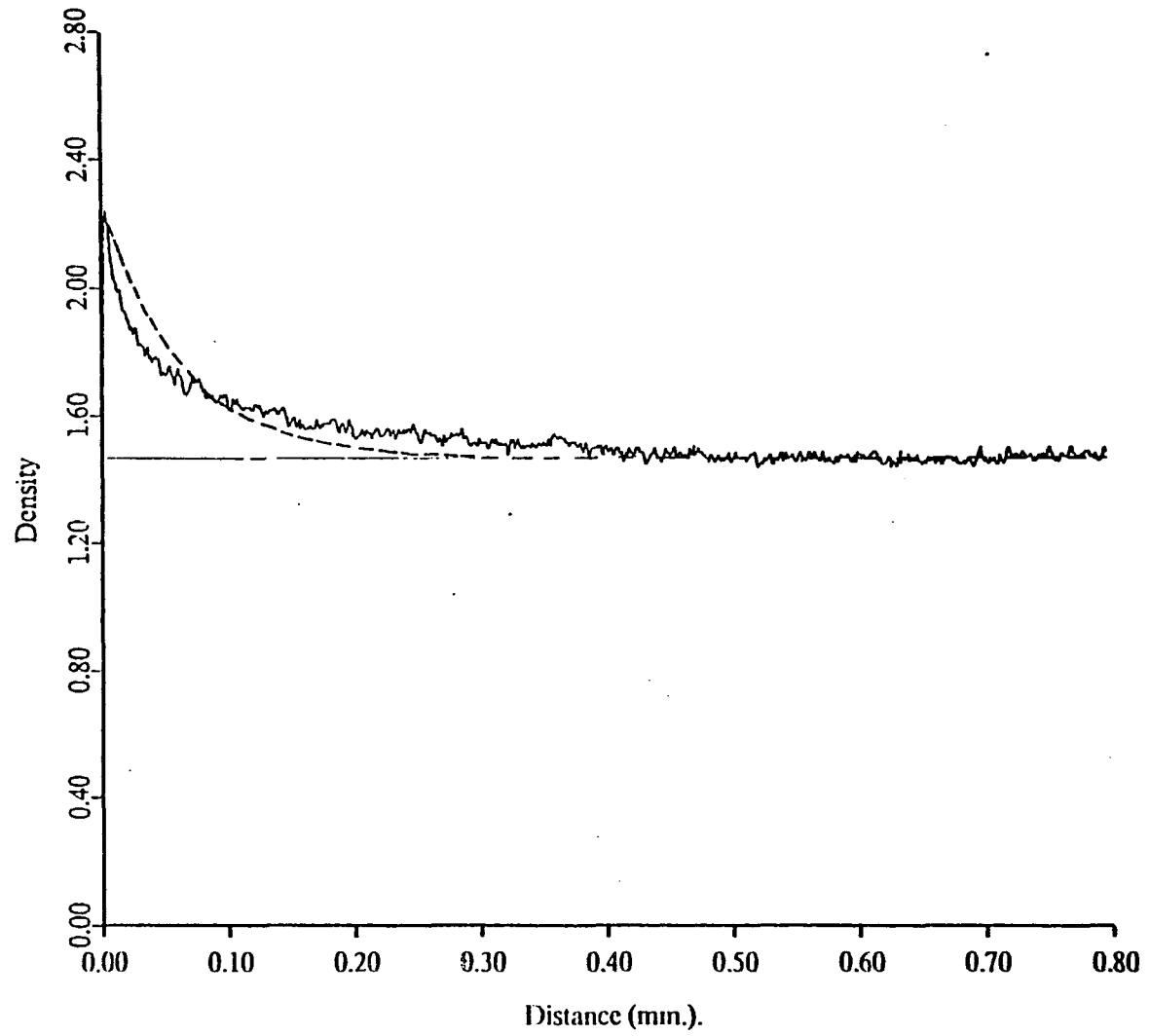


Fig. 5.3. Exponential fit to data from edge number 5.

identical results only the function associated with Eq.(5.2) was plotted. This function was found to be

$$1.45 + 0.78 \exp \{- 16.11 x\} \quad (5.4)$$

The initial rate of change of the actual data is obviously much greater than the exponential function. Then it gradually decreased until it was less than the exponential function. Clearly, Figure 5.3 indicates an unacceptable edge fit.

The segmented polynomial approach was based on an extension of the application of segmented 2nd degree polynomials to D log H curves (Levine,1976). For segmented 2nd degree polynomials the individual segmented functions must be equal at their common boundary locations (knots) and the first derivatives of these adjacent functions must also be equal at the knots (Fuller,1969). An extension to segmented 3rd degree polynomials (cubic spline functions) was preferred since it has been found to minimize the oscillatory effect often found in polynomial fitting methods and also provided high quality estimates of derivatives of the original functions (Barosi, 1973).

The empirical function, called a cubic spline, is obtained by fitting piecewise cubic polynomials to some predetermined curve segments. The method of the piecewise fits provides a continuous function at the knot locations as well as continuous first and second derivatives at these locations.

The approach used in the application of the cubic spline functions was based on the spline algorithms developed by deBoor and Rice (1968a, 1968b). The algorithm was provided a given set of knot locations and varied them one at a time in order to determine the knot locations that minimized the least squares error term. The process was initiated with the right most interior knot and proceeded sequentially to the left most interior knot. The basic cubic spline function was given by

$$S(T) = ((C(I,3) D + C(I,2)) D + C(I,1) D + Y(I) \quad (5.5)$$

where

T = the interval I

D = the independent distance variable given by $D = T - XK(I)$

C = the array containing the coefficient values

Y = the array containing the Y-intercept values

XK = the array containing the knot locations

The spline coefficients were computed based on the fact that the knots locations were ordered.

The spline algorithms were capable of sequentially varying up to twenty eight knots. For the edge fits only seven knot locations were used since the upper edge profiles were slowly varying functions. The initial knot locations were independently set at distances of 0.000, 0.025, 0.050, 0.075, 0.100, 0.200, 0.400 and 0.600 mm from the edge boundary. The optimal knot locations, spline coefficients, Y- intercept values and least squares error terms resulting from the cubic fits are given in Tables 5.1 through 5.5. The corresponding analytic fits are illustrated in Figures 5.4 through 5.8. In each case the cubic spline function provides an excellent fit to the original edge profile.

Calculation of Smooth CSF's

The segmented polynomials of the cubic spline approach provided an analytic edge with continuous first and second derivatives. Since derivative discontinuities were eliminated the derivative for each segmented polynomial was calculated and used for the derivative term required by Eq. (5.1). The CSF's were calculated using 600 samples spaced at 0.001 mm along the edge profile. This ensured that the entire CSF would be obtained.

The results from this procedure are shown in Figures 5.9 through 5.13. Note that they were all truncated at values less than 3.0 % of the peak amplitude. The peak negative values were found to range from approximately 0.013 to 0.019. Also, the largest negative peak value occurred for edge number 2, a low exposure edge, rather than edge number 5, the highest exposure edge, as initially expected.

Table 5.1. Cubic spline parameters: Edge number 1.

| Knot | Spline coefficients | | | Y-Intercept |
|-----------|---------------------|---------|----------|-------------|
| Locations | | | | Y(I) |
| (mm.) | C(I,3) | C(I,2) | C(I,1) | Density |
| 0.000 | - 4313.953 | 373.310 | - 12.116 | 1.189 |
| 0.028 | - 7.607 | 5.158 | - 1.350 | 1.047 |
| 0.122 | - 6.722 | 3.033 | - 0.587 | 0.960 |
| 0.347 | 11.665 | - 1.506 | - 0.243 | 0.905 |
| 0.473 | - 40.119 | 2.901 | - 0.068 | 0.873 |
| 0.517 | 81.761 | - 2.482 | - 0.049 | 0.872 |
| 0.600 | | | | |

Least squares error: $\epsilon = 0.0067$

Table 5.2. Cubic spline parameters: Edge number 2.

| Knot | Spline coefficients | | | Y-Intercept |
|-----------|---------------------|---------|---------|-------------|
| Locations | | | | Y(I) |
| (mm.) | C(I,3) | C(I,2) | C(I,1) | Density |
| 0.000 | -4994.422 | 558.379 | -23.552 | 1.614 |
| 0.036 | -50.517 | 18.980 | -2.767 | 1.257 |
| 0.154 | -9.099 | 1.089 | -0.398 | 1.112 |
| 0.250 | 57.886 | -1.526 | -0.439 | 1.076 |
| 0.267 | -1.219 | 1.515 | -0.440 | 1.068 |
| 0.367 | -2.688 | 1.150 | -0.173 | 1.038 |
| 0.600 | | | | |

Least squares error: $\epsilon = 0.01725$

Table 5.3. Cubic spline parameters: Edge number 3.

| Knot | Spline coefficients | | | Y-Intercept |
|-----------|---------------------|----------|----------|-------------|
| Locations | | | | Y(I) |
| (mm.) | C(I,3) | C(I,2) | C(I,1) | Density |
| 0.000 | - 2284.728 | 347.017 | - 19.692 | 1.838 |
| 0.049 | - 31.452 | 12.512 | - 2.146 | 1.437 |
| 0.195 | 15.498 | - 1.238 | - 0.504 | 1.293 |
| 0.364 | - 196.330 | 6.629 | 0.409 | 1.247 |
| 0.403 | 183.519 | - 16.341 | 0.030 | 1.262 |
| 0.447 | - 56.146 | 7.986 | - 0.339 | 1.247 |
| 0.600 | | | | |

Least squares error: $\epsilon = 0.01915$

Table 5.4. Cubic spline parameters: Edge number 4.

| Knot | Spline coefficients | | | Y-Intercept |
|-----------|---------------------|---------|----------|-------------|
| Locations | | | | Y(I) |
| (mm.) | C(I,3) | C(I,2) | C(I,1) | Density |
| 0.000 | - 2556.259 | 413.732 | - 24.220 | 2.119 |
| 0.053 | - 2.992 | 5.999 | - 1.904 | 1.617 |
| 0.122 | - 19.534 | 5.385 | - 1.125 | 1.513 |
| 0.180 | - 2.816 | 1.956 | - 0.695 | 1.462 |
| 0.441 | 4.271 | - 0.248 | - 0.250 | 1.364 |
| 0.528 | 26.520 | 0.872 | - 0.195 | 1.343 |
| 0.600 | | | | |

Least squares error: $\epsilon = 0.1362$

Table 5.5. Cubic spline parameters: Edge number 5.

| Knot | Spline coefficients | | | Y-Intercept |
|-----------|---------------------|---------|----------|-------------|
| Locations | | | | Y(I) |
| (mm.) | C(I,3) | C(I,2) | C(I,1) | Density |
| 0.000 | - 6436.797 | 733.387 | - 31.771 | 2.271 |
| 0.036 | - 184.542 | 38.213 | - 3.993 | 1.778 |
| 0.095 | - 9.763 | 5.728 | - 1.415 | 1.637 |
| 0.175 | - 8.433 | 3.375 | - 0.684 | 1.556 |
| 0.353 | 7.578 | - 1.141 | - 0.285 | 1.493 |
| 0.540 | - 110.109 | 3.099 | 0.081 | 1.450 |
| 0.600 | | | | |

Least squares error: $\epsilon = 0.01375$

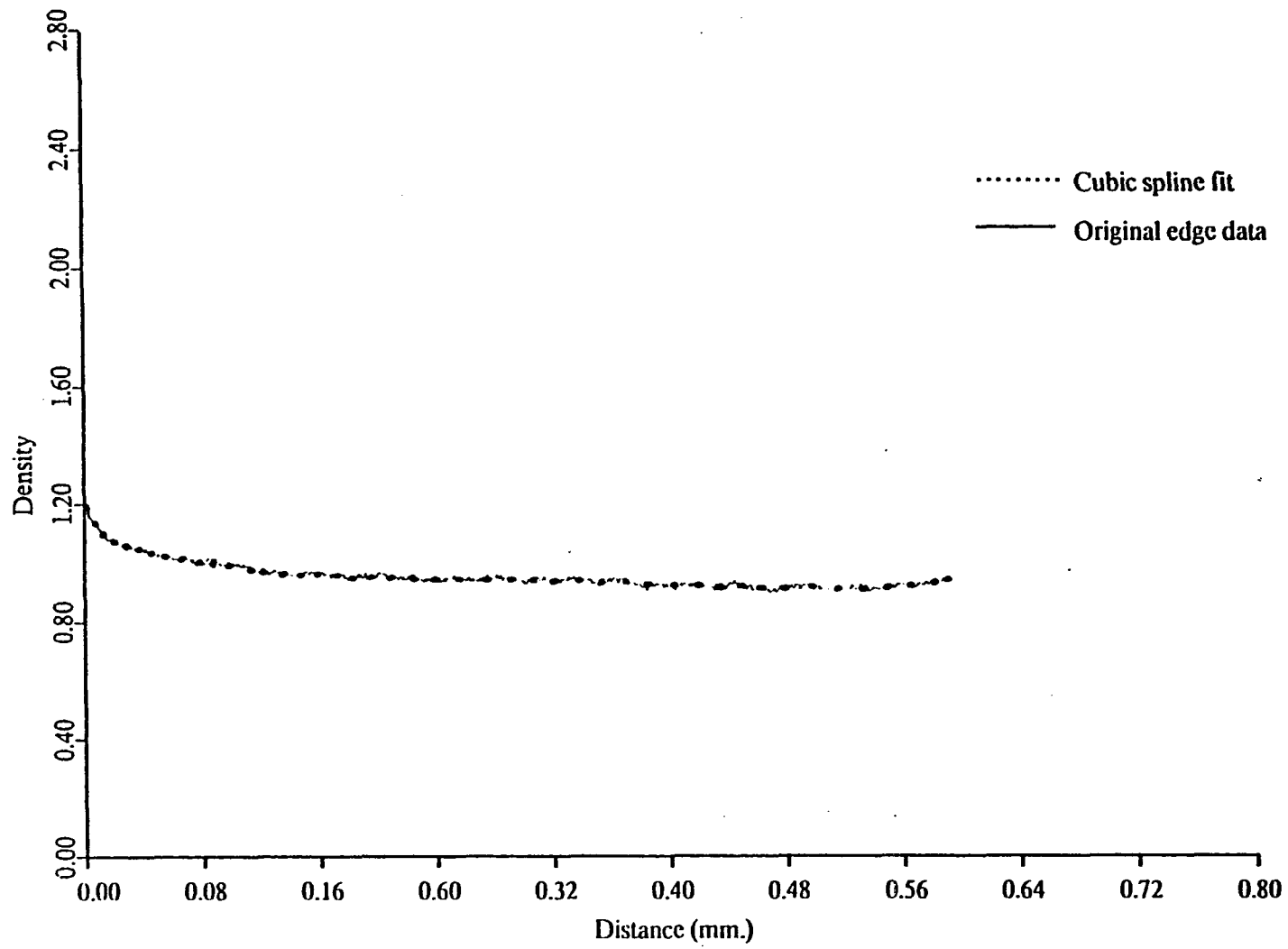


Fig. 5.4. Cubic spline fit to data from edge number 1.

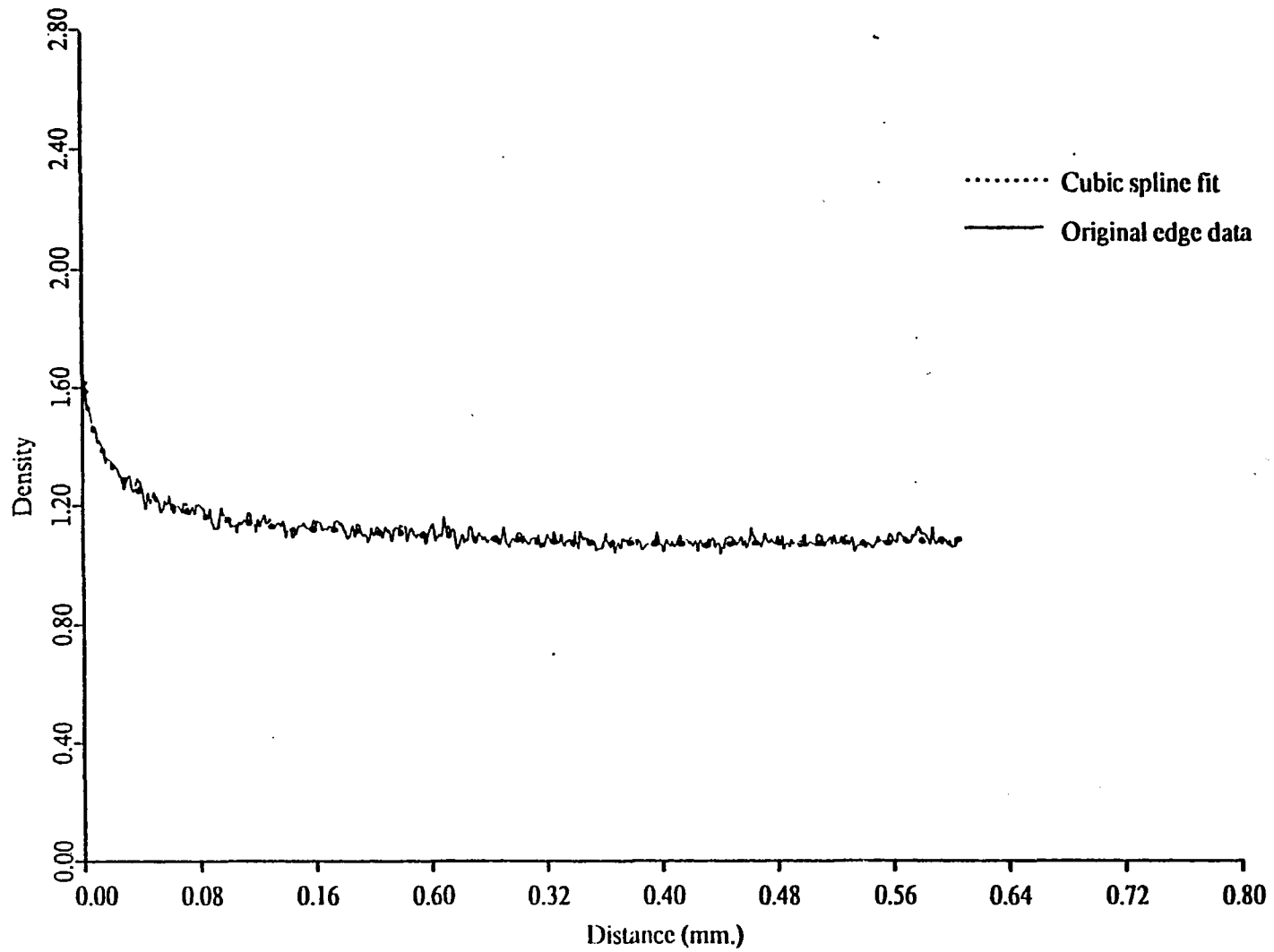


Fig. 5.5. Cubic spline fit to data from edge number 2.

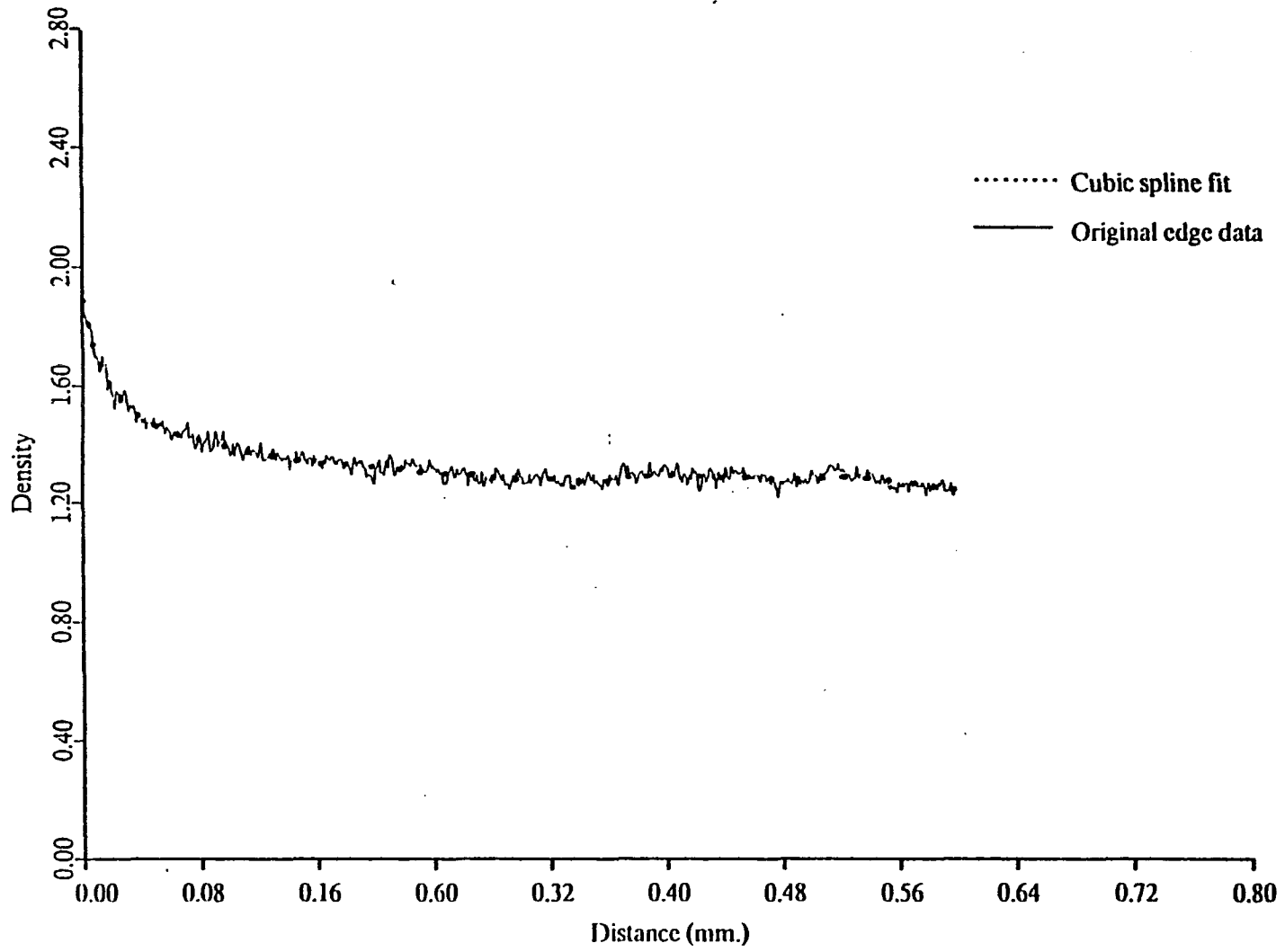


Fig. 5.6. Cubic spline fit to data from edge number 3.

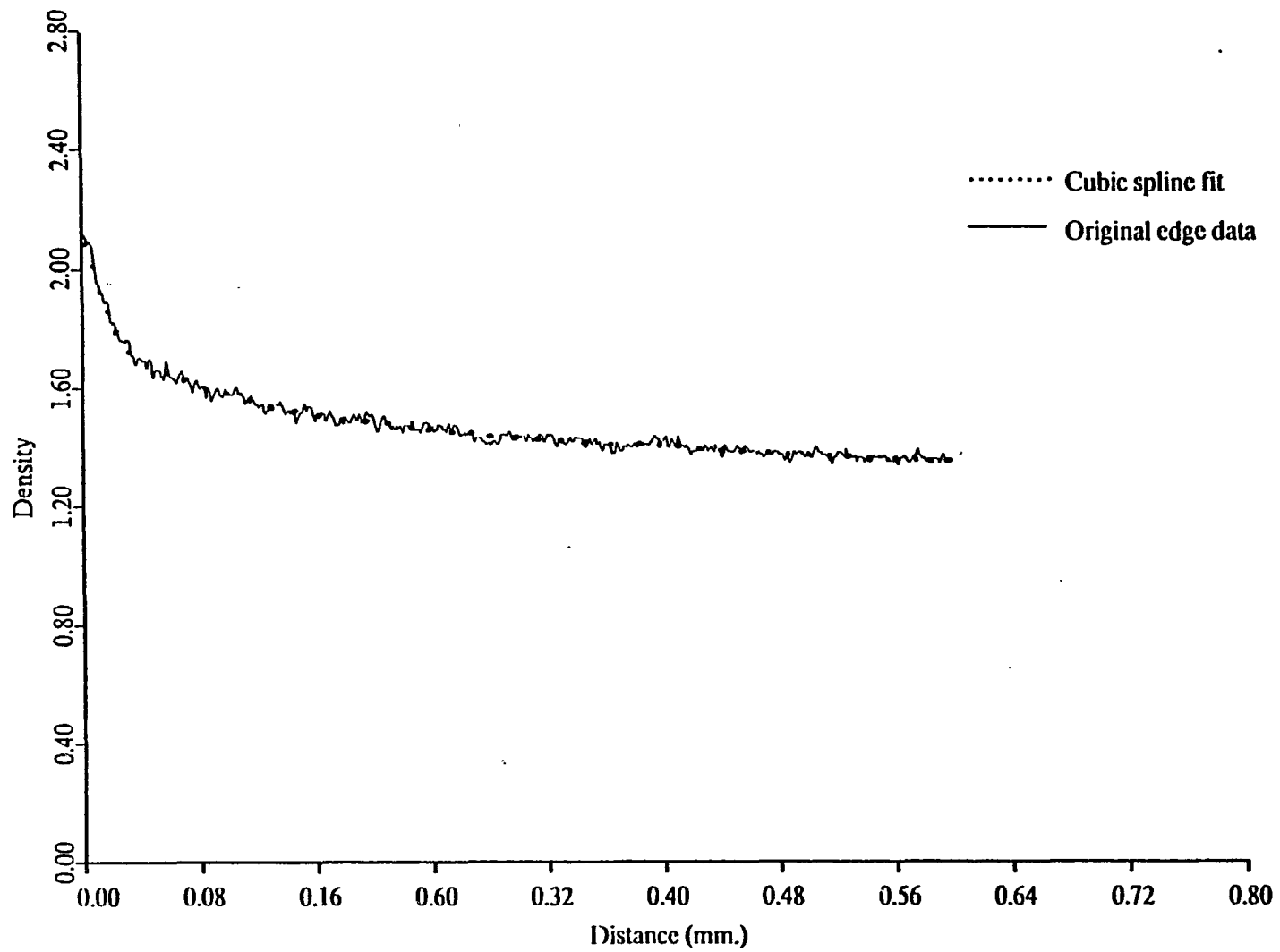


Fig. 5.7. Cubic spline fit to data from edge number 4.

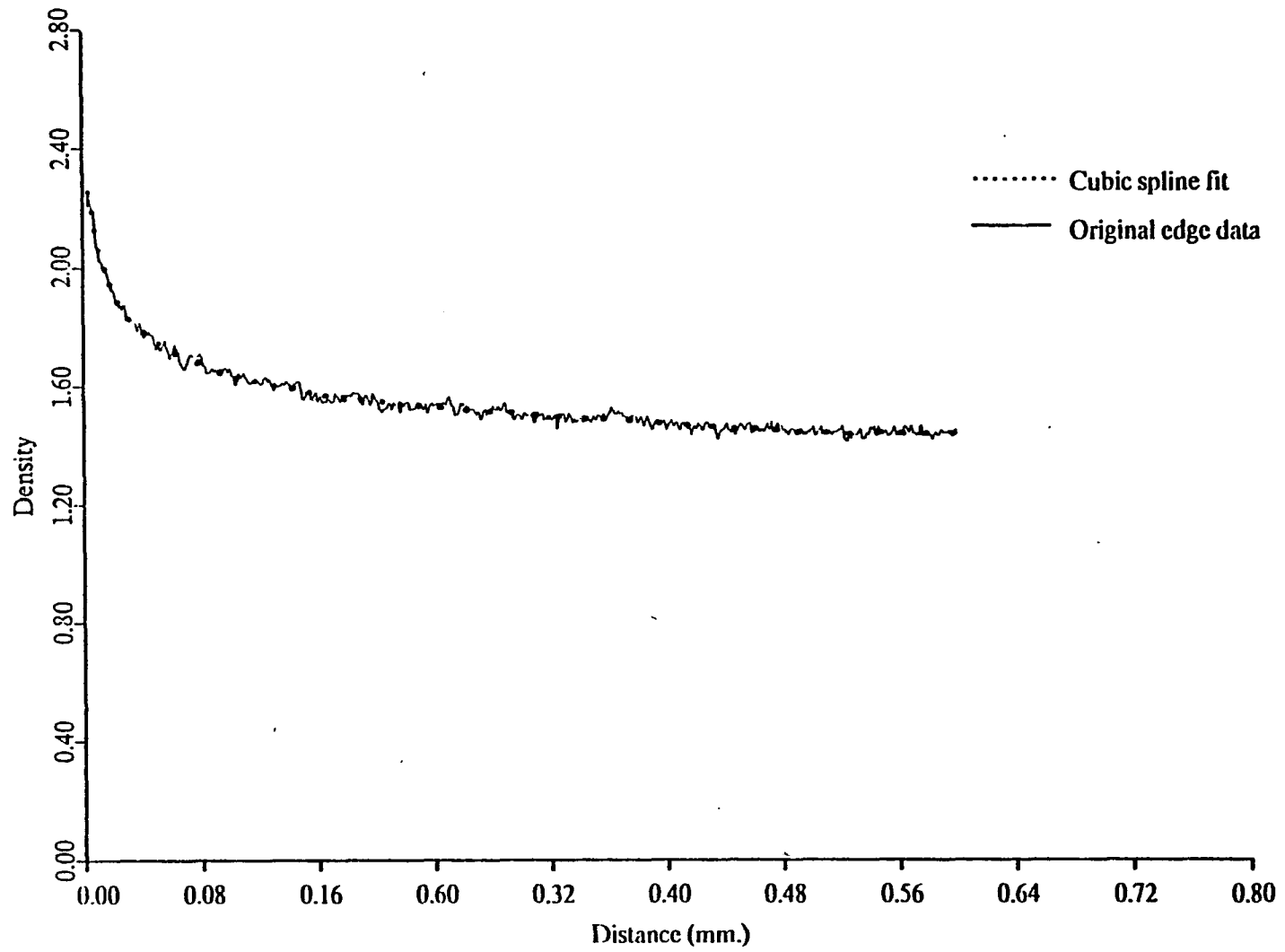


Fig. 5.8. Cubic spline fit to data from edge number 5.

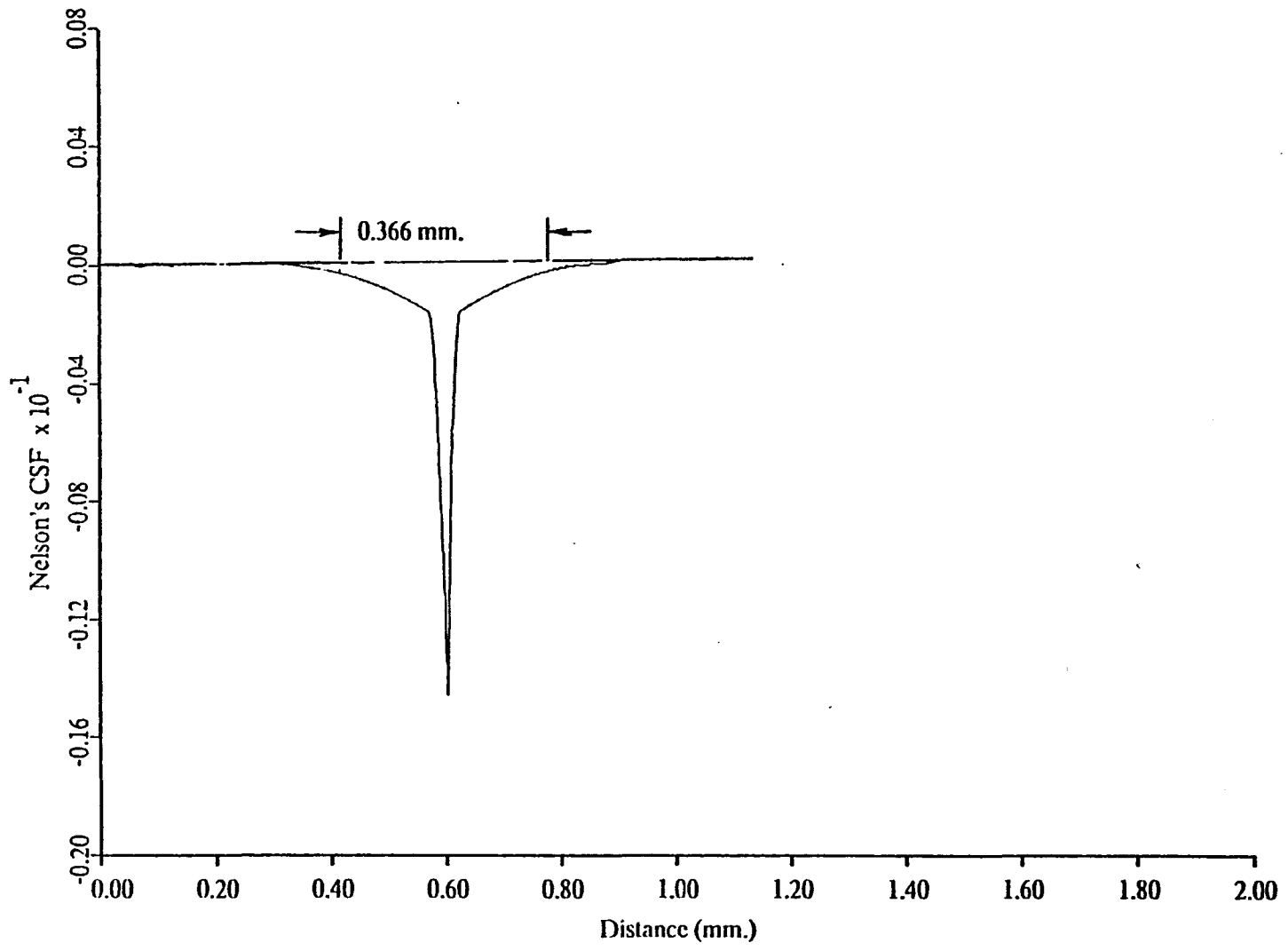


Fig. 5.9. Nelson's CSF from analytic fit of edge number 1.

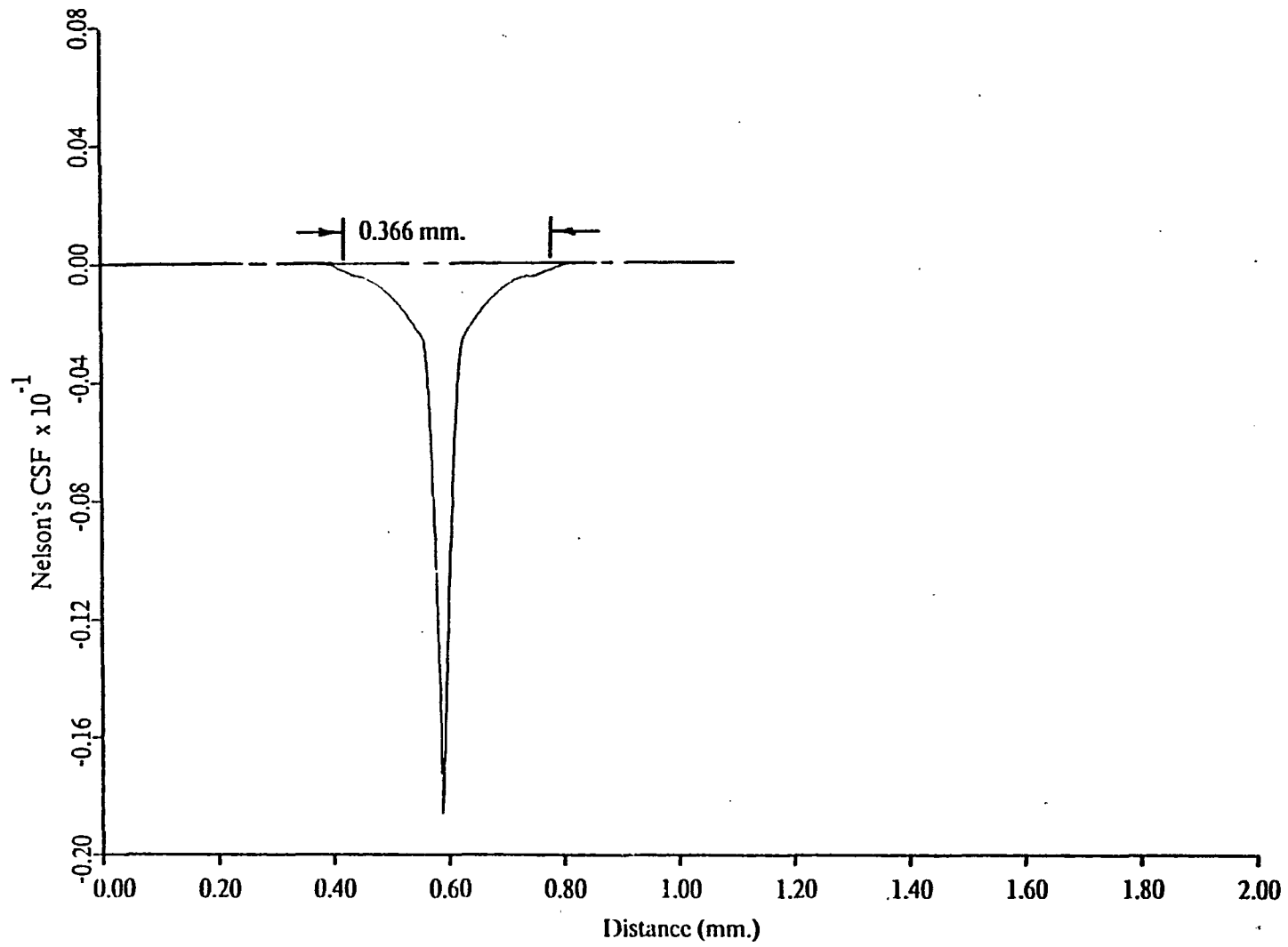


Fig. 5.10. Nelson's CSF² from analytic fit of edge number 2.

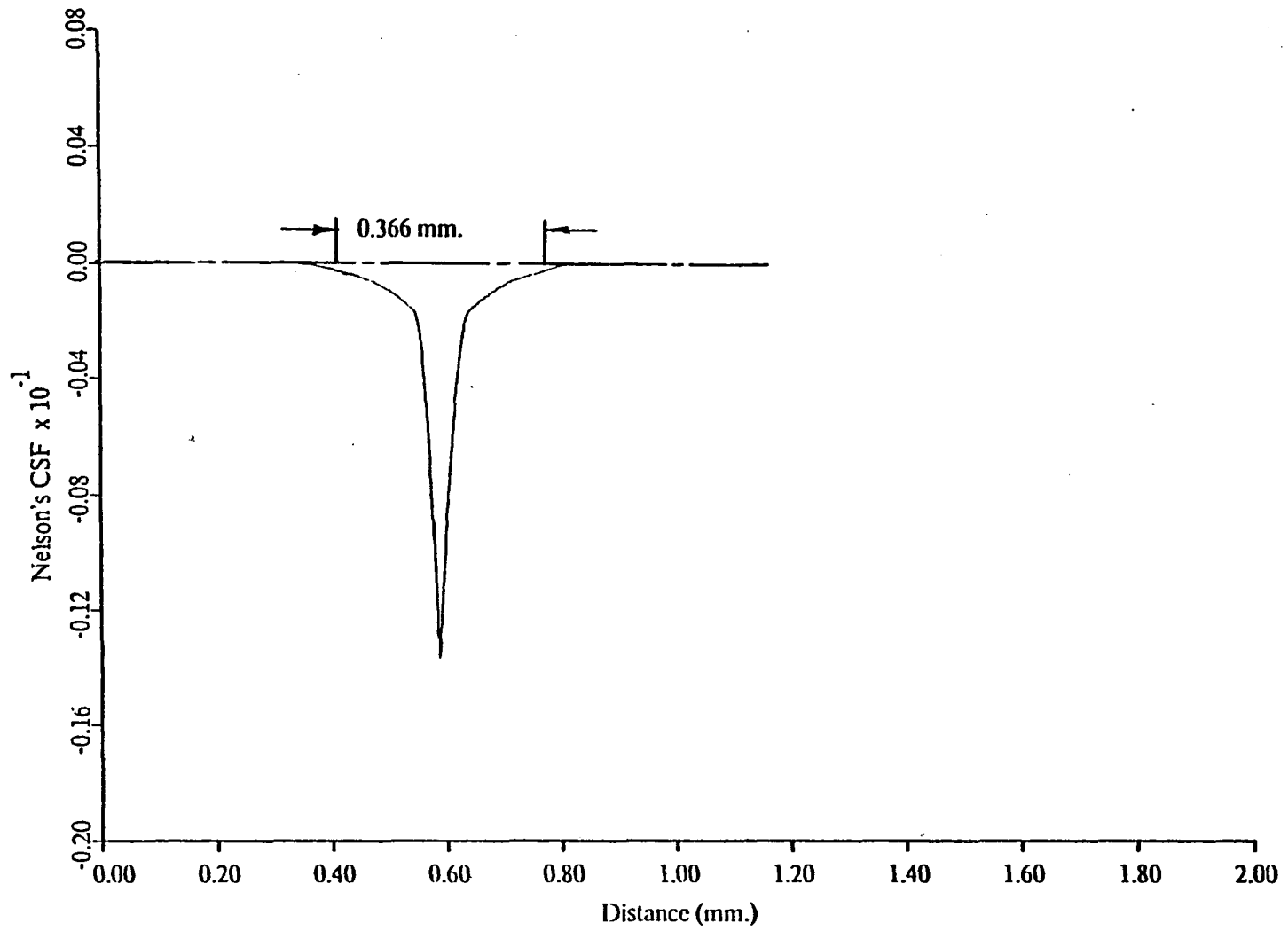


Fig. 5.11. Nelson's CSF² from analytic fit of edge number 3.

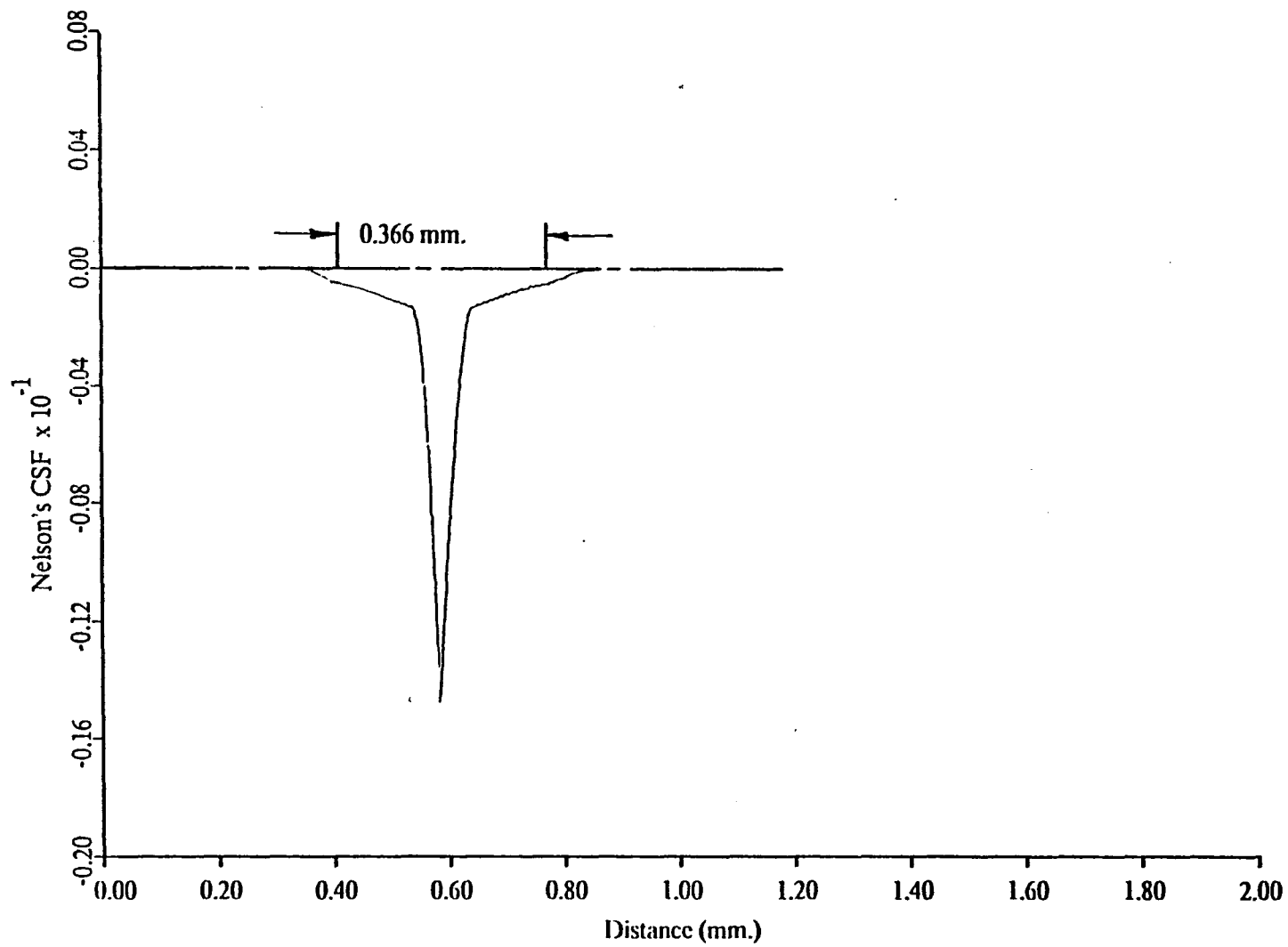


Fig. 5.12. Nelson's CSF from analytic fit of edge number 4.

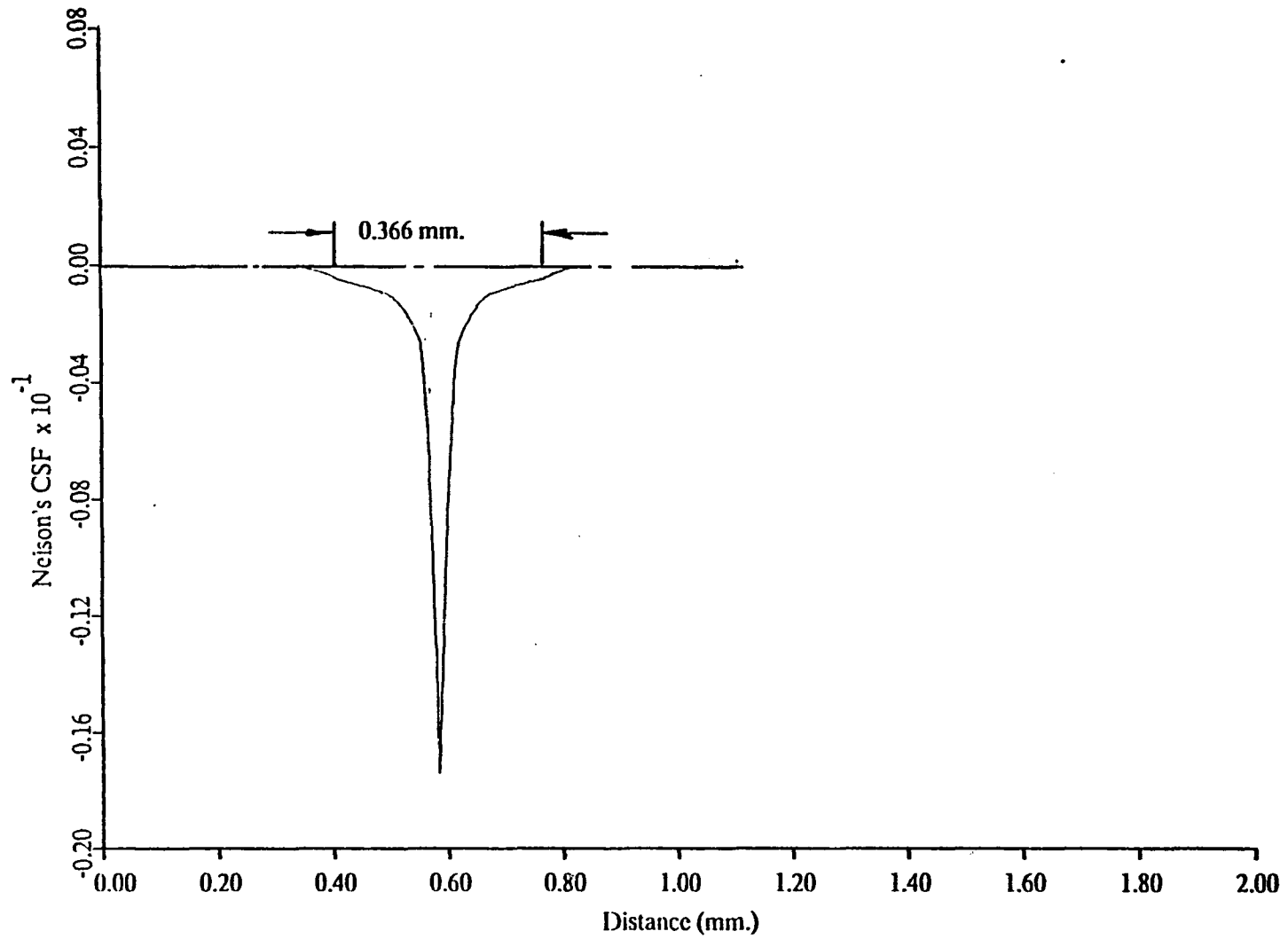


Fig. 5.13. Nelson's CSF from analytic fit of edge number 5.

Further insight into the significance of the negative peak variations were obtained from the CSF area calculations. Two area values were calculated, one for the entire width of 1.200 mm and one for the truncated width of 0.366 mm for each CSF. The results shown in Table 5.6 indicate that the CSF's for edges number 2 through 5 had nearly the same areas whereas edge number 1 had a much smaller area. Thus, the negative peak and the CSF area values were nearly the same, with one exception (edge number 1) even though the edge gross grain density values were significantly different. This was further supported by plots of the integrated area under the CSF as shown in Figure 5.14. Note that the curve associated with edge number 1 had a significantly slower rate of change compared to the remaining integrated area curves which were all quite similiar. Also, the curves demonstrated the effect of the truncation of the CSF's on the integrated area. The integrated area is a slowly varying, almost linear function outside the truncation region.

Table 5.6. Chemical spread function area values.

| Edge Number | Chemical Spread Function Width | |
|-------------|--------------------------------|-----------|
| | 1.200 mm. | 0.366 mm. |
| 1 | 0.779 | 0.673 |
| 2 | 1.055 | 0.885 |
| 3 | 1.010 | 0.814 |
| 4 | 1.071 | 0.891 |
| 5 | 1.023 | 0.875 |

The overall results indicate that either the CSF's are relatively independent of exposure, beyond a given threshold exposure level, or that the lack of agitation used during development

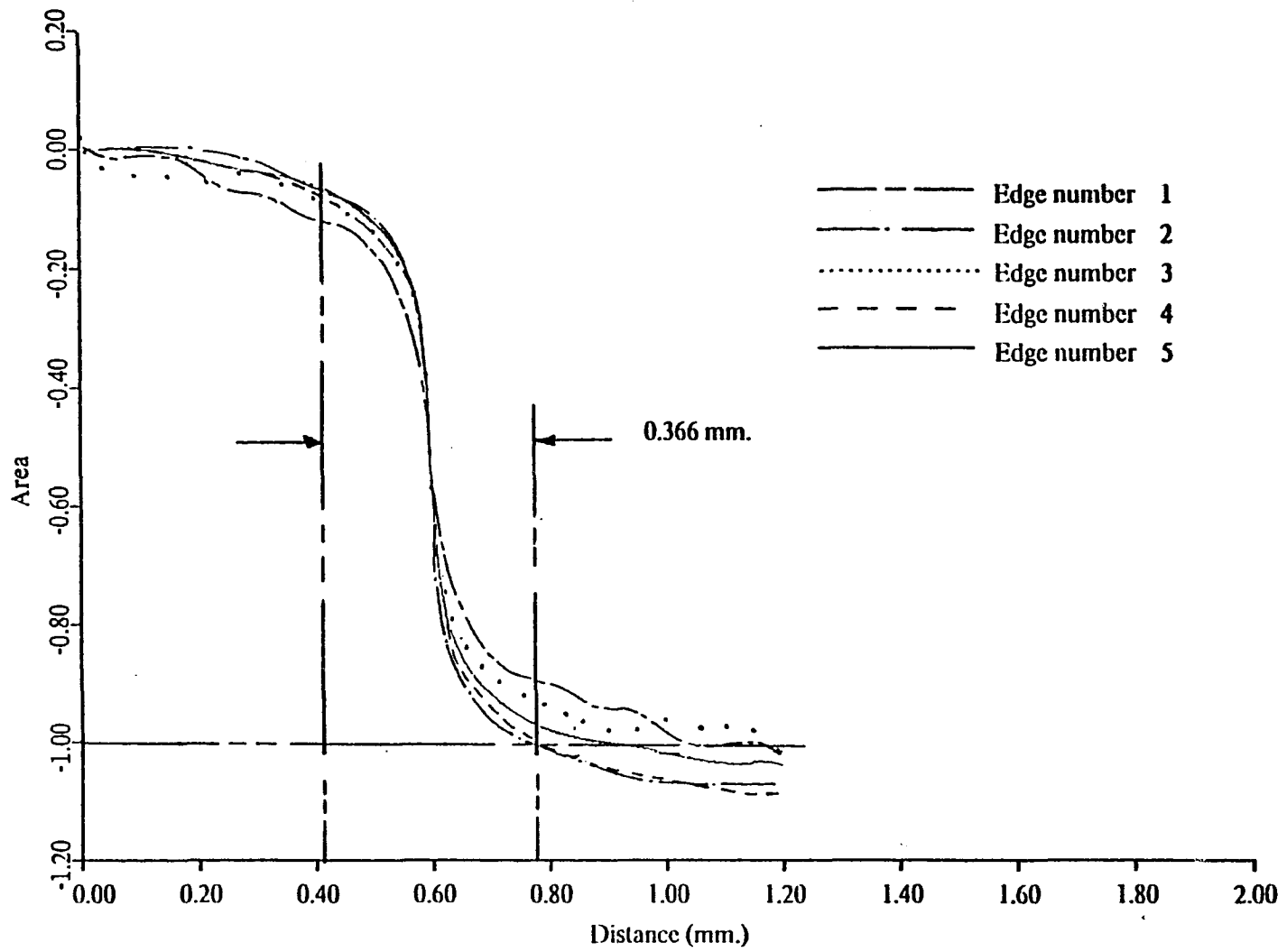


Fig. 5.14. Integrated area under analytic CSF.

process suppressed the peak density values and thus suppressed the absolute magnitudes and areas of the CSF's. Further comment on this relationship is withheld until the results of the EE have been reviewed.

Evaluation of the Eberhard Effect

The evaluation of the EE was based on a comparison of selected density values within the 0.010 mm fine line and the 1.00 mm broad line images. Several magnitude estimates of the EE were calculated from both the experimental data and one data set published by Nelson (1971). In addition, the magnitudes are compared to the previously calculated CSF area values.

EE for Exposure Levels

The data provided by the five replicate microdensitometer scans of each of the twelve line images indicated that a selection of six of the scan line profiles adequately represented all images. The exposure replicates were virtually identical with the exception of the lines receiving the lowest x-ray exposure level. One of the two low exposure replicates contained film processing nonuniformities. The five replicate microdensitometer scans of each line image provided nearly equivalent peak density values that were all within plus-or-minus 0.03 of the average peak value.

Preprocessing of the six fine line images was not required. Averaging of the entire data profile provided by the five replicate microdensitometer scans was not necessary since only the peak density values were of primary interest. Also, minimal microdensitometer transfer function degradation occurred before the 100 cycle/mm spatial frequency cutoff of the 0.010 mm fine line images.

The Eberhard results provided by the line and large area images show the general type of pattern, illustrated in Figure 5.15, typically found for various film-developer combinations. The center curve, representing the density value found in the central region of the 0.100 mm line images at each exposure level, has been included to provide insight into data trends for intermediate line

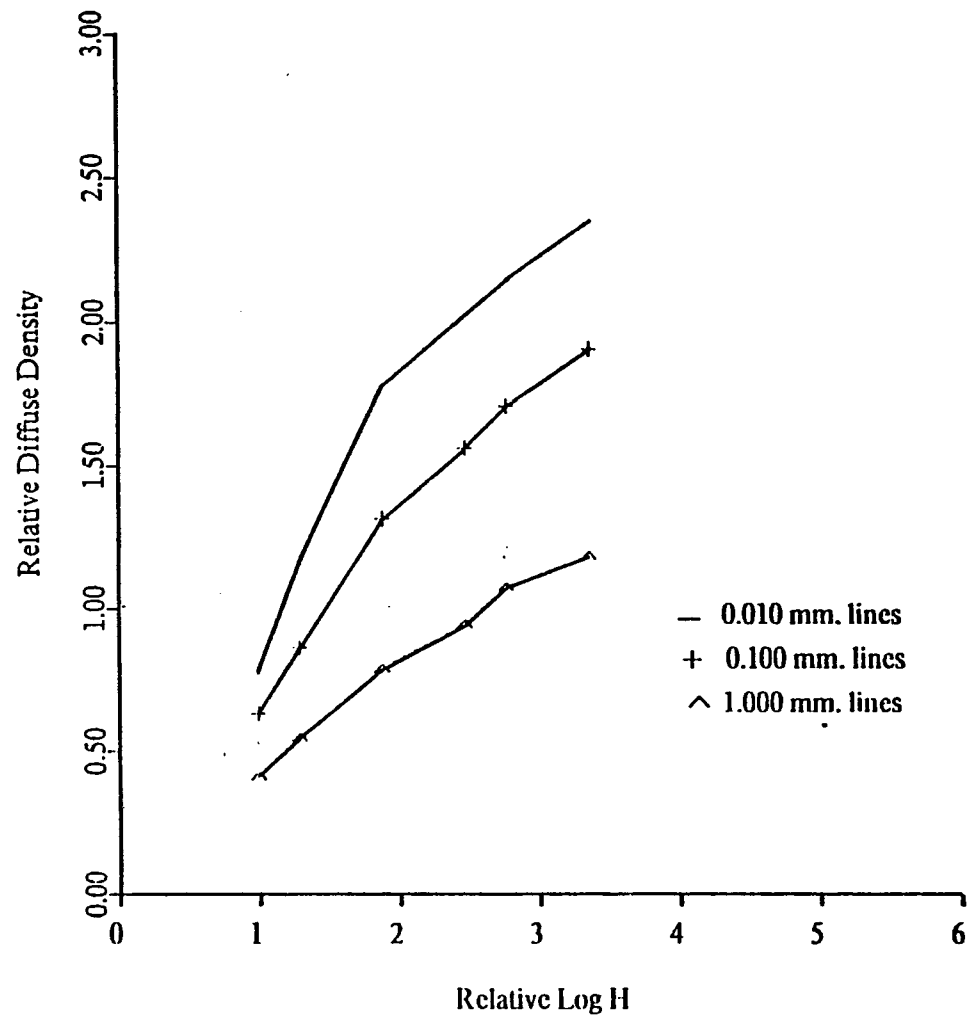


Fig. 5.15. Eberhard effect from x-ray exposures.

widths. The film base density of 0.25 has been subtracted from the actual density values to provide the relative diffuse density values shown in the figure.

Magnitude Estimate of the EE

The results of Figure 5.15 seem to support Nelson's observations that the "magnitude" of the EE increases in a nonlinear manner with the increasing large area density level. The magnitude of the effect, being defined as the density difference between the fine line and large area sensitometric curves, shown in Figure 5.15, at each large area density level. However, closer observation of the experimental data indicates that the relative rate of change between the fine line and large area sensitometric curves starts to decrease for the upper three exposure levels. It appears that the adjacency effect initially caused a rapidly increasing EE which gradually decreased. Additional confirmation of the observation is indicated in Figure 5.16 and 5.17. These figures provide plots of the EE values as functions of large area mass of silver and relative diffuse density, respectively. The initial rapid increase and eventual thresholding of the EE is quite obvious.

The calculated EE values of the experimental data compared to those estimated from previously published fine line and large area sensitometric curves (Nelson, 1971) are also shown in Figure 5.16 and 5.17. The later data set was obtained by estimating data points from the EE and mass of silver conversion curves provided in Figures 4 and 6 (lower left) of Nelson's (1971) publication. These published curves were experimentally derived from Panatomic-x film processed in D-76 for 7 minutes with continuous agitation. A film base density of 0.20 was assumed in the calculation.

The comparison of the two data sets confirms previous observations concerning the reduction of the rate of change of the EE for the experimental data. It also illustrates the limited range of the developed mass of silver obtained for a given film-developer combination when developer agitation is not performed. The lack of development agitation initially provided a large adjacency effect because of strong local development diffusion and depletion. However, the same lack of agitation limited the peak density to much lower values than would normally be achieved. This combination of factors

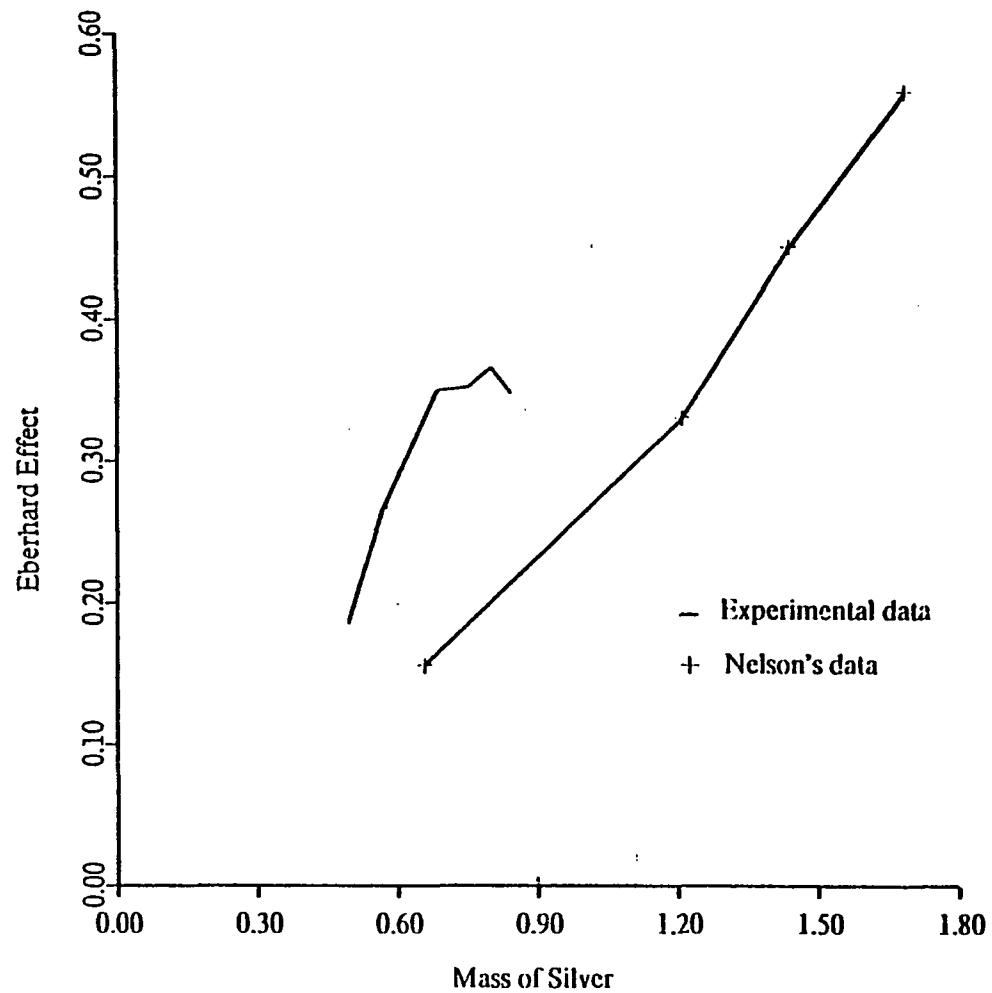


Fig. 5.16. Eberhard effect as a function of mass of silver.

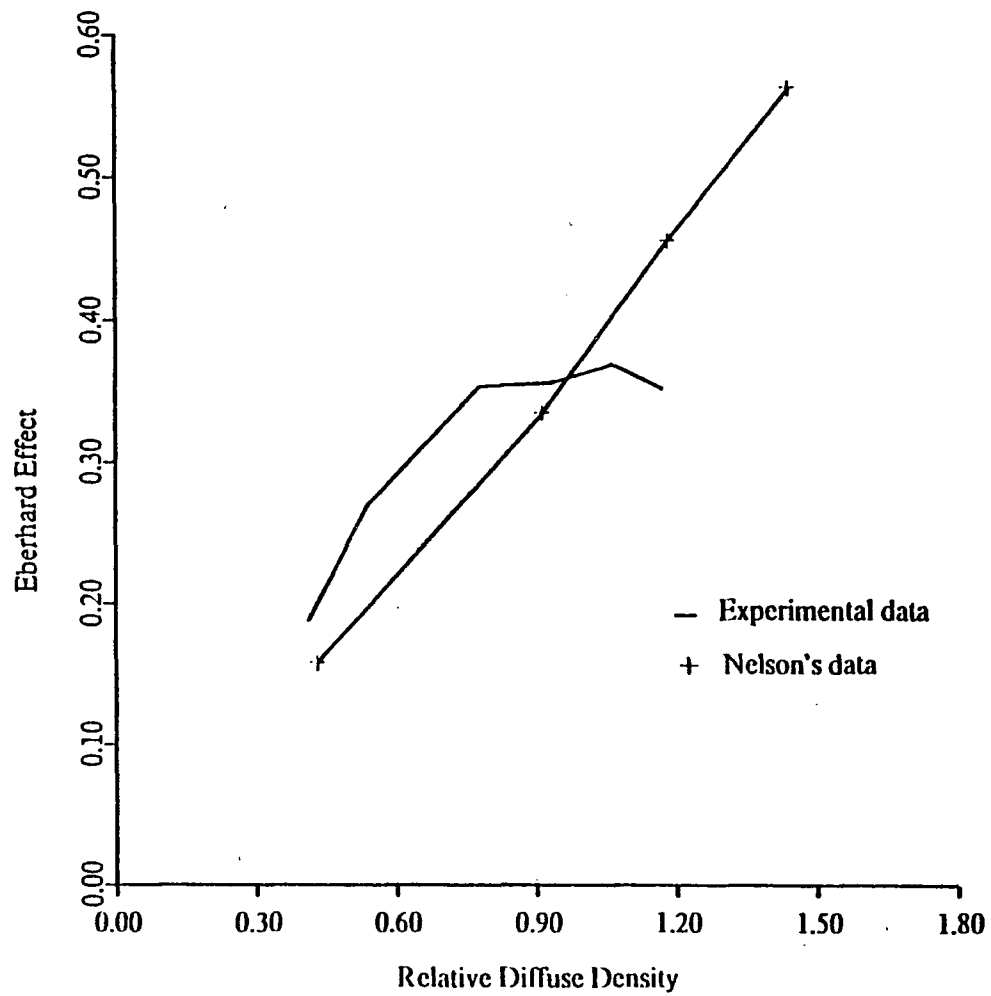


Fig. 5.17. Eberhard effect as a function of density.

provided the very large initial EE followed by a substantially lower limit on its magnitude then would be achieved for a continuously agitated process.

The results of Figures 5.16 and 5.17 also relate to the area values, given in Table 5.6, for the truncated CSF's. The area values quickly reached threshold for relatively low exposure values. The oscillations in area for edges number 2 through 5 represent combined variations in the edge density levels, edge noise effects and numerical errors generated by the least squares fit using cubic spline functions.

Eberhard Ratio Calculations

Nelson (1971) also observed that, in general, as the large area density level increased the EE increased by an amount that was proportional to the square of the large area density level. The rule was found to be accurately obeyed by some film-developer combinations but only approximately by others. Also, conversion of the rule from density values to mass of silver units improved the accuracy of the relationship.

Nelson's (1971) ratio, NR, can be analytically stated as

$$NR = (f - g) / g^2 \quad (5.6)$$

where f and g represent the fine line and gross grain mass of silver values, respectively.

It should be recalled that comparisons of Nelson's model to the restoration model have been previously discussed in Chapter 2. The mathematical derivation of the restoration model preceding this comparison included an algorithm, Eq. (2.9), which related fine line and gross grain mass of silver values to the area under the chemical spread function. This algorithm can be written as

$$A = MR = (\alpha f_i - g) / f_i g \quad (5.7)$$

Assuming a value of $\alpha = 1$, Eq. (5.6) and Eq. (5.7) become quite similar. The value of A , which will be referred to as the model ratio, MR, will always be less than NR in the presence of adjacency effects since $f > g$.

The results of the application of NR and MR to both the experimental data and Nelson's published data, are illustrated in Figures 5.18 through 5.21. The ratio values are plotted as functions of both large area mass of silver and density values for the case $\alpha = 1$. The intermediate and final calculation results are listed in Table 5.7 and 5.8.

The relative magnitude of MR is found to be greater than NR as predicted. The application of both ratio values to Nelson's published curves indicate a nearly linear relationship particularly for large area relative diffuse density values above approximately 0.9.

Nelson's (1971) observations, which lead to Eq. (5.6), appear to have been limited to a density range above a given density threshold value. At very low large area relative diffuse density values the fine line and large area density values must converge. Thus, NR and MR must begin at a zero value for this low density value. In the analysis of both the experimental data and Nelson's (1971) published curve data, the low large area relative diffuse density value was approximately 0.1 assuming a film base density value of approximately 0.2. The extrapolated values shown in Figure 5.18 through 5.21 serve to roughly approximate this behavior.

At saturated large area density values the fine line density values must also become saturated. Thus, NR and MR must approach a constant value in the saturated density regions. It is quite possible that this constant ratio value is approached well below the density saturation threshold as Nelson's (1971) data appears to suggest. The fine line and large area sensitometric curves from which Nelson's (1971) data was estimated did not reach a density saturation threshold.

A comparison between the estimated data, Figures 5.18 and 5.19, and the experimental data, Figures 5.20 and 5.21, again emphasizes the effect of the amount of development agitation. The ratio values for the experimental data are much higher than those associated with the estimated data set over the limited density range available. Also, the ratio values never achieved a constant level for the experimental data due to the premature thresholding of the fine line density values.

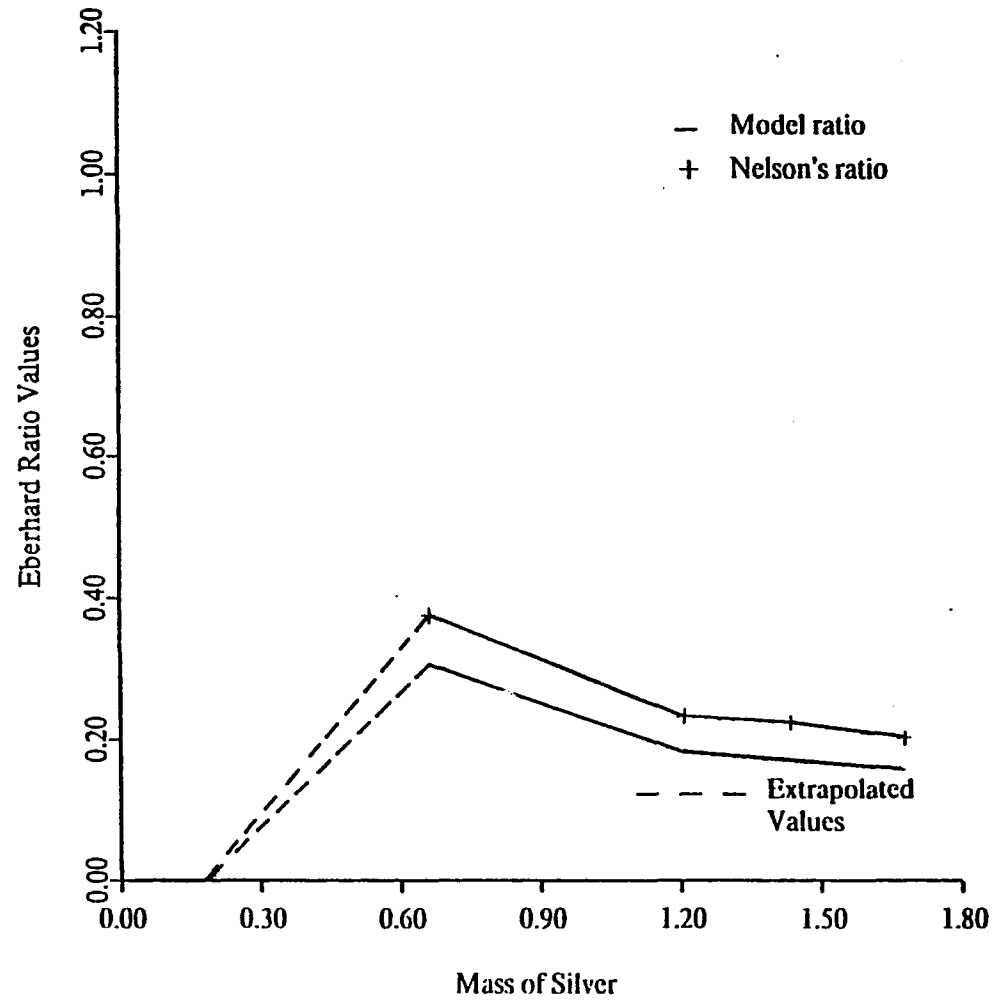


Fig. 5.18. Eberhard ratio as a function of mass of silver for Nelson's data.

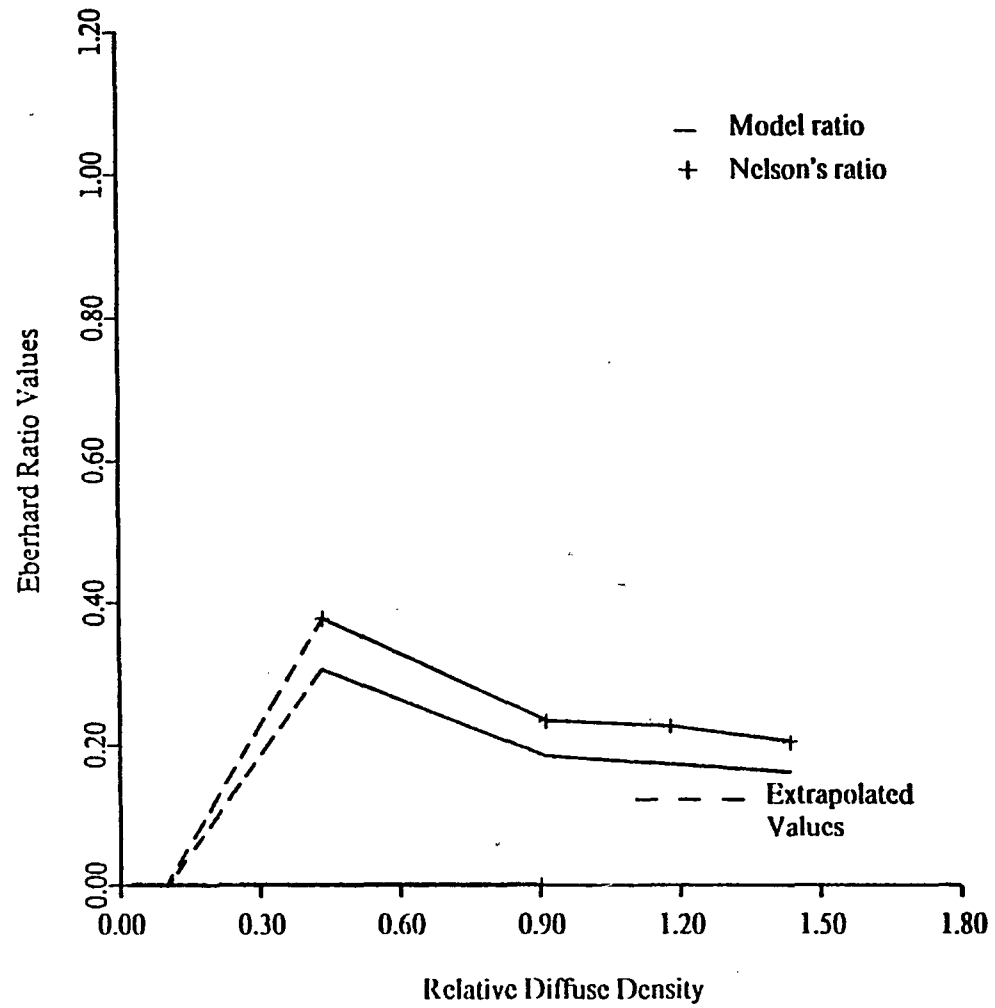


Fig. 5.19. Eberhard ratio as a function of density for Nelson's data.

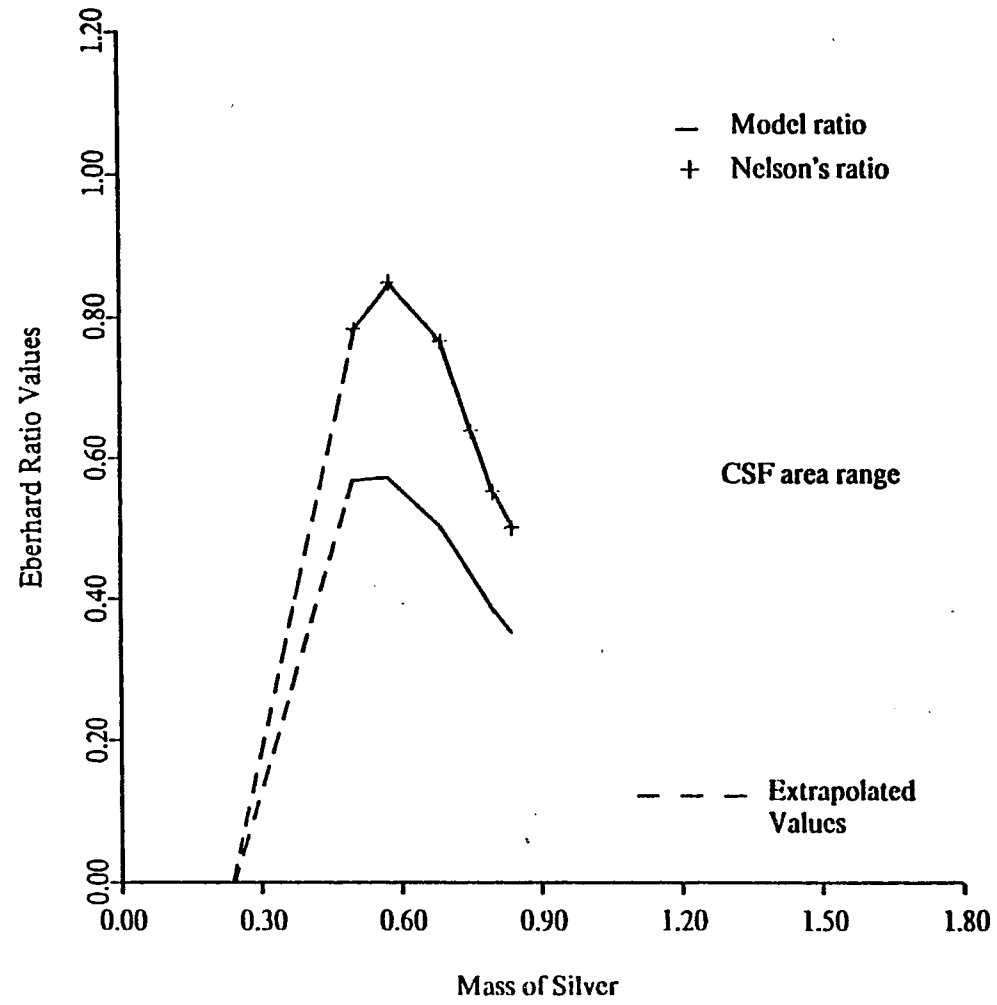


Fig. 5.20. Eberhard ratio as a function of mass of silver for experimental data.

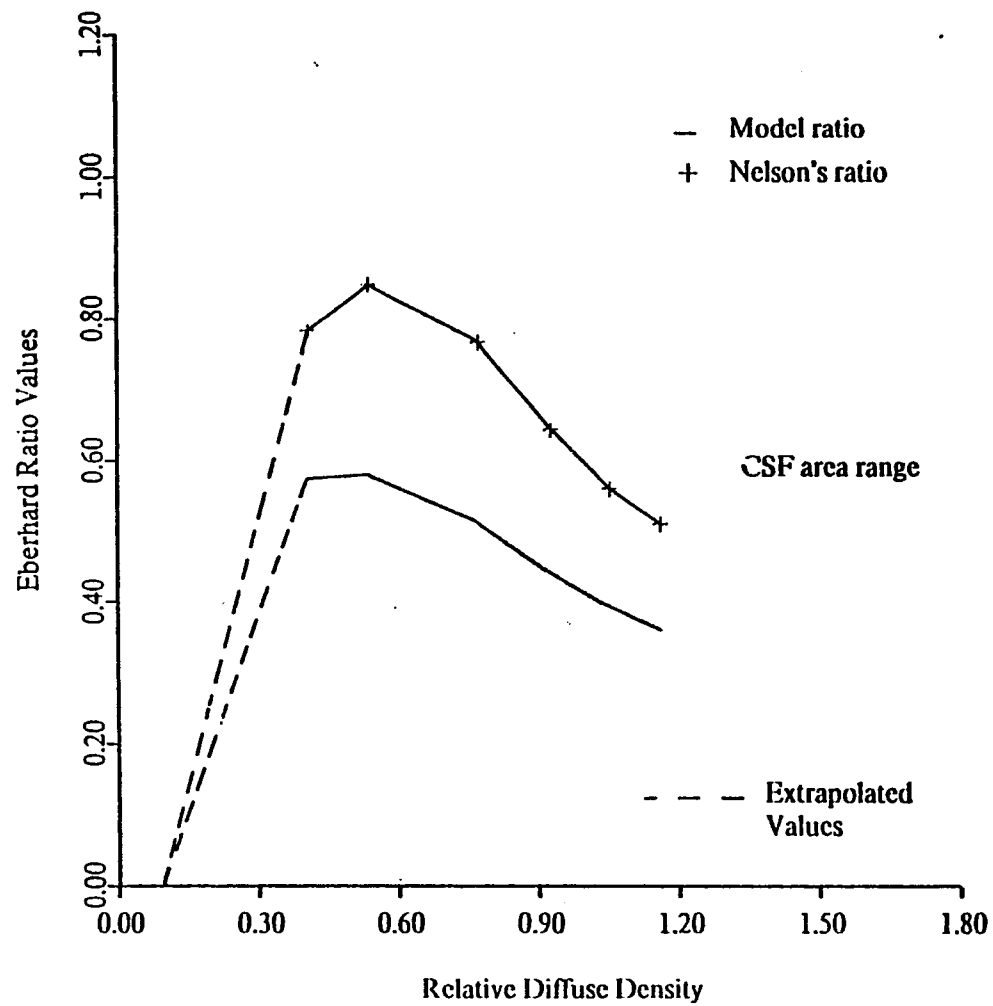


Fig. 5.21. Eberhard ratio as a function of density for experimental data.

Table 5.7. Calculation of Eberhard ratios from experimental data.

| Line Number | g_{D-D_b} | $g_{m.s.}$ | f_{D-D_b} | $f_{m.s.}$ |
|-------------|-------------|------------|-------------|------------|
| 1 | 0.400 | 0.487 | 0.760 | 0.671 |
| 2 | 0.530 | 0.561 | 1.150 | 0.826 |
| 3 | 0.770 | 0.676 | 1.770 | 1.024 |
| 4 | 0.930 | 0.743 | 2.020 | 1.094 |
| 5 | 1.060 | 0.793 | 2.190 | 1.139 |
| 6 | 1.170 | 0.833 | 2.350 | 1.180 |

| Line Number | E.E. $f_{m.s.} - g_{m.s.}$ | N.R. $(f - g) / g^2$ | M.R. $(f - g) / (fg)$ | $B / (f - g) / (fg)$ |
|-------------|-------------------------------|-------------------------|--------------------------|----------------------|
| 1 | 0.184 | 0.776 | 0.563 | ---- |
| 2 | 0.265 | 0.842 | 0.571 | 1.180 |
| 3 | 0.348 | 0.761 | 0.502 | 1.760 |
| 4 | 0.351 | 0.636 | 0.432 | 1.880 |
| 5 | 0.346 | 0.550 | 0.383 | 2.330 |
| 6 | 0.347 | 0.500 | 0.353 | 2.480 |

| | |
|---|---|
| D_b = density of film base | f_{D-D_b} = fine line density $\cdot D_b$ |
| g_{D-D_b} = gross grain density $\cdot D_b$ | $f_{m.s.}$ = fine line mass of silver |
| $g_{m.s.}$ = gross grain mass of silver | B = area of empirical c.s.f. |

Table 5.8. Calculation of Eberhard ratios from Nelson's published data.

| Line Number | ξ_{D-D_b} | $\xi_{m.s.}$ | f_{D-D_b} | $f_{m.s.}$ |
|-------------|---------------|--------------|-------------|------------|
| 1 | 0.42 | 0.65 | 0.56 | 0.804 |
| 2 | 0.91 | 1.21 | 1.28 | 1.540 |
| 3 | 1.18 | 1.44 | 1.81 | 1.890 |
| 4 | 1.44 | 1.69 | 2.34 | 2.150 |

| Line Number | E.E. $f_{m.s.} \cdot \xi_{m.s.}$ | N.R. $(f - g) / g^2$ | M.R. $(f - g) / (fg)$ |
|-------------|-------------------------------------|-------------------------|--------------------------|
| 1 | 0.154 | 0.364 | 0.295 |
| 2 | 0.330 | 0.225 | 0.177 |
| 3 | 0.450 | 0.217 | 0.165 |
| 4 | 0.560 | 0.196 | 1.540 |

| | |
|---|---|
| D_b = density of film base | f_{D-D_b} = fine line density - D_b |
| ξ_{D-D_b} = gross grain density - D_b | $f_{m.s.}$ = fine line mass of silver |
| $\xi_{m.s.}$ = gross grain mass of silver | |

The comparison of the MR, as applied to the experimental data, to the previously calculated CSF area values is also illustrated in Figures 5.20 and 5.21. The CSF area range is that given in Table 5.6. The CSF area values are much higher than those predicted by the MR for the $\alpha = 1$ case. The ratios of the CSF area values to the MR are given in Table 5.7. For the four cases where the CSF area has reached its peak the CSF area was found to be approximately 1.75 to 2.5 times higher than the MR value.

Application of Image Restoration "Recipe"

The first three stages of the image restoration "recipe", which implement the removal of chemical adjacency effects, are applied to one dimensional edge and line images. The discussion begins with a description of the selected images, data resampling procedures and analytic insight into the application of the gross grain mass of silver algorithm (GGMSA) given by Eq. 2.19. This is followed with a brief review of the software methodology and detailed discussions of the one dimensional restoration results.

Selection of One Dimensional Images

A line, 0.500 mm in width, was selected from the 1 cycle/mm line set, group 1, element 1 (group number - element number - line number, 1-1-8). The 0.500 mm line width was sufficiently large, compared to the truncated CSF width of 0.366 mm, that it could be considered a large area image consisting of two edges. The lines were scanned with a 0.005 x 0.080 mm slit aperture using a sample spacing of 0.0025 mm as previously discussed in Chapter 4.

Line images containing higher spatial frequencies were chosen after reviewing a large quantity of line image profiles provided by the two dimensional (raster) microdensitometer scans of group 2 and group 3 of the high resolution target images. As discussed in Chapter 4, these groups were scanned with a 0.005 mm circular aperture using a sample spacing of 0.0025 mm in both dimensions. Table 5.9 provides a complete list of all lines used in the analysis.

Table 5.9. Selected line images for use in restoration "recipe".

| Group Number | Element Number | Line Number | Spatial Frequency (cycles/ mm.) |
|-----------------|-------------------|----------------|---------------------------------------|
| 1 | 1 | 8 | 1.00 |
| 2 | 1 | 1-15 | 10.00 |
| 2 | 3 | 1-15 | 15.85 |
| 2 | 4 | 1-15 | 19.56 |
| 2 | 5 | 1-15 | 25.12 |
| 2 | 7 | 1-15 | 39.82 |

A one dimensional, as opposed to a two dimensional, analysis was preferred to simplify the software requirements and minimize computer CPU time. The literature has adequately documented the circular symmetry of the CSF such that a one dimensional analysis fully describes the physical process. In an extension of this theory to psychophysical perception a two dimensional analysis would be required.

Data Resampling Considerations

The results of the line image profiles provided by the two dimensional microdensitometer scans indicated a misalignment between the odd and even numbered scan lines of less than one sample spacing, 0.0025 mm. The misalignment was attributed to an error in the film platen position as it moved in opposite directions while raster scanning the film image. The probable source of the error was an irregularity in the triggering mechanism used to initiate the image sampling process for each scan line. Rather than writing a subroutine to realign the image scans the data was analytically

resampled at a 0.005 mm sample spacing. This eliminated the error between scan lines. High quality images were now available in each of the two orthogonal scan directions. The 0.005 mm sample spacing satisfied the minimum requirements of the sampling theorem as discussed in Chapter 4.

Review of Gross Grain Mass of Silver Algorithm (GGMSA)

Some insight into the applicability of the GGMSA to the photographic line images can be obtained from consideration of two special cases, an edge image and an isolated fine line image.

In the case of an edge image, the mass of silver of the developed image, $\langle m_k \rangle$, is equivalent to the gross grain mass of silver, $\langle g_k \rangle$, in regions I and V of Figure 2.5. The GGMSA then becomes

$$\langle g_k \rangle = \alpha \langle g_j \rangle / (\alpha + A \langle g_j \rangle - \sum_j A_{jk} \langle g_j \rangle) \quad (5.8)$$

since $\langle g_k \rangle = \langle g_j \rangle$ is a constant, this reduces to

$$\langle g_k \rangle = \alpha \langle g_k \rangle / (\alpha + A \langle g_k \rangle - \langle g_k \rangle \sum_j A_{ij}) \quad (5.9)$$

The $\sum_j A_{jk}$ is simply the area under the CSF, A , such that

$$\langle g_k \rangle = \alpha \langle g_k \rangle / (\alpha + A \langle g_k \rangle - A \langle g_k \rangle) \quad (5.10)$$

$$\langle g_k \rangle = \alpha \langle g_k \rangle / \alpha = \langle g_k \rangle$$

Thus, the algorithm will only effect the mass of silver of the developed image in areas which do not approach a constant level of large area mass of silver.

For an isolated fine line image, the mass of silver of the developed image, $\langle m_k \rangle$, becomes f_k to yield

$$\langle g_k \rangle = \alpha f_k / (\alpha + A f_k \sum_j A_{ij} f_j) \quad (5.11)$$

Assuming f_j to be a very narrow function its relationship to A_{jj} can be described by invoking the sampling properties of the Dirac delta function (Bracewell, 1965, pp. 69-97; Gaskill, 1978, pp. 50-66) to obtain

$$\langle g_k \rangle = \alpha f_k / (\alpha + A f_k - C_s) \quad (5.12)$$

where C_s is the magnitude of the sample taken on the CSF. Since $A f_k \gg C_s$

$$\langle g_k \rangle \sim \alpha f_k / (\alpha + A f_k) \quad (5.13)$$

we find that the peak value of f_k could be substantially reduced dependent upon the values assigned to α and A . Assuming $\alpha = 1.0$ and $A = 0.9$, a reasonable assumption as previously shown,

$$\langle g_k \rangle = f_k / (1 + 0.9 f_k) \quad (5.14)$$

which predicts a value $\langle g_k \rangle = 0.572$ for $f_k = 1.180$, provided by Table 5.7. The predicted value of $\langle g_k \rangle$, being much lower than the experimentally obtained gross grain mass of silver value of 0.833, again provided by Table 5.7, implies that the CSF required by the restoration model is a scaled version of Nelson's (1971) CSF. This was investigated as discussed in the following sections.

Analysis Approach

The procedure followed in performing the restoration analysis is summarized in Figure 5.22. The CSF calculation procedures, previously discussed, are outlined in the left column of the figure. The selection, resampling and analysis procedures followed for the line images are shown in the right column. As in the case of the CSF calculations the film base density was subtracted from the film image density prior to conversion to mass of silver values.

The GGMSA was applied to the line image mass of silver values in two stages. First, the reduction product term, consisting of the convolution of the CSF with the line image, was calculated. The reduction product term was then used as a data input in the final GGMSA calculation.

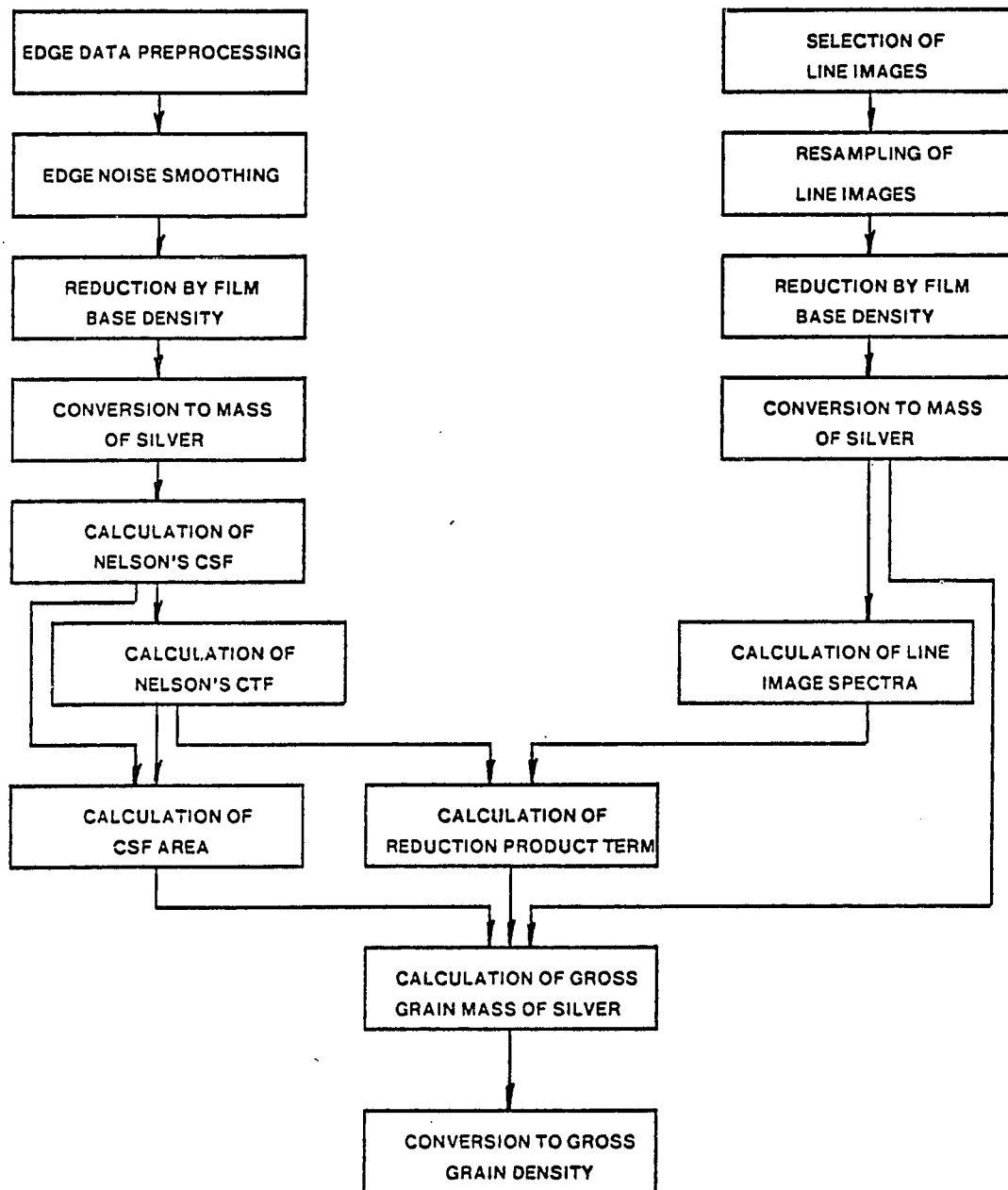


Fig. 5.22. Restoration analysis procedure.

The discrete convolution required to calculate the reduction product term was performed in the frequency domain using a Fast Fourier Transform (FFT) algorithm. The application of the FFT approach is a more efficient approach than performing the direct convolution. The computation time is proportional to $N \log_2 N$ for the frequency domain approach as opposed to N^2 for the direct convolution approach (Brigham, 1974, p. 110).

Image overlap effects due to cyclic convolution (Anuta, 1970; Brigham, 1974, p. 200) were eliminated by restructuring the data using the relationship

$$N = P + Q - 1 \quad (5.15)$$

where

P = period of line spectrum data

Q = period of CTF

N = total period of data array

The spatial frequency bandlimit of the CTF was estimated to be approximately 10 to 20 cycles/mm since the truncated CSF contained a large impulse type function with a width of approximately 0.085 mm. In order to obtain a reasonable number of spatial frequency samples over this interval a sample spacing of 1/3 cycle/mm was selected. Since $N = 1/(dx df)$ and $dx = 0.005$ mm, the desired value of N was 600 samples. To achieve this the CSF, being 0.366 mm in width, contained 72 samples and was surrounded by 264 zero values. The line image data was restructured in a similar manner dependent upon the record length of the image data being analyzed.

Restoration of Line Images

The restoration results obtained for the images listed in Table 5.9 are discussed in this section. The initial image restoration results included all intermediate and final functional forms, such as the CSF, CTF, input image profile, reduction product term and restored images profiles. Subsequent

restoration results include only the significant changes that occurred to some of these functional forms. Multiple plots are provided in certain cases to emphasize certain important functional differences.

Initial Large Area Image (1 cycle/mm) Restoration. The restoration model was initially applied to the large area density values provided by the line images that were 0.5 mm in width. The value of the proportionality constant, a , was set equal to unity.

The actual CSF used in the analysis, obtained from edge number 5, and its frequency domain equivalent, the CTF, are illustrated in Figures 5.23 and 5.24. As expected, the CTF had a low frequency impulse and negligible amplitude beyond approximately 10 cycles/mm. The abrupt change in the amplitude observed in the low spatial frequency region was created by the choice of the 1/3 cycle/mm frequency space sampling interval. Finer precision would have provided a smoother function. However, this had negligible impact on the accuracy of the results. Six sample points already existed before the 2 cycle/mm cutoff frequency of the 0.5 mm line image as illustrated in Figure 5.25 through 5.29. These figures also illustrate density and mass of silver profiles for line images 1-1-(7-9). The entire restoration analysis was performed only for line 1-1-8 since it was representative of all 15 remaining line images.

The filtering performed by the CTF on the target spectrum is illustrated in Figure 5.30. As expected, only the low frequency content remains and even that is significantly attenuated. The reduction product term is illustrated in Figures 5.31 and 5.32. The attenuation performed by the low frequency CTF bandlimited filter is readily apparent in the reduction product term.

The comparison of the restored line image gross grain mass of silver to the original mass of silver, illustrated in Figure 5.33, indicates the removal of all sharp edge boundary values. It also indicates that a considerable smoothing of the edge has occurred. A function defined as the correction ratio, the ratio of the restored mass of silver to the original mass of silver, is illustrated in Figure 5.34. This function illustrates the proportional magnitude of the restoration achieved. A unity value signified that the original image was not affected by the GGMSA.

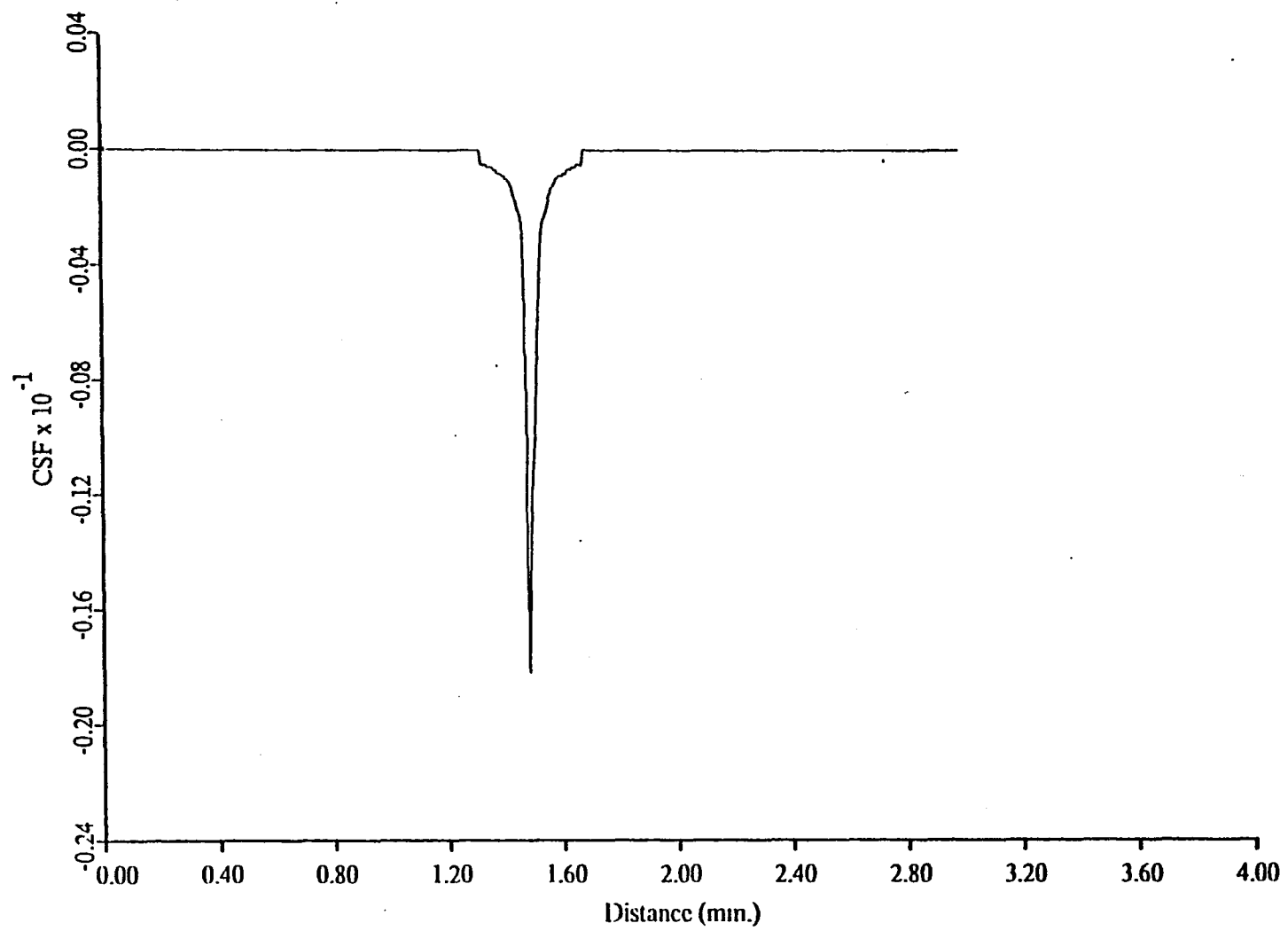


Fig. 5.23. CSF obtained from edge number 5.

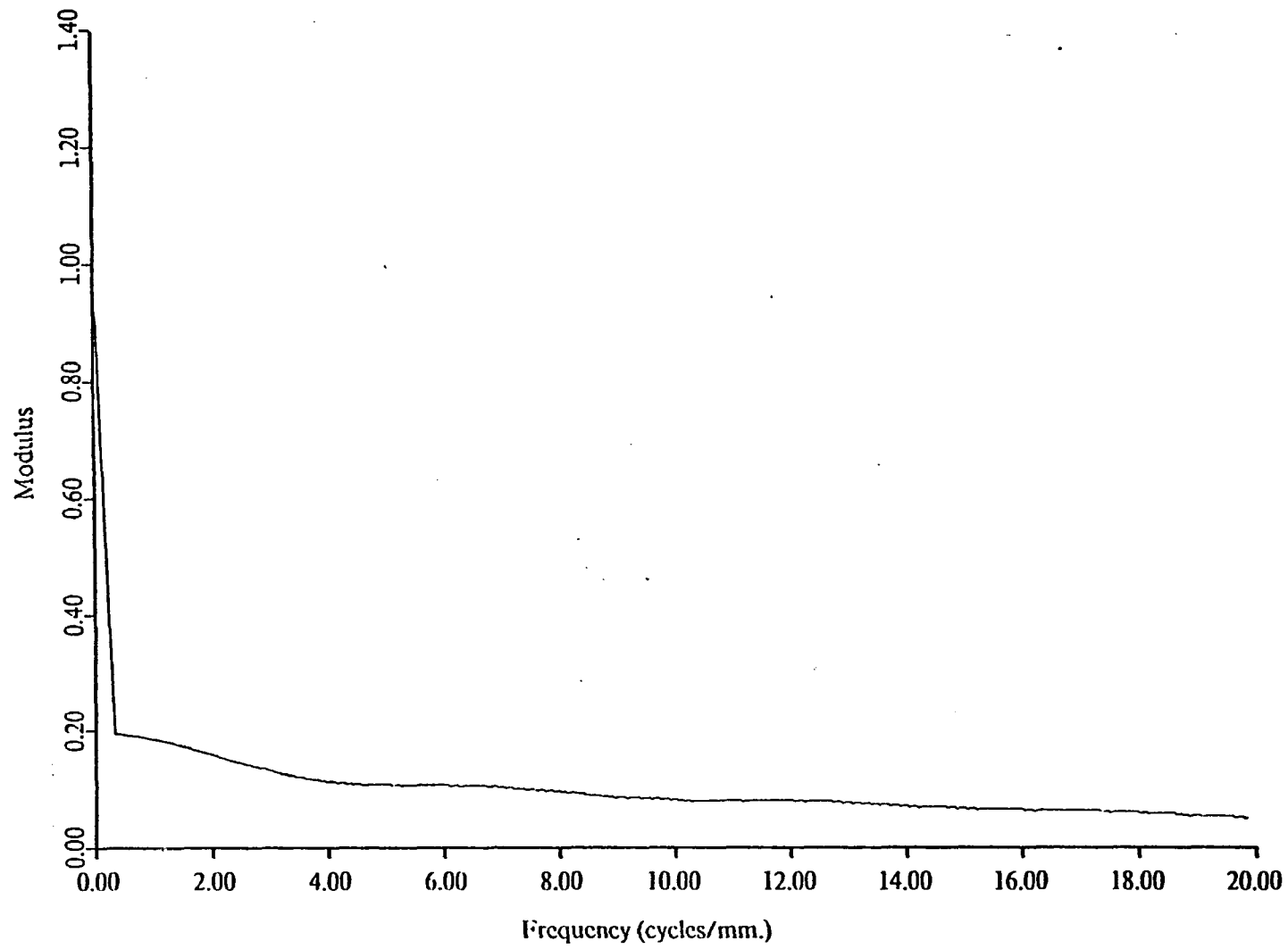


Fig. 5.24. Modulus of CTF for edge number 5.

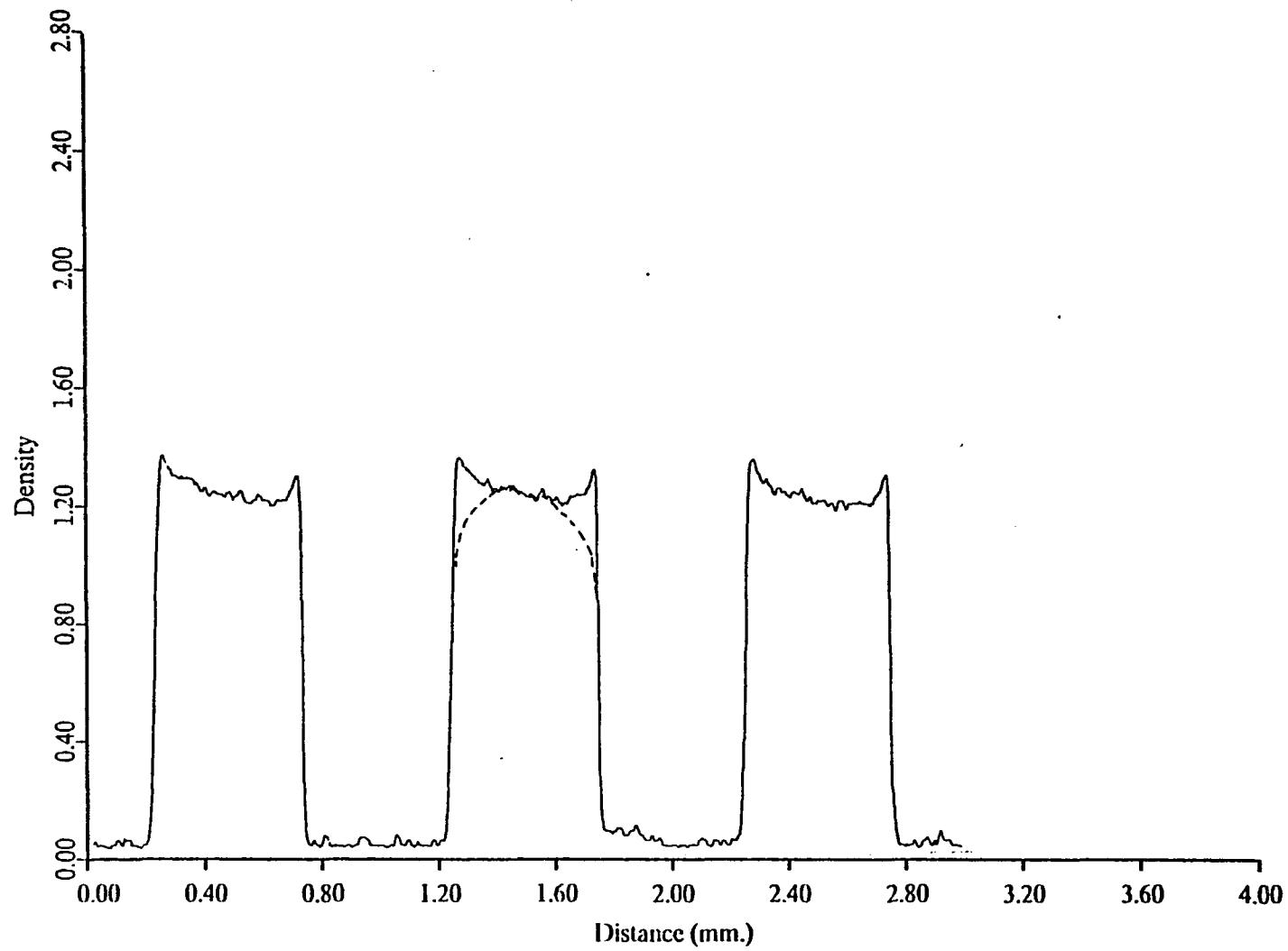


Fig. 5.25. Density profiles for 0.5 mm. line widths (lines number 7, 8 and 9).

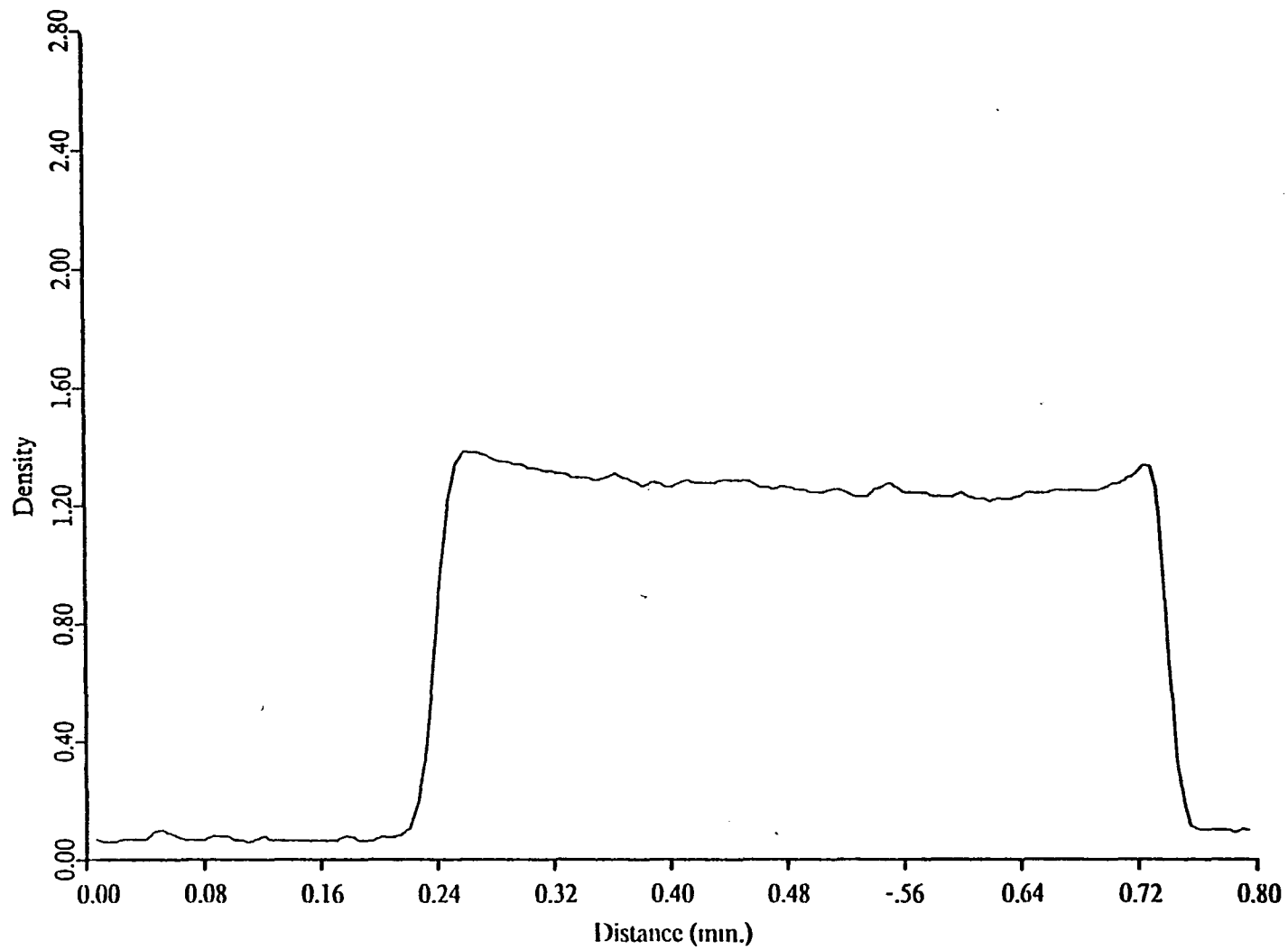


Fig. 5.26. Density profile for 0.5 mm line width (line number 8).

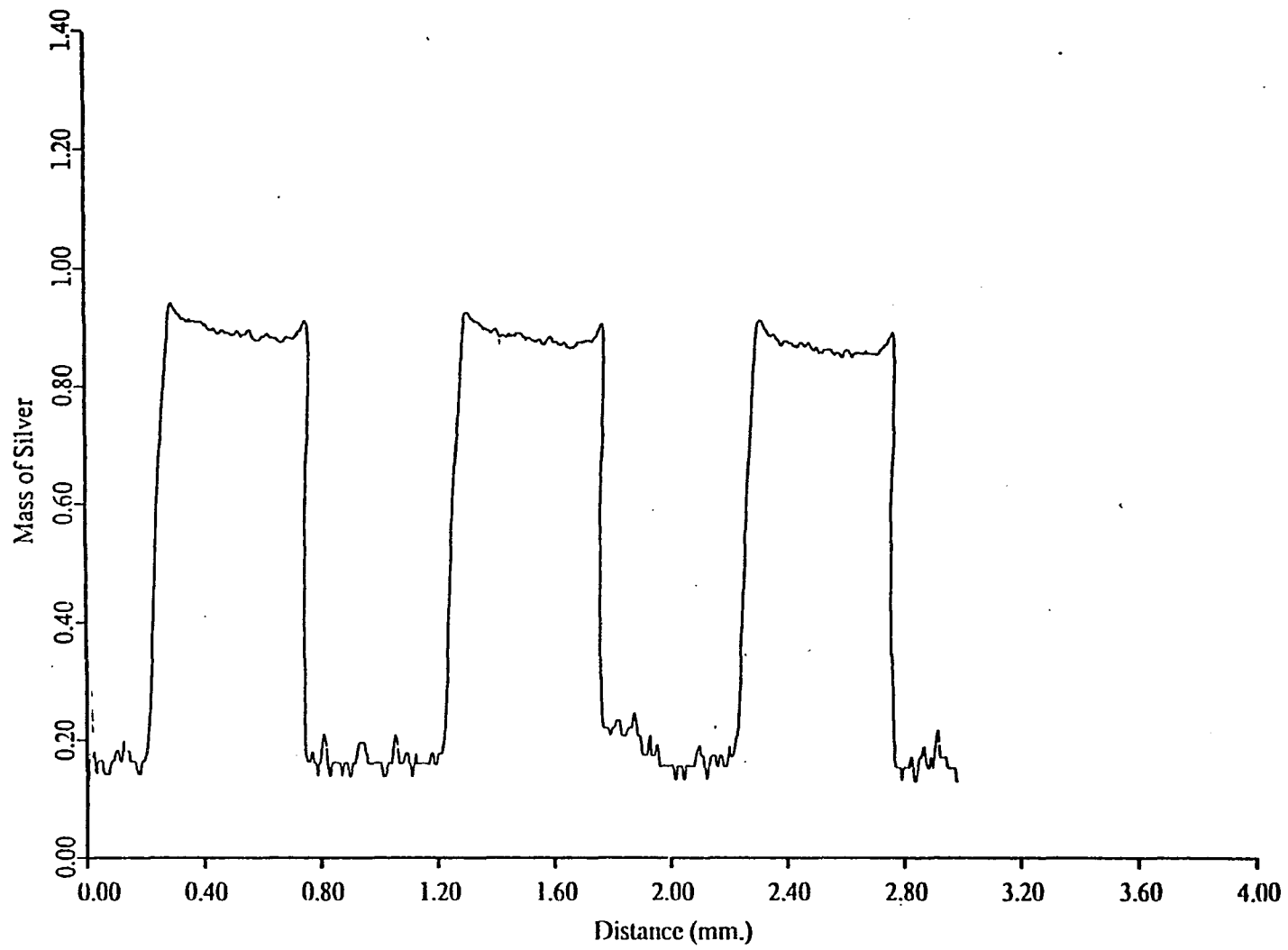


Fig. 5.27. Mass of silver profiles for 0.5 mm. line widths (lines number 7, 8 and 9).

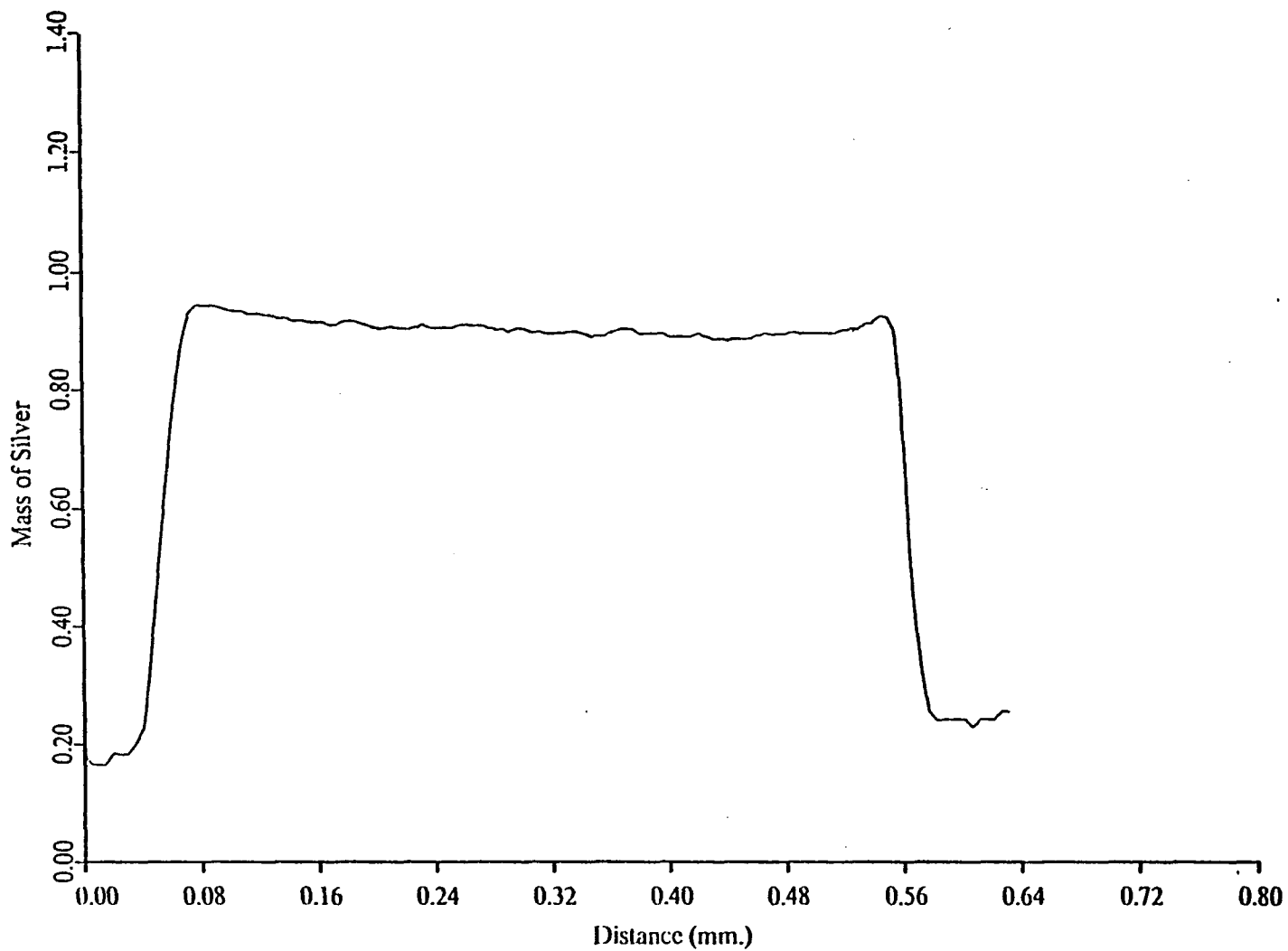


Fig. 5.28. Mass of silver profile for 0.5 mm. line width (line number 8).

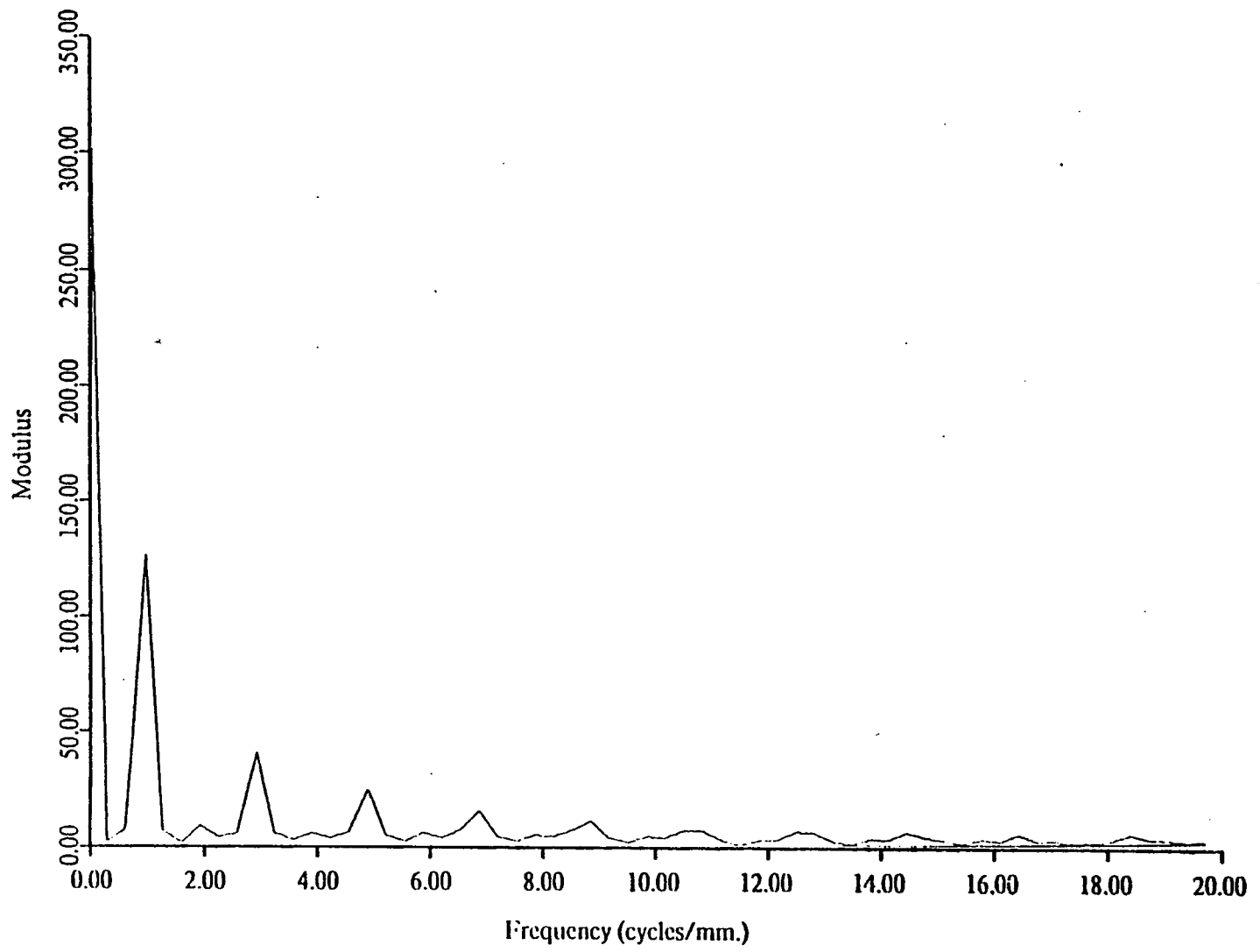


Fig. 5.29. Modulus of input spectrum (line number 8).

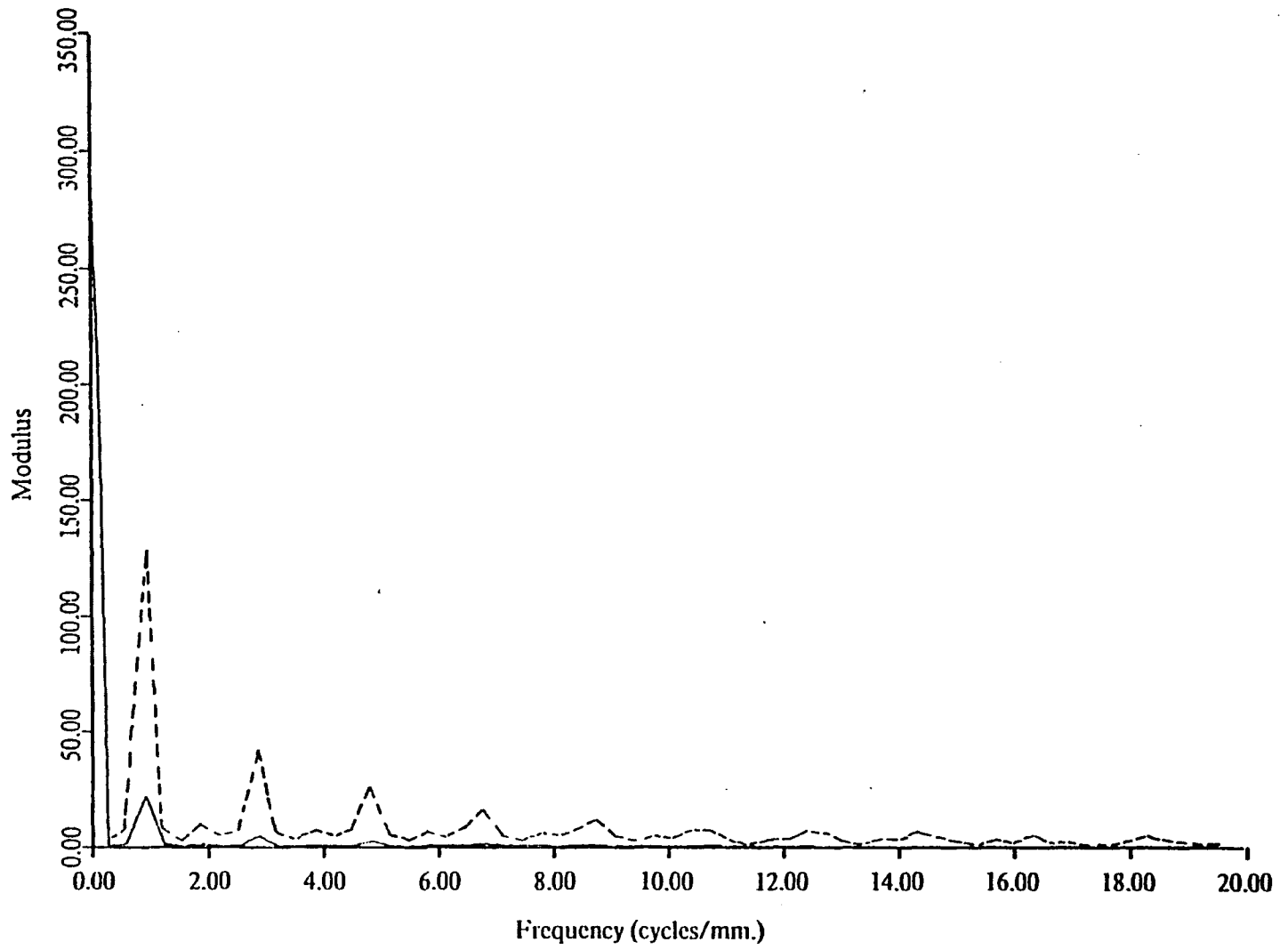


Fig. 5.30. Product of CTF modulus and input modulus (line number 8).

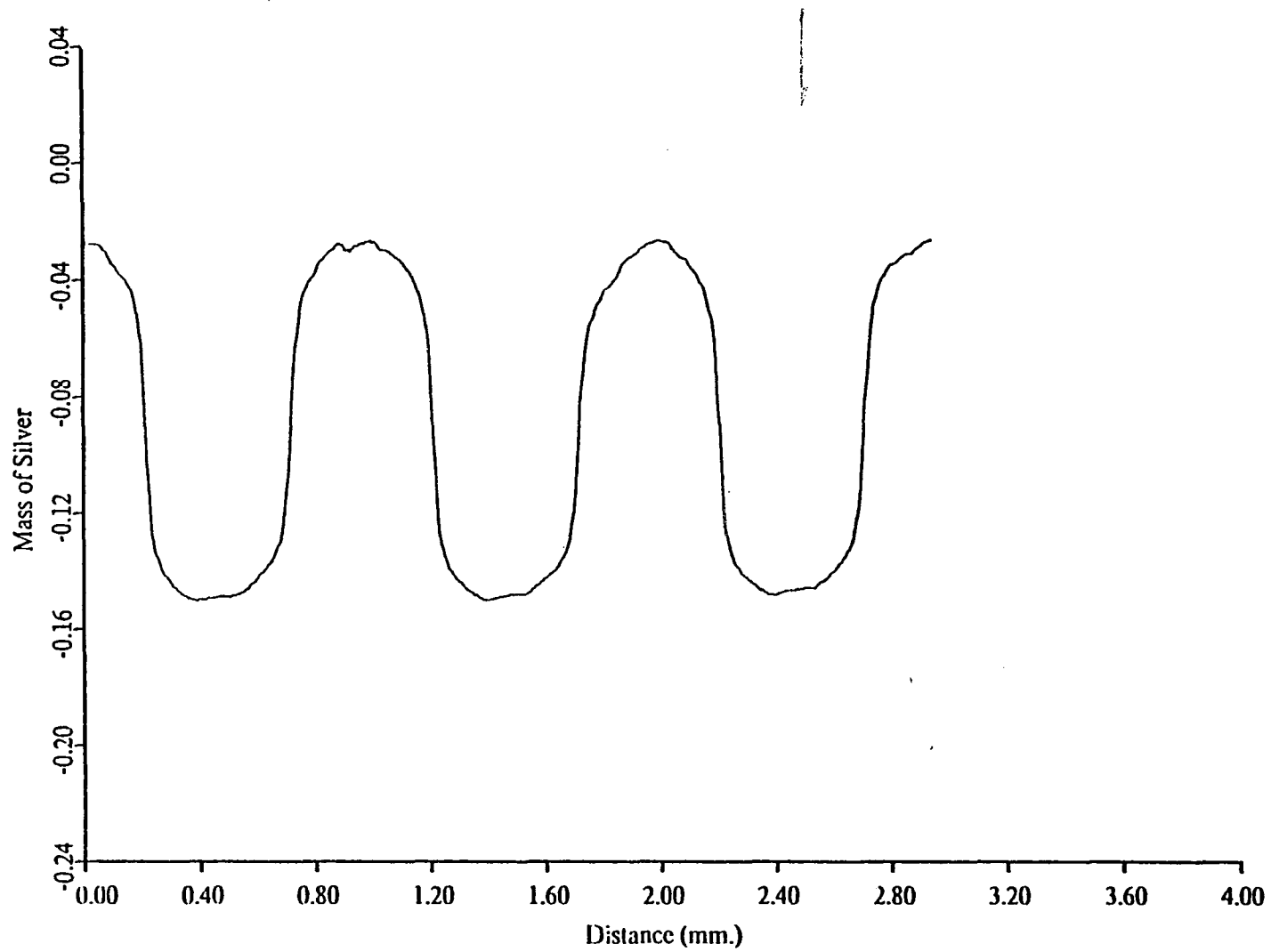


Fig. 5.31. Reduction product term for 0.5 mm. line widths (lines number 7, 8 and 9).

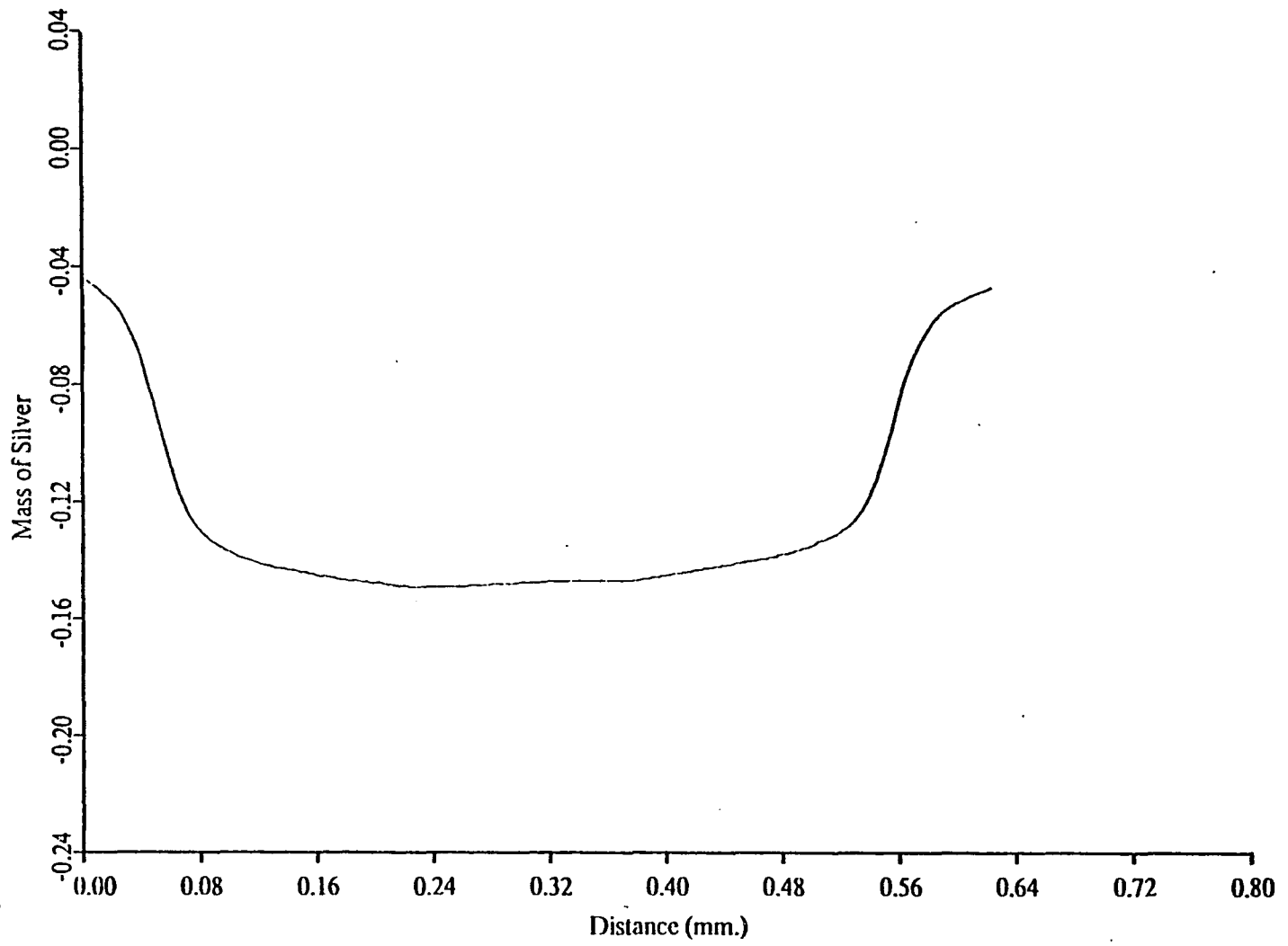


Fig. 5.32. Reduction product term for 0.5 mm. line width (line number 8).

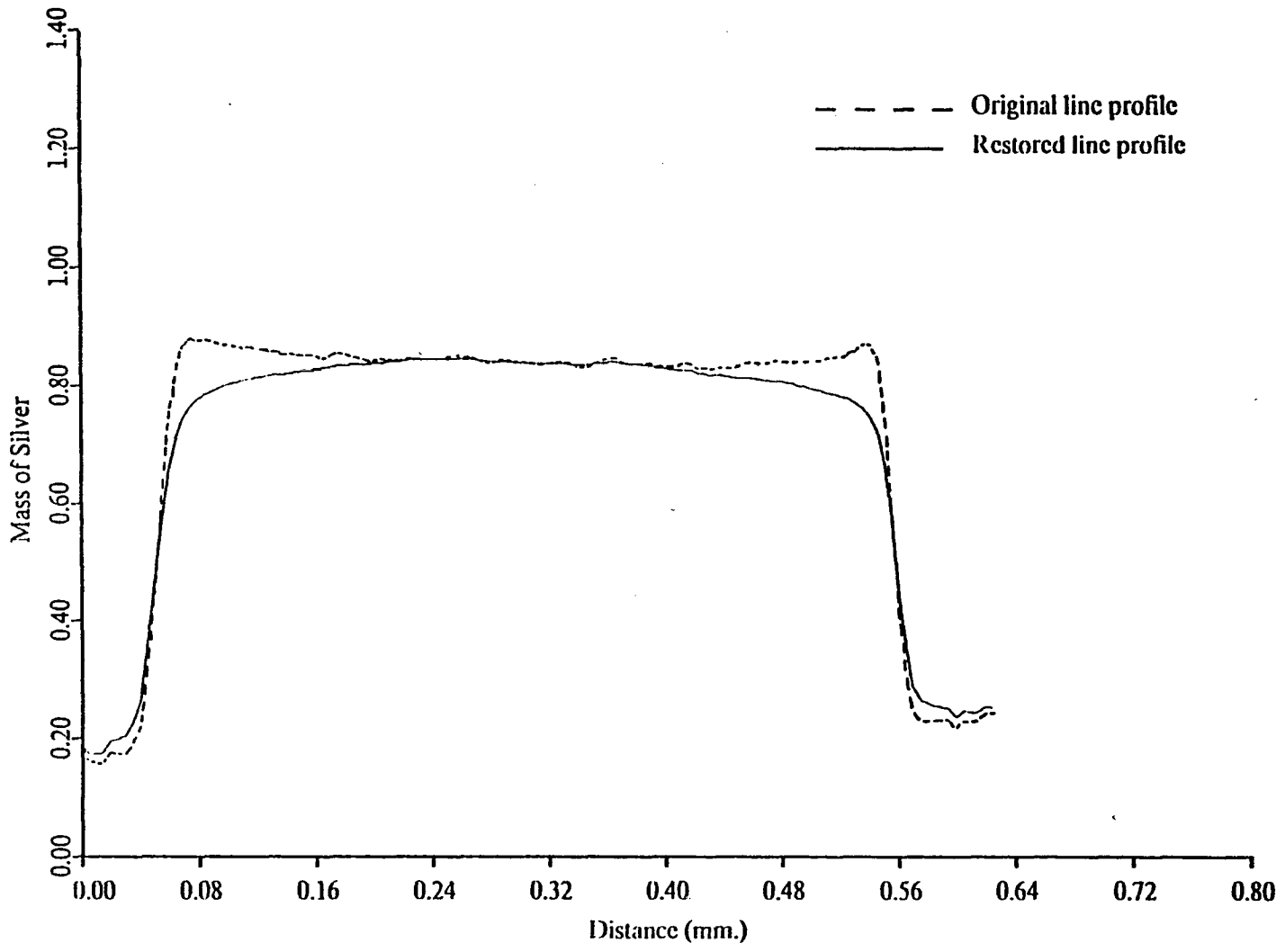


Fig. 5.33. Gross grain mass of silver for 0.5 mm. line width (line number 8).

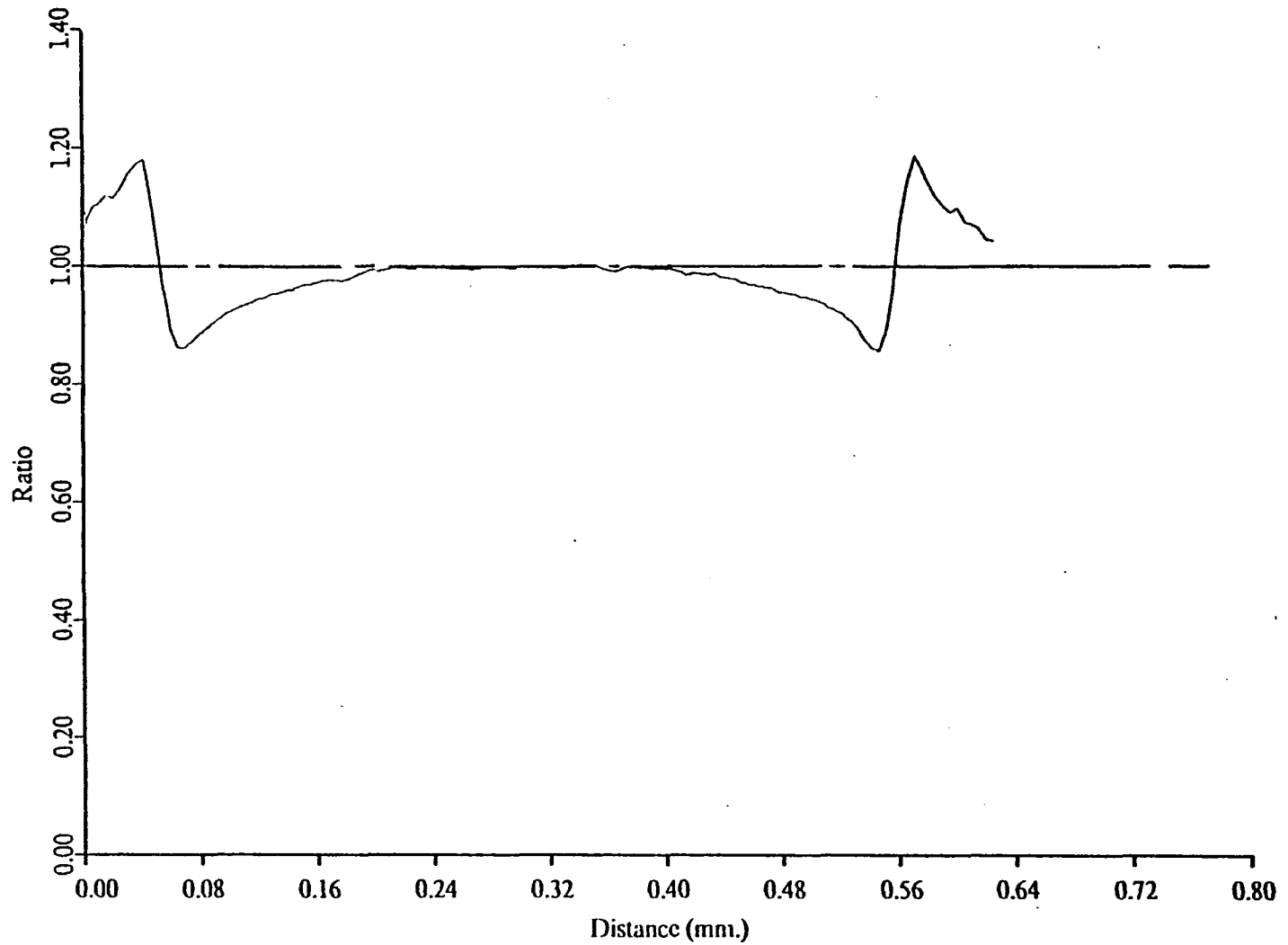


Fig. 5.34. Correction ratio for 0.5 mm. line width (line number 8).

The restored gross grain density images are illustrated in Figures 5.35 and 5.36. These results, along with gross grain mass of silver results, indicate that the GGMSA performed more than a restoration operation. It significantly attenuated the edges beyond the removal of adjacency edge effects. A second observation is that the GGMSA modified the original image only near the edge boundaries. The large area gross grain density remained the same as predicted by Eq. (5.8).

CSF Impact on Large Area Image Restoration. The attenuation of the edge boundaries could only be attributed to the magnitude of the CSF. The large area image restoration was repeated using the CSF's illustrated in Figures 5.9 through 5.13.

The restoration results calculated from the use of CSF's obtained from edge numbers 2 through 5 were quite similar. Thus, only the results obtained from using two of the CSF's are illustrated in Figures 5.37 through 5.40. The two CSF's selected were obtained from edge numbers 1 and 5, which represented a large x-ray exposure range. A maximum difference of approximately 0.05 was found in the amplitude of the two CTF's, as illustrated in Figure 5.37. Similar results were found for the product of the CTF's and the large area image spectrum. The correction ratio and gross grain density profiles both illustrate that the differences between the CSF's had a very small impact on the overall restoration of the large area image. This also suggests that small errors in the accuracy of the calculated CSF's, such as truncation error and least squares fit error, would have negligible impact on the restored images.

Thus far, observations of both the EE and the initial restoration results have indicated that the area of the CSF's maybe unreasonably high for the restoration model. This was also theoretically supported in the comparison of the restoration model to Nelson's (1971) model, as indicated in Eq. (2.22). The CSF of the restoration model was noted to be proportional to Nelson's (1971).

Additional insight into the importance of this proportionality factor, β , was investigated using the CSF obtained from edge number 5 and a range of β values which varied from 1 to 10. Selected

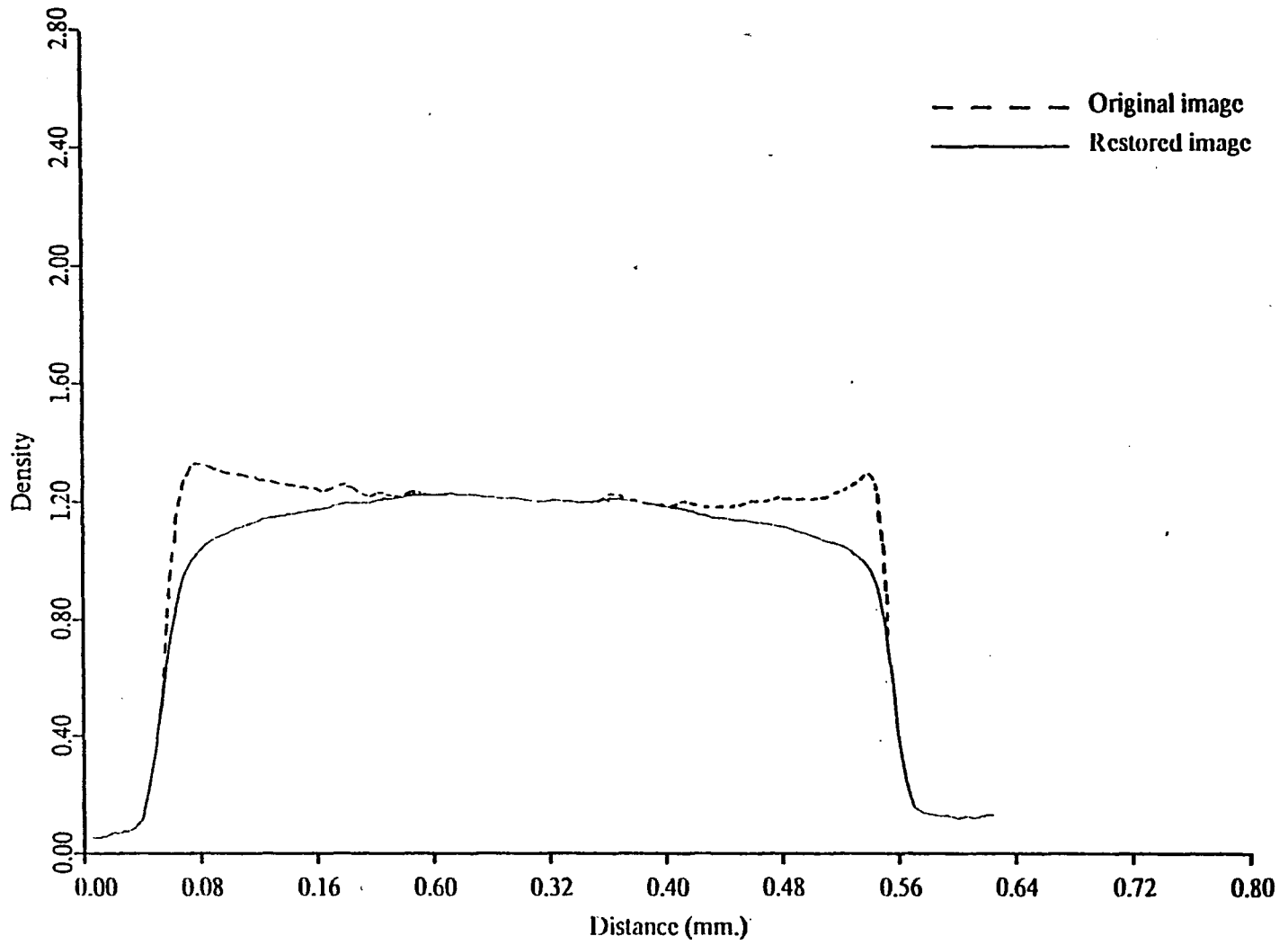


Fig. 5.35. Gross grain density for 0.5 mm. line width (line number 8).

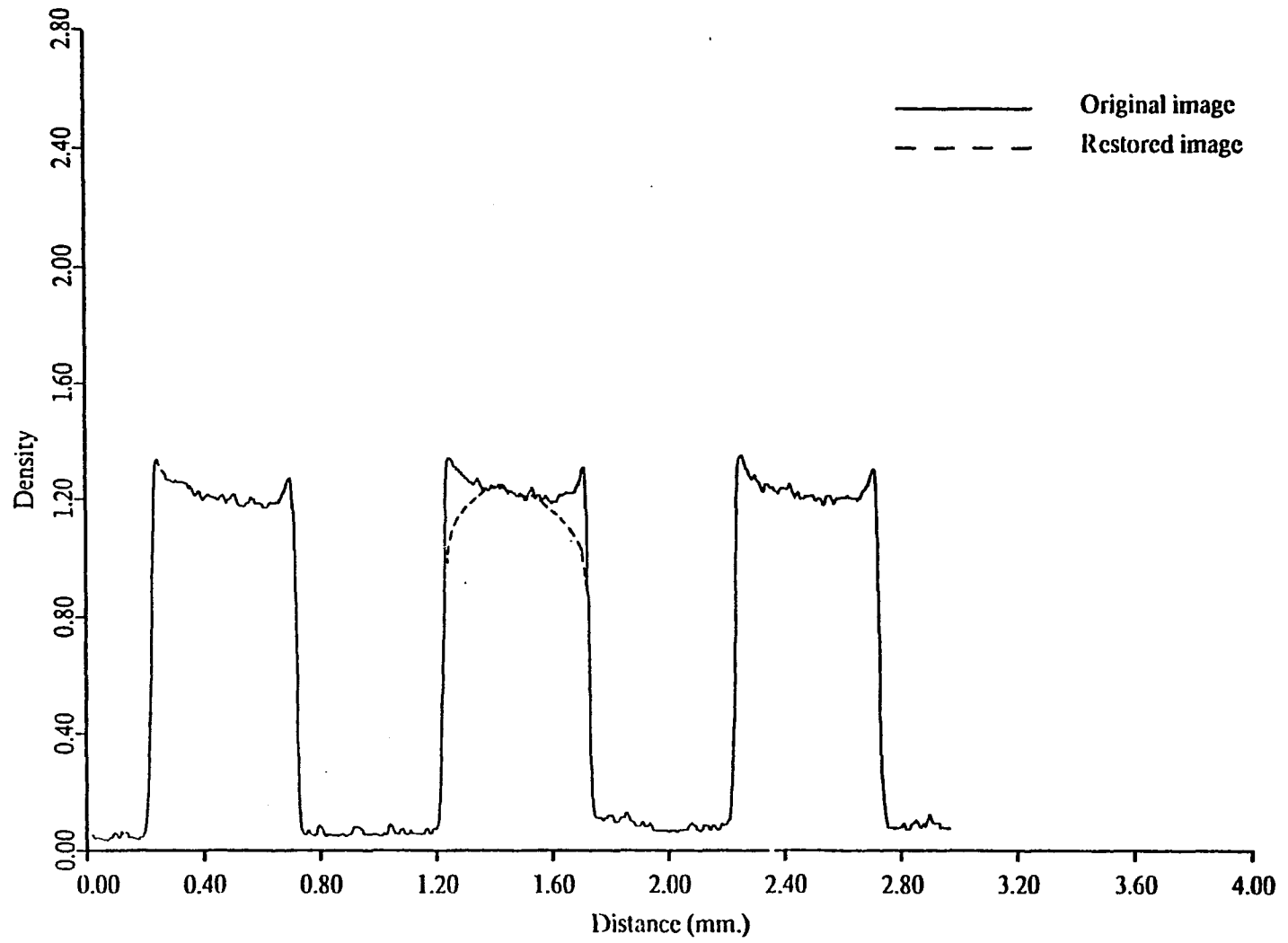


Fig. 5.36. Gross grain density (line number 8) compared to target image density profiles (lines number 7, 8 and 9).

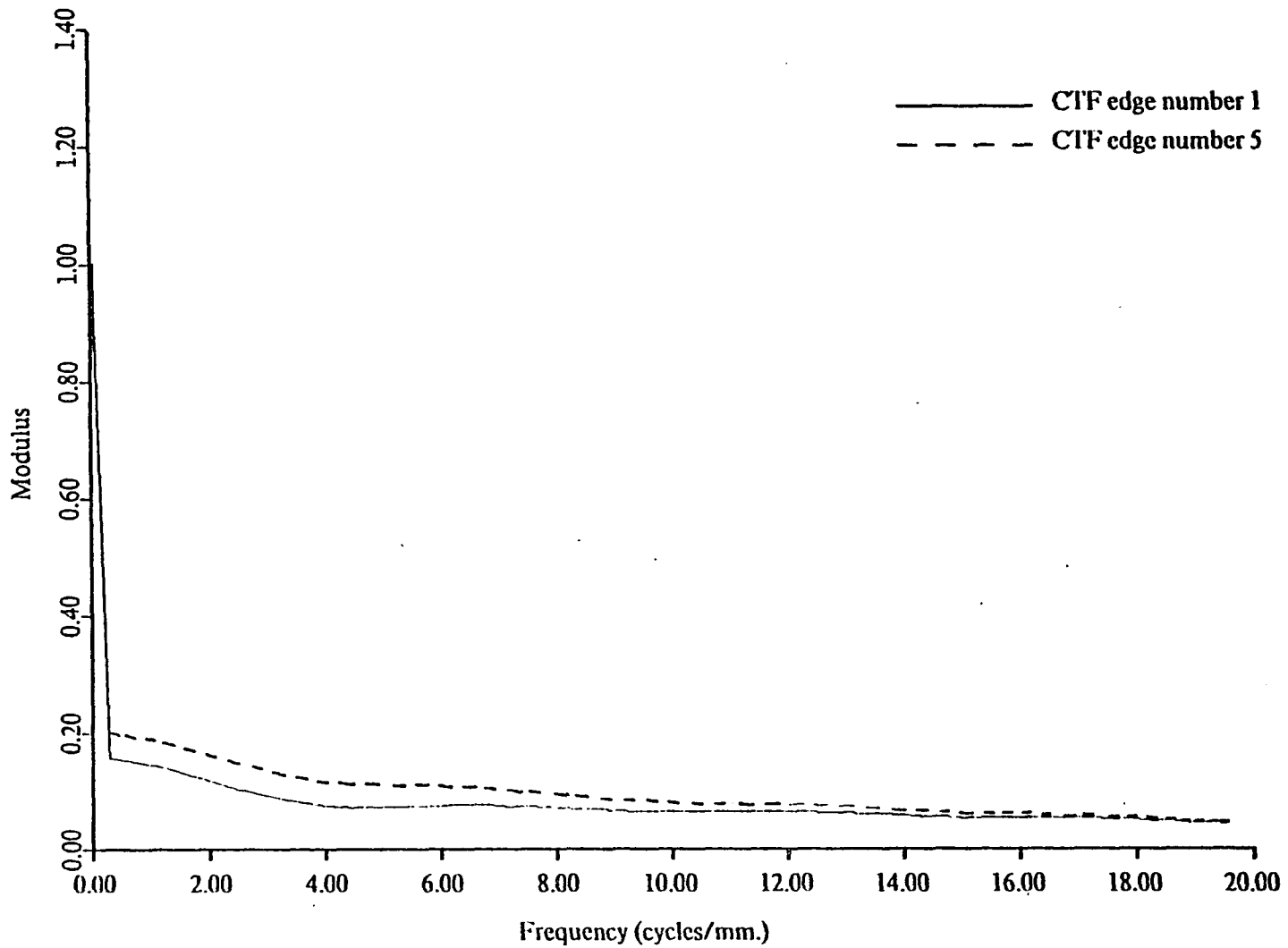


Fig. 5.37. Modulus of CTF for edges number 1 and 5.

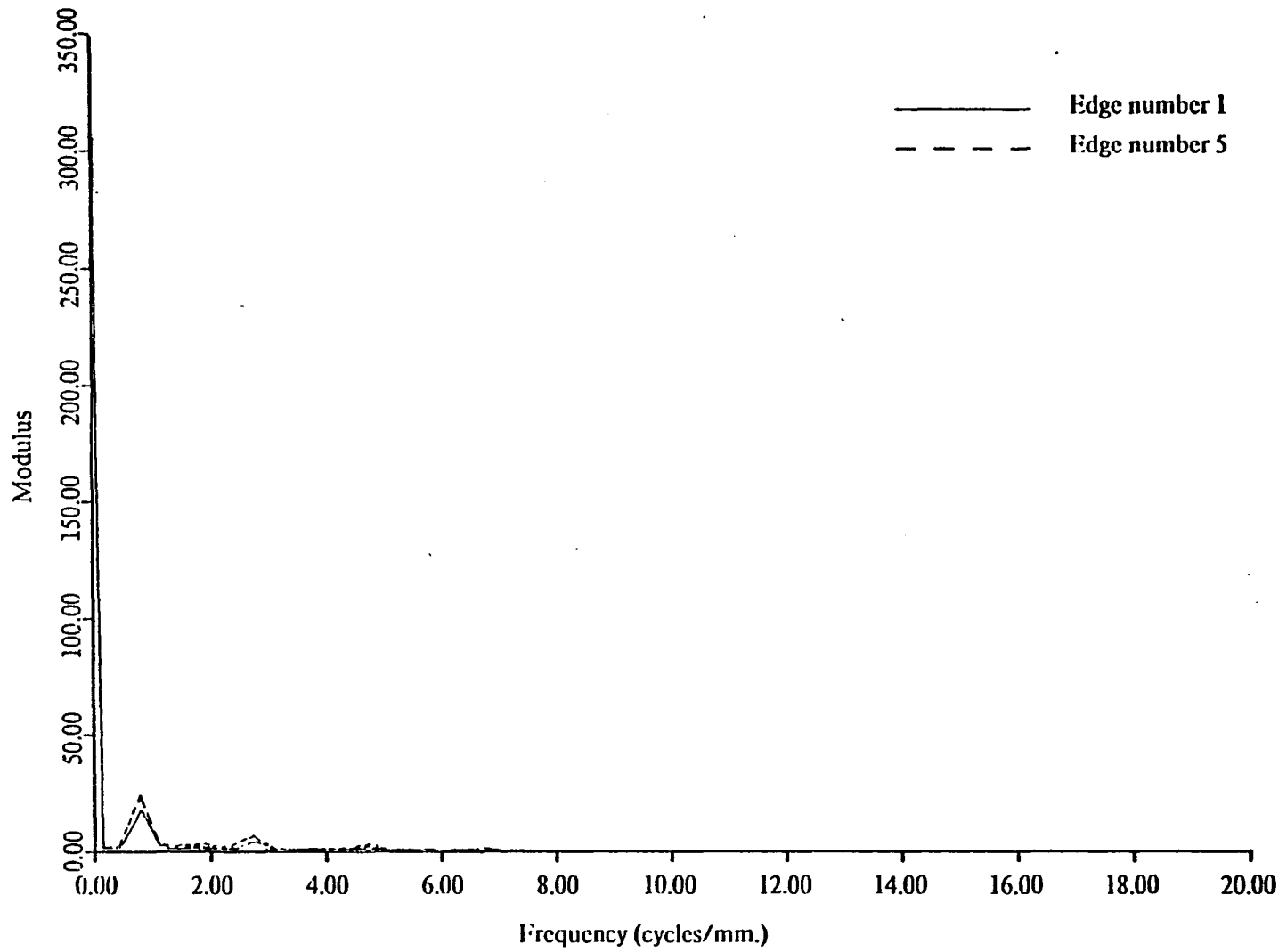


Fig. 5.38. Product of edge modulus values and input modulus (line number 8).

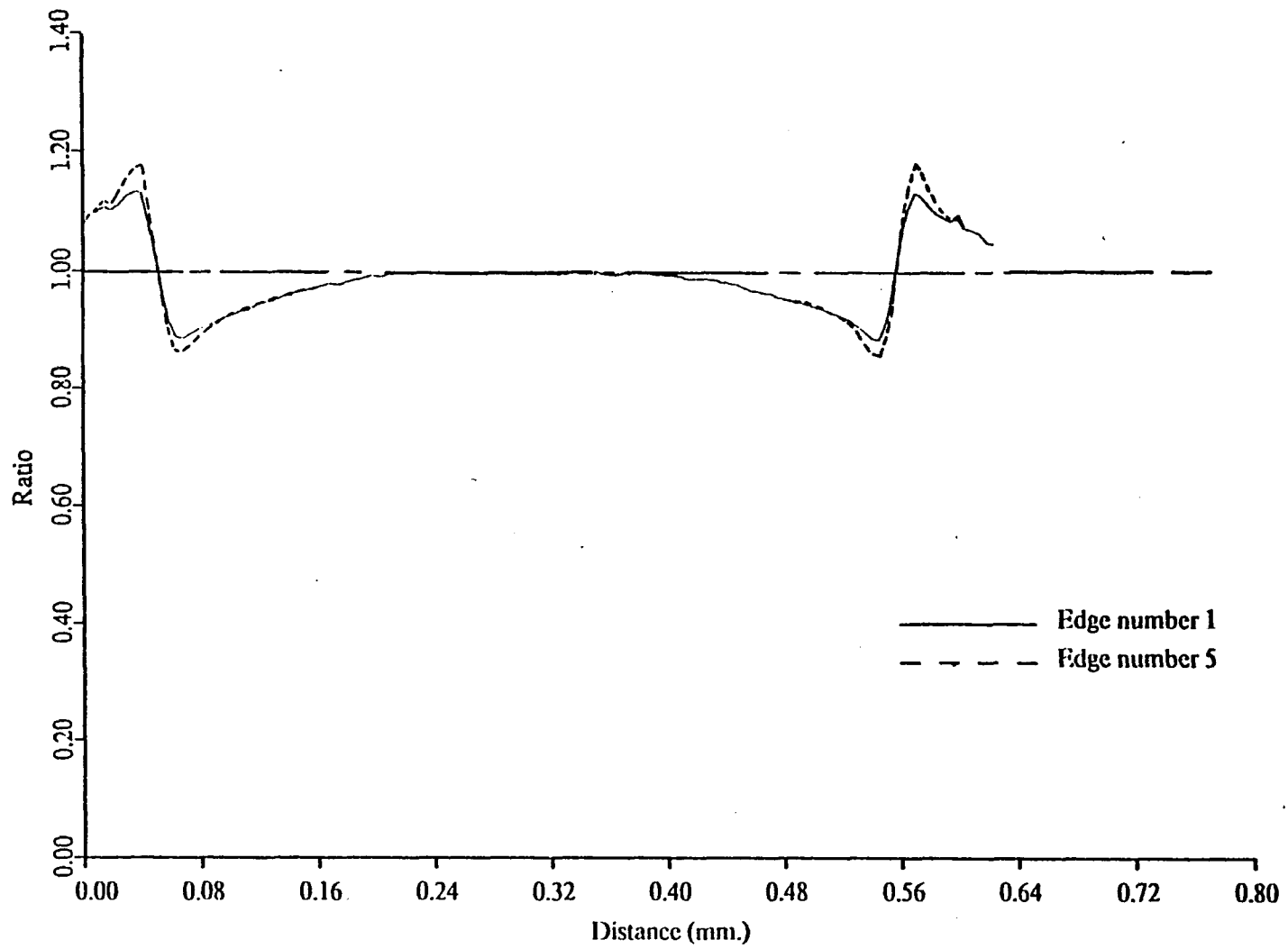


Fig. 5.39. Correction ratio for 0.5 mm. line width (line number 8) using two CSF values.

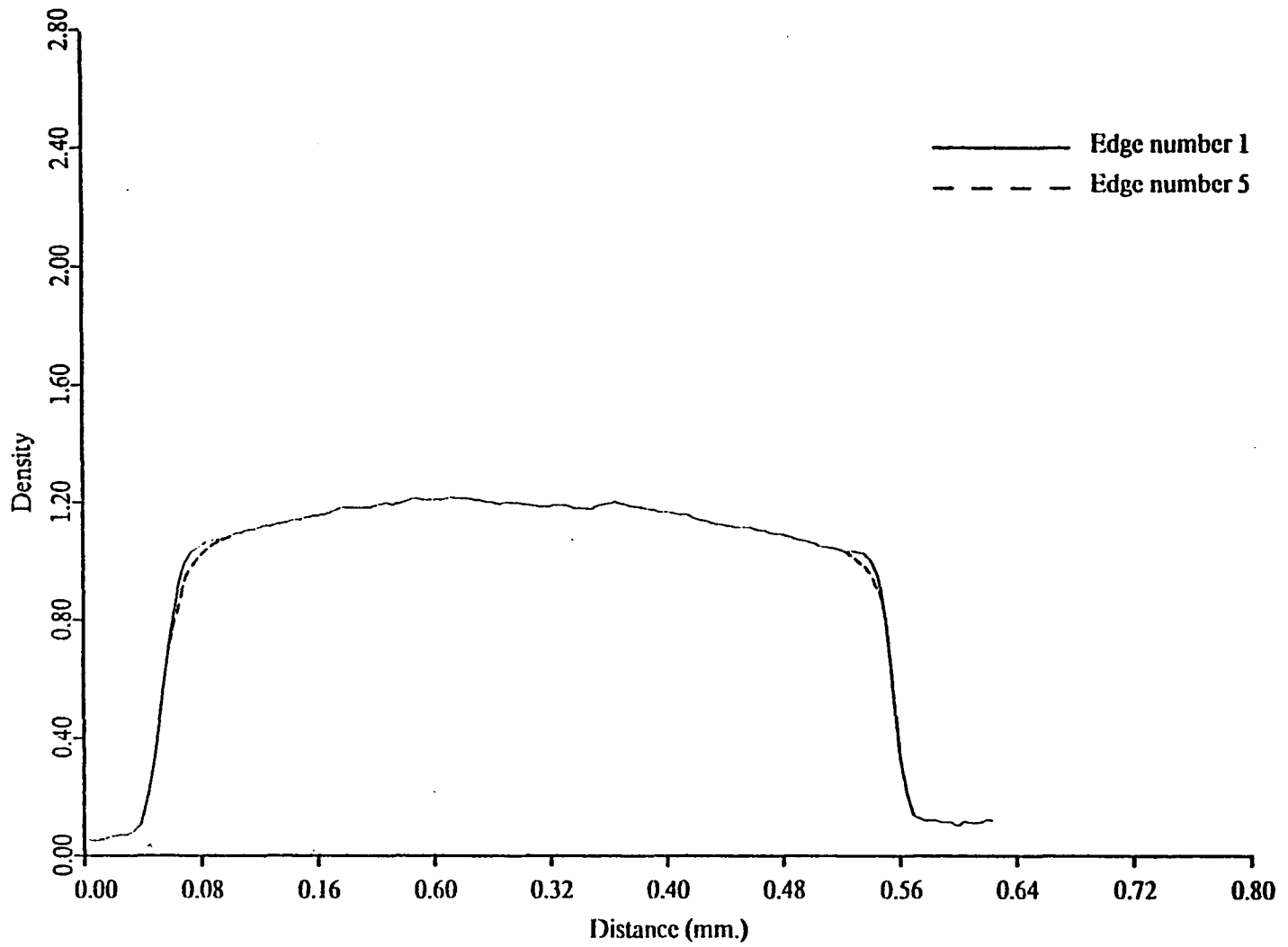


Fig. 5.40. Gross grain density for 0.5 mm. line width (line number 8) using two CSF values.

gross grain mass of silver restorations, for β values of 1.0, 1.75, 2.5 and 10.0, are illustrated in Figure 5.41. The correction ratios and the gross grain density restorations are illustrated in Figures 5.42 and 5.43, respectively. CSF magnitude variations of this order are found to provide significant differences in the restored images. A value of β in the range from 1.75 to 2.5 appeared to eliminate the adjacency effect without attenuating the edge boundary. This was the range of the ratio previously observed to exist between the area under the CSF and the magnitude of the value of the Eberhard ratio, MR.

This suggests that the magnitude of MR could be used as an independent measure of the proportionality constant, β , to provide the scaling factor for Nelson's (1971) CSF. Unfortunately, this cannot be absolutely verified in the present study due to the development limitation of the fine line density values. However, the range of variation in β from 1.75 to 2.5 provided restored images that were quite similar. This included at least one value, $\beta = 1.75$, which did not appear to be limited by fine line development.

Line Image Restoration (10 cycles/mm). The image restoration procedure was applied to the 10 cycle/mm line set, 2-1-(1-15), using the CSF obtained from edge number 5 and $b = 2.5$. The results, illustrated in Figures 5.44 and 5.49, indicated that the model restored the fine line density values to the gross grain density level of the large area images (1 cycle/mm).

It is also interesting to note that the restoration algorithm had a greater effect on the extreme lines in the group than on the central lines. It appears that the combined group of lines behaved similar to a large area. The restoration algorithm not only restored the fine lines but also tended to remove the edge effect associated with a large area. The development activity must have been greater at the ends of the line pattern and became less or more depleted towards the center of the line pattern.

Line Image Restoration (19.56 - 39.82 cycles/mm). The restoration procedure was repeated for the line sets with spatial frequencies of 15.85 (2-3-(1-15)), 19.56 (2-4-(1-15)), 25.12 (2-5-(1-15)) and

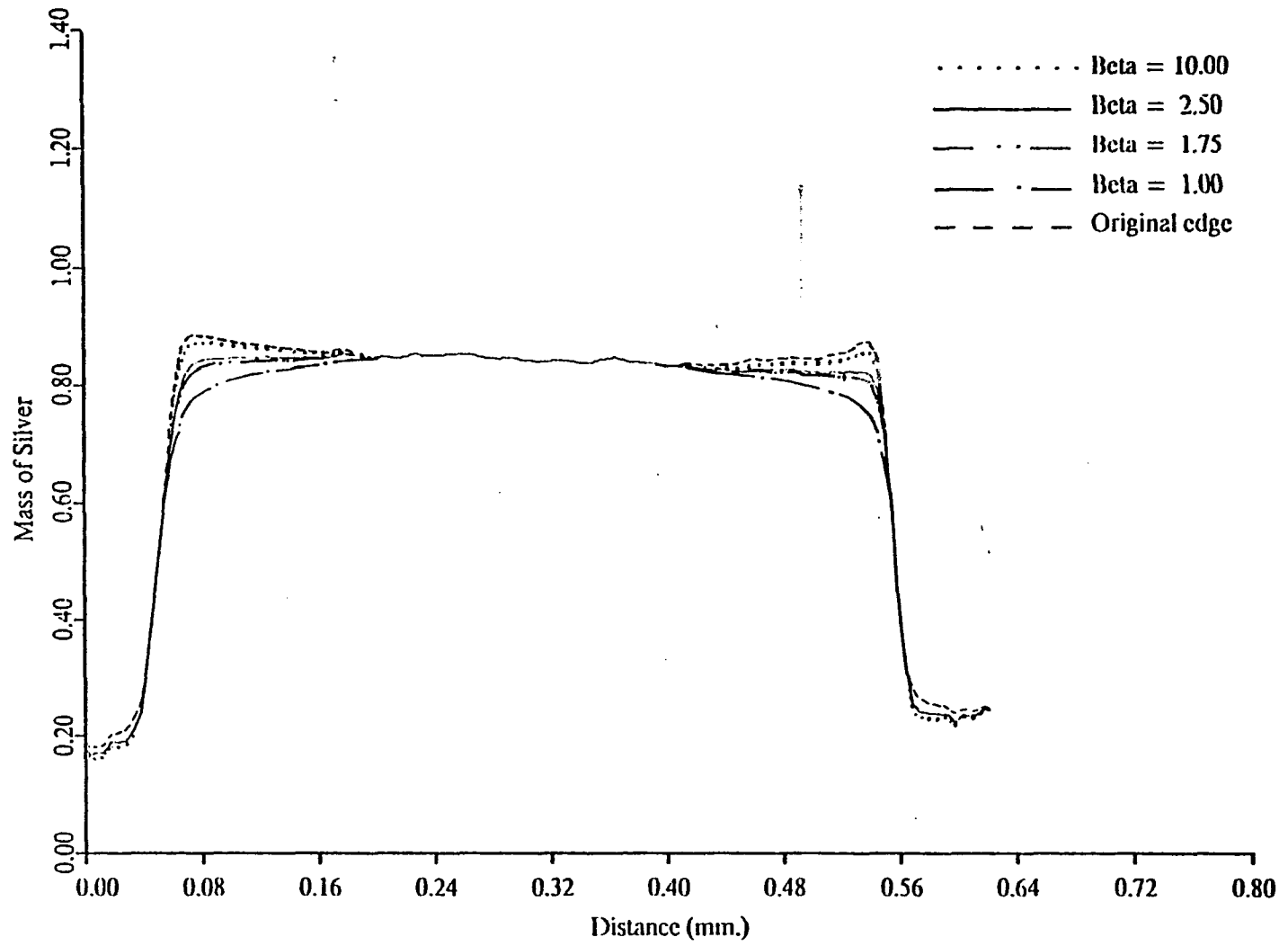


Fig. 5.41. Gross grain mass of silver for 0.5 mm. line width (line number 8) using several beta values..

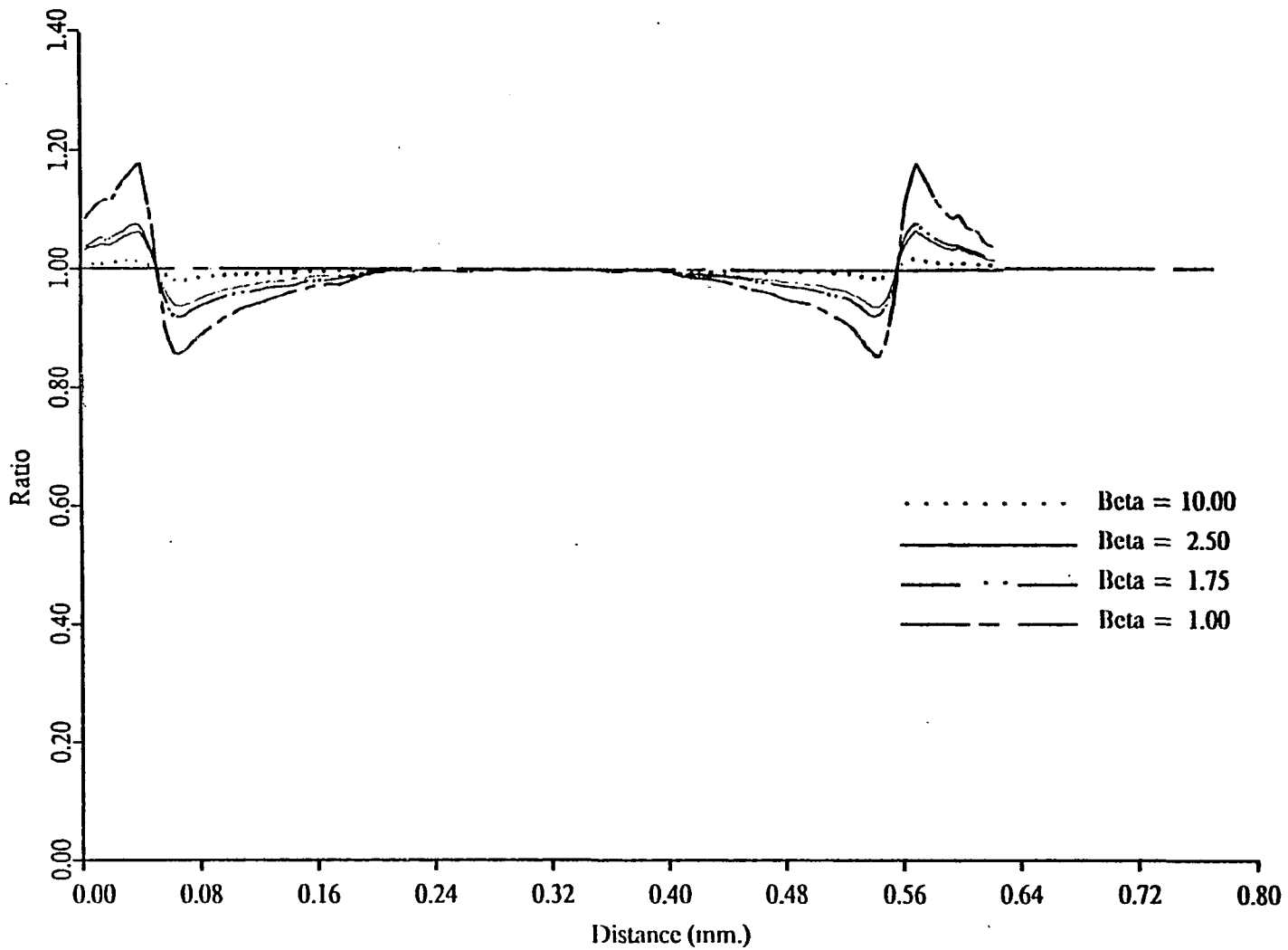


Fig. 5.42. Correction ratio for 0.5 mm. line width (line number 8) using several beta values.

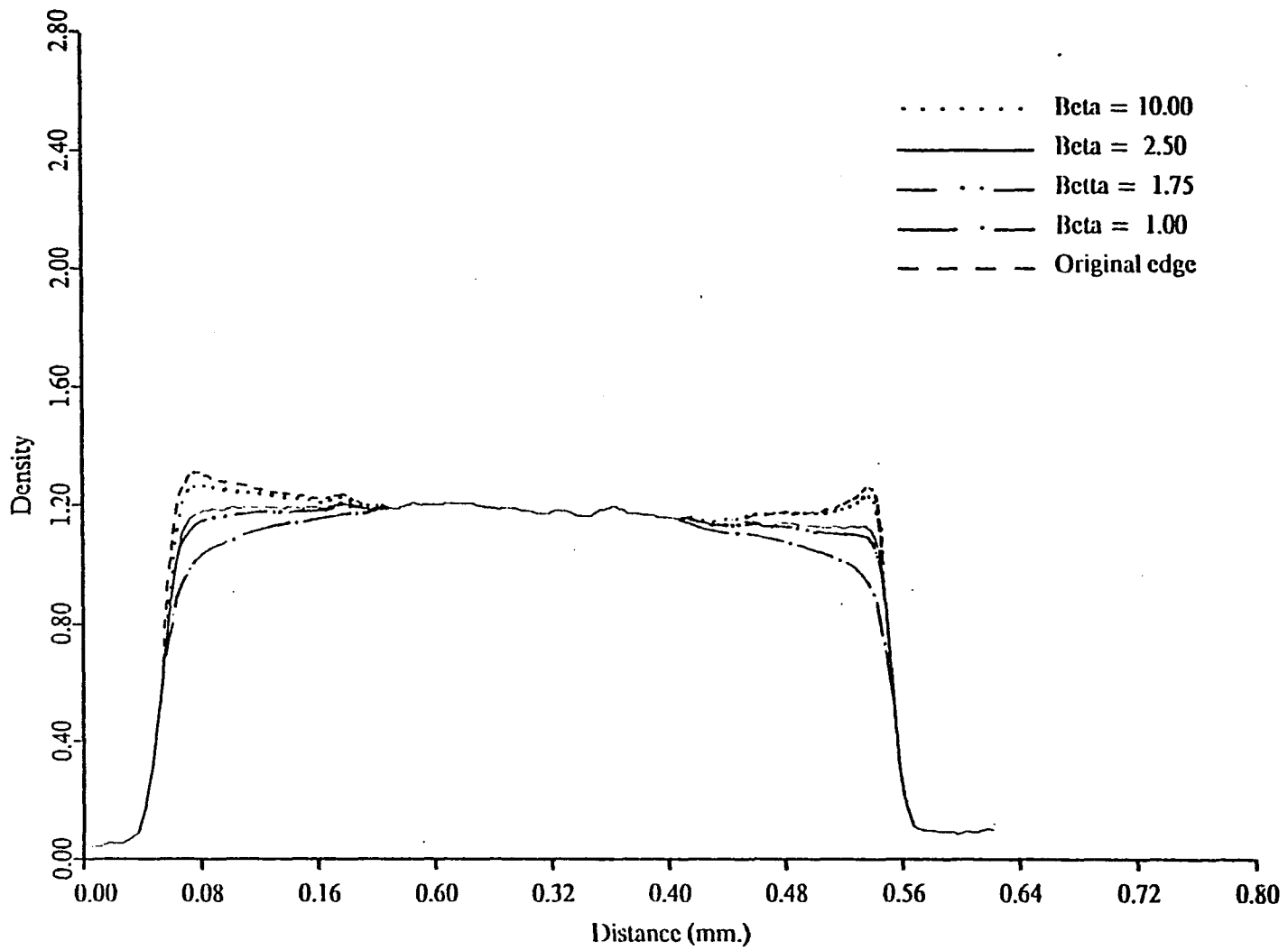


Fig. 5.43. Gross grain density for 0.5 mm. line width (line number 8) using several beta values.

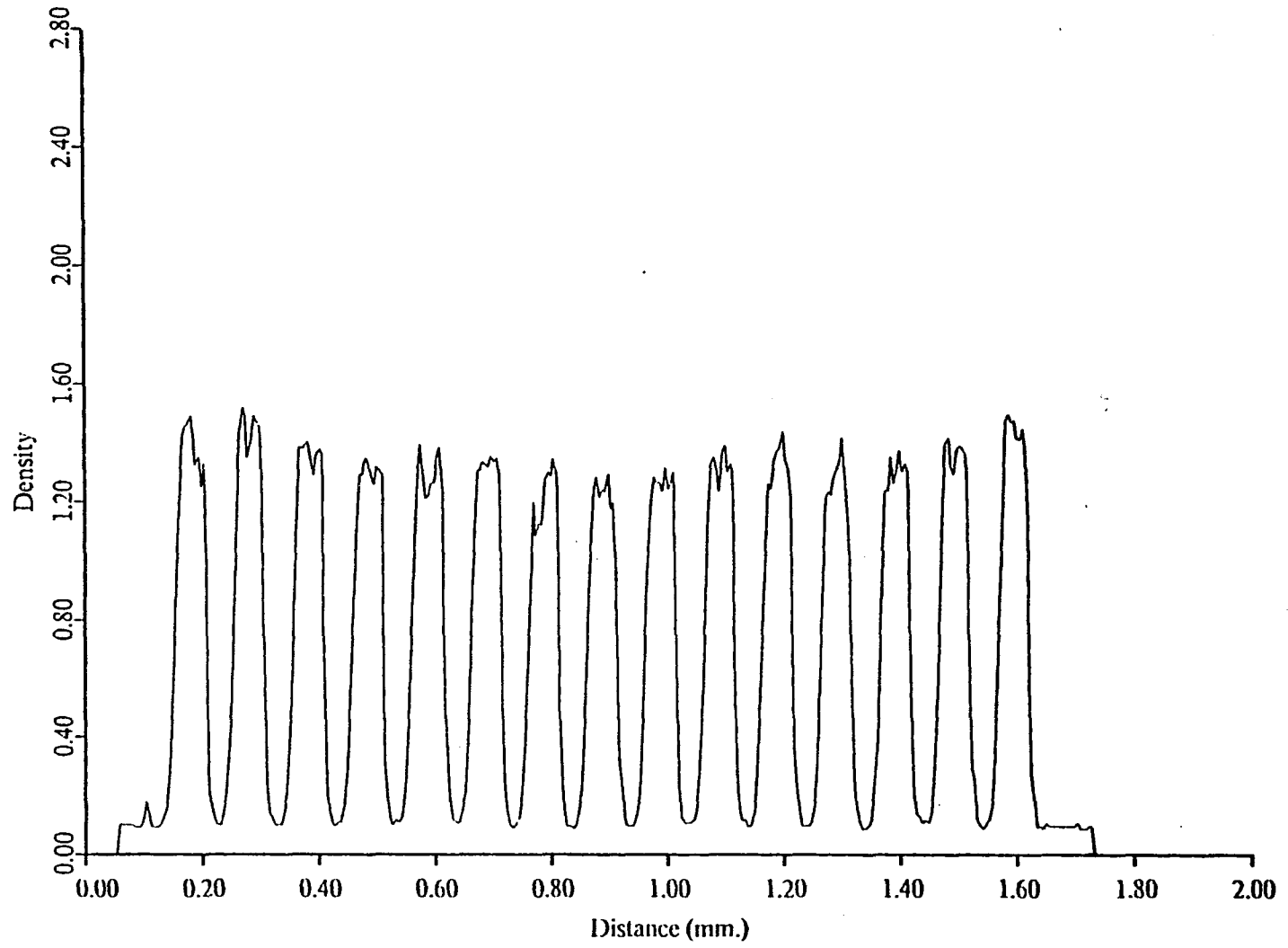


Fig. 5.44. Density profiles for 10 cycle/mm. line images.

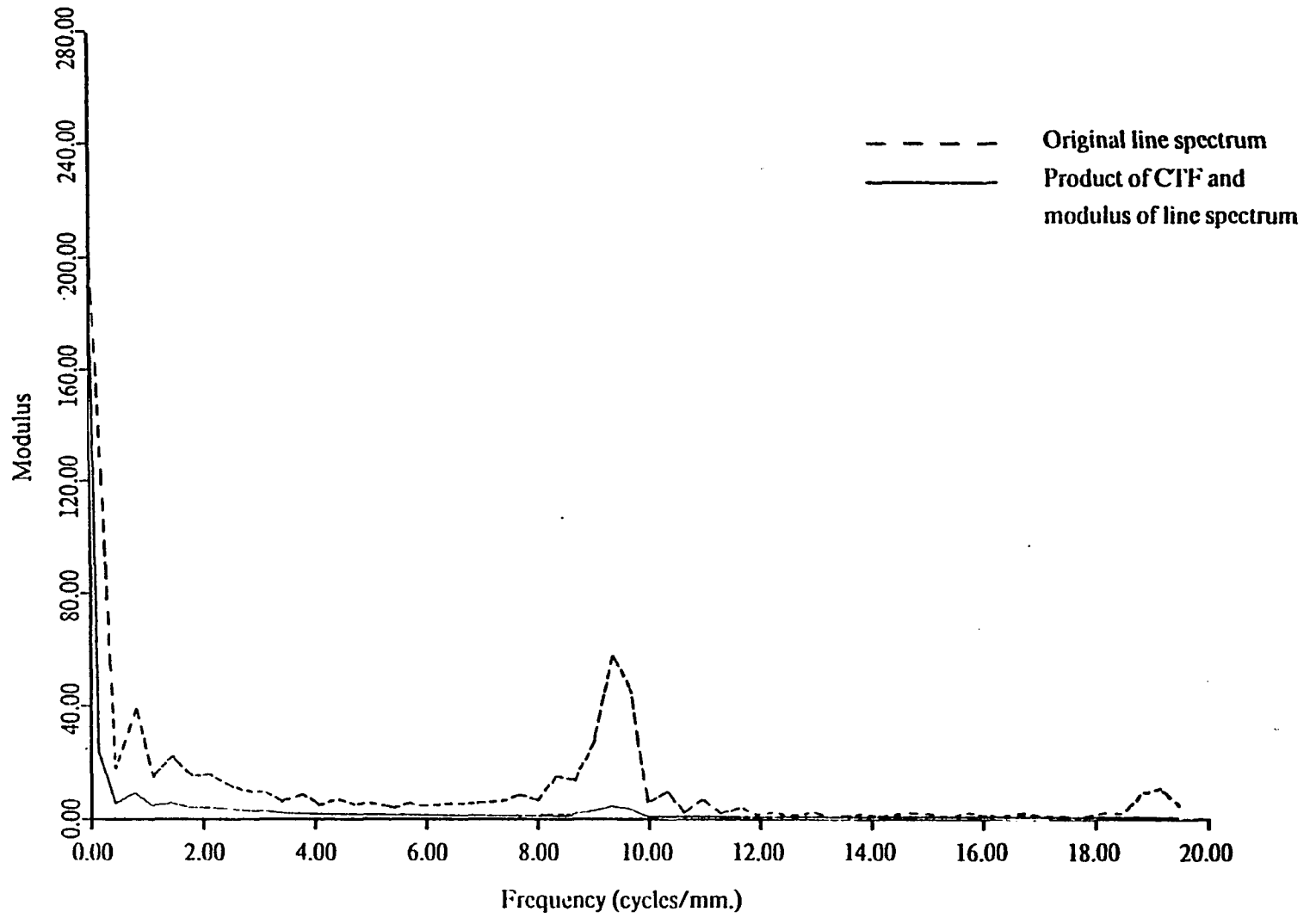


Fig. 5.45. Product of CTF modulus and input modulus (10 cycle/mm. line images).

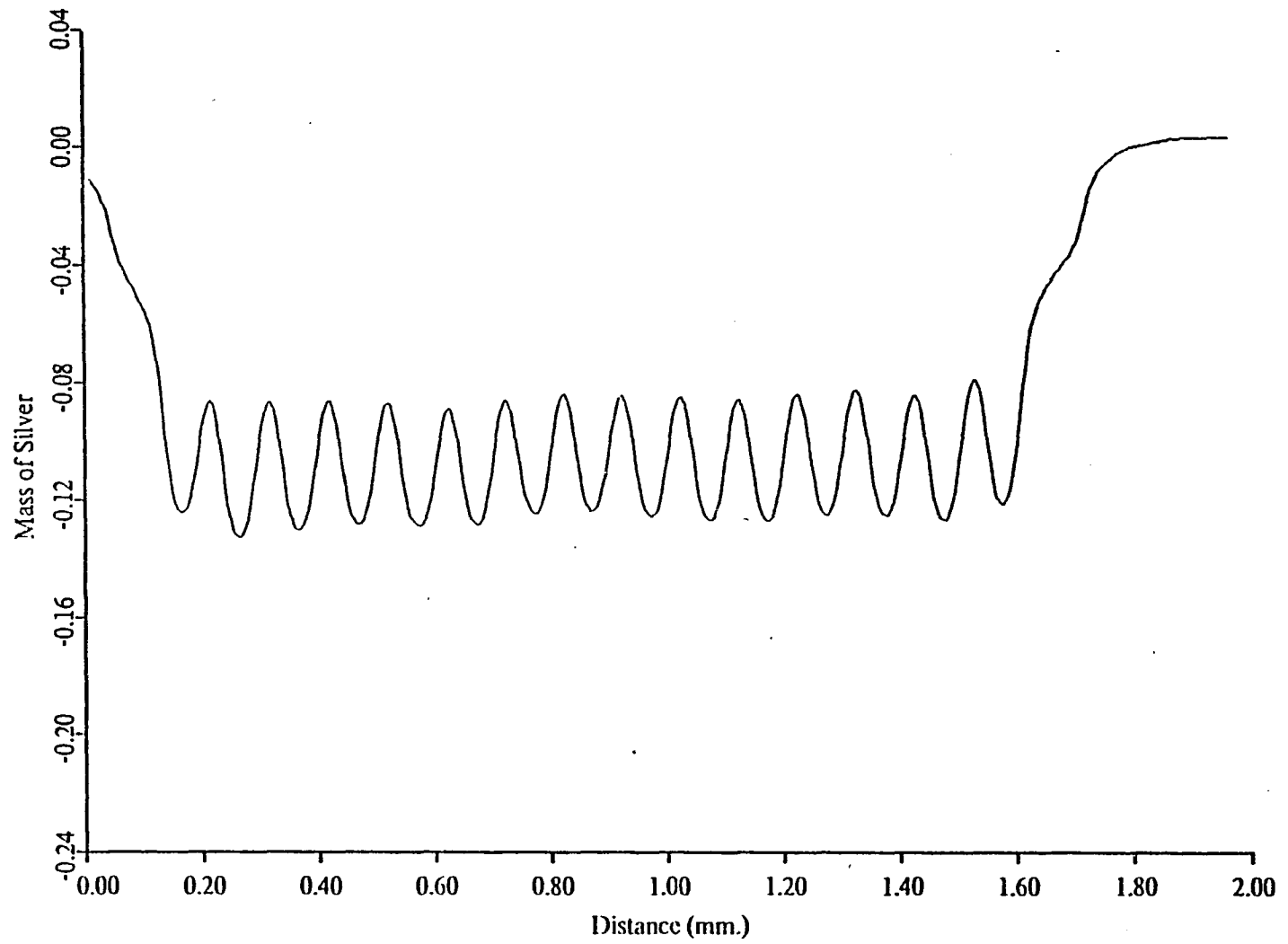


Fig. 5.46 Reduction product term for 10 cycle/mm. line images.

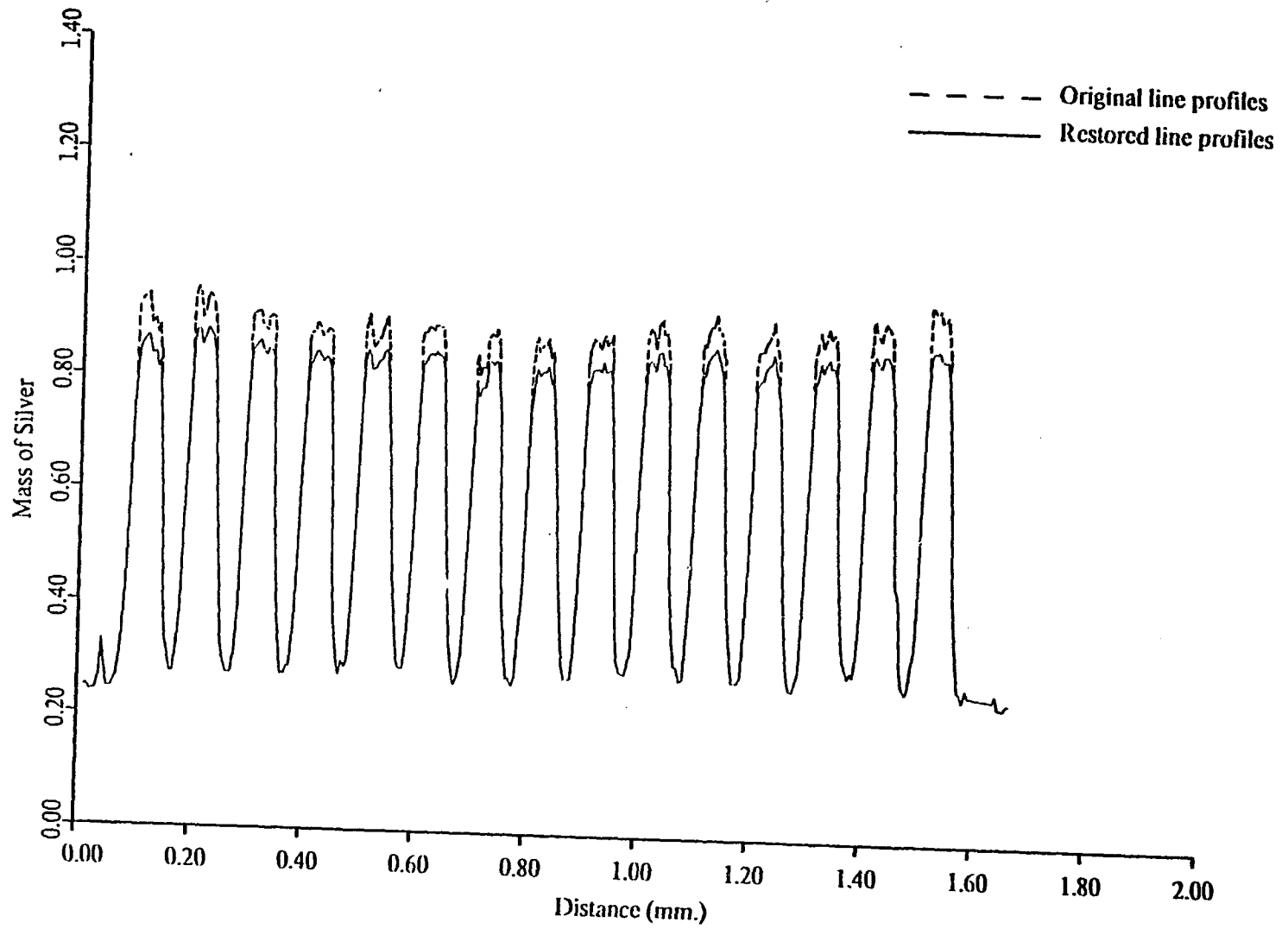


Fig. 5.47. Gross grain mass of silver for 10 cycle/mm. line images.

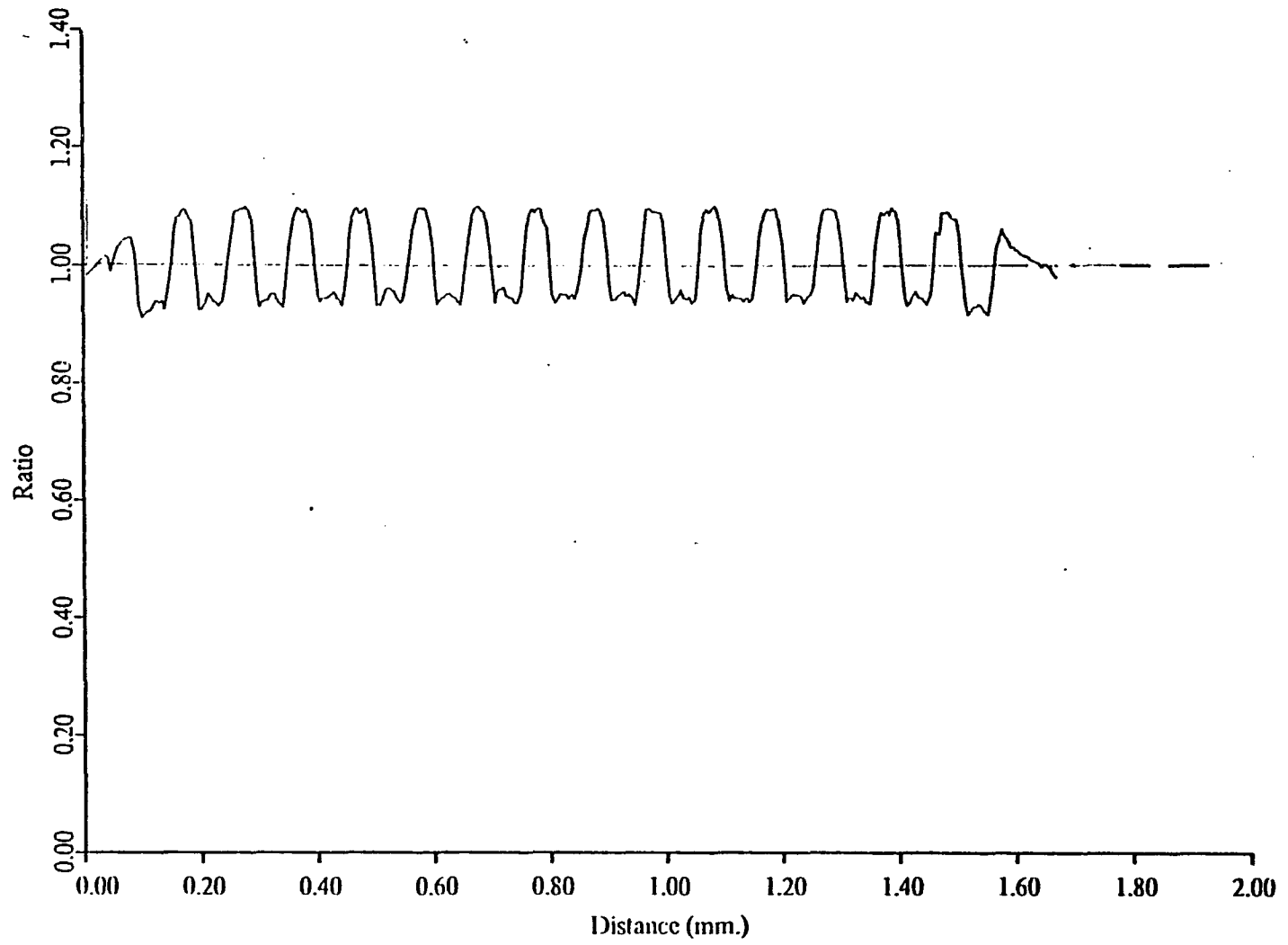


Fig. 5.48. Correction ratio for 10 cycle/mm. line images.

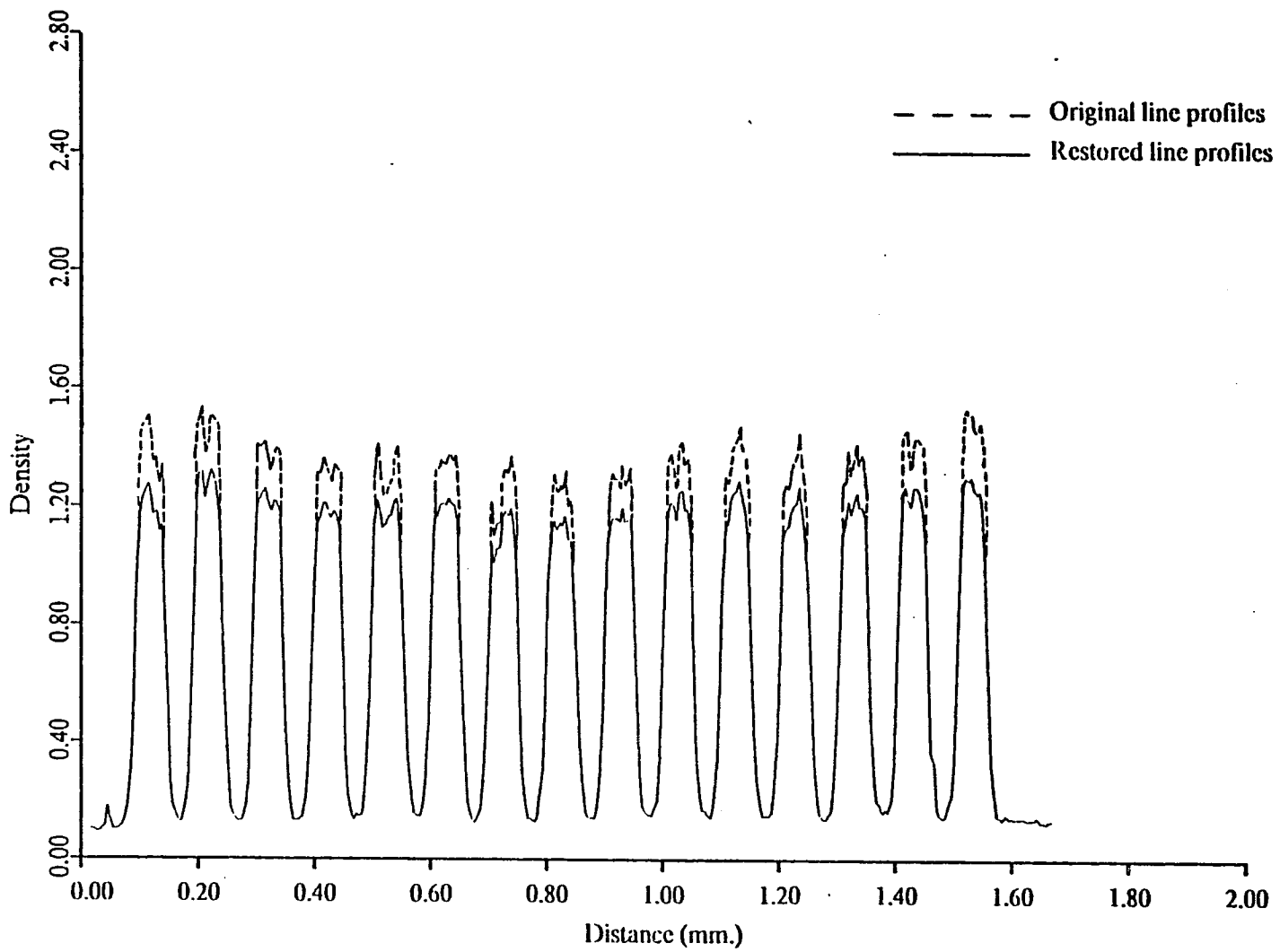


Fig. 5.49. Gross grain density for 10 cycle/mm. line images.

39.82 (2-7-(1-15)) cycles/mm. The final gross grain density restorations are illustrated in Figures 5.50 and 5.51. The line sets containing the three lowest spatial frequencies all had peak line density values which were restored to approximately the gross grain density level. The final restoration results for these line sets were quite similar to those obtained for the 10 cycle/mm line set.

The 39.83 cycle/mm line set, illustrated in Figure 5.51, was restored to a density level below that of the gross grain density level. Since initial line density values were near or below the gross grain density level this result was logical. The original density level of the line set was probably limited by the film transfer function which would have an amplitude of approximately 0.6 at 40 cycles/mm.

The density profile located between the 15.85 and 39.82 cycle/mm line sets, illustrated in Figure 5.51, results from a microdensitometer scan through the elements in group 3 of the high resolution target. Since the original target elements contained spatial frequency values ranging from 100 to 1000 cycles/mm the individual line images were not resolved. Note that the higher density peaks were slightly smoothed to lower density values.

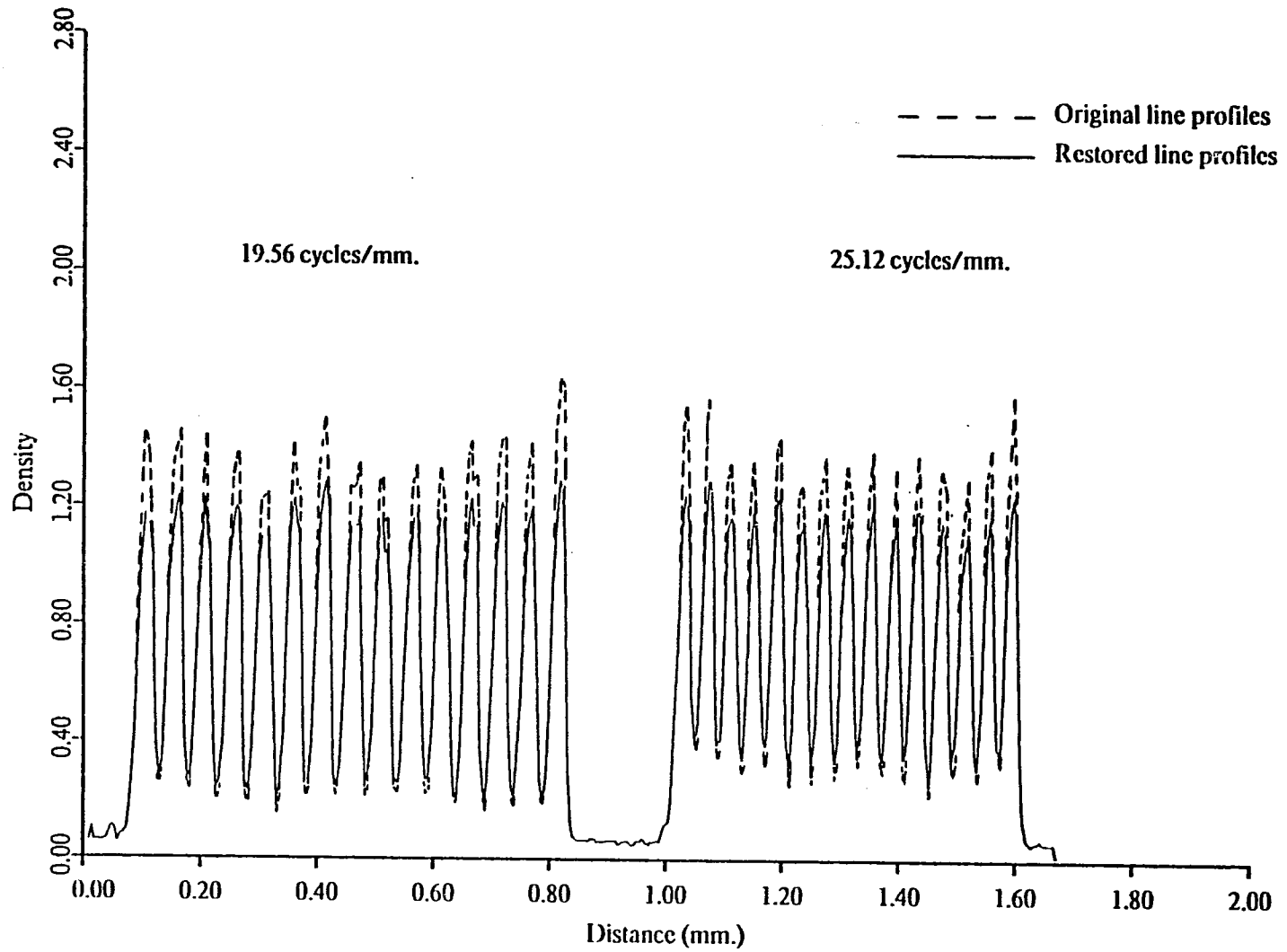


Fig. 5.50. Gross grain density for 19.56 and 25.12 cycle/mm. line images.

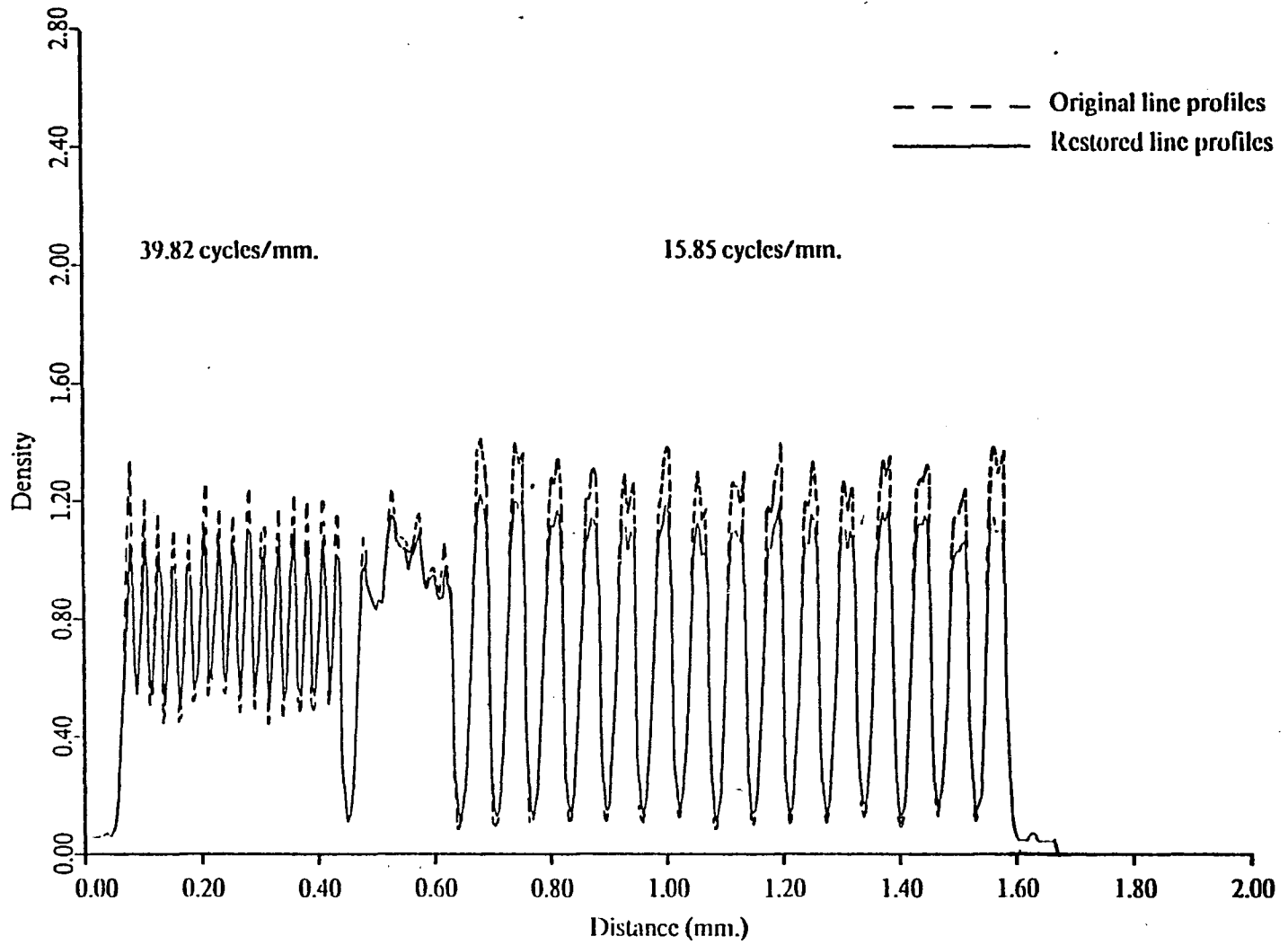


Fig. 5.51. Gross grain density for 15.85 and 39.82 cycle/mm. line images.

CHAPTER 6

CONCLUSIONS

The scope of this dissertation was concerned with the influence of adjacency effects on the restoration of noisy photographic images. The method of study was to review the theoretical development of a statistical restoration model (Burke, 1974) and to perform the first experimental application of this model to the removal of adjacency effects from selected photographic line images. The objective was the verification, including appropriate modification, of the statistical restoration model. The restoration results presented herein have verified that this objective has been satisfied. The statistical restoration model has successfully compensated for developer depletion and diffusion effects, i.e., adjacency effects, from several areas within a noisy photographic image. A scaling parameter, β , was used to reduce the smoothing effects of an empirically derived chemical spread function.

Summary of Results

The important results obtained during this investigation are outlined below. However, caution must be observed in the generalization of these results because they were derived from the application of the statistical restoration model to only one film-developer-process combination.

1. The first three steps of the restoration "recipe" have been successfully applied to the restoration of photographic line images with spatial frequency content ranging from approximately 1 through 40 cycles/mm. The results, summarized in Table 6.1, have indicated that peak edge and fine line density values have been restored to gross grain density levels and that the maximum magnitude of the restoration achieved was approximately 28 % of the gross grain density level.

Table 6.1. Restoration summary for magnitude of correction.

| Spatial Frequency (cycles/ mm.) | Density Correction (ΔD) | % Gross Grain Density ($\Delta D / G.G.D.$) | Descriptive Comments |
|---------------------------------------|---|---|-------------------------|
| 1.00 | 0.14 | 11.1 | Edge image |
| 10.00 | 0.15 - 0.23 | 12.8 - 18.2 | Line image |
| 15.85 | 0.14 - 0.35 | 11.7 - 28.3 | Line image |
| 19.56 | 0.14 - 0.36 | 14.4 - 27.8 | Line image |
| 25.12 | 0.16 - 0.24 | 14.4 - 20.7 | Line image |
| 39.82 | 0.09 - 0.28 | 8.8 - 26.3 | Line image |

Chemical spread function from edge number 5

Nominal gross grain density value (G.G.D.) = 1.20

$$\beta = 2.50 \quad A / \beta = 0.35$$

Note: ΔD and % G.G.D. calculations based on individual line density values. These were not necessarily the same as the nominal G.G.D. value.

Restoration of edge effects on large-area images were used to establish the scaling parameter required by the GGMSA. The edge effects were reduced by as much as 0.14 density units or 11% of the gross grain density level. Subsequent application of the GGMSA to fine line images resulted in density corrections ranging from approximately 0.14 to 0.36 density units, 8.8% to 28.3% correction, for line widths ranging from 0.500 mm to approximately 0.020 mm. Finer line images, approximately

0.0125 mm in width, were also restored but the magnitude of the restoration could not be measured since the restored peak line density values were below the gross grain density level.

2. Nelson's (1971) CSF and EE were calculated for Panatomic-X, processed without agitation in D-76 developer (diluted 1:1), at six different x-ray quanta exposure levels. The lack of development agitation was found to limit the peak edge and line density values, thus limiting the magnitude of both the CSF area values and the EE. The average values of the CSF area and the EE were, 0.673 and 0.866, respectively, for the four highest exposure levels. This limitation was emphasized through comparison to data estimated from previously published results (Nelson, 1971) using EE magnitude ratio values.

3. A magnitude estimate, MR, of the EE was derived from the theoretical restoration model and compared to an estimate, NR, based on Nelson's observations of previous data. The MR was shown to be a scaled version of NR yielding lower relative values. The scaling factor was the ratio of the gross grain mass of silver to the fine line mass of silver, g/f , for the condition that $\alpha = 1$.

The comparison of the MR values to the CSF area values, calculated using Eq. (5.1), indicated that the CSF area values were significantly greater by a factor ranging from 1.75 to 2.5. Use of this proportionality factor, β , in the restoration algorithm, GGMSA, indicated that adjacency effects were successfully removed over this entire range. Based on this observation, the average value of the CSF area required by the statistical model for this film-developer combination was $A = 0.346$ (assuming $\beta = 2.5$).

The use of this scaling factor did not alter the functional form of the statistical model given by Eq. 2.8. However, the implications in the comparison to Nelson's (1971) forward model, given by Eq. (2.21) and Eq. (2.22), are that $A = B/\beta$ for $\alpha = 1$. The constant of proportionality, β , was used to scale the CSF, rather than α as described in these equations. This allowed α to remain at or near unity so that a large number of grains, αf_i , were not developed in the absence of adjacency effects.

A value of $\alpha f_1 = 2.5$ did not appear to be reasonable. Additional verification of this technique would be required before any generalized statement could be set forth.

4. The study included the first known application of segmented polynomials (cubic spline functions) to the investigation of adjacency effects. This is significant because the application of the cubic spline function can be extended to the investigation of the entire edge effect. A more accurate estimate of the apparent MTF might be obtained due to the greater accuracy of the analytic piecewise fit and the inherent edge noise reduction properties of an analytic function.

Experimental Error Sources

1. The largest potential contributor to error in the analysis of this data was the diffuse density nonuniformity of the film caused by lack of agitation in the development process. The maximum measured density nonuniformity was found to be 0.27 at the maximum gross grain density level of a sensitometric step tablet image. Great care was taken to avoid these areas of nonuniformity during the selection of all images analyzed in this study. The largest standard deviation observed in the large-area specular density value was 0.43, as given in Table 4.3. Although nonuniformities did not appear to exist in the fine line images, this was not statistically verified due to the difficulty in separating them from nonlinear diffusion and depletion effects.

2. The measured specular density values were not corrected for the microdensitometer OTF. The most significant error would have been for the high resolution target images scanned with a 0.005 mm circular aperture. From the spatial frequency content of the line images selected for restoration, less than 40 cycles/mm, a maximum attenuation of 7 % could have occurred. However, the bandwidth of the CTF filter was of the order of 10 cycles /mm which would have reduced the attenuation error to less than 2%.

3. The noise associated with the edge data used for the calculation of the CSF had an insignificant impact on the results. First, the analytic cubic spline function smoothed the noise;

second, variations in the CSF, larger than potential noise errors, were shown to have a relatively minor effect on the restoration of the images. No attempt was made to smooth or reduce the noise that existed in the photographic line images beyond the smoothing properties of the convolution process required by the GGMSA. The intent of the model was to remove the adjacency effects from images in the presence of noise and perform noise reduction in the optical scattering statistical estimation stage. A review of the restored images will verify that the spatial frequency noise, relatively high with respect to the CTF bandlimit, had little effect on the algorithm.

Recommendations

The first four recommendations regarding future application of this model are based on problems encountered during the analysis of the experimental data and observations made during the review of the literature. The last, and potentially very important, is based on the application of this statistical approach to nonsilver photoconductive materials.

1. The lack of development agitation provided large adjacency effects at relatively low exposure levels. However, it also created large areas of density nonuniformity and a limitation on maximum density values obtained. The application of this model should be considered for a film-development process using development agitation. Several film-development combinations might be considered including viscous development which exhibits significantly large adjacency effects. Such an investigation would provide additional insight into the relationship between the EE and the CSF area value required by the statistical model. A generalized relationship might then be verified.

2. The limits of the model should be investigated for photographic images containing variable levels of signal-to-noise ratios. This would provide the insight from which one could determine the relative importance of addressing the removal of adjacency effects as part of the restoration process. Adjacency effects would not be as important at very low signal-to-noise ratios.

3. The application of all five stages of the restoration "recipe" should be considered for the restoration of noisy two-dimensional images. This could be related to a psychophysical investigation of image quality for given targets or a photointerpretation measurement task using low contrast aerial images.

4. A controlled experiment should be performed to compare the range of application of the two known adjacency effect inversion models. A systematic comparison should be made between the statistical restoration model and the Eikonix inverse diffusion model (Silevitch, Gonsalves and Ehn, 1977) for a variety of film-developer combinations, noise attributes and image types.

5. The statistical restoration methods used to derive the present restoration model should be applied to photoconductive and electrophotographic films and photoreceptor coatings. These materials are capable of exhibiting image properties representative of photographic images which contain very large amounts of adjacency effect. They also encompass a wide range of signal-to-noise level depending upon the specific photosensitive material and the properties of the liquid/solid developer applied to the material.

APPENDIX A

U.M.L.E. OF THE IDEAL IMAGE

An estimate of the ideal image, $\hat{\sigma}$, is obtained from the probability density function (p.d.f.) of the ideal image, $P(\hat{\sigma})$, and the conditional p.d.f. of the exposure image, $P(\hat{\epsilon}/\langle\hat{\epsilon}\rangle)$. The estimate is obtained through application of an Unconditional Maximum Likelihood Estimator (U.M.L.E.). The ideal and exposure p.d.f. given by Eq. (2.3) and Eq. (2.4) are

$$P(\hat{\sigma}) = \prod_k ((\exp\{-\langle\sigma_k\rangle\} \langle\sigma_k\rangle^{\sigma_k}) / \sigma_k!) \quad (\text{A.1})$$

$$P(\hat{\epsilon}/\langle\hat{\epsilon}\rangle) = P(\hat{\epsilon}) = \prod_j ((\exp\{-\langle\epsilon_j\rangle\} \langle\epsilon_j\rangle^{\epsilon_j}) / \epsilon_j!) \quad (\text{A.2})$$

where

$$\langle\epsilon_j\rangle = \beta \sum_k S_{jk} \sigma_k$$

An U.M.L.E. of $\hat{\sigma}$, given $\hat{\epsilon}$, is that $\hat{\sigma} = \hat{\sigma}^*$. It maximizes the joint p.d.f. of $\hat{\epsilon}$ and $\hat{\sigma}$ through setting its partial derivative with respect to σ_k equal to zero.

$$\begin{aligned} P(\hat{\epsilon}, \hat{\sigma}) &= P(\hat{\epsilon}/\hat{\sigma}) P(\hat{\sigma}) = \text{maximum} \\ \partial / \partial \sigma_k [P(\hat{\epsilon}, \hat{\sigma}) P(\hat{\sigma})]_{\sigma_k = \sigma_k^*} &= 0 \end{aligned} \quad (\text{A.3})$$

Rather than maximizing $P(\hat{\epsilon}, \hat{\sigma})$ itself, we maximize its natural logarithm, which obtains a maximum value for the same $\hat{\sigma}$ as $P(\hat{\epsilon}, \hat{\sigma})$.

$$\begin{aligned} \ln P(\hat{\epsilon}/\langle\hat{\epsilon}\rangle) &= \sum_{j=1}^J (-\langle\epsilon_j\rangle + \epsilon_j \ln \langle\epsilon_j\rangle - \ln \epsilon_j!) \\ \partial / \partial \sigma_k [\ln P(\hat{\epsilon}/\hat{\sigma})] &= \sum_{j=1}^J (-\partial / \partial \sigma_k \langle\epsilon_j\rangle + (\epsilon_j / \langle\epsilon_j\rangle) \partial \langle\epsilon_j\rangle / \partial \sigma_k) \\ &= \sum_{j=1}^J ((\epsilon_j - \langle\epsilon_j\rangle) / \langle\epsilon_j\rangle) \partial \langle\epsilon_j\rangle / \partial \sigma_k \end{aligned} \quad (\text{A.4})$$

$$\ln P(\hat{\sigma}) = \sum_{k=1}^K (-\langle \sigma_k \rangle + \sigma_k \ln \langle \sigma_k \rangle - \ln \sigma_k!) \quad (\text{A.5})$$

Using Stirling's approximation for $\ln \sigma_k!$

$$\ln \sigma_k! = -\sigma_k \ln \sigma_k + \sigma_k \quad (\text{A.6})$$

and inserting into Eq. (A.5) we obtain

$$\begin{aligned} \partial / \partial \sigma_k [\ln P(\hat{\sigma})] &= \sum_{k=1}^K (\ln \langle \sigma_k \rangle \partial \sigma_k / \partial \sigma_k - \sigma_k (1 / \sigma_k) \partial \sigma_k / \partial \sigma_k \\ &\quad - \ln \sigma_k \partial \sigma_k / \partial \sigma_k + \partial \sigma_k / \partial \sigma_k) \\ &= (\ln \langle \sigma_k \rangle - \ln \sigma_k) \\ &= \ln (\langle \sigma_k \rangle / \sigma_k) \text{ for } k = k \end{aligned} \quad (\text{A.7})$$

Taking Eq. (A.4) and Eq. (A.7) and equating to satisfy Eq. (A.3) we obtain

$$\ln (\sigma_k / \langle \sigma_k \rangle) = \sum_{j=1}^J ((\epsilon_j - \langle \epsilon_j \rangle) / \langle \epsilon_j \rangle) \partial \langle \epsilon_j \rangle / \partial \sigma_k \quad (\text{A.8})$$

where

$$\partial \langle \epsilon_j \rangle / \partial \sigma_k = \partial / \partial \sigma_k (\beta \sum_k s_{jk} \sigma_k) = \beta s_{jk}$$

Therefore, the U.M.L.E. of the ideal image, σ_k^* , is

$$\sigma_k^* = \langle \sigma_k \rangle \exp \{ -\beta \sum_j [(\epsilon_j - \langle \epsilon_j \rangle) / \langle \epsilon_j \rangle] s_{jk} \} \quad (\text{A.9})$$

where

$$\langle \epsilon_j \rangle = \beta \sum_l s_{jl} \sigma_l^*$$

APPENDIX B

RMS ERROR OF THE IDEAL IMAGE

The root-mean-square error (R.M.S.E.) associated with the most likely estimate, $\langle \sigma_k \rangle$, of the ideal image, σ_k , is derived assuming Poisson statistics.

$$\begin{aligned} \text{M. S. E.} &= E \{ [\sigma_k - \langle \sigma_k \rangle]^2 \} \\ &= E \{ \sigma_k^2 - 2\sigma_k \langle \sigma_k \rangle + \langle \sigma_k \rangle^2 \} \\ &= \langle \sigma_k \rangle^2 - 2\langle \sigma_k \rangle^2 + \langle \sigma_k \rangle^2 = \langle \sigma_k^2 \rangle - \langle \sigma_k \rangle^2 \\ \text{R. M. S. E.} &= (\langle \sigma_k^2 \rangle - \langle \sigma_k \rangle^2)^{1/2} \end{aligned} \tag{B.1}$$

but, in general the variance is

$$\text{VARIANCE} = E \{ X^2 \} - E \{ X \}^2 = \langle X^2 \rangle - \langle X \rangle^2 \tag{B.2}$$

thus

$$\text{R. M. S. E.} = (\text{VARIANCE})^{1/2} \tag{B.3}$$

Since, for a Poisson process, the mean and the variance are equal

$$\text{VARIANCE} = \langle \sigma_k \rangle \tag{B.4}$$

and

$$\text{R. M. S. E.} = (\text{VARIANCE})^{1/2} = (\langle \sigma_k \rangle)^{1/2} = \sigma_k^{1/2} \tag{B.5}$$

APPENDIX C

U. M. L. E. OF THE LATENT IMAGE

An U.M.L.E. is obtained for the latent image, f_k , from the conditional p.d.f., $P(\hat{m}/\hat{f})$, and the p.d.f. of the latent image, $P(\hat{f})$, assuming Poisson statistics.

The required conditional p.d.f. of the measured grain density given the latent image and the p.d.f. of the latent image, from Eq. (2.12) and Eq. (2.13), can be stated as

$$\begin{aligned} P(\hat{m}/\hat{f}) &= \prod_{i=1}^M P(m_i/\langle m_i(\hat{f}) \rangle) \\ &= \prod_{i=1}^M (\exp \{ -\langle m_i \rangle \} \langle m_i \rangle^{m_i} / m_i!) \end{aligned} \quad (C.1)$$

$$P(\hat{f}) = \prod_{k=1}^N (\exp \{ -\langle f_k \rangle \} \langle f_k \rangle^{f_k} / f_k!) \quad (C.2)$$

To obtain the estimate we must find the \hat{f}^* which maximizes

$$P(\hat{m}, \hat{f}) = P(\hat{f}) P(\hat{m}/\hat{f}) = \text{maximum} \quad (C.3)$$

Following the procedure of Appendix A, we form the partial derivatives of Eq. (C.3) with respect to each f_j and equate them to zero.

$$\partial / \partial f_j [P(\hat{f}) P(\hat{m}/\hat{f})] = 0 \quad (C.4)$$

Since $\ln P(\hat{m}, \hat{f})$ becomes a maximum for the same \hat{f} value as Eq. (C.3), we use it to simplify the procedure. Thus,

$$\begin{aligned} \ln P(\hat{m}/\hat{f}) &= \sum_{i=1}^M (-\langle m_i \rangle + m_i \ln \langle m_i \rangle - \ln (m_i!)) \\ \partial / \partial f_k [\ln P(\hat{m}/\hat{f})] &= \sum_{i=1}^M (-\partial \langle m_i \rangle / \partial f_k \\ &\quad + m_i (1 / \langle m_i \rangle) \partial \langle m_i \rangle / \partial f_k) \end{aligned} \quad (C.5)$$

$$\partial / \partial f_k [\ln P(\hat{m} / \hat{f})] = \sum_{i=1}^M (-1 + m_i / \langle m_i \rangle) \partial \langle m_i \rangle / \partial f_k \quad (C.6)$$

$$\ln P(\hat{f}) = \sum_{k=1}^N (-\langle f_k \rangle + f_k \ln \langle f_k \rangle - \ln f_k!) \quad (C.7)$$

Using Stirling's approximation for $\ln f_k!$

$$\ln f_k! = f_k \ln f_k + f_k \quad (C.8)$$

and inserting into Eq. (C.7) and taking the partial derivatives we obtain

$$\begin{aligned} \partial / \partial f_k [\ln P(\hat{f})] &= \sum_{k=1}^N (\ln \langle f_k \rangle \partial f_k / \partial f_k - f_k (1 / f_k) \partial f_k / \partial f_k \\ &\quad - \ln f_k \partial f_k / \partial f_k + \partial f_k / f_k) \\ &= \sum_{k=1}^N (\ln \langle f_k \rangle - \ln f_k) \\ &= \ln (\langle f_k \rangle / f_k) \text{ for } k = k \end{aligned} \quad (C.9)$$

Now, inserting Eq. (C.6) and Eq. (C.9) into Eq. (C.3) we obtain

$$\begin{aligned} \sum_{i=1}^M ((m_i - \langle m_i \rangle) / \langle m_i \rangle) \partial \langle m_i \rangle / \partial f_k + \ln (\langle f_k \rangle / f_k) &= 0 \\ - \ln (\langle f_k \rangle / f_k) &= \sum_{i=1}^M ((m_i - \langle m_i \rangle) / \langle m_i \rangle) \partial \langle m_i \rangle / \partial f_k \\ \ln (f_k / \langle f_k \rangle) &= \sum_{i=1}^M ((m_i - \langle m_i \rangle) / \langle m_i \rangle) \partial \langle m_i \rangle / \partial f_k \end{aligned} \quad (C.10)$$

which for $f_k = f_k^*$ we obtain the vector f_k^* that maximizes $P(\hat{f}, \hat{m})$.

$$f_k^* = \langle f_k \rangle \exp \left\{ \sum_{i=1}^M ((m_i - \langle m_i \rangle) / \langle m_i \rangle) \partial \langle m_i \rangle / \partial f_k \right\} \quad (C.11)$$

APPENDIX D

DERIVATION OF DIFFERENTIAL MEAN GRAIN DENSITY

An explicit expression is derived for the rate of change of the measured mean grain density with respect to the individual components of the latent image, $\partial \langle m_i \rangle / \partial f_k$. Using Eq. (2.8)

$$\langle m_i \rangle = f_i (\alpha - \sum_j A_{ij} \langle m_j \rangle) \quad (D.1)$$

we find

$$\begin{aligned} \partial \langle m_i \rangle / \partial f_k &= \delta_{ik} (\alpha - \sum_j A_{ij} \langle m_j \rangle) - f_i \sum_j A_{ij} \partial \langle m_j \rangle / \partial f_k \\ D_{ik} &= \delta_{ik} (\alpha - \sum_j A_{ij} \langle m_j \rangle) - f_i \sum_j A_{ij} D_{jk} \end{aligned} \quad (D.2)$$

This can be rewritten in terms of the matrices

$$\begin{aligned} D &= [D_{ik}] \\ C &= [\delta_{ik} (\alpha - \sum_j A_{ij} \langle m_j \rangle)] \\ B &= [f_i A_{ij}] \end{aligned} \quad (D.3)$$

which, when combined with Eq. (D.2) provide

$$D = C - BD \quad (D.4)$$

By factoring the matrix D and defining I as an identity matrix, this simplifies to

$$C = (I + B) D \quad (D.5)$$

Solving for D, we obtain the differential mean grain density in terms of the inverse relationship

$$D = (I + B)^{-1} C \quad (D.6)$$

which can be expanded in terms of a binomial series

$$(I + B)^{-1} C = (I - B + B^2 - B^3 + \dots) C \quad (D.7)$$

The magnitude of B is a function of the subscript j during the convolution of the chemical spread function A_{ij} with the differential mean grain density. The absolute value of B must be smaller for values of $j \neq i$ than for $j = i$ since the chemical spread function is only centered at i for $j = i$.

$$f_i A_{ij} \leq f_i A_{ii} \quad (D.8)$$

In addition, the absolute magnitude of $A_{ij} \ll 1$ so that $A_{ij} f_i < 1$. Thus, only the low order terms of Eq. (D.7) can have significant magnitude. Matrix D becomes

$$D = C - BC \quad (D.9)$$

Combining Eq. (D.2) and Eq. (D.9)

$$\begin{aligned} D_{ik} &= \delta_{ik} (\alpha - \sum_j A_{ij} \langle m_j \rangle) - \sum_j B_{ij} C_{jk} \\ &= \delta_{ik} (\alpha - \sum_j A_{ij} \langle m_j \rangle - \sum_i f_i A_{ij} (\delta_{ik} (\alpha - \sum_l A_{jl} \langle m_l \rangle))) \\ &= \delta_{ik} (\alpha - \sum_j A_{ij} \langle m_j \rangle) - \sum_i f_i A_{ij} (\delta_{ik} \langle m_j \rangle / f_j) \end{aligned} \quad (D.10)$$

where the δ_{jk} eliminates all terms except $j = k$ to yield

$$D_{ik} = \delta_{ik} (\alpha - \sum_j A_{ij} \langle m_j \rangle - f_i A_{ik} \langle m_k \rangle / f_k) \quad (D.11)$$

Combining with Eq. (D.1) the differential mean grain density becomes

$$\begin{aligned}
\partial \langle m_i \rangle / f_k &= \delta_{ik} (\alpha - \sum_j A_{ij} \langle m_j \rangle) \\
&\quad - A_{ik} (\langle m_i \rangle (\alpha - \sum_j A_{kj} \langle m_j \rangle) / (\alpha - \sum_j A_{ij} \langle m_j \rangle)) \\
&= \delta_{ik} (\alpha - \sum_j A_{ij} \langle m_j \rangle) \\
&\quad - A_{ik} \langle m_i \rangle (\alpha - \sum_j A_{kj} \langle m_j \rangle) / (\alpha - \sum_j A_{ij} \langle m_j \rangle)
\end{aligned} \tag{D.12}$$

Inserting into Eq. (2.14) the U.M.L.E. f_k^* reduces to

$$\begin{aligned}
f_k^* &= \langle f_k \rangle \exp \left\{ \sum_i ((m_i - \langle m_i \rangle) / \langle m_i \rangle) \partial \langle m_i \rangle / \partial f_k \right\}_{f_k = f_k^*} \\
f_k^* &= \langle f_k \rangle \exp \left\{ \sum_i ((m_i - \langle m_i \rangle) / \langle m_i \rangle) \left(\delta_{ik} (\alpha - \sum_j A_{ij} \langle m_j \rangle) \right. \right. \\
&\quad \left. \left. - A_{ik} \langle m_i \rangle (\alpha - \sum_j A_{kj} \langle m_j \rangle) / (\alpha - \sum_j A_{ij} \langle m_j \rangle) \right) \right\} \\
f_k^* &= \langle f_k \rangle \exp \left\{ \sum_i \left(\delta_{ik} (\alpha - \sum_j A_{ij} \langle m_j \rangle) (m_i - \langle m_i \rangle) / \langle m_i \rangle \right. \right. \\
&\quad \left. \left. - \sum_j A_{ik} \langle m_i \rangle (\alpha - \sum_j A_{kj} \langle m_j \rangle) / (\alpha - \sum_j A_{ij} \langle m_j \rangle) \right) \right. \\
&\quad \left. (m_i - \langle m_i \rangle) / \langle m_i \rangle \right\} \\
f_k^* &= \langle f_k \rangle \exp \left\{ (\alpha - \sum_j A_{kj} \langle m_j \rangle) (m_k - \langle m_k \rangle) / \langle m_k \rangle \right. \\
&\quad \left. - (\alpha - \sum_j A_{kj} \langle m_j \rangle) \sum_i A_{ik} (m_i - \langle m_i \rangle) / (\alpha - \sum_j A_{ij} \langle m_j \rangle) \right\}
\end{aligned} \tag{D.13}$$

to obtain Eq. (2.16), the most likely latent image estimate, f_k^* .

$$\begin{aligned}
f_k^* &= \langle f_k \rangle \exp \left\{ (\alpha - \sum_j A_{kj} \langle m_j \rangle) [(m_k - \langle m_k \rangle) / \langle m_k \rangle] \right. \\
&\quad \left. - \sum_i (m_i - \langle m_i \rangle) A_{ik} / (\alpha - \sum_j A_{ij} \langle m_j \rangle) \right\}
\end{aligned} \tag{D.14}$$

APPENDIX E

THEORETICAL COMPARISON TO NELSON'S MODEL

A comparison is given between the statistical restoration model and Nelson's model. Based on the initial relationships of the statistical model, as derived in Chapter 2, it is shown that the lower order terms of the statistical model are in agreement with Nelson's model. In addition, it is probable that the higher order terms associated with the statistical model make it more accurate than Nelson's for higher contrast images.

From Eq. (2.10)

$$\langle m_i \rangle = \langle g_i \rangle (\alpha - \sum_j A_{ij} \langle m_j \rangle) / (\alpha - A \langle g_i \rangle) \quad (\text{E.1})$$

reorganizing in terms of A/α

$$\langle m_i \rangle = \langle g_i \rangle (1 - \sum_j (A_{ij}/\alpha) \langle m_j \rangle) / (1 - (A/\alpha) \langle g_i \rangle) \quad (\text{E.2})$$

and multiplying through by the denominator $(1 + (A\alpha) \langle g_i \rangle)$

$$\langle m_i \rangle = \langle g_i \rangle (1 + (A/\alpha) \langle g_i \rangle) (1 - \sum_j (A_{ij}/\alpha) \langle m_j \rangle) / (1 - ((A/\alpha) \langle g_i \rangle)^2) \quad (\text{E.3})$$

Now, for low to moderate density profiles, such that the adjacency effects are low, we can assume that $A \langle g_i \rangle < \alpha$ providing

$$(1 - ((A/\alpha) \langle g_i \rangle)^2) \sim 1$$

$$\langle m_i \rangle = \langle g_i \rangle (1 + (A/\alpha) \langle g_i \rangle) (1 - \sum_j (A_{ij}/\alpha) \langle m_j \rangle) \quad (\text{E.4})$$

and we may approximate $\langle m_j \rangle$ by $\langle g_j \rangle$ to obtain

$$\begin{aligned}
 \langle m_i \rangle &= \langle g_i \rangle (1 + (A/\alpha) \langle g_i \rangle) (1 - \sum_j (A_{ij}/\alpha) \langle g_i \rangle) \\
 &= \langle g_i \rangle (1 + (A/\alpha) \langle g_i \rangle - \sum_i (A_{ij}/\alpha) \langle g_i \rangle \\
 &\quad - (A/\alpha) \langle g_i \rangle \sum_j (A_{ij}/\alpha) \langle g_i \rangle) \\
 &= \langle g_i \rangle + (A/\alpha) \langle g_i \rangle^2 - \langle g_i \rangle \sum_j (A_{ij}/\alpha) \langle g_i \rangle \\
 &\quad - (A/\alpha) \langle g_i \rangle^2 \sum_j (A_{ij}/\alpha) \langle g_j \rangle
 \end{aligned} \tag{E.5}$$

Comparing to Nelson's model, from Eq. (2.21) we see that the chemical spread function, A_{ij} , is proportional to Nelson's, B , and only equal for the case $\alpha = 1$. In addition, the only other difference in the form of the models is the presence of the higher order terms in the statistical models. These terms may cause the necessary adjustment to make the statistical model more accurate for higher density levels.

REFERENCES

- Anuta, Paul E., "Spatial Registration of Multispectral and Multitemporal Digital Imagery using Fast Fourier Transform Techniques," IEEE Transactions on Geoscience Electronics, GE-8, No. 4, October 1970, pp. 353-368.
- Barakat, Richard, "Determination of the Optical Transfer Function Directly from the Edge Spread Function," J. Opt. Soc. Am., 55, No. 10, October 1965, pp. 1217-1221.
- Barosi, N. J., "Industrial Application of Cubic Spline Functions," Technical Conference of The American Society for Quality Control and The American Statistical Association, October 1973.
- Barrows, Robert E., and Wolfe, Robert N., "A Review of Adjacency Effects in Silver Photographic Images," Photogr. Sci. & Engr., 15, No. 6, November-December 1971, pp. 472-479.
- Benton, S. A., and Kronauer, R. E., "Properties of Granularity Weiner Spectra," J. Opt. Soc. Am., 61, 1971, p. 524.
- Blackman, E. S., "Effects of Noise on the Determination of Photographic System Modulation Transfer Functions," Photogr. Sci. & Engr., 12, No. 5, September-October 1968, pp. 244-250.
- Bracewell, Ron, The Fourier Transform and It's Applications, McGraw-Hill Book Co., 1965.
- Brigham, E. Oran, The Fast Fourier Transform, New Jersey, Prentice-Hall, 1974.
- Burke, James J., "Estimating Objects from their Blurred and Grainy Images," Proceedings of the Electro-Optical Systems Design Conference, San Francisco, California, November 5 - 7, 1974, pp. 65 - 80.
- Butler, John C., "Laser Interferometer Controlled Microdensitometer," Opt. Engr. 12, No.6, November-December 1973, pp. 213-217.
- Colson, R., "Photographic Development," Compt. Rend., 126, 1898, p. 470-473.
- Dainty, J. C., and Shaw, R., Image Science, Academic Press, 1974.
- Data Corporation, The Mann-Data Micro-Analyzer, Model II, Raster Scan Version, May 1970.
- deBoor, C. and Rice, J. R., "Cubic Spline Approximation I - Fixed Knots," Computer Sciences Department, T.R. 20, Purdue University, 1968a.
- deBoor, C. and Rice J. R., "Cubic Spline Approximation II - Variable Knots," Computer Sciences Department, T.R. 21, Purdue University, 1968b.

- Duffieux, P. M., *The Fourier Integral and its Applications in Optics*, Second Edition, Masson and Cie, Paris, 1970.
- Dutton, David, "Noise and Other Artifacts in OTF Derived from Image Scanning," *Appl. Opt.*, 14, No. 2, February 1975, pp. 513-521.
- Eastman Kodak Company, *Kodak Neutral Density Attenuators*, Phamplet No. P - 114, July 1967.
- Eberhard, G., "The Mutual Influence of Adjacent Fields upon the Silver Bromide Plate," *Phys. Z.*, 13, 1912, p.288-292.
- Eberhard, G., "Photographische-Photometrische Untersuchungen," *Publ. Astrophys. Observ. Potsdam*, 26, Nr. 84, Heft 1, 1926, p. 45.
- Ehn, Dennis C., and Silevitch, Michael B., "Diffusion Model for the Adjacency Effect in Viscous Development," *J. Opt. Soc. Am.*, 64, No. 5, May 1974, pp. 667-676.
- Eyer, James A., "Spatial Frequency Response of Certain Photographic Emulsions," *J. Opt. Soc. Am.*, 48, No. 12, December 1958, pp. 938-944.
- Feller, W., *Introduction to Probability Theory and Its Applications*, Vol. I., Wiley, New York, 1968.
- Fellgett, P. B., and Linfoot, E. H., "On the Assessment of Optical Images," *Phil. Trans. Roy. Soc.*, 247A, 1955, p. 369.
- Findley, J. D., and Marshall, W. W., *Image Assessment Research*, Data Corporation Final Report FR-65-9, July 1965.
- Fuller, W. A., "Grafted Polynomials as Approximating Functions," *Australian Journal of Agricultural Economics*, 13, 1969, p. 35.
- Gaskill, Jack D., *Linear Systems, Fourier Transforms, and Optics*, John Wiley & Sons, 1978.
- Goodman, Joseph W., *Introduction to Fourier Optics*, McGraw-Hill Book Co., 1968.
- Gurney, R. W., and Mott, N. F., "The Theory of the Photolysis of Silver Bromide and the Photographic Latent Image," *Proc. Roy. Soc. (London)*, Ser A, 164, 1938, p. 151.
- Hendeberg, L. O., "The Contrast Transfer of Periodical Structures in a Photographic Emulsion Developed with Adjacency Effects," *Arkiv For Fysik*, Band 16 nr 39, 1960, pp. 457-468.
- Higgins, G. C., "Methods for Analyzing the Photographic System, Including the Effects of Nonlinearity and Spatial Frequency Response," *Photogr. Sci. & Engr.*, 15, No. 2, March-April 1971, pp. 106-118.
- Hopkins, H. H., *Wave Theory of Aberrations*, Oxford Clarendon Press, 1950.
- Hopkins, H. H., "The Frequency Response of Optical Systems," *Proc. Phys. Soc.*, 69, 1956, pp. 562-576.

- Hurter, F., and Driffield, V. C., "Photo-Chemical Investigations," *J. Soc. Chem. Ind. (London)*, 9, 1890, p. 725.
- Ingelstam, E., Djurle, E., and Sjogren, B., "Contrast-Transmission Functions Determined Experimentally for Asymmetrical Images and for the Combination of Lens and Photographic Emulsion," *J. Opt. Soc. Am.*, 46, 1956, p. 707.
- Ingelstam, Erik, "Linear and Non-Linear Links in Optical Image Transfer," *Communication and Information Theory Aspects of Modern Optics Symposium, General Electric Company, Electronics Laboratory*, August 1962, pp. 5-30.
- Jones, Robert A., "An Automated Technique for Deriving MTF'S from Edge Traces," *Photogr. Sci. & Engr.*, 11, No. 2, March-April 1967, pp. 102-106.
- Jones, Robert A. and Yeadon, Edward C., "Determination of the Spread Function from Noisy Edge Scans," *Photogr. Sci. & Engr.*, 13, No. 4, July-August, 1969, pp. 200-204.
- Kelly, D. H., "Systems Analysis of the Photographic Process. I. A Three-Stage Model," *J. Opt. Soc. Am.*, 50, No. 3, March 1960, pp. 269-276.
- Kelly, D. H., "Systems Analysis of the Photographic Process. II. Transfer Function Measurements," *J. Opt. Soc. Am.*, 51, No. 3, March 1961, pp. 319-330.
- Kriss, M. A., Nelson, C. N., and Eisen, F. C., "Modulation Transfer Function in Photographic Systems Containing Development Adjacency Effects," *Photogr. Sci. & Engr.*, 18, No. 2, March-April 1974, pp. 131-138.
- Lehmbeck, Donald R. and Jakubowski, James J., "Optical Principles and Practical Considerations for Reflection Microdensitometry," *J. of App. Photogr. Engr.*, 5, No. 2, Spring 1979, pp. 63-77.
- Levine, Bruce M., "A Segmented Polynomial Linear Model for the D Log E Curve," M. S. Thesis, Colorado State University, 1976.
- Marechal, A., "The Transmission of Spatial Frequencies by Optical Instruments," *Rev. Opt.*, 35, 1956, p.603-607.
- Mees, C. E. Kenneth, and James, T. H., *The Theory of the Photographic Process, Third Edition*, Macmillan Co., 1966.
- Middleton, D., *Statistical Communication Theory*, McGraw-Hill, New York, 1960.
- Moore, J. E., Happ, G. P. and Stewart, D. W., "Automatic Direct-Reading X-Ray Spectrometry Application to Determination of Silver," *Anal. Chem.*, 33, No. 1, January 1961, pp. 61-64.
- Nelson, C. N., "Prediction of Densities in Fine Detail in Photographic Images," *Photogr. Sci. & Engr.*, 15, No. 1, January-February 1971, pp. 82-97.
- O'Neill, Edward L., "The Analysis and Synthesis of Linear Coherent and Incoherent Optical Systems," Tech. Note No. 122, Optical Research Laboratory, Boston University, 1955.

- O'Neill, Edward L., Introduction to Statistical Optics, Addison-Wesley Publ. Co., 1963.
- Powell, P., G., "Some Applications of a Microdensitometer to the Study of the Photographic Reproduction of Fine Detail," J. of Photogr. Sci., 7, 1959, pp. 157-161.
- Powell, P., G., "The Frequency Response of Photographic Reproductions in the Presence and the Absence of Diffusion Effects during Development," J. of Photogr. Sci., 9, 1961, pp. 312-315.
- Rabedeau, M. E., "Effect of Truncation of Line-Spread and Edge-Response Functions on the Computed Optical Transfer Function," J. Opt. Soc. Am., 59, No. 10, October 1969, pp. 1309-1314.
- Rice, S. O., "Mathematical Analysis of Random Noise", Elected Papers on Noise in Stochastic Processes, Ed. by Nelson Wax, Dover Publications, 1954, pp. 133-295.
- Sayanagi, Kazuo, "Fourier Analysis of the Adjacency Effect in Photographic Emulsion," Appl. Phys. Japan, 29, February 1960, p. 185.
- Schade, O. H., "Image Gradation, Graininess, and Sharpness in Television and Motion-Picture Systems; I. Image Structure and Transfer Characteristics," J. Soc. Motion Pict. Tel. Engr., 56, No. 2, February 1951, p. 137-177.
- Schade, O. H., "Image Gradation, Graininess, and Sharpness in Television and Motion-Picture Systems; IV. Image Analysis in Photographic and Television Systems." J. Soc. Motion Pict. Tel. Engrs., 64, No. 11, November 1955, pp. 593-617.
- Schade, Otto H., "An Evaluation of Photographic Image Quality and Resolving Power," J. Soc. Motion Pict. Tel. Engrs., 73, No. 2, February 1974, pp. 81-119.
- Schowengerdt, R. A., Antos, R. L. and Slater, P. N., "Measurement of the Earth Resources Technology Satellite (ERTS-1) Multi-Spectral Scanner OTF from Operational Imagery," Proc. of S.P.I.E. , 46, May 20-22, 1974, pp. 247-257.
- Schowengerdt, Robert A., "A Method for Determining the Operational Imaging Performance of Orbital Earth Resources Sensors," Ph. D. Dissertation, University of Arizona, 1975.
- Scott, F., Scott, R. M. and Shack, R. V., "The Use of Edge Gradients in Determining Modulation-Transfer Functions," Photogr. Sci. & Engr., 7, No. 6, November-December 1963, pp. 345-349.
- Sherwood, H. F., "Apparatus for Making Sharp Photographic Images with X-Rays," Rev. of Sci. Instr., 38, No. 11, November 1967, pp. 1619-1622.
- Silevitch, M. B., Gonsalves, R. A., and Ehn, D. C., "Prediction and Removal of Adjacency Effects from Photographic Images," Photogr. Sci. & Engr., 21, No. 1, January-February 1977, pp. 7-13.
- Simonds, J. L., "Reproduction of Fine Line Structure in Photographic Printing: II. Spatial Interactions of the Development Process," Photogr. Sci. & Engr., 8, 1964, pp. 174-177.

- Simonds, J. L., "Analysis of Nonlinear Photographic Systems," *Photogr. Sci. & Engr.*, 9, No. 5, September-October 1965, pp. 294-300.
- Smith, Warren J., *Modern Optical Engineering - The Design of Optical Systems*, McGraw-Hill Book Co., 1966.
- Swing, R. E. and McCamy, C. S., "Edge Gradient Analysis: A Critique," National Bureau of Standards, TR. No. 10 119, October 1969, pp. 1-35.
- Swing, Richard E., "Microdensitometer Optical Performance: Scalar Theory and Experiment," *Opt. Engr.*, 15, No. 6, November-December 1976, pp. 559-577.
- Takeda, Mitsuo and Ose, Teruji, "Effect of Truncation of Noisy Line Spread Function on the Computed Optical Transfer Function," *Optica Acta*, 21, No. 6, June 1974, pp. 477-487.
- Tatian, Berge, "Method for Obtaining the Transfer Function from the Edge Response Function," *J. Opt. Soc. Am.*, 55, No. 8, August 1965, pp. 1014-1019.
- Tatian, Berge, "Asymptotic Expansions for Correcting Truncation Error in Transfer Function Calculations," *J. Opt. Soc. Am.*, 61, No. 9, September 1971, pp. 1214-1224.
- Van Trees, H. L., *Detection Estimation and Modulation Theory Part I*, Wiley & Sons, New York, 1968.
- Wolfe, Robert N. and Barrows, Robert S., "Adjacency Effects in Photography," *P. S. A. J.*, 13, September 1947, pp. 554-556.
- Wyatt, Clair L., *Radiometric Calibration: Theory and Methods*, Academic Press, 1978.